Coupling lattice, charge and topological reconstructions at oxide interfaces

van Thiel, T.C.

DOI
10.4233/uuid:8079a208-fda0-49ab-9048-df1f9a0158e0

Publication date
2022

Document Version
Final published version

Citation (APA)
van Thiel, T. C. (2022). *Coupling lattice, charge and topological reconstructions at oxide interfaces*. [Dissertation (TU Delft), Delft University of Technology]. https://doi.org/10.4233/uuid:8079a208-fda0-49ab-9048-df1f9a0158e0

Coupling lattice, charge and topological reconstructions at oxide interfaces

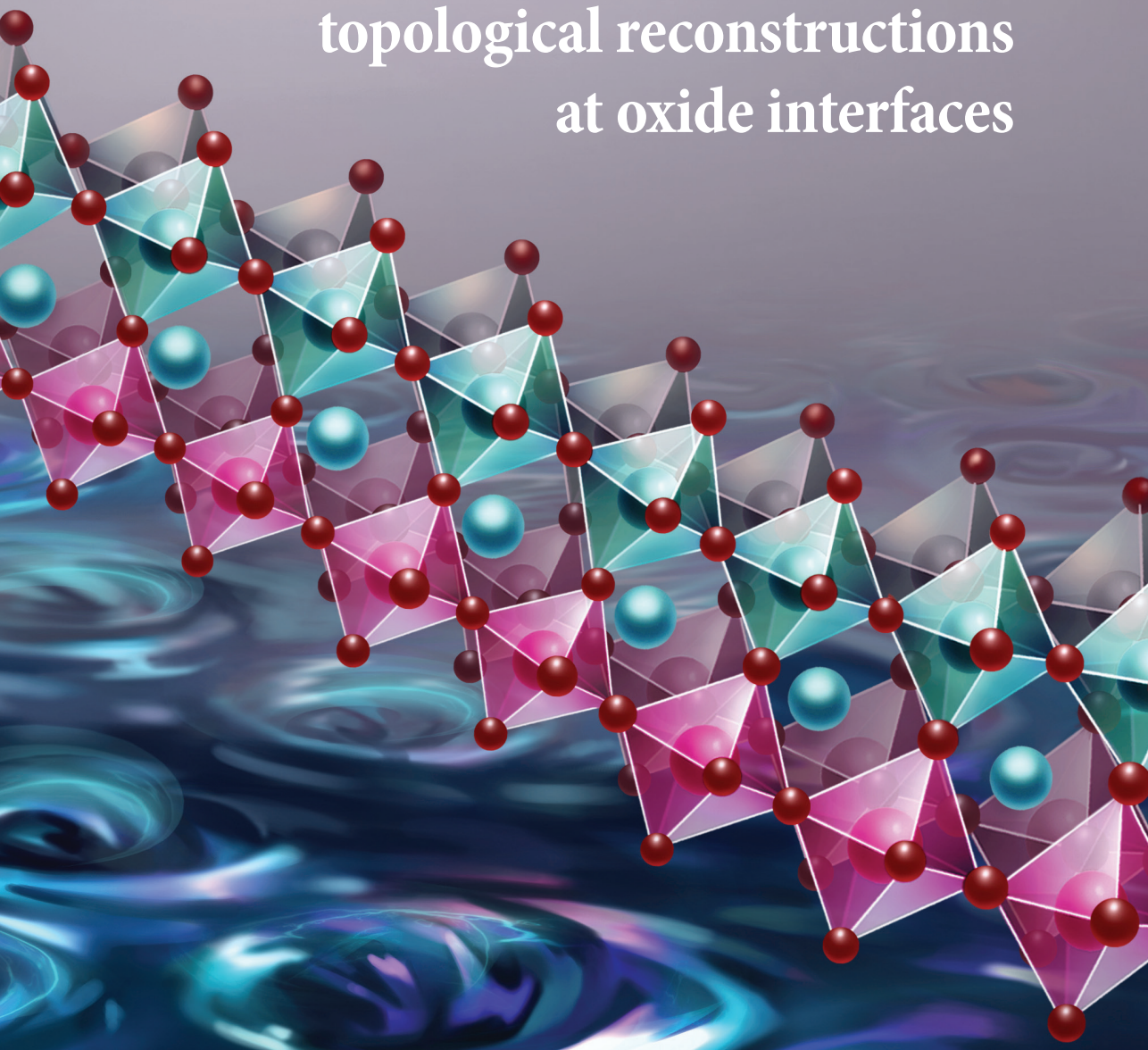

Thierry van Thiel

COUPLING LATTICE, CHARGE AND TOPOLOGICAL RECONSTRUCTIONS AT OXIDE INTERFACES

COUPLING LATTICE, CHARGE AND TOPOLOGICAL RECONSTRUCTIONS AT OXIDE INTERFACES

Proefschrift

ter verkrijging van de graad van doctor
aan de Technische Universiteit Delft,
op gezag van de Rector Magnificus prof.dr.ir. T.H.J.J. van der Hagen,
voorzitter van het College voor Promoties,
in het openbaar te verdedigen op maandag 31 januari 2022 om 15:00 uur.

door

Thierry Christiaan VAN THIEL

Natuurkundig Ingenieur,
Technische Universiteit Delft, Nederland

geboren te Hoogeveen, Nederland.

Dit proefschrift is goedgekeurd door de promotoren

Dr. A.D. Caviglia
Dr. A.R. Akhmerov

Samenstelling promotiecommissie:

Rector Magnificus,	voorzitter
Dr. A.D. Caviglia,	Technische Universiteit Delft (promotor)
Dr. A.R. Akhmerov,	Technische Universiteit Delft (promotor)

Onafhankelijke leden:

Prof.dr. Y.M. Blanter,	Technische Universiteit Delft
Dr. S.C. Conesa-Boj,	Technische Universiteit Delft
Dr. M. Cuoco,	Università degli Studi di Salerno (Italy)
Prof.dr. B. Kalisky,	Bar-Ilan University (Israel)
Prof.dr. T.T.M. Palstra,	Universiteit Twente
Prof.dr. P.G. Steeneken	Technische Universiteit Delft (reserve)

Keywords: Complex oxides, oxide interfaces, lattice instabilities, anomalous Hall effect, topological reconstructions, polar discontinuity

Printed by: Gildeprint, Enschede

Front & Back: Artistic impression of two-dimensional momentum-space topological charges in a perovskite crystal. Image produced by Ella Maru Studio.

Casimir PhD series 2021-48
ISBN 978-90-8593-511-7

To my family

Contents

SUMMARY

Modern materials synthesis techniques allow for the layer-by-layer assimilation of structurally similar, yet compositionally different materials into artificial crystals, with atomic scale precision. At the resulting heterointerfaces, structural, electronic and magnetic reconstructions can lead to physical phenomena that are otherwise absent in the individual constituents. Composing so-called heterostructures is therefore one of the key approaches towards realizing the ultimate goal of designer materials with tailored properties. In this context, perovskite oxides represent a promising class of materials, owing to the combination of a delicate balance among competing electronic and magnetic interactions, as well as excellent structural compatibility among its members. This thesis describes a collection of investigations into interface-driven reconstructions in heterostructures composed of such perovskite oxides.

In the first chapter, I provide a brief introduction into the field of complex oxide heterostructures, describing a number of characteristic examples of interface phenomena and identifying the motivations that drive research into this subject. Then, I reveal the protagonist materials of this thesis, namely spin-orbit semimetal $SrIrO_3$ and itinerant ferromagnet $SrRuO_3$, which — owing to a fascinating interplay between crystal symmetry, spin-orbit coupling and magnetic interactions — are actively studied, with a particular focus on the topological properties of their electronic structures. Lastly, I touch upon how avoided level crossings in band structures act as sources and sinks of momentum-space Berry curvature, thereby producing the anomalous Hall effect. In the second chapter, I delve into the methodology of the synthesis and characterization of thin films and heterostructures, discussing the technical aspects of pulsed-laser deposition, reflection high-energy electron diffraction, X-ray diffraction and finally lithographic fabrication and cryogenic magnetotransport measurements.

Having set the stage, we proceed with Chapter 3, where we interface $SrIrO_3$ with the bandgap insulator $SrTiO_3$. In transport measurements, we observe an anomaly in the temperature-dependence of the resistivity at the cubic-to-tetragonal transition temperature of the $SrTiO_3$ substrate. Aided by synchrotron X-ray diffraction measurements, we show that this anomaly can be ascribed to a coupling of orthorhombic structural domains in the overlying $SrIrO_3$ film to the tetragonal multi-domain state of the $SrTiO_3$ substrate that manifests below 105 K. These results identify the coupling of lattice instabilities across heterointerfaces as a promising avenue to control functional properties in complex oxides.

In Chapter 4, we interface $SrRuO_3$ with both $SrIrO_3$ and $SrTiO_3$, and show that the two possible heterointerfaces — namely $SrRuO_3/SrIrO_3$ and $SrRuO_3/SrTiO_3$ — promote positive and negative signs, respectively, of the momentum-space Berry curvature and

anomalous Hall effect. In asymmetric $SrTiO_3/SrRuO_3/SrIrO_3$ heterostructures, the competition between positive and negative contributions causes peculiar bump features in the magnetic field dependence of the anomalous Hall effect. This observation is well captured by a phenomenological two-channel model and interpreted as a spatially inhomogeneous profile of the magnetization in the vicinity of a sign change of the momentum-space Berry curvature. Finally, we show that this effect can be mimicked by two $SrRuO_3$ layers of slightly different thicknesses separated by an insulating $SrTiO_3$ spacer, thereby creating an all-oxide extraordinary Hall balance device. Then, in Chapter 5, we build upon the insights obtained in Chapter 4 and create heterointerfaces between $SrRuO_3$ and the bandgap insulator $LaAlO_3$. Transmission electron microscopy measurements reveal a $SrO/RuO_2/LaO$ interface configuration, creating a charge-frustrated state in the top layer of the $SrRuO_3$ film. The resulting charge profile along the growth axis is found to lower both the magnetization and Curie temperature, and to drive an evolution of the momentum-space topological charges, thereby changing the sign of the Berry curvature. The findings obtained in these chapters illustrate how interface-engineering may be used to manipulate the magnetic and topological properties of ultrathin ferromagnetic metals, and highlight the potential of ultrathin $SrRuO_3$ for spintronic applications.

In Chapter 6, we synthesize $SrRuO_3$ thin films on $SrTiO_3$ substrates with a (111) crystal orientation, realizing a hexagonal lattice configuration in the plane of the film, as opposed to the square configuration of the (001) oriented films considered in the previous chapters. We propose that the triaxial compressive strain exerted by the $SrTiO_3$ substrate is in part accommodated by so-called Ruddlesden-Popper defects, thereby diminishing monoclinic shearing effects. In transport, a nonlinear classical Hall effect is observed, which becomes more prominent towards the ultrathin limit i.e., for a strong confinement of the electronic bands along the growth axis. High-field measurements reveal an unsaturating positive linear magnetoresistance, which is suggestive of a semiclassical contribution in magnetotransport, namely guiding center motion. These results highlight the combination of crystal symmetry and spatial confinement as an important factor determining the structural and electronic features of oxide thin films.

In the concluding chapter, we summarize the findings of this thesis and provide several research directions worthy of further pursuit; spatially-resolved magnetometry in $SrRuO_3$ ultrathin films, polar $SrIrO_3$-based heterostructures and the design of Berry curvature dipoles in time-reversal invariant oxide heterostructures.

SAMENVATTING

Moderne materiaalsynthese technieken maken het mogelijk om structureel vergelijkbare, doch compositioneel verschillende materialen laag-voor-laag te integreren in artificiële kristallen, met een nauwkeurigheid op atomaire schaal. Bij de resulterende grensvlakken leiden structurele, elektronische en magnetische veranderingen mogelijkerwijs tot fysieke verschijnselen welke anders afwezig zouden zijn in de individuele bestandsdelen. Het samenstellen van zogenaamde heterostructuren is daarom één van de belangrijkste technieken om het ultieme doel van 'designer materialen' met op maat gemaakte eigenschappen te realiseren. In deze context vertegenwoordigen perovskiet oxiden een veelbelovende categorie van materialen, wat toegeschreven kan worden aan de combinatie van zowel een gevoelige balans tussen concurrerende elektronische and magnetische wisselwerkingen, als een uitstekende onderlinge structurele compatibiliteit. Dit proefschrift omvat een verzameling van onderzoeken naar grensvlak modificaties in heterostructuren bestaande uit zulke perovskiet oxiden.

In het eerste hoofdstuk introduceer ik het vakgebied van heterostructuren van complexe oxiden met behulp van een aantal karakteristieke voorbeelden van grensvlak fenomenen en identificeer ik de drijfveren voor onderzoek naar dit onderwerp. Vervolgens onthul ik de materialen met een hoofdrol in dit proefschrift, namelijk het spin-baan semimetaal $SrIrO_3$ en het ferromagnetische metaal $SrRuO_3$, welke beide — vanwege een fascinerende combinatie tussen kristalsymmetrie, spin-baan koppeling en magnetische wisselwerkingen — actief worden onderzocht, met een nadruk op de topologische eigenschappen van hun elektronische structuren. Tot slot beschrijven we kort hoe vermeden niveau kruisingen in bandstructuren zich gedragen als bronnen van Berry kromming in de impulsruimte en zodoende leiden tot het anomalous Hall effect. In het tweede hoodstuk beschrijf ik de methodiek van de synthese en karakterisatie van dunne films en heterostructuren, en bediscussieer ik de technische kanten van gepulseerde laser afzetting, reflectie hoog-energie elektron diffractie, röntgendiffractie en uiteindelijk lithografie en cryogene magnetotransport metingen.

De toon gezet hebbende gaan we verder met Hoofdstuk 3, waar we $SrIrO_3$ koppelen aan de bandkloof isolator $SrTiO_3$. In transportmetingen zien we een onregelmatigheid in de temperatuurafhankelijkheid van de soortelijke weerstand, bij de temperatuur waar het $SrTiO_3$ substraat overgaat van een kubische naar een tetragonale toestand. Door middel van onder andere synchrotron röntgendiffractie metingen laten we zien dat de onregelmatigheid toegeschreven kan worden aan een koppeling tussen orthorhombische structurele domeinen in de bovenliggende $SrIrO_3$ film en de tetragonale multidomein toestand van het $SrTiO_3$ substraat dat manifesteert onder de 105 K. Deze resultaten identificeren de koppeling tussen roosterinstabiliteiten over grensvlakken als een veelbelovende aanpak om functionele eigenschappen in complexe oxiden te kunnen bepalen.

In Hoofdstuk 4 koppelen we $SrRuO_3$ aan zowel $SrIrO_3$ als $SrTiO_3$ en demonstreren we dat de twee mogelijke grensvlakken — namelijk $SrRuO_3/SrIrO_3$ en $SrRuO_3/SrTiO_3$ — positieve en negatieve tekens, respectievelijk, bevorderen van de Berry kromming in de impulsruimte en het anomalous Hall effect. In asymmetrische $SrTiO_3/SrRuO_3/SrIrO_3$ heterostructuren veroorzaakt de concurrentie tussen positieve en negatieve bijdragen ongebruikelijke uitstulpingen in de magnetische veldafhankelijkheid van het anomalous Hall effect. Deze observatie wordt goed beschreven door middel van een twee kanalen model, geïnterpreteerd als een ruimtelijk inhomogeen profiel van de magnetisering in de nabijheid van een tekenwissel van de Berry kromming. Tot slot laten we zien dat dit effect nagebootst kan worden door twee $SrRuO_3$ lagen met marginaal verschillende dikten, gescheiden door een isolerende $SrTiO_3$ tussenlaag, waarbij een volledig oxide *extraordinary Hall balance* gecreëerd wordt. In Hoofdstuk 5 bouwen we vervolgens voort op de inzichten vergaard in Hoofdstuk 4 en vervaardigen we grensvlakken tussen $SrRuO_3$ en de bandkloof isolator $LaAlO_3$. Transmissie elektronen microscopie metingen onthullen een $SrO/RuO_2/LaO$ configuratie van het grensvlak, wat een ladingsgefrustreerde toestand produceert. Het resulterende ladingsprofiel langs de groeias blijkt de magnetisering en Curie temperatuur te verlagen en een evolutie van de topologische ladingen in de impulsruimte teweeg te brengen, waarbij het teken van de Berry kromming wisselt. De gedane bevindingen in deze hoofdstukken schetsen hoe grensvlakontwerp gebruikt kan worden om de magnetische en topologische eigenschappen van ultradunne ferromagnetische metalen te manipuleren, en benadrukken de potentie van ultradun $SrRuO_3$ voor toepassingen in de spintronica.

In Hoofdstuk 6 vervaardigen we dunne $SrRuO_3$ films op $SrTiO_3$ substraten met een (111) kristaloriëntatie, wat een hexagonale roosterconfiguratie in het vlak van de film produceert. Dit staat in tegenstelling tot de vierkante configuratie van de (001) films beschouwd in de voorgaande hoofdstukken. We beargumenteren dat de triaxiale drukspanning, die wordt uitgeoefend door het $SrTiO_3$ substraat, deels geaccommodeerd wordt door zogenaamde Ruddlesden-Popper defecten, wat monoklinische schuifspanningseffecten vermindert. In transportmetingen observeren we een nonlineair klassiek Hall effect, wat prominenter wordt richting de ultradunne limiet, ofwel een steeds sterkere ruimtelijke beperking van de elektronische banden. Hoog-veldmetingen ontsluieren een onverzadigende positieve lineaire magnetoweerstand, wat een semiklassieke bijdrage in magnetotransport suggereert, namelijk krommingsmiddelpunt beweging. Deze resultaten onderstrepen de combinatie van kristalsymmetrie en ruimtelijke beperking als een belangrijke factor die de structurele en elektronische kenmerken van dunne oxide films bepaalt.

In het laatste hoofdstuk vatten we de bevindingen van dit proefschrift samen en verschaffen we verscheidene onderzoeksrichtingen die de moeite waard zijn om verder te verkennen; ruimtelijk gedefinieerde magnetometrie in ultradrun $SrRuO_3$, polaire op $SrIrO_3$ gebaseerde heterostructuren en het ontwerp van Berry kromming dipolen in tijdomkering-invariante oxide heterostructuren.

1

Introduction

"The answers we have found have only served to raise a whole set of new questions. In some ways we feel that we are as confused as ever, but we think we are confused on a higher level, and about more important things."

– Earl C. Kelley

This chapter begins with a brief introduction to the field of complex oxide interfaces and introduces the two protagonist materials of this thesis; spin-orbit semimetal $SrIrO_3$ and the itinerant ferromagnet $SrRuO_3$. Next, the momentum-space Berry curvature and its relationship to the intrinsic anomalous Hall effect are discussed. Finally, an outline of the remainder of the thesis is provided.

1

DOES consciousness arise from neurons in the brain? Why does a bee colony function as a superorganism? How does life develop from non-living matter? Perhaps many of such questions, if not all, boil down to: How do the properties of a complex system *emerge* from its constituent parts? This matter has been at the center of attention in science throughout history and continues to puzzle researchers today. Narrowing the scope to condensed matter systems, one might pose the question: How do atoms in a solid produce macroscopic phenomena such as superconductivity or magnetic order? It is not obvious that a set of particles would exhibit coordinated collective behaviour, similar to swarming insects, murmurating starlings or schooling fish (see Fig. 1.1). All of these systems have one thing in common; their constituents *interact* with one another to produce so-called *emergent* phenomena.

How macroscopic properties emerge from interacting microscopic particles is one of the research questions that drives the field of condensed matter physics and in particular the field of complex oxides[1]. The properties of a complex oxide system are all but trivial to predict, as seemingly similar materials can have radically different ground states; $LaTiO_3$ is a Mott insulator, while $BaTiO_3$ is ferroelectric. $SrRuO_3$ is a ferromagnet, whereas $CaRuO_3$ is a paramagnet and yet $CaMnO_3$ is an antiferromagnet. The emergence of an ordered state out of seemingly unordered components coincides with a spontaneous breaking of some symmetry of the system e.g., time-reversal symmetry in magnets, gauge symmetry in superconductors or inversion symmetry in ferroelectrics. It is then very tempting to ask the converse question; if we deliberately break a given symmetry of a condensed matter system, can we realize new physical properties? This question is central to the field of complex oxide interfaces.

Figure 1.1: Emergence in complex systems. (Left) murmurating starlings in the shape of a sperm whale and (right) schooling fish. Each individual unit of the flock or school reacts to stimuli from its local environment. This leads to the emergence of collective behaviour, without a form of centralized control.

[1] An oxide containing two or more different cations.

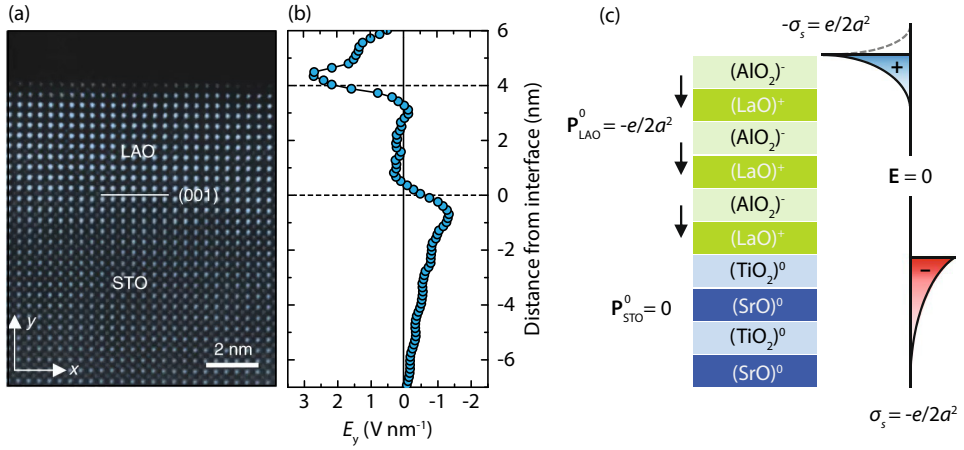

Figure 1.2: Polar discontinuity and charge reconstruction in LAO/STO. (a) Transmission electron microscopy image of a 10 u.c. LAO/STO (001) heterostructure. (b) Out-of-plane component (E_y) of the internal electric field generated by the polar layers in LAO (determined through electron holography measurements). (c) Illustration of the polar discontinuity between LAO and STO and the resulting accumulation of excess positive and negative charges at the boundaries of the LAO layer. The charge configuration compensates the in-built polarization of LAO. Figure adapted from ref. [1].

1.1. COMPLEX OXIDE INTERFACES

A heterostructure or heterojunction consists of two or more structurally compatible, yet compositionally different materials, integrated into a crystal. In the 1950s, the semiconducting heterojunction was proposed as an alternative to the homojunction[2] to reduce the unwanted backflow of majority carriers from the base into the emitter in the bipolar transistor [2–4]. The proposal was that, if two semiconductors with different bandgaps were used as opposed to the same material with regions of different doping levels, the resulting band realignment would lead to a strong suppression of backflow from the base into the emitter, thereby allowing heavier doping of the base to improve its speed [5]. The notion of band alignments and offsets between dissimilar materials further lead to the development of the semiconductor quantum well [6], where free carriers could be confined to a region of the crystal narrower than the Fermi wavelength λ_F, thereby creating a highly mobile two-dimensional electron gas.

In 2004, the concept of heterostructure band alignment made its way into the field of perovskite oxides, with the discovery of a conducting state at the interface between the wide bandgap insulators $LaAlO_3$ (LAO) and $SrTiO_3$ (STO) [7], which was later shown to be superconducting and controllable via electrostatic gating [8, 9]. Importantly, there is a difference in the nominal valence state between Sr^{2+} and La^{3+}, as well as Ti^{4+} and Al^{3+}. Along the (001) crystallographic direction, STO consists of neutral SrO and TiO_2 planes. In contrast, LAO consists of charged LaO^+ and AlO_2^- planes, leading to an energetically costly polar discontinuity at the interface (see Fig. 1.2). This can be compensated for

[2] An interface between two of the same semiconducting materials with different doping characteristics.

either through ionic intermixing, or by creating an electron-doped layer of STO near the interface, combined with a positively charged LAO surface [1, 10]. While it was known that electron-doping of $SrTiO_3$ produces a superconducting state [11], a number of advantages came with the LAO/STO heterostructure. Near the interface, inversion symmetry i.e., invariance with respect to the operation $\mathbf{r} \rightarrow -\mathbf{r}$, is broken. Electronic processes that were previously symmetry forbidden, such as nearest-neighbour hopping between different orbitals, may now be possible, which can have a strong impact on the electronic structure. An example is the Rashba effect which, in conjunction with the atomic spin-orbit interaction, couples an electron spin to its momentum [12]. This mechanism is of interest for spintronics, since it allows for the conversion of a charge into a spin current and vice versa [13, 14]. Additionally, the intriguing combination of a strong spin-orbit coupling and intrinsic two-dimensional superconductivity has attracted attention in the context of realizing topologically non-trivial superconducting gaps [15].

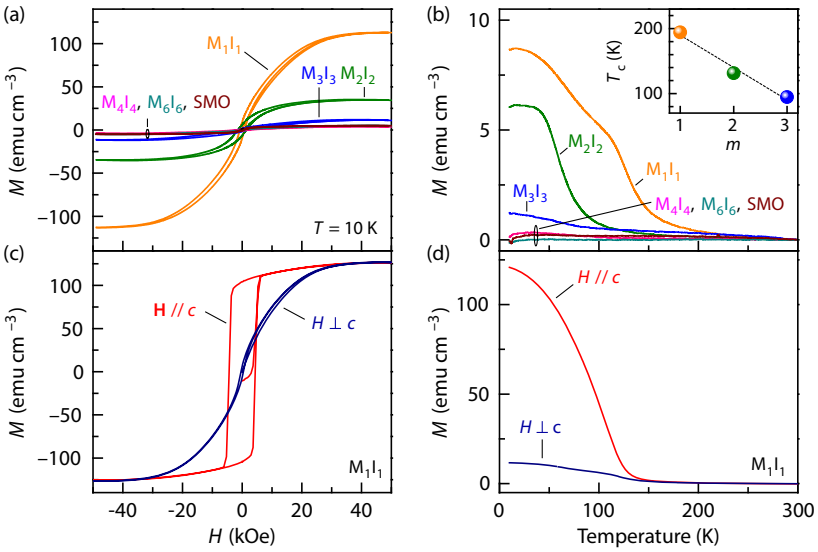

Figure 1.3: Emerging magnetism in manganite-iridate superlattices. (a) Magnetization M as a function of external field H of SMO_n/SIO_n superlattices (labeled M_nI_n) at $T = 10$ K after zero-field cooling. (b) M as a function of temperature T at $H = 1$ kOe after field cooling in $H = 1$ kOe. The inset shows the thickness (m) dependence of the Curie temperature. (c) $M(H)$ of M_1I_1 at $T = 10$ K after zero-field cooling. (d) $M(T)$ of M_1I_1 at $H = 1$ kOe after field cooling in $H = 1$ kOe. The c-axis is oriented perpendicular to the sample plane. Figure adapted from ref. [16].

LAO/STO may have been one of the first examples of novel phenomenology in heterostructures, but it is by no means the only one. Heteroepitaxial growth[3] of thin films and superlattices[4], for example, has on multiple occasions been used to impose crystal strain in adjacent crystal layers, leading to a lattice structure that is distinct from

[3] Crystal growth with a coherent well defined orientation with respect to another crystal layer.
[4] A repeating structure of different epitaxial crystal layers.

the bulk form and a concomitant change in the physical properties. Examples of this approach include strain-induced enhancement of the superconducting critical temperature in $SrTiO_3$ [17], strain-induced superconductivity in RuO_2 thin films [18, 19] and strain-dependent modulation of the metal–insulator transition in $ANiO_3$ nickelates [20–22]. Apart from static strain, it has also been demonstrated that phonons[5] can couple across interfaces, thereby affecting conductivity through electron-phonon scattering [23] or even drive a metal–insulator transition through changes in the metal-oxygen bonds, driven by optically excited phonons in the substrate [24].

A particularly rich area of interface-driven phenomena is found in magnetic heterostructures, a research direction that has been receiving an increasing amount of attention since the discovery of the giant magnetoresistance effect in magnetic/non-magnetic multilayers [25, 26]. In oxide heterostructures, magnetic and electronic properties might be altered by e.g., charge transfer [16, 27–29] or so-called octahedral tilting [30, 31]. Fig. 1.3 shows another example of a magnetic heterostructure i.e., superlattices consisting of antiferromagnetic $SrMnO_3$ (SMO) and paramagnetic $SrIrO_3$ (SIO) [16]. The combination of these two materials leads to ferromagnetism, yet neither exhibits ferromagnetic order on their own. The ferromagnetic signature, which arises from electronic charge transferred from Ir to Mn, was found to originate mainly from Mn spin moments, with a small contribution from Ir orbital moments. Another example of emerging magnetism in heterostructures has been demonstrated in $LaNiO_3/LaMnO_3$ (LNO/LMO) superlattices [32], where the interface interaction between ferromagnetic LMO and paramagnetic LNO leads to antiferromagnetic order in the latter, as well as an exchange bias effect in the multilayer stack. From a spintronics perspective, heterostructures incorporating half-metallic $La_{2/3}Sr_{1/3}MnO_3$ (LSMO) are of particular interest since, due to the near total spin-polarization of ferromagnetic LSMO [33], they may be used as highly efficient magnetic tunnel junctions i.e., magnetoresistive random access memory devices [34].

Lastly, we briefly touch upon a relatively recent trend in the field i.e., the pursuit of engineering real-space chiral magnetic textures, e.g., skyrmions (see Figs. 1.4a-b), which are characterized by a wrapping of the magnetic spin texture around a unit sphere that cannot be removed through an adiabatic transformation, thereby representing a topological object [38]. One of the main motivations that drives this research is the possibility of inducing fast skyrmion motion with low current densities, which could have a profound impact on magnetic memory devices [35]. The combination of interface symmetry breaking and atomic spin-orbit coupling leads to an additional contribution to the magnetic exchange mechanism, known as the Dzyaloshinskii-Moriya interaction

$$\hat{H}_{ij} = \mathbf{D}_{ij} \cdot \left(\hat{\mathbf{S}}_i \times \hat{\mathbf{S}}_j\right), \tag{1.1}$$

where S_{ij} are spins situated at sites i and j and $\mathbf{D}_{ij}$ is a vector oriented perpendicularly to the plane spanned containing the two spins and the ion that couples them. This mechanism favours mutually orthogonal orientations between neighbouring spins (spin canting) and may therefore stabilize, among other spin textures, magnetic skyrmions. A

[5] Collective vibrational modes of the crystal lattice.

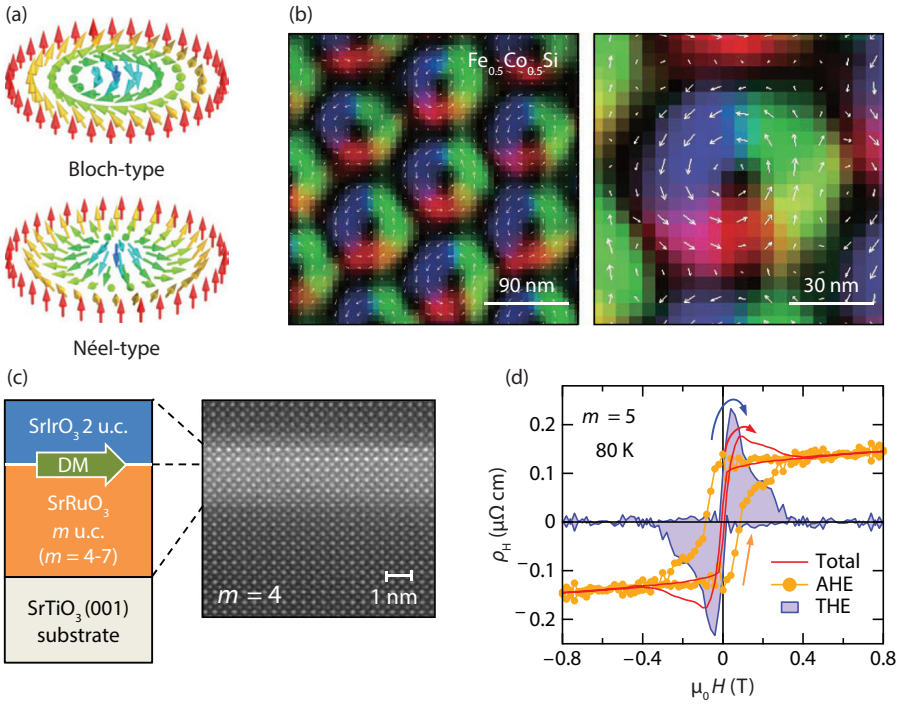

Figure 1.4: Magnetic skyrmions and the topological Hall effect. (a) Illustration of a Bloch and Néel type magnetic skyrmion (adapted from ref. [35]). (b) Lorentz TEM images of skyrmions in helimagnet $Fe_{0.5}Co_{0.5}Si$ (adapted from ref. [36]). (c) Illustration and HAADF-STEM image of a SRO/SIO heterostructure and (d) topological Hall component extracted from the Hall effect through subtraction of the magnetic hysteresis loop (anomalous component). Panels (c-d) adapted from ref. [37].

distinction is made between the two-site mechanism, which occurs between two spins coupled via e.g., an oxygen atom [39] and the three-site mechanism, which is a correction to the Ruderman-Kittel-Kasuya-Yosida (RKKY) exchange between two spins coupled to a non-magnetic cation via itinerant electrons [40]. In the former case, the spin-orbit correction is from the magnetic ions themselves, whereas in the latter it comes from the non-magnetic cation. Importantly, this contribution vanishes if i and j are connected by a center of inversion, which can be broken at an interface (see Fig. 1.4c), or through e.g., buckling of metal-oxygen bonds. Both mechanisms have been explored in the context of perovskite oxides, frequently with heterostructures incorporating the itinerant ferromagnet $SrRuO_3$ (SRO) [37, 41] and/or spin-orbit semimetal SIO [42] which, due to their $4d$ and $5d$ orbitals, have a sizeable spin-orbit coupling and are therefore suitable candidates for realizing this type of phenomenology. However, convincing magnetic imaging of interface-driven magnetic skyrmions in these systems is yet to be demonstrated[6]. Rather, claims of magnetic skyrmions have mainly been supported by the observations of unusual peaks in the Hall effect, such as shown in Fig. 1.4d. Nevertheless,

[6] A clear example of interface-driven nanoscale skyrmions has been observed in Ir on (111) oriented Fe [43].

4d and 5d oxides provide an exciting platform for emergent properties, which is why the prototypical examples SRO and SIO are the subject of this thesis. In the next section, we will discuss some of the essential features of these two materials.

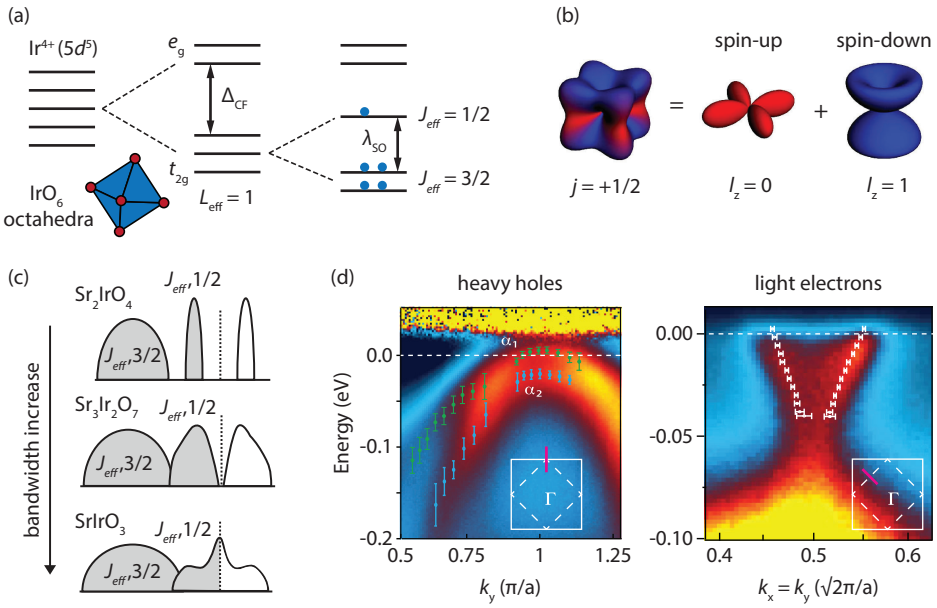

Figure 1.5: Spin-orbit mixed bands. (a) Orbitals of Ir^{4+} in the presence of an octahedral crystal field and atomic spin-orbit coupling λ_{SO}. (b) Visualization of the $|1/2\ 1/2\rangle$ orbital as a combination of spin-orbitals in the cubic harmonic basis, adapted from ref. [44]. (c) Correlation-induced insulating and semimetallic states in the Ruddlesden-Popper series of strontium iridates $Sr_{n+1}Ir_nO_{3n+1}$, adapted from ref. [45]. (d) ARPES measurements showing (left) a heavy hole-like dispersion and (right) light electron-like dispersion, adapted from ref. [46].

1.2. SPIN-ORBIT SEMIMETAL SIO

Iridates have, over the past decade, been a heavily studied class of materials, owing to the equal footing of various competing energy scales. In an octahedral crystal field, the $5d^5$ orbital configuration of the Ir^{4+} ion splits into a lower energy t_{2g} and a higher energy e_g manifold, with an energy splitting of several eV (see Fig. 1.5a). The large energy separation between the two manifolds means that they are decoupled and can be treated within their own subspace [47]. The threefold degenerate t_{2g} states, resembling p-orbitals, have an effective angular momentum[7] $L_{\text{eff}} = 1$. In terms of the cubic harmonics, the states in the t_{2g} subspace are $|xy\rangle$, $|yz\rangle$ and $|zx\rangle$, which in turn are linear combinations of the spherical harmonics with opposite magnetic quantum numbers. For many perovskites, the t_{2g} orbitals are an appropriate basis for the electronic ground state, since other energy scales can usually be considered as a perturbation[8]. However, the Ir 5d orbitals

[7] Expressed in the p-orbital basis, the effective angular momentum of the t_{2g} states have $L = -1$.
[8] Some other exceptions are systems with Jahn-Teller distortions, such as the manganites.

have a rather large atomic spin-orbit coupling [48] $\lambda_{SO} \sim 0.4\,\text{eV}$, which cannot be considered as a perturbation, but instead gives rise to mixed spin-orbital states that further lift the orbital degeneracy. In perovskite iridates, this translates to a lower energy $J_{\text{eff}} = 3/2$ quartet and a higher energy $J_{\text{eff}} = 1/2$ doublet. The two levels of the latter (in a cubic approximation) are given by

$$
\begin{aligned}
|1/2\rangle\,|1/2\rangle &= \frac{1}{\sqrt{3}}\big(|xy\rangle\,|\uparrow\rangle + |yz\rangle\,|\downarrow\rangle + i\,|zx\rangle\,|\downarrow\rangle\big) \\
|1/2\rangle\,|-1/2\rangle &= \frac{1}{\sqrt{3}}\big(|xy\rangle\,|\downarrow\rangle + |yz\rangle\,|\uparrow\rangle - i\,|zx\rangle\,|\uparrow\rangle\big),
\end{aligned}
\tag{1.2}
$$

which can be interpreted as isospin up and down states [44] (see Fig. 1.5b). The level splitting causes a reduction in bandwidth W with respect to the t_{2g} band, enhancing the effective electron-electron repulsion U/W and therefore rendering these systems prone to Mott behaviour, similar to their $3d$ counterparts. The layered members of the $Sr_{n+1}Ir_nO_{3n+1}$ Ruddlesden-Popper series of strontium iridates Sr_2IrO_4 ($n = 1$) and $Sr_3Ir_2O_7$ ($n = 2$), have the smallest bandwidth due to a reduced coordination of the Ir–Ir network i.e., c-axis hopping is suppressed due to double SrO planes interrupting the connectivity between adjacent Ir sites (see Fig. 1.5c). The small bandwidth results in a lower- and upper Hubbard $J_{\text{eff}} = 1/2$ band and localized carriers with antiferromagnetic order. Accordingly, these materials are referred to as spin-orbit Mott insulators [49, 50].

The $n = \infty$ member $SrIrO_3$ has the largest connectivity of the Ir sites, due to each site having six direct neighbours (two along each pseudocubic lattice direction). In contrast to the layered iridates, this leads to a (paramagnetic) semimetallic state, with a degree of mixing between the $J_{\text{eff}} = 1/2$ lower Hubbard bands and the $J_{\text{eff}} = 3/2$ quartet. In thin film form, SIO has been shown to host a combination of heavy hole- and light electron-like bands [46, 51] (see Fig. 1.5d), as well as a large spin Hall effect [52], which is of interest for applications in spintronics [53]. The lattice symmetry of bulk SIO is monoclinic $6H$-type hexagonal perovskite (space group $C2/c$), characterized by sublattices of corner and face-shared octahedral networks [54]. The orthorhombic $Pbnm$ perovskite form exhibiting solely corner-shared octahedra can be stabilized either by external pressure or epitaxial strain [55] (see Fig. 1.6a). In the pseudocubic (Glazer) representation, the unit cell of the latter is depicted with 2×4 octahedra that are rotated mutually out-of-phase about two lattice vectors and in-phase about the third over $\sim 10°$ [56, 57], denoted $a^-b^-c^+$ in Glazer notation [58] (see Fig. 1.6b). Orthorhombic SIO has been proposed to host a Dirac nodal line, resulting from an intersection between two shifted Dirac cones. The nodal line is protected by time-reversal invariance and the non-symmorphic n-glide symmetry, which consists of a mirror operation in the $a-c$ plane of the orthorhombic unit cell, followed by a translation along its diagonal[9]. It has been shown that monoclinic distortions induced by epitaxial strain cause the nodal line to be gapped [60] (see Figs. 1.6c-d). Furthermore, breaking of the mirror symmetry through e.g., staggered potentials along the c-axis has been suggested to be able drive the system into various

[9] Earlier reports argued that the nodal line was protected by the mirror symmetry [59]

topological phases, ranging from a Dirac semimetal to a topological and band insulator, depending on the strength of the symmetry breaking potential [61]. Clearly, lattice symmetry is a crucial aspect that determines the electronic ground state of SIO. Furthermore, apart from global lattice symmetries, the magnitudes of octahedral rotations and Ir−O−Ir bond angles have also been shown to have a strong impact on the electronic properties [62]. This property, as well as its manipulation through heteroepitaxy, will be further explored in Chapter 3.

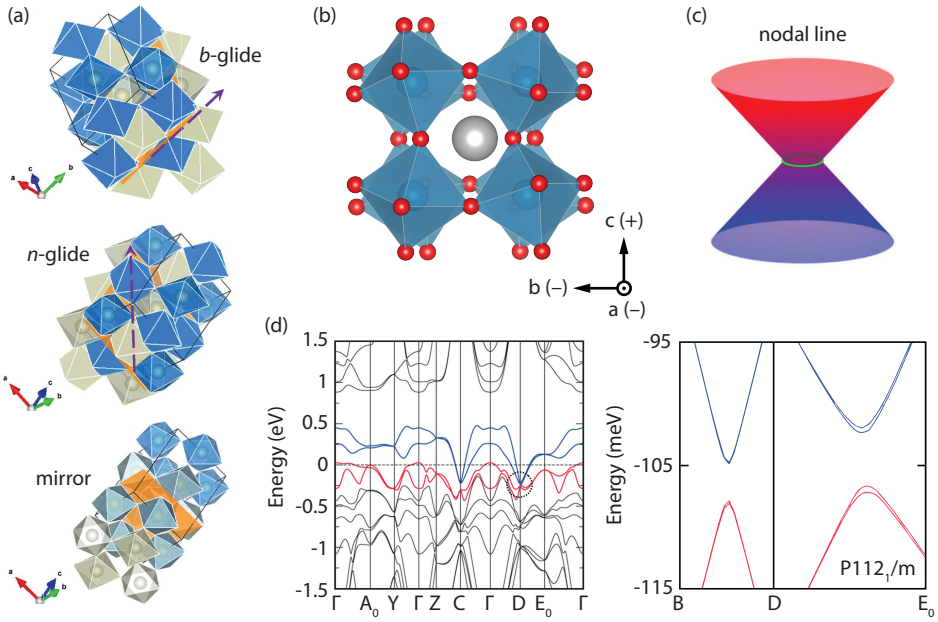

Figure 1.6: Gapped nodal line. (a) Symmetries of the $Pbnm$ orthorhombic perovskite structure. (b) Pseudocubic representation of the $Pbnm$ orthorhombic perovskite unit cell, exhibiting a $a^-b^-c^+$ rotation pattern. (c) Illustration of a nodal line semimetallic state, resulting from the intersection of two Dirac cones (adapted from ref. [63]). (d) Electronic structure for $SrIrO_3$ epitaxially grown on $GdScO_3$ (001), with the red and blue curves denoting the hole- and electron-like $J_{\text{eff}} = 1/2$ bands. The right panel represents an enlarged view around the gapped nodal line. Panels (a) and (c) adapted from ref. [60].

1.3. ITINERANT FERROMAGNET SRO

Similar to perovskite SIO, SRO has a $Pbnm$ orthorhombic symmetry characterized by a $a^-b^-c^+$ Glazer rotational pattern i.e., out-of-phase rotations about two pseudocubic axes and an in-phase rotation about the third (see Fig. 1.7a). In bulk single-crystal form, it has octahedral rotations of ~ 6° [66], which are strongly affected by heteroepitaxy. In particular, when grown on compressive substrates such as STO (see Fig. 1.7b), the lattice symmetry reduces to a tetragonal $a^0a^0c^-$ rotation pattern, with a uniaxial magnetic anisotropy that points out-of-plane [66, 67]. Being a $4d$ element, it has a moderately strong atomic spin-orbit coupling of ~ 0.1 eV [68] which, in contrast to the iridates, can be considered as a perturbation in the t_{2g} subspace. The larger bandwidth compared to

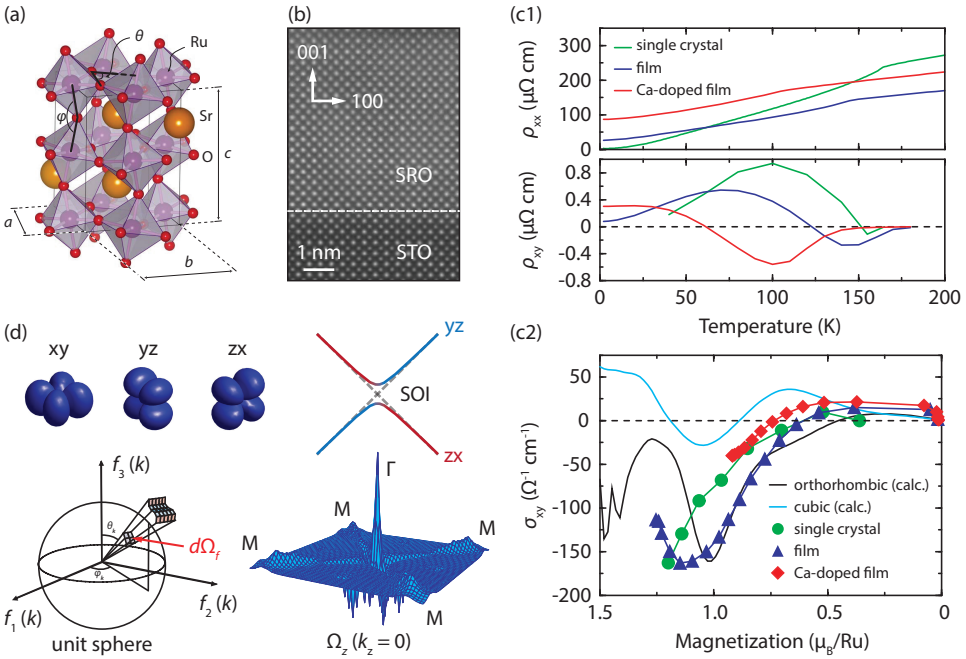

Figure 1.7: Avoided band crossings in ferromagnetic SRO. (a) $Pbnm$ orthorhombic unit cell of SRO (adapted from ref. [64]). (b) HAADF-STEM image of a SRO thin film grown on a STO (001) substrate. (c1) Longitudinal (top) and anomalous Hall resistivity (bottom) for a SRO single crystal, as well as pristine and Ca-doped SRO thin films grown on STO. (c2) Theoretical and experimental anomalous Hall conductivity as a function of magnetization. (d) Illustration of a magnetic monopole arising from avoided level crossings between different t_{2g} bands. Panels (c1), (c2) and (d) adapted from ref. [65].

the iridates translates to a smaller U/W ratio, rendering SRO a moderately correlated t_{2g} metal [64, 69]. Perhaps most importantly, SRO is an itinerant ferromagnet with a bulk Curie temperature $T_C = 160\,\mathrm{K}$ [70]. Interestingly, its seemingly more correlated isostructural sister compound $CaRuO_3$ (CRO) is a paramagnet, a difference which has been attributed to smaller octahedral rotations in SRO as compared to CRO, resulting in a more spiked density of states at the Fermi energy and a concomitant Stoner instability [71]. The ferromagnetic transition, which can be identified from a rather abrupt slope change in the $\rho_{xx}(T)$ curve, can be suppressed by e.g., Ca doping (see Fig. 1.7c1). An important consequence of the ferromagnetic phase transition is a spontaneously broken spin rotation and time-reversal symmetry, which permits a nonzero Berry curvature when integrating over all occupied states of the Brillouin zone. The result is an emergent gauge field that strongly depends on the electronic structure and magnetization, and produces the anomalous Hall effect (see Fig. 1.7c) [72]. The Berry curvature is generally not uniformly spread throughout the Brillouin zone, but is typically spiked at points in k-space near avoided crossings between bands that are mixed by e.g., the spin-orbit coupling (see Fig. 1.7d). In the vicinity of such an avoided crossing, the three-dimensional Hamiltonian can be parametrized as a two-level system, with a vector f projected onto the

Bloch sphere. Then the gauge field for a surface on the sphere is given by half the subtended solid angle. In bulk SRO, such a point has been shown to occur at the Γ point, between $|yz\rangle$ and $|zx\rangle$ derived bands, which produces a singular source of the gauge field, referred to as a momentum-space magnetic monopole [65]. It should be noted however, that extrinsic mechanisms [73, 74] of the anomalous Hall effect (AHE) have also been proposed to play a role in SRO, particularly close to T_C [75]. In the next section, we delve a bit deeper into the concepts of anomalous transport and how in two-dimensions it can be expressed in terms of a topological quantity known as the Chern number.

1.4. ANOMALOUS TRANSPORT

We consider a wavefunction in k-space $\psi_{\mathbf{k}}$ and displace it by an infinitesimally small amount $\delta\mathbf{k}$. This yields

$$\psi_{\mathbf{k}+\delta\mathbf{k}} \approx \psi_{\mathbf{k}} + \delta\mathbf{k}\cdot\nabla_{\mathbf{k}}\psi_{\mathbf{k}}, \tag{1.3}$$

such that

$$\begin{aligned}\langle\psi_{\mathbf{k}}|\nabla_{\mathbf{k}}|\psi_{\mathbf{k}}\rangle &= \lim_{\delta\mathbf{k}\to 0}\frac{\langle\psi_{\mathbf{k}}|\psi_{\mathbf{k}+\delta\mathbf{k}}\rangle - \langle\psi_{\mathbf{k}}|\psi_{\mathbf{k}}\rangle}{\delta\mathbf{k}} \\ &= -i\mathscr{A}_{\mathbf{k}}.\end{aligned} \tag{1.4}$$

In the presence of a k-space gauge field, or curvature, the quantity $\mathscr{A}_{\mathbf{k}}$, known as the Berry connection or gauge potential, may be nonzero. The overlap between the two wavefunctions separated by $\delta\mathbf{k}$ is given by

$$\lim_{\delta\mathbf{k}\to 0}\langle\psi_{\mathbf{k}}|\psi_{\mathbf{k}+\delta\mathbf{k}}\rangle = \lim_{\delta\mathbf{k}\to 0}\left[1+\langle\psi_{\mathbf{k}}|\nabla_{\mathbf{k}}|\psi_{\mathbf{k}}\rangle\cdot\delta\mathbf{k}\right] \tag{1.5}$$

$$= \exp\left(i\mathscr{A}_{\mathbf{k}}\cdot\mathrm{d}\mathbf{k}\right). \tag{1.6}$$

Then, by integrating around a closed loop, one finds

$$\begin{aligned}\oint_{\mathscr{C}}\langle\psi_{\mathbf{k}}|\nabla_{\mathbf{k}}|\psi_{\mathbf{k}}\rangle\cdot\mathrm{d}\mathbf{k} &= \exp\left(i\oint_{\mathscr{C}}\mathscr{A}_{\mathbf{k}}\cdot\mathrm{d}\mathbf{k}\right) \\ &= \exp\left(i\gamma\right),\end{aligned} \tag{1.7}$$

with γ known as the (closed-path) Berry phase, which is acquired as the wavefunction adiabatically traverses a closed loop $\mathscr{C}$ in parameter space, in the presence of a gauge potential [76]. Using Stokes' theorem, the contour integral can be written as a surface integral

$$\oint_{\mathscr{C}}\mathscr{A}_{\mathbf{k}}\cdot\mathrm{d}\mathbf{k} = \iint_{\mathscr{S}}(\nabla_{\mathbf{k}}\times\mathscr{A}_{\mathbf{k}})\cdot\mathrm{d}^2\mathbf{k}, \tag{1.8}$$

with $\nabla_{\mathbf{k}} \times \mathscr{A}_{\mathbf{k}} = \Omega_{\mathbf{k}}$ the momentum-space Berry curvature, which represents the flux that penetrates the surface area that is enclosed by the contour $\mathscr{C}$ i.e., the gauge field. In a curved space, the usual derivative operation is not gauge invariant. Therefore, the introduction of a gauge-covariant derivative is required as $\nabla_{\mathbf{k}} \rightarrow \nabla_{\mathbf{k}} - i\mathscr{A}_{\mathbf{k}}$. In a momentum-space basis, the gauge-covariant position operators are given by [65]

$$\begin{aligned} \hat{x} &= \nabla_{k_x} - i\mathscr{A}_{k_x} \\ \hat{y} &= \nabla_{k_y} - i\mathscr{A}_{k_y}. \end{aligned} \tag{1.9}$$

We consider a perturbation in the form of a simple electric field $\hat{H}' = -e\mathscr{E}_x\hat{x}$. The additional contribution to the time-evolution of the position operators is then given by

$$\begin{aligned} \left\langle \frac{\mathrm{d}\hat{y}}{\mathrm{d}t} \right\rangle &= \frac{i}{\hbar}\left[\hat{H}', \hat{y}\right] \\ &= -\frac{ie\mathscr{E}_x}{\hbar}\left[\hat{x}, \hat{y}\right] \\ &= \frac{e\mathscr{E}_x}{\hbar}\left(\frac{\partial \mathscr{A}_{k_y}}{\partial k_x} - \frac{\partial \mathscr{A}_{k_x}}{\partial k_y}\right) \\ &= \frac{e}{\hbar}\mathscr{E}_x\Omega^z_{\mathbf{k}} = v_y^{\mathrm{AH}} \end{aligned} \tag{1.10}$$

and is known as the anomalous velocity. Since it manifests perpendicularly to the applied field, one can define the transverse anomalous conductance $\sigma_{xy}^{\mathrm{AH}} = v_y^{\mathrm{AH}} e/\mathscr{E}_x$, which is found by integrating over all occupied states throughout the Brillouin zone and summing over all electronic bands n

$$\sigma_{xy}^{\mathrm{AH}} = \frac{e^2}{2\pi h}\sum_n \iint_{\mathrm{BZ}} f\left(\epsilon_{\mathbf{k}}^n\right)\Omega_n^z \,\mathrm{d}^2\mathbf{k}, \tag{1.11}$$

with $f\left(\epsilon_{\mathbf{k}}^n\right)$ the Fermi-Dirac distribution of the dispersion relation $\epsilon_{\mathbf{k}}$ of band n. For systems with time-reversal symmetry, the Berry curvature is an odd function with respect to $\mathbf{k}$, meaning that its integration throughout the Brillouin zone reduces to zero. For systems with inversion symmetry, the Berry curvature is an even function of $\mathbf{k}$, which means it reduces to zero everywhere in the presence of simultaneous time-reversal and inversion symmetry [77]. At zero temperature and for a single fully occupied band n, equation (1.11) simplifies to

$$\begin{aligned} \sigma_{xy,n}^{\mathrm{AH}} &= \frac{e^2}{2\pi h}\iint_{\mathrm{BZ}} \Omega_n^z \,\mathrm{d}^2\mathbf{k} \\ &= \frac{e^2}{h} C_n, \end{aligned} \tag{1.12}$$

with C_n the Chern number of band n, which is a topological quantity that constitutes a quantized contribution to the anomalous Hall conductance. It may be interpreted as the

winding number of a chiral vortex-like object of the Berry connection with an associated topological charge. For a fully occupied band (Chern insulator), the anomalous Hall conductance is quantized. In the case of partially occupied bands i.e., band structures with a Fermi surface, the conductance is not quantized due to contributions from states at the Fermi energy [77]. For a given (Bloch) wavefunction ψ, the Berry curvature can be written as

$$\begin{aligned}\Omega_{\mathbf{k}}^{z} = i\nabla_{k_x}\mathscr{A}_{k_y} - i\nabla_{k_y}\mathscr{A}_{k_x} &= \nabla_{k_x}\langle\psi|\nabla_{k_y}\psi\rangle - \nabla_{k_y}\langle\psi|\nabla_{k_x}\psi\rangle \\ &= i\langle\nabla_{k_x}\psi|\nabla_{k_y}\psi\rangle - i\langle\nabla_{k_y}\psi|\nabla_{k_x}\psi\rangle \\ &= -i\big[\,|\nabla_{\mathbf{k}}\psi\rangle \times \langle\nabla_{\mathbf{k}}\psi|\,\big]_z. \end{aligned} \tag{1.13}$$

For two wavefunctions ψ_m and ψ_n, we can write

$$\begin{aligned}\big\langle\psi_m\big|\nabla\big|\hat{H}\psi_n\big\rangle &= \epsilon_n\langle\psi_m|\nabla\psi_n\rangle + \langle\psi_m|\psi_n\rangle\nabla\epsilon_n \\ &= \big\langle\psi_m\big|\nabla\hat{H}\big|\psi_n\big\rangle + \big\langle\psi_m\big|\hat{H}\big|\nabla\psi_n\big\rangle \\ &= \big\langle\psi_m\big|\nabla\hat{H}\big|\psi_n\big\rangle + \epsilon_m\langle\psi_m|\nabla\psi_n\rangle, \end{aligned} \tag{1.14}$$

which gives

$$\langle\psi_m|\nabla\psi_n\rangle = \frac{\big\langle\psi_m\big|\nabla\hat{H}\big|\psi_n\big\rangle}{\epsilon_n - \epsilon_m}. \tag{1.15}$$

Then the total Berry curvature of band n is given by

$$\begin{aligned}\Omega_{\mathbf{k}}^{n} &= -i\sum_{m\neq n}\big[\,\langle\psi_m|\nabla_{\mathbf{k}}\psi_n\rangle \times \langle\nabla_{\mathbf{k}}\psi_n|\psi_m\rangle\,\big]_z \\ &= -i\sum_{m\neq n}\frac{\big[\,\big\langle\psi_m\big|\nabla_{\mathbf{k}}\hat{H}\big|\psi_n\big\rangle \times \big\langle\psi_n\big|\nabla_{\mathbf{k}}\hat{H}\big|\psi_m\big\rangle\,\big]_z}{(\epsilon_m - \epsilon_n)^2} \\ &= -2\sum_{m\neq n}\mathrm{Im}\,\frac{\big\langle\psi_m\big|\nabla_{k_x}\hat{H}\big|\psi_n\big\rangle\big\langle\psi_n\big|\nabla_{k_y}\hat{H}\big|\psi_m\big\rangle}{(\epsilon_m - \epsilon_n)^2} \end{aligned} \tag{1.16}$$

which illustrates that when two bands m and n are nearly degenerate, the Berry curvature is singularly enhanced. Additionally, since equation (1.16) is odd with respect to permuting m and n, the sum over all bands $\sum_n \Omega_{\mathbf{k}}^n$, as well as the sum over all Chern numbers $\sum_n C_n$, returns zero. The topology and anomalous properties of SRO in the two-dimensional limit, as well as its manipulation through interface engineering will be explored in Chapters 4, 5 and 6.

1.5. OUTLINE OF THIS THESIS

In this thesis, we study heterostructures and thin films consisting of the $4d$ and $5d$ transition-metal oxides $SrRuO_3$ and $SrIrO_3$, with a focus on interface-driven structural, electronic

and magnetic reconstructions. The remainder of this thesis is outlined as follows.

Chapter 2 describes the main experimental techniques used throughout this thesis for the synthesis, structural analysis and electronic characterization of $SrIrO_3$– and $SrRuO_3$–based heterostructures and thin films; pulsed-laser deposition, X-ray diffraction, device fabrication and cryogenic magnetotransport measurements.

In Chapter 3, we study the octahedral connectivity across the interface between $SrTiO_3$ and $SrIrO_3$, which exhibits an anomaly in the resistivity at the $SrTiO_3$ cubic-tetragonal structural phase transition. Through transport measurements, synchrotron X-ray diffraction measurements and density-functional theory (DFT) calculations, we show that this behaviour can be understood as orthorhombic structural domains of the SIO film adapting to the tetragonal multi-domain state of the STO substrate.

In Chapter 4, we describe a theoretical analysis of $SrRuO_3$ in the ultrathin limit, showing that the anomalous Hall effect of monolayer $SrRuO_3$ can be understood in terms of sets of topological bands. We subsequently show that the sign of the anomalous Hall effect can be manipulated by creating symmetric interfaces of $SrRuO_3$ with both $SrTiO_3$ and $SrIrO_3$. In asymmetric $SrIrO_3/SrRuO_3/SrTiO_3$ heterostructures, we find that the anomalous Hall effect is well described by a phenomenological two-channel AHE model. We subsequently show that this behavior can be mimicked by ultrathin $SrRuO_3$ bilayers, separated by an insulating $SrTiO_3$ spacer.

In Chapter 5, we interface ultrathin $SrRuO_3$ with the wide bandgap insulator $LaAlO_3$. Transmission electron microscopy and magneto-optical characterization reveal a polar $SrO/RuO_2/LaO$ interface configuration, that experiences a magnetic reconstruction as a result of charge-frustration. We subsequently show through DFT, tight-binding calculations and magnetotransport that the resulting inversion symmetry breaking and pinning of excess charge have a profound effect on the anomalous Hall effect, driving a reorganization of the topological charges in momentum space and changing the sign of the momentum-space Berry curvature.

In Chapter 6, we synthesize $SrRuO_3$ thin films on $SrTiO_3$ (111) substrates. We argue, based on transmission electron microscopy and X-ray diffraction, that the films are coherently strained with the orthorhombic in-phase rotation axis oriented along the (001) lattice direction. Through high-field magnetotransport measurements, we show evidence of a high mobility hole-like band that becomes more prominent towards the ultrathin limit. Thick films exhibit an unsaturating linear positive magnetoresistance, which we attribute to guiding center motion magnetoresistance.

Chapter 7 summarizes the findings of this thesis and provides a number of suggestions for future directions to be explored.

2

Experimental techniques

"No amount of experimentation can ever prove me right;
a single experiment can prove me wrong."

– Albert Einstein

This chapter describes the main experimental techniques used throughout this thesis for the synthesis, structural analysis and electronic characterization of $SrIrO_3$– and $SrRuO_3$–based heterostructures and thin films; pulsed-laser deposition, X-ray diffraction, lithographic device fabrication and cryogenic magnetotransport characterization.

2

HETEROEPITAXY in complex oxides is a powerful and versatile method towards realizing novel phenomena in condensed matter systems. In pursuit of this goal, material synthesis, structural analysis and electronic characterization are indispensable tools. In this chapter, we describe the main experimental techniques used throughout this thesis to synthesize and characterize SRO- and SIO-based oxide thin films and heterostructures. A typical workflow consists of sample synthesis through bottom-up growth using pulsed-laser deposition, followed by surface and structural characterization such as reflection high-energy electron diffraction (RHEED), atomic force microscopy (AFM) and X-ray diffraction. Finally, devices are fabricated using electron-beam lithography and characterized electronically through cryogenic magnetotransport measurements. In the next sections, we discuss the basic concepts and methodology used throughout this thesis regarding pulsed-laser deposition, X-ray diffraction, device fabrication and magnetotransport characterization.

2.1. PULSED-LASER DEPOSITION

Pulsed-laser deposition (PLD) is a technique for the synthesis of thin films and heterostructures. It was first demonstrated in the 1960s [78], but only became more widely used after its capabilities for the efficient synthesis of thin film cuprate high-temperature superconductors were demonstrated [79, 80]. Another milestone was the TiO_2 single termination of STO substrates through subsequent treatments with, water, buffered hydrofluoric acid and high temperature O_2 annealing [81, 82], enabling the PLD growth of atomically smooth ultrathin films and heterostructures with well-defined interfaces [7].

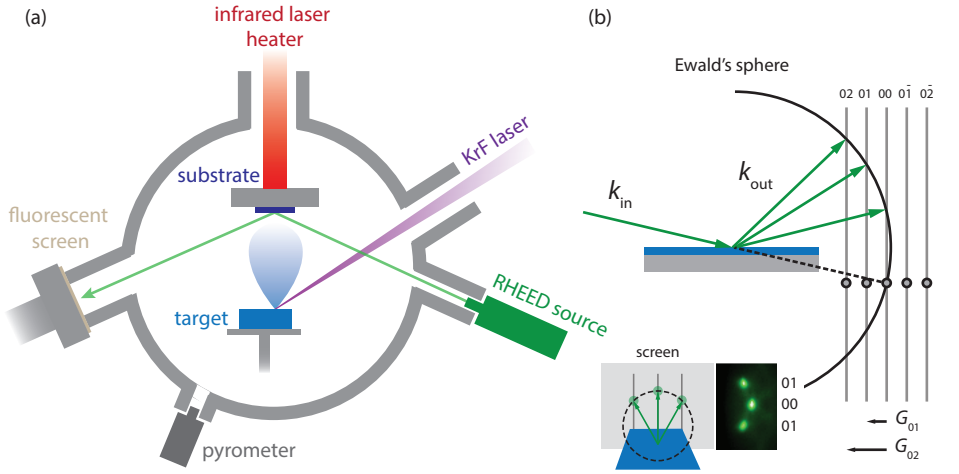

Figure 2.1: Pulsed-laser deposition. (a) Illustration of a pulsed-laser deposition setup incorporating a pulsed KrF excimer laser, infrared diode laser heater, in-situ RHEED, rotating target and pyrometer. (b) Illustration of the Ewald's sphere intersecting reciprocal lattice rods and an example of a diffraction pattern visible on the fluorescent screen.

Fig. 2.1a illustrates the configuration of the PLD setup, as used throughout this thesis. A 5 mm × 5 mm × 0.5 mm substrate (typically STO) is mechanically clamped on a

heater stage and positioned in the center of a vacuum chamber with a base pressure $p < 5 \times 10^{-8}$ mbar. Gases such as O_2 and Ar can be inserted and the chamber gas pressure can be controlled using a combination of gas flow controllers and variable valve positioning of the main turbomolecular pump. The substrate temperature is controlled by an infrared diode laser incident on the backside of the metal holder. The temperature is estimated with a pyrometer measuring infrared thermal radiation, aimed at the substrate holder from the front. In practice, the diode laser heater current is used to benchmark the growth temperature. To avoid damage due to thermal shock, substrates are heated and cooled slowly (typically $10-20\,^{\circ}$C/min). Deposition is performed with a pulsed (1 Hz) KrF ultraviolet (excimer) laser ($\lambda = 248$ nm) incident onto a sintered (SRO, SIO) or single-crystal (STO, LAO) target of the desired material to be grown. The interaction of the laser with the target causes atomic species to be ablated, creating a plasma plume that is incident on the heated substrate at 55 mm distance. During this process, the kinetic energy of ablated species can vary from tens of eV to tenths of eV, depending on the background gas pressure, substrate-target distance and laser fluence [83–85]. The latter is determined by dividing the nominal laser power per pulse incident on the target ~ 25 mJ by the measured (rectangular) laser spot size ~ 1 mm $\times$ 2 mm and correcting for the attenuation of the laser entry window. A typical value for the fluence is 1 J/cm^2.

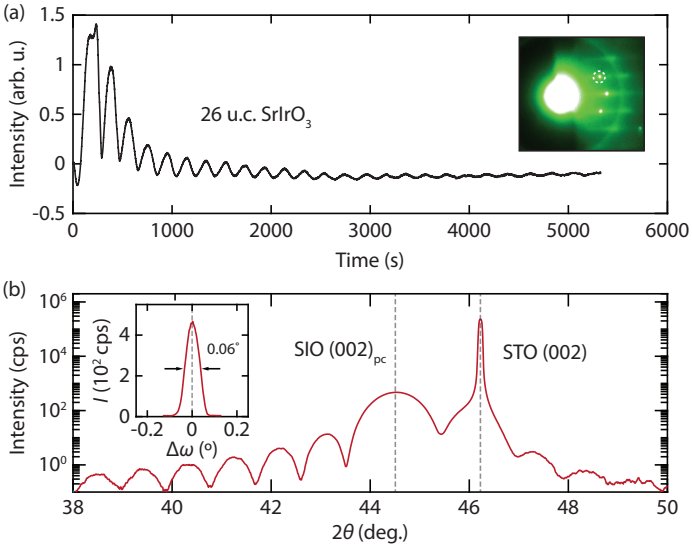

Figure 2.2: Synthesis of perovskite thin films. (a) Intensity of the first-order RHEED spot during the growth of a 26 u.c. SIO film. The inset shows the RHEED pattern after the growth has been completed. (b) X-ray $\theta - 2\theta$ scan for the film from (a). The inset shows the rocking curve around the $(002)_{pc}$ peak of the SIO film.

Thin film growth is monitored using in-situ RHEED, which utilizes a 30 kV electron beam with an emission current of typically 1–10 µA. The beam is incident on the substrate at a grazing angle, producing a spotted diffraction pattern that can be observed using a fluorescent screen and a camera. A crystalline surface exhibits a RHEED pattern

characterized by concentric spots or streaks (see Fig. 2.1b), which arise due to the intersection of the reciprocal lattice rods with the Ewald's sphere [86, 87]. During Frank-van der Merwe (layer-by-layer) growth, the intensity of the RHEED spots oscillates as the surface alternates between low and high densities of step-like defects. Such a growth mode occurs when the mean free path of adatoms on surface is smaller than the size of the terraces exhibited by miscut crystal surfaces (typically several hundred nm). In contrast, step-flow growth occurs when the mean free path is larger and adatoms collide with the steps at the terrace edges. Since this process preserves a constant step-defect density during the growth, it does not produce RHEED oscillations, but is usually identified from pronounced intensity drops after every laser pulse, followed by exponential recoveries [88]. Fig. 2.2a illustrates the layer-by-layer growth of a 26 u.c. SIO film on a STO (001) substrate, with the inset showing the post-growth RHEED pattern. The growth parameters are $p_{O_2} = 0.1\,\text{mbar}$, substrate temperature $T \approx 600\,°\text{C}$ and laser fluence of $F = 1\,\text{J/cm}^2$. After the growth is complete, samples are annealed in $p = 300\,\text{mbar}$ O_2 gas at 550 °C for 1 hour and subsequently cooled to room temperature in the same pressure. All samples are capped either with a crystalline or amorphous layer (typically STO) to prevent sample decay from exposure to ambient conditions, as described in ref. [89].

Further structural information can be gathered from X-ray characterization (discussed in the next section), such as shown in Fig. 2.2b. The (002) diffraction conditions for the STO substrate and SIO films are indicated by the dashed lines. The position of the SIO diffraction pattern indicates a larger c-axis lattice parameter ($c_{\text{pc}} = 4.08\,\text{Å}$) compared to the cubic STO substrate ($c = 3.905\,\text{Å}$). In-plane lattice matching therefore leads to compressive strain exerted by the substrate on the SIO film. The Laue oscillations[1] observed in the vicinity of the SIO peak arise due to the combination of the finite thickness of the SIO layer and long-range crystal coherence. The inset shows the rocking curve around the SIO (002) peak, which measures the mosaicity of the crystal planes perpendicular to the c-axis.

2.2. X-RAY DIFFRACTION

As illustrated prior, X-ray diffraction is a useful technique for the characterization of crystals. Diffraction measurements in this thesis have been performed either at a synchrotron facility[2] or using a Bruker D8 Discover with a Cu K–α source producing an 8 keV ($\lambda = 1.54\,\text{Å}$) X-ray beam (see Fig. 2.3a). Crystallographic characterization of thin films can be performed through techniques such as Bragg diffraction, reflectometry, rocking curves, reciprocal space mapping and crystal truncation rod measurements. A typical setup consists of a microfocus radiation source, beam slit, monochromator, beam attenuator and a pinhole collimator. The radiation diffracted from the sample subsequently passes through a motorized slit onto a 1D silicon strip detector. The monochromator improves spectral resolution at the expense of beam intensity and can be omitted, if the photon count takes priority over angular resolution (e.g., for reflectivity measurements). The attenuator is included to moderate the beam intensity and to avoid damage to the

[1] Colloquially referred to as finite-size oscillations or thickness fringes.
[2] Diamond Light Source, Beamline I16 (Didcot, UK)

detector due to overexposure. If the detector is used in 0D mode i.e., summing the intensity of all pixels on the 1D grid, the slit opening (typically < 1 mm) determines the acceptance angle of the detector and therefore the angular resolution (typically ~ 0.02°).

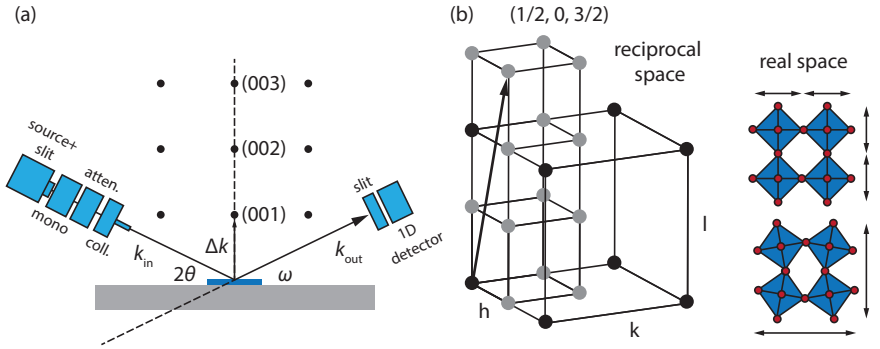

Figure 2.3: X-ray diffraction. (a) Illustration of an X-ray diffraction setup in a Bragg geometry. (b) Doubling of the unit cell vertices in real and reciprocal space due to octahedral rotations.

In the far-field approximation, the diffracted X-ray amplitude of a crystal is given by [90]

$$A = \left(\sum_m \exp(-i\Delta\mathbf{k}\cdot\mathbf{r}_m)\right)\left(\sum_n f_n \exp(-i\Delta\mathbf{k}\cdot\mathbf{r}_n)\right), \tag{2.1}$$

where the first term sums over all lattice points m and the second term over all atoms in the chosen basis n associated with each lattice point, referred to as the structure factor. The term $\Delta\mathbf{k}$ constitutes the scattering vector given by $\mathbf{k}_{\text{in}} - \mathbf{k}_{\text{out}}$ and f denotes the form factor of the constituent atoms i.e., a measure of the scattering amplitude from the atomic electron density. Constructive interference between diffracted waves occurs when the so-called Laue conditions are satisfied, given by

$$\begin{aligned} \Delta\mathbf{k}\cdot\mathbf{a} &= 2\pi h \\ \Delta\mathbf{k}\cdot\mathbf{b} &= 2\pi k \\ \Delta\mathbf{k}\cdot\mathbf{c} &= 2\pi l, \end{aligned} \tag{2.2}$$

with $(\mathbf{a},\mathbf{b},\mathbf{c})$ the basis vectors of the real-space unit cell. The $\Delta\mathbf{k}$ that satisfy (2.2) are known as the reciprocal lattice points and produce a peak in the diffracted X-ray intensity for a given reflection (hkl). The intensities of different (hkl) reflections respect the symmetry equivalent sites. For example, the inversion symmetric monoclinic space group $P2/m$ has a two-fold rotation symmetry with a perpendicular mirror plane. Therefore, if the mirror plane is normal to the z-axis, a point (x,y,z) is equivalent to $(x,y,\bar{z})$, $(\bar{x},\bar{y},\bar{z})$ and $(\bar{x},\bar{y},z)$ and the reflections (hkl), $(hk\bar{l})$ $(\bar{h}\bar{k}\bar{l})$ and $(\bar{h}\bar{k}l)$ will have (approximately) equal intensities, whereas the intensity of e.g., $(\bar{h}kl)$ may differ. It is also possible for waves to interfere destructively, which are known as forbidden or systematically absent reflections. The presence or absence of different reflections therefore underlies the

unit cell symmetry and can be used to identify to which of the 230 possible crystal space groups it belongs. High-symmetry unit cells such as cubic, tetragonal and orthorhombic have right angles between their vertices, which translates to right angles in reciprocal space. When the vertices deviate from right angles (e.g., monoclinic, rhombohedral), the degeneracy of the shearing direction causes the formation of structural domains and subsequently a splitting of the off-specular reflections, which can be visualized through reciprocal space maps [91].

The octahedral rotations mentioned in the previous chapter double the perovskite unit cell vertices in real space, which translates to a halving in reciprocal space (see Fig. 2.3b). Therefore, the measurement of half-order reflections can be employed to verify the presence or absence of certain lattice distortions, as well as to quantify their magnitude [57, 92]. A general guide to half-order reflections has been given by A.M. Glazer [58], from which the eponymous classification of oxygen octahedral rotations came forth. Table 2.1 describes the six possible octahedral rotations and the half-order diffraction peaks they produce. Octahedral rotations may also promote A-site cation displacements via steric forces. For example, in the $a^-b^-c^+$ $Pbnm$ structure, A-site cation displacements occur in the plane spanned by the two out-of-phase axes, which is perpendicular to the in-phase axis [57]. A second example is the rhombohedral $a^-a^-a^-$ structure (e.g., $LaAlO_3$), where cation displacements occur along the $(111)_{pc}$ direction [58].

Table 2.1: Half-order reflections arising from octahedral rotations. Symbols a, b and c denote the pseudocubic lattice axis of rotation and ± whether that rotation be (+) in-phase or (-) out-of-phase. The reciprocal lattice points (h, k, l) are expressed in terms of the doubled unit cell. Adapted from ref. [58].

rotation	(h, k, l)	condition	example
a^+	even–odd–odd	$k \neq l$	(013), (031)
b^+	odd–even–odd	$h \neq l$	(103), (301)
c^+	odd–odd–even	$h \neq k$	(130), (310)
a^-	odd–odd–odd	$k \neq l$	(131), (113)
b^-	odd–odd–odd	$h \neq l$	(113), (311)
c^-	odd–odd–odd	$h \neq k$	(131), (311)

Similar to RHEED, half-order reflections can be identified by measuring crystal truncation rods (CTRs), which can be observed when a reciprocal lattice point intersects the Ewald's sphere. The incidence angle of the beam is kept fixed at a small value to maximize surface sensitivity, while the polar and azimuthal exit angles of the beam, as well as the azimuthal rotation angle of the sample are varied. A two-dimensional detector is used to record the diffraction intensities in l-scans i.e., a moving along the l-axis in reciprocal space while recording the diffracted radiation. The intensity of a given reflection I_{hkl} is denoted by [57]

$$I_{hkl} = I_0 \frac{L_p}{\sin\eta} \sum_j D_j |F_{hkl}|^2, \tag{2.3}$$

where the sum $\sum_j D_j$ takes into account fractions of different rotational domains, the factor $L_p/\sin\eta$ corrects for the angular dependence of the beam footprint and polarization, and F_{hkl} is the atomic structure factor. For a perovskite in the pseudocubic representation, the latter can be expressed as [57]

$$\begin{aligned} F_{hkl} = f_{O^{2-}} &\sum_{m=1}^{24} \exp\left[2\pi i(hu_m + kv_m + lw_m)\right] \\ &+ f_A \sum_{n=1}^{8} \exp\left[2\pi i(hu_n + kv_n + lw_n)\right] \\ &+ f_B \sum_{p=1}^{8} \exp\left[2\pi i\big(hu_p + kv_p + lw_p\big)\right], \end{aligned} \tag{2.4}$$

with f_{O_2}, f_A and f_B the form factors of elemental oxygen, the A-site and B-site, respectively and the coordinates (u, v, w) the real-space positions of the atoms in the pseudocubic unit cell. The coordinates (u, v, w) are functions of the rotation angles about the a, b and c axes α, β and γ, respectively. Accordingly, experimental data can be fit to simulated diffraction spectra for the quantification of octahedral rotation patterns [57, 92, 93].

2.3. DEVICE FABRICATION

METHOD A

Devices used for electrical characterization of $SrIrO_3$– and $SrRuO_3$–based thin films and heterostructures are fabricated by one of two methods, labeled A and B (see Fig. 2.4). Method A is visually depicted in Fig. 2.4a. A bilayer liftoff resist (PMMA 495kDa + 950 kDa) is deposited on the sample through spin-coating at 4000 rpm[3]. The shapes of electrical contacts are written using electron-beam lithography[4], which are subsequently developed by immersing the sample consecutively in DI water (15s), a 1:3 mixture of MIBK:IPA (60s) and pure IPA (15s). After development, metal contacts (typically 5 nm Pd + 30-50 nm Au) are evaporated after a 10 s in-situ Ar-milling cleaning step. Subsequent liftoff is done by immersing the sample in warm (50 °C) acetone or (80 °C) [5] (NMP). To define devices suitable for electrical transport measurements, a second lithography step is required. After another spin coating step, the non-device areas are exposed and developed. The conductive film is then etched away using Ar-milling at an etch rate of ~ 1 nm per minute, using the PMMA resist layers as an etch mask. Finally, the PMMA etch mask is removed through immersion in warm acetone or NMP.

METHOD B

If metal contacts are not required i.e., if Ohmic contacts can be obtained through wedge/ball bonding directly to the sample, method B can be used, which requires only a single

[3] To prevent charging effects during electron-beam exposure, a conductive layer of water-soluble ~ 30 nm Electra92 is spun on top of the PMMA bilayer.

[4] With a dose ~ 750 μC/cm^2 and an acceleration voltage 100 kV

[5] N-methyl-2-pyrrolidone

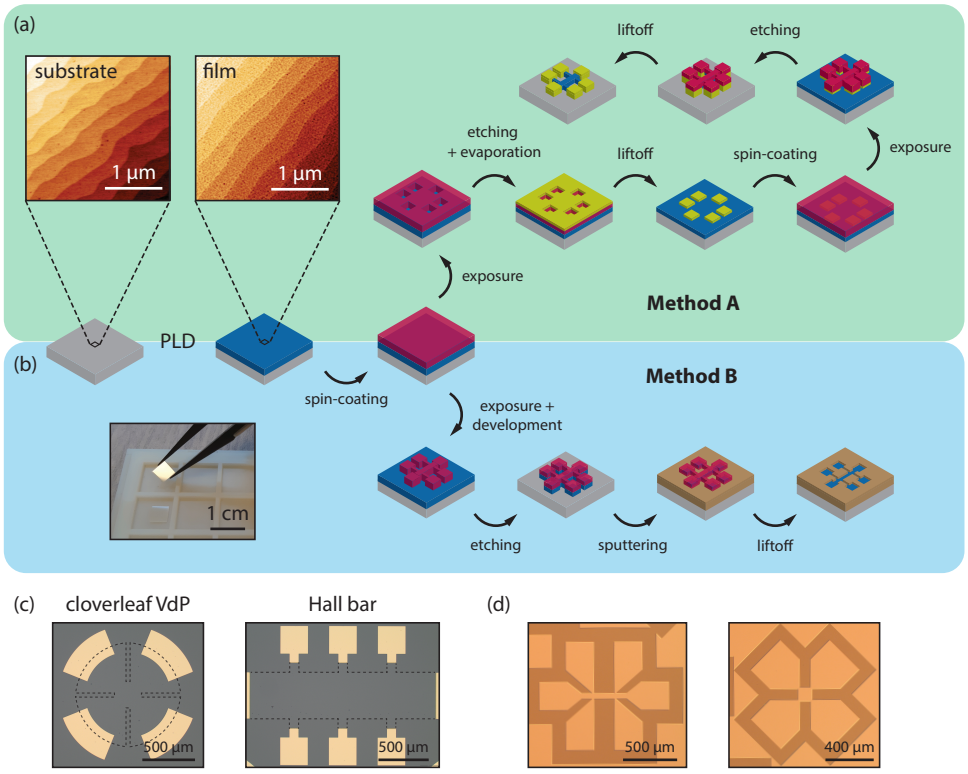

Figure 2.4: Device fabrication. (a-b) Schematic illustration of two different methods (labeled A and B) for the fabrication of electronic devices in complex oxide heterostructures. The top left images are AFM topographic scans of a TiO_2-terminated STO substrate and a 6 u.c. SIO film with a 10 u.c. crystalline STO capping. (c) Optical microscope images of Van der Pauw (VdP) and Hall bar devices using method A and (d) using method B. The dashed lines are a guide to the eye.

lithography step (see Fig. 2.4b). After spin-coating, non-device areas are exposed, developed and etched away using Ar-milling. To obtain an optical contrast between device and non-device areas, a dielectric oxide (e.g., SiO_x or HfO_x) with a thickness of ~ 30 nm is RF-sputtered after the etching step. After lifting off the remaining resist, samples are annealed on a hot plate (350 °C) for several hours to cure any oxygen vacancies that may have formed in the STO substrate during the etching step[6]. Some examples of devices fabricated using methods A and B are shown in Fig. 2.4c and Fig. 2.4d, respectively.

2.4. TRANSPORT CHARACTERIZATION

After the fabrication procedure, samples are pasted onto a printed circuit board (PCB) attached to chip carriers with electrical contact pins. Electrical connections between the PCB and devices are subsequently made through ultrasonic wedge bonding with

[6] Electric shorts between devices can easily occur due to conductive oxygen-deficient STO.

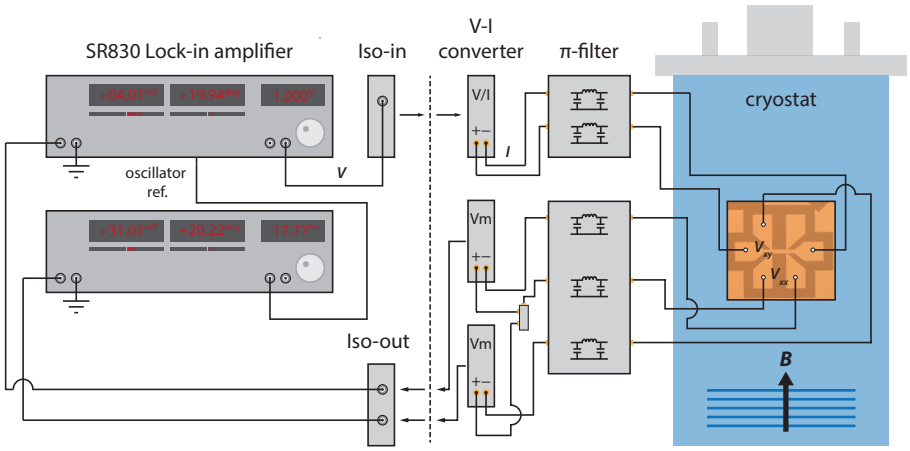

Figure 2.5: Magnetotransport characterization. Schematic illustration of the setup used for the transport characterization of devices at cryogenic temperatures and in magnetic fields up to 12 T.

Al/Si wire. The chip carrier is then attached to a probe stick and inserted into a cryostat. The bulk of the transport measurements in this thesis have been performed in an Oxford flow cryostat with a base temperature of 1.5 K, equipped with a superconducting magnet. Transport measurements are performed as schematically illustrated in Fig. 2.5. Using a lock-in amplifier, a low frequency (17.77 Hz) AC voltage is applied coaxially to a voltage-current converter via a differential amplifier isolator. The resulting current is sourced through the sample via room temperature low-pass π-filters. The resulting longitudinal (V_{xx}) and transverse (V_{xy}) voltages are amplified with CMOS or JFET gate input differential amplifiers and recorded by two lock-in amplifiers with coupled oscillators, via a second differential isolator amplifier[7]. Quantities such as sheet resistance are calculated by dividing the measured voltage drop by the sourced current and multiplying by the sample aspect ratio (or van der Pauw factor $\pi/\ln 2 \approx 4.53$). The sample temperature is controlled with an Oxford ITC4, incorporating a resistive heater and a resistance thermometer that is in direct contact with the metal backplate of the chip carrier. Resistance versus temperature characteristics are determined by cooling the sample from 300 K down to base temperature at a rate of ~ 2 K/min, while sourcing a constant current and measuring the resulting voltage drops. Field-dependent magnetoresistance and Hall effect measurements are performed at fixed temperature, while sweeping the superconducting magnet in a chosen field range at rates between 0.1 T/min and 0.5 T/min.

[7] Further information regarding the measurement electronics can be found in ref. [94].

3

COUPLING LATTICE INSTABILITIES IN SIO/STO HETEROSTRUCTURES

"Well begun is half done."

– Aristotle

Oxide heterointerfaces constitute a rich platform for realizing novel functionalities in condensed matter. A key aspect is the strong link between structural and electronic properties, which can be modified by interfacing materials with distinct lattice symmetries. In this chapter, we determine the effect of the cubic-tetragonal distortion of $SrTiO_3$ on the electronic properties of thin films of $SrIrO_3$, a nodal line semimetal hosting a delicate interplay between spin-orbit coupling and electronic correlations. The compressive strain exerted by the $SrTiO_3$ substrate is found to force a binary domain structure in the $SrIrO_3$ film. We further demonstrate that, below the transition temperature at 105 K, $SrIrO_3$ orthorhombic domains couple directly to tetragonal domains in $SrTiO_3$. The close proximity to the metal-to-insulator transition in ultrathin $SrIrO_3$ causes the individual domains to have anisotropic transport properties, driven by a reduction of bandwidth along the in-phase axis. The strong structure–property relationships in perovskites make these compounds particularly suitable for static and dynamic coupling at interfaces, providing a promising route towards realizing novel functionalities in oxide heterostructures.

Parts of this chapter have been published by T.C. van Thiel, J. Fowlie, C. Autieri, N. Manca, M. Šiškins, D. Afanasiev, S. Gariglio and A.D. Caviglia in *ACS Mater. Lett.* **2(4)**, 389-394 (2020).

Simulation of the rotation angles was performed by J. Fowlie. DFT calculations were performed by C. Autieri.

ENGINEERING matter with tailored properties is one of the main objectives in condensed matter physics. Perovskite oxides have been at the center of attention due to the combination of a flexible lattice structure and strong structure-property relationships. At heterointerfaces, structural phases and domain patterns that are not present in bulk can manifest [95–97]. Such artificial phases can have a marked effect on electronic and magnetic properties and have been shown to modify features such as magnetic anisotropy [30, 31], interfacial ferromagnetism [98–100] and ferroelectricity [101]. Recent years have seen an increasing amount of attention focused on the exploration of nanoscale domains, which have emerged as an abundant source of novel physical properties [102–106]. Control of such domain patterns however, remains an open challenge. A possible way forward is to incorporate materials that undergo structural phase transitions. A canonical example is $SrTiO_3$ (STO), a widely used material that undergoes a transition from a cubic to a tetragonal phase when lowering the temperature below 105 K. At this temperature, STO breaks up into ferroelastic domains in which TiO_6 octahedra rotate about one of three possible directions [107]. When STO is used as a substrate for heteroepitaxial growth, the rotational distortion and resulting domain pattern can interact with the thin film due to octahedral connectivity across the interface [23]. In this context, semimetal $SrIrO_3$ (SIO) is of particular interest, since dimensionality and octahedral rotations have been shown to be pivotal in the delicate interplay between spin-orbit coupling (SOC) and electronic correlations [46, 108, 109]. Efforts to study SIO have primarily been fueled by theoretical predictions of a Dirac nodal ring, which is at the boundary between multiple topological classes, depending on the type of lattice symmetry-breaking [61, 110, 111]. In this respect, the interplay between the correlation strength and electronic bandwidth is crucial as it determines the position of the Dirac node with respect to the Fermi level [46, 110, 112]. The bandwidth is, among other things, governed by the Ir−O−Ir bond angle, which may be controlled through cation substitution, pressure tuning [113] or heteroepitaxy.

In this chapter, we demonstrate manipulation of the structural domain pattern of SIO thin films, through interaction with the tetragonal distortion of STO. We find (i) that the compressive strain exerted by the STO substrate forces a binary domain structure in the SIO film and (ii) that STO tetragonal domains couple to SIO orthorhombic domains. In ultrathin films, the STO tetragonal distortion induces an anisotropy in the longitudinal resistivity of SIO, which can manifest as a metal-to-insulator transition. Density-functional theory (DFT) calculations on ultrathin films corroborate the anisotropic character of the domains, revealing a depletion of states at the Fermi level along one lattice axis, while along the other the system remains metallic.

3.1. TRANSPORT ANOMALY

The resistivity (ρ) versus temperature (T) characteristics of three SIO/STO heterostructures measured in a Hall bar (HB) geometry are shown in Fig. 3.1a. The film thicknesses were chosen to be just above the critical point for the metal-to-insulator transition, such that the properties of the films are most sensitive to interface effects while maintaining a semimetallic ground state [108]. At $T = 105\,\mathrm{K}$, $\rho(T)$ displays a sudden change of slope. This change in resistivity of the SIO film occurs simultaneously with the structural

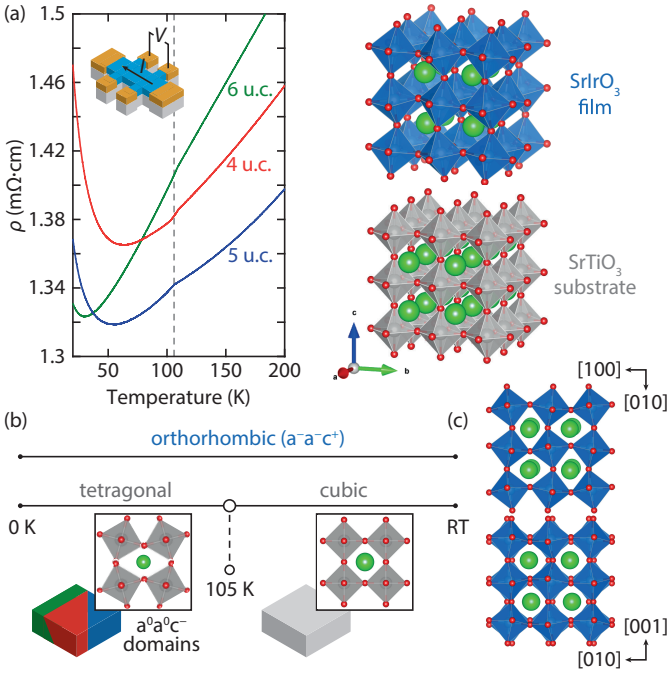

Figure 3.1: Simultaneous structural and electronic transition. (a) $\rho(T)$ curves of SIO films of different thicknesses, measured in a HB geometry oriented along the (100) lattice axis. (b) Phase diagrams of SIO and STO. Perovskite SIO is orthorhombic at all temperatures while STO undergoes a transition from a cubic to a tetragonal phase below 105 K. (c) Octahedral rotations and cation displacements of orthorhombic SIO viewed along the pseudocubic [001] (top) and [100] (bottom) directions.

phase-transition in the STO substrate, indicating a strong octahedral connectivity across the interface that couples the lattice degrees of freedom of the STO substrate to the electronic properties of the SIO film. We note that thicker films display similar behavior, albeit less pronounced (see also section 3.5.1). The structural phase diagrams and lattice structures of SIO and STO are shown in Figs. 3.1b-c [114]. Perovskite SIO has an orthorhombic structure (space group *Pbnm*) from 300 K down to low temperature, with rotation angles of typically 10° or larger about the pseudocubic lattice axes [56, 115]. STO is cubic ($Pm\bar{3}m$) but transforms into a tetragonal phase ($I4mcm$) below 105 K, where it forms three possible domains. Its transition temperature, as well as the magnitude of the distortion can be controlled by e.g., Ca- or Ba-doping [116–118].

3.2. BINARY DOMAIN STRUCTURE

Octahedral rotations double the perovskite unit cell vertices in real space, a phenomenon that gives rise to half-order Bragg peaks in X-ray diffraction measurements. The presence of specific half-order peaks is governed by symmetry [58], and the measurement of a set of half-order peaks can be used to fully determine the rotational pattern of the film [57]. STO is characterized by $a^0a^0c^-$ i.e., an out-of-phase rotation about the c-axis, which

is slightly elongated [119]. Orthorhombic SIO is denoted by $a^-b^-c^+$, having out-of-phase rotations of the same amplitude about two axes and in-phase rotations of different amplitude about the third axis [60]. To study the octahedral rotations in the SIO/STO heterostructures, we performed synchrotron X-ray diffraction measurements. The films have thicknesses of 40, 25, and 15 u.c. and are capped by an amorphous STO layer, preventing an additional diffraction signal from the capping layer while shielding the film from exposure to ambient conditions [89].

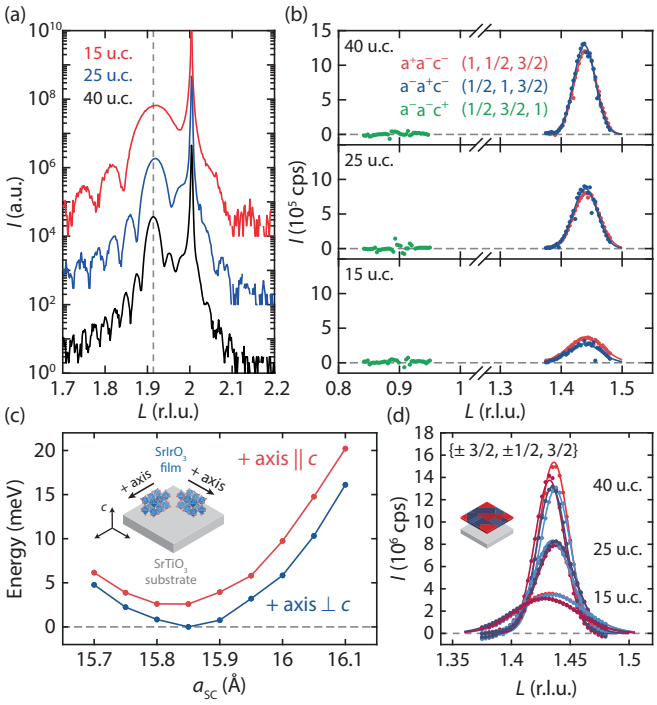

Figure 3.2: Binary domain structure. (a) XRD L-scans of SIO films of different thicknesses, measured in the vicinity of the (002) reflection of the STO substrate. (b) Half-order peaks arising from in-phase octahedral rotations. (c) DFT calculated energy difference per formula unit for the in-phase axis (red) parallel and (blue) perpendicular to the c-axis (growth axis) as a function of lattice constant for supercells consisting of four formula units of STO and SIO. (d) Half-order peaks from different geometric domains.

Measurements of the (002) diffraction peak of these films are shown in Fig. 3.2a, which demonstrate that the films are compressively strained. We first consider (h,k,l) Bragg conditions where one of the three reciprocal lattice positions is an integer and the other two are unequal half-order positions $(1/2, 1, 3/2)$. This peak is present if the integer reciprocal lattice vector is parallel to the real-space direction of the in-phase axis [120]. As shown in Fig. 3.2b, a peak is present when the integer reciprocal lattice vector is along h and k, but not along l. From this we infer that the in-phase rotation (+) axis lies in the plane of the film, and it exhibits a mixed population of $a^+a^-c^-$ and $a^-a^+c^-$ domains[1],

[1] We denote $a = b$ due to the approximately square in-plane symmetry imposed by the substrate.

consistent with previous reports [46, 121]. In the ABO_3 *Pbnm* structure, the *B*-*B* distance along the in-phase axis is slightly shorter compared to the out-of-phase axis. Therefore, to minimize the lattice mismatch with the compressive substrate, the in-phase axis should lie in-plane. The a^- axis, which experiences the largest strain, should then be oriented along the c^- axis of STO tetragonal domains, such that $a^-a^+c^-$ ($a^+a^-c^-$) domains in the film couple to $c^-a^0a^0$ ($a^0c^-a^0$) domains in the substrate. This is supported by DFT calculations (Fig. 3.2c), which show that forming $a^-a^-c^+$ domains is energetically unfavourable due to a larger in-plane lattice parameter when the in-phase axis is oriented out-of-plane (a_{pc} = 3.9430 Å) as compared to in-plane (a_{pc} = 3.9411 Å) [56]. In addition, alignment of the c^- and a^- axes of STO and SIO, respectively, preserves the continuity of the rotational symmetry across the interface. Different rotational domains arise depending on whether the octahedron closest to the origin rotates clockwise or counterclockwise about each axis. This can be probed by the $\{3/2, 1/2, 3/2\}$ series of half-order reflections [57]. Peaks are present for all reflection conditions (Fig. 3.2d), indicating that the SIO film consists of four geometric domains with *a* (anti-)parallel to [100] and [010], with approximately equal volume fractions.

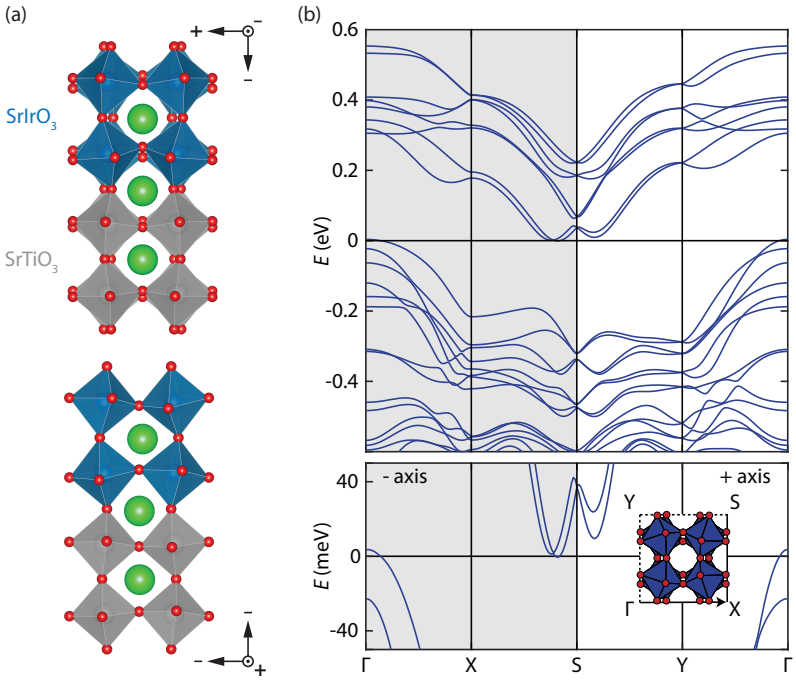

Figure 3.3: Electronic structure. (a) DFT calculated relaxed structure, viewed along the (top) a^- axis and (bottom) a^+ axis, (b) electronic structure with the out-of-phase (−) axis along Γ—X and the in-phase (+) axis along Γ—Y. The grey and white areas indicate parts of the Brillouin zone comprising transport either fully or partially along the out-of-phase and in-phase axis, respectively. The bottom panel shows an enlarged view around the Fermi energy. The inset shows the two-dimensional Brillouin zone of the orthorhombic unit cell.

Having established a coupling between the binary domain structure in the SIO film

and the tetragonal domains in the STO substrate, we turn to the question of how this interfacial domain coupling affects the electronic properties and the connection with the observed anomaly in the ρ-T curve. While in the *Pbnm* structure, the B−B distance along the in-phase axis is shorter compared to the out-of-phase axis, the B−O−B bond angles are more tilted [122]. Accordingly, one would expect a reduction of bandwidth along the in-phase axis due to reduced oxygen-mediated hopping [123], with anisotropic transport properties as a consequence. Fig. 3.3 shows the DFT-calculated relaxed lattice structure (Fig. 3.3a), as well as the electronic structure (Fig. 3.3b), assuming a correlation strength $U = 1.47$ eV, similar to previous work [108]. The out-of-phase (-) axis is oriented along Γ—X and the in-phase (+) axis along Γ—Y, with Γ the center of the Brillouin zone. Electron wavepackets along Γ—X have a group velocity oriented purely along the out-of-phase axis and those along X—S include a component along the in-phase axis, which is smaller than or equal to the component along the out-of-phase axis. Accordingly, Γ—X—S (gray region) comprises carrier transport oriented either fully or predominantly along the out-of-phase axis (and analogously for S—Γ—Y and the in-phase axis). Two electron-like pockets are present along X—S and S—Y. However, only the former intersects the Fermi level and the latter remains unoccupied. As a consequence, electronic bands along the in-phase axis are depleted at the Fermi level and the system is anticipated to favour insulating behaviour along the in-phase axis and remain metallic along the out-of-phase axis. This is a remarkable scenario, where the electronic structure is finely tuned between a metallic and insulating phase by a reduction of bandwidth along the in-phase axis.

Experimentally, we indeed observe anisotropic electronic properties. Fig. 3.4a shows $\rho(T)$ measured in a HB geometry and in two patterned van der Pauw (VdP) squares with sizes of 375 and 750 µm for two electrical configurations. We directly observe that the anomaly in ρ is much more pronounced in the VdP geometry than in the Hall bar and that a strong anisotropy develops below 105 K. As shown in Fig. 3.4b, the transition can be remarkably sharp and can manifest as a metal-to-insulator transition. The derivative $\mathrm{d}\rho/\mathrm{d}T$ is shown in the bottom panel, which shows opposite behaviour in the two electrical configurations i.e., a positive (metallic) or negative (insulating) slope depending on the orientation. Microscopically, this can be viewed as current traversing an unequal domain population in the probing region of the VdP device (see Figs. 3.4c-d). Domains in STO can be sized up to ~ 100 µm, which suggests, in accordance with our observations, that the anisotropic character should be most pronounced in small devices and reduced in larger devices due to statistical averaging over complex domain patterns [103, 104, 124]. The $\rho(T)$ anomaly at 105 K can then be ascribed to a sudden reconfiguration of the current paths as the SIO domains adapt to the onset of the tetragonal multi-domain state of the STO substrate. We remark that at the boundaries between adjacent structural domains, the crystal unit cells are typically distorted [104]. Considering the strong structure-property relationship in iridates, it is likely that the domain walls have different electronic properties compared to the undistorted areas. Measuring transport and spatially-resolved current flow, e.g., through scanning SQUID microscopy [125], may elucidate their electronic properties.

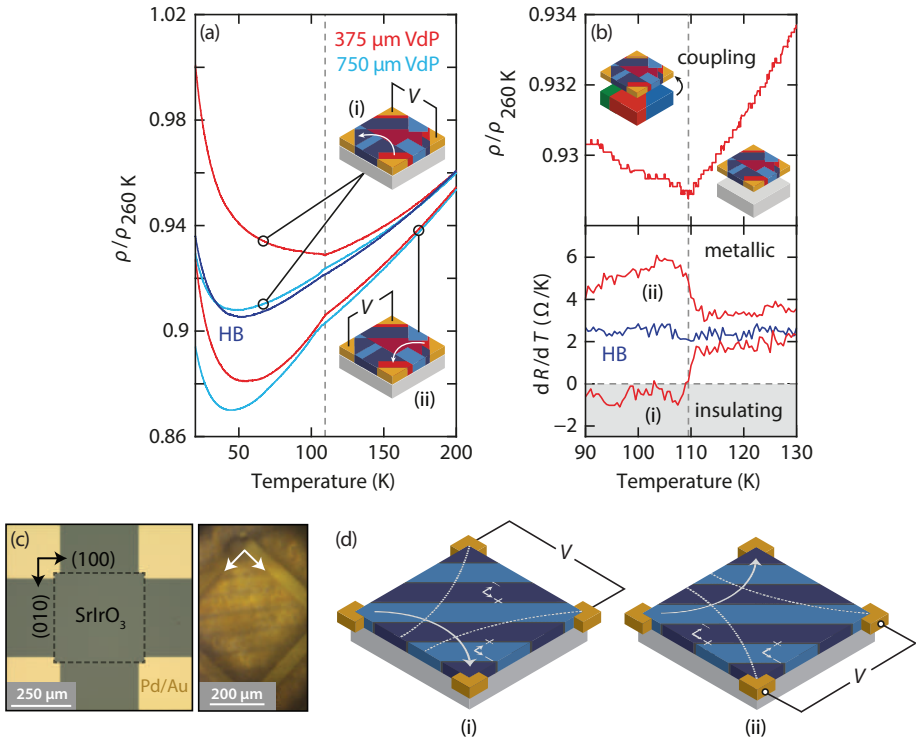

Figure 3.4: Anisotropic electronic transport. (a) $\rho(T)$ curves of a 5 u.c. film comparing (light blue) a large (750µm) and (red) small (375µm) VdP geometry, measured in two mutually orthogonal configurations of current and voltage probes. The dark blue curve represents the $\rho(T)$ curve recorded in a 150µm wide Hall bar (aspect ratio 3:1). (b) Enlarged view of $\rho(T)$ around the cubic-to-tetragonal transition of STO at 105 K (top) and the corresponding $\mathrm{d}R/\mathrm{d}T$ curves (bottom). (c) Optical microscope images of (left) the 375µm VdP device and (right) $c^-a^0a^0$ and $a^0c^-a^0$ tetragonal domains in a STO substrate in a 375µm square area. (d) Illustration of current traversing a binary domain population in the probing region of the device.

3.3. SUPPRESSION OF OCTAHEDRAL ROTATIONS

To further explore the effect of the STO tetragonal distortion on the octahedral rotations in SIO, we performed temperature-dependent diffraction measurements across the transition temperature. By fitting the half-order Bragg peaks with a Gaussian function and comparing the areas under the curves, we quantify the octahedral rotation angles and cation displacements as a function of temperature [92]. The oxygen positions are obtained by comparing the intensities of the peaks with the calculated structure factor of the oxygen octahedra. Standard nonlinear regression is used to determine the optimal values of α and γ, defined in Fig. 3.5. The determined in- and out-of-plane rotation angles α and γ, respectively, are plotted versus temperature for SIO films of different thicknesses in Fig. 3.5a. The angles are found to be nearly constant over the entire temperature range and weakly dependent on the film thickness (Fig. 3.5b). Fig. 3.5c visualizes the low temperature lattice structure. The rotational angles are substantially reduced with respect to bulk SIO. Considering that STO has been reported to strongly

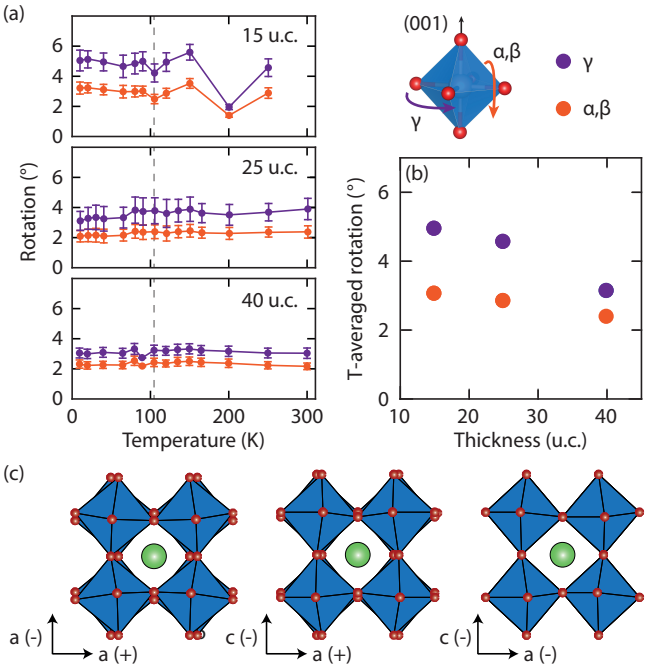

Figure 3.5: Temperature dependence of octahedral rotations. (a) Rotation angles of the 15, 25, and 40 u.c. films as a function of temperature. (b) Temperature-averaged rotation angles as a function of film thickness. (c) Visualization of the octahedral rotation pattern as seen (from left to right) along the c^-, a^- and a^+ axes, respectively.

suppress octahedral rotations in other oxide heterostructures [30], we attribute this to the interaction with the STO substrate [126]. We also find an enhancement of the angles for the thinner films, possibly pointing to larger rotational distortions in the unit cells closest to the STO/SIO interface. Interestingly, we do not observe a clear deviation of the SIO rotation angles across 105 K, further pointing to the reconfiguration of the multidomain state as the underlying cause of the observed resistivity anomaly at 105 K.

3.4. CONCLUSIONS

In summary, we established an interfacial coupling in ultrathin STO/SIO heterostructures and demonstrated the emergence of a binary orthorhombic domain pattern in SIO that couples directly to the tetragonal domains in the STO substrate. For each domain, the electronic bandwidth along the in-phase rotational axis is suppressed, resulting in strongly anisotropic transport properties that can manifest as a metal–insulator transition. This coupling mechanism is not limited to iridates, but may be extended to control physical properties such as magnetism, multiferroicity and superconductivity in a wide variety of orthorhombic materials, e.g., ferrites, manganites and nickelates [24, 93, 127–131].

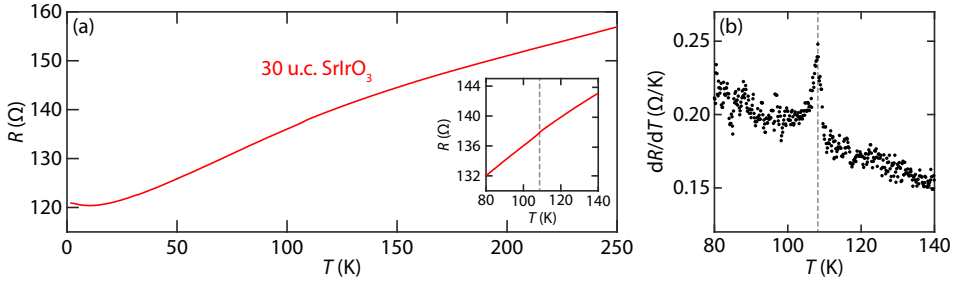

Figure 3.6: Resistivity anomaly in 30 u.c. film. (a) Resistance as a function of temperature for a 30 u.c. SIO film. The inset shows an enlarged view in the vicinity of 105 K. Panel (b) shows the derivative $\mathrm{d}R/\mathrm{d}T$.

3.5. SUPPLEMENTARY INFORMATION

3.5.1. RESISTIVITY ANOMALY IN A 30 U.C. SIO FILM

In Fig. 3.6, we show transport measurements of a 30 u.c. SIO film. The full resistance curve as a function of temperature is shown in Fig. 3.6a, with the inset representing an enlarged view around the cubic-tetragonal transition of the STO substrate. While not as pronounced as in the thinner films, an anomaly is observed at the transition temperature, also identified from the derivative with respect to temperature shown in panel Fig. 3.6b. The underlying reason for the less pronounced features in thicker films is their more strongly metallic and three-dimensional character, resulting in more pockets intersecting the Fermi energy, therefore rendering the anisotropic properties less prominent.

3.5.2. DETERMINATION OF THE OCTAHEDRAL ROTATIONS

The X-ray diffraction measurements were carried out at the I16 beamline at Diamond Light Source in the form of a series of off-specular crystal truncation rods (CTRs), centered on half-integer Bragg diffraction positions. The CTRs were recorded on a Pilatus 100k photon-counting pixel detector, at a fixed incidence angle of 4° and a photon energy of 8 keV. For each sample, the same series of CTRs was recorded at temperatures ranging from 10 K to 300 K. We find that that all films, at all temperatures, adhere to the $Pbnm$ symmetry with the short (in-phase) axis always perpendicular to the growth axis. In other words, the system can be described in Glazer notation as a combination of $a^+a^-c^-$ and $a^-a^+c^-$ [58]. The population fractions of these domains can be estimated by comparing the intensities of e.g., $(1/2, 1, 3/2)$ and $(1, 1/2, 3/2)$, which were found to be approximately equal in the area of the beam spot. Rotations about the a and b axes, whether they be out-of-phase or in-phase, are assumed to be equal in magnitude given the approximate square in-plane symmetry of the heterostructure [57]. Finally, four geometric domains (oriented along $[100], [\bar{1}00], [010]$ and $[0\bar{1}0]$) are found to exist in approximately equal proportion from observing the presence of equally intense Bragg peaks that belong to the same family, such as $(3/2, 1/2, 3/2)$, $(-3/2, 1/2, 3/2)$, $(3/2, -1/2, 3/2)$ and $(-3/2, -1/2, 3/2)$, which amount to rotations of the sample about its own normal by 90°. Further quantitative information of the rotation angles was obtained from the intensities of the allowed half-integer Bragg peaks in the manner first introduced by May and coworkers [57, 92]. The experimental integrated intensity, I_{exp}, was extracted from each

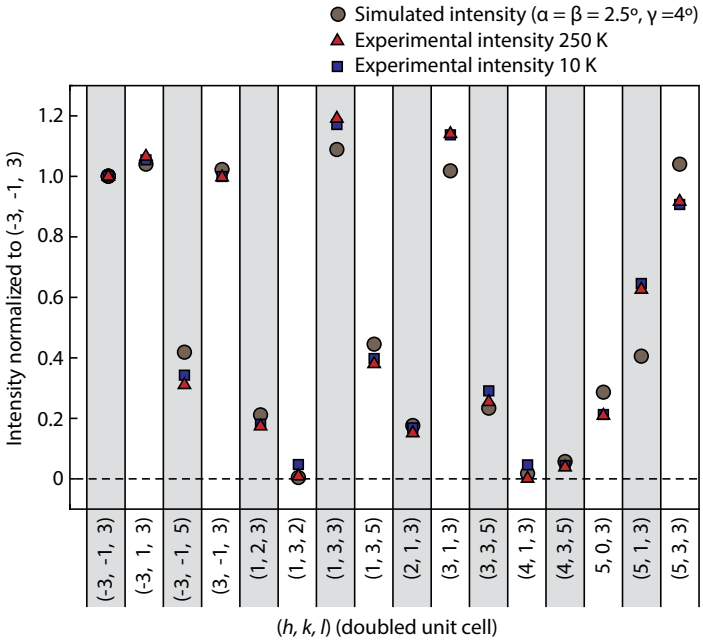

Figure 3.7: Half-order peak fit. Experimental and simulated half-order peak intensities of a 25 u.c. SIO film for temperatures 10 K and 250 K. The black dots indicate simulated half-order peak intensities for $\alpha = \beta = 2.5°$ and $\gamma = 4°$.

CTR and compared to a simulated diffraction intensity, I_{sim}, for the same (h,k,l) and for a given set of Glazer angles, α, β and γ. Then, upon varying the input angles, the best fit simulated structure is found by the minimizing the residual sum of squares (RSS), defined as

$$\text{RSS} = \sum_n \left| I_{\text{sim}}(h,k,l)_n - I_{\text{exp}}(h,k,l) \right|^2 \tag{3.1}$$

with

$$I_{\text{sim}}(h,k,l) = \sum_{v=1}^{2} \sum_{p=1}^{4} \left[f_{O^{2-}} \sum_{n=1}^{24} \exp\left(2\pi i \left(h x_{npv} + k y_{npv} + l z_{npv}\right)\right) \right] \tag{3.2}$$

The simulated diffraction intensity is calculated from the square of the structure factors for the 24 O^{2-} ions that constitute the perovskite pseudocubic unit cell of SIO doubled in all three directions. The two equally populated orthorhombic domains as well as the four equally populated geometric domains must also be summed over, represented by the indices v and p respectively. The atomic positions, $(x_{nvp}, y_{nvp}, z_{nvp})$ for each of the n oxygen atoms used to generate the structure factors are obtained after careful application of three dimensional rotation matrices to an undistorted octahedron, as described

in ref. [93]. This method permits determination of Sr-cation displacements, however the best fitting results were obtained by locking them to a cubic sublattice.

Fig. 3.7 shows an example of a fitting result for a 25 u.c. film, comparing temperatures 250 K and 10 K. As discussed previously, the rotation angles are nearly independent of temperature and significantly reduced with respect to bulk SIO, presumably due to compressive strain exerted by the substrate.

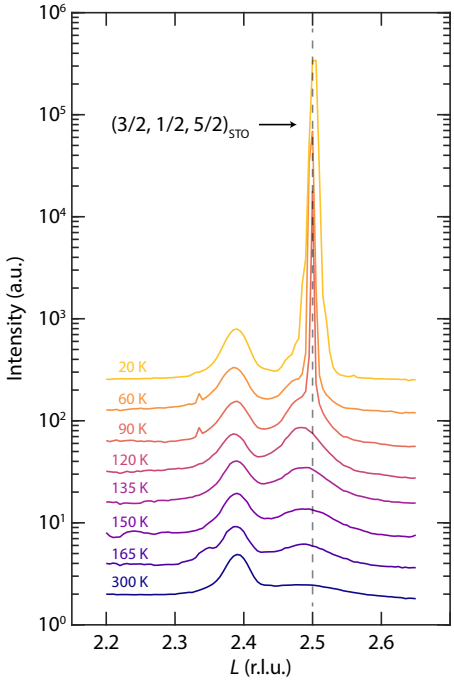

Figure 3.8: Distortions in STO. L-scan in the vicinity of the $(3/2, 1/2, 5/2)$ reflection of the STO substrate.

3.5.3. DISTORTIONS IN STO ABOVE THE CONDENSATION POINT

Fig. 3.8 shows XRD L-scans in the vicinity of the STO $(3/2, 1/2, 5/2)$ reflection for a 30 u.c. SIO film, which probes out-of-phase rotations. We first focus on the curve at 20 K, which is well below the cubic-to-tetragonal transition temperature of STO. The intense peak at $L = 2.5$ originates from the substrate, whereas the broader peak situated slightly below $L = 2.4$ originates from the SIO film. As the temperature is increased, the substrate contribution is seen to diminish, but it does not vanish entirely. For temperatures 120 K and above, the sharp feature is no longer present but a broader peak around $L = 2.5$ remains discernible up to 300 K. This indicates the presence of tetragonality in STO well above 105 K. As discussed prior, the strong octahedral connectivity across the interface causes the STO substrate to force a rotational pattern on the SIO film. Such a coupling can work both ways, meaning that the SIO film may also promote rotations in the top layers of the

substrate. Alternatively, this could be the result of the STO surface layers behaving differently from the bulk [132, 133]. We remark that the degree of tetragonality in STO above 105 K is small and that macroscopic condensation of the entire substrate into a tetragonal state, coinciding with a redistribution of the domain configuration and current paths in the SIO film, only occurs at 105 K. Nevertheless, it is possible that it contributes to the pinning of domains, meaning there is a larger probability of encountering a similar (or identical) domain structure in STO (and possibly SIO) across different heating/cooling cycles. Possibly, this contributes to the degree of anisotropy already present above 105 K in Fig. 3.4a.

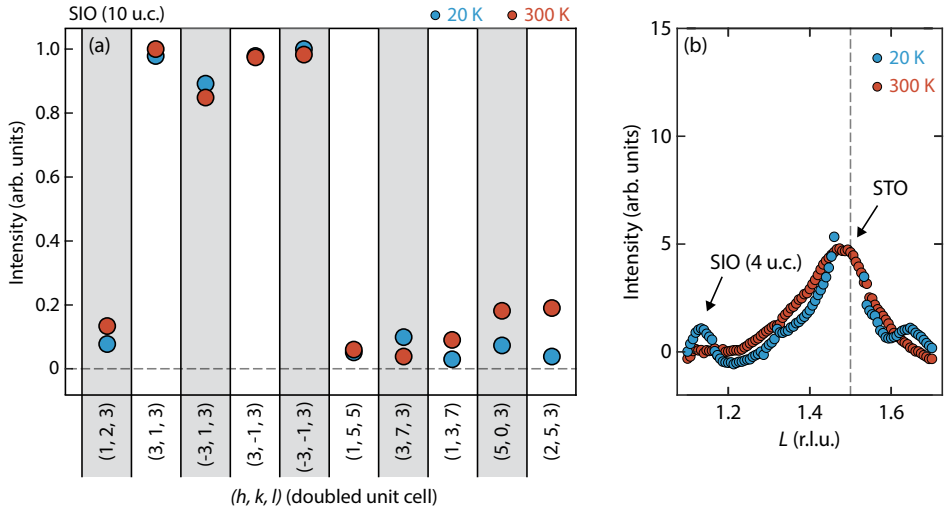

Figure 3.9: Half-order peaks in ultrathin films. (a) Half-order peak intensities for a 10 u.c. SIO film on STO measured at (red) 300 K and (blue) 20 K. The intensity values have been normalized to the (3,1,3) peak intensity. (b) L-scan in the vicinity of the $(3/2, 1/2, 3/2)$ reflection for a 4 u.c. SIO film, comparing high (300 K, red) and low temperature (20 K, blue).

3.5.4. DIFFRACTION MEASUREMENTS ON ULTRATHIN FILMS

In Fig. 3.9, we show diffraction data on a 10 u.c. and 4 u.c. film, comparing half-order peak intensities at 300 K and 20 K. We find that for the 10 u.c. film, some subtle structural differences between 300 K and 20 K are present. For the 4 u.c. film, not all reflections had a sufficient signal intensity to perform a complete analysis. Nevertheless, the comparison between high and low temperature in panel (b) reveals a significant change of the $(3/2, 1/2, 3/2)$ reflection at low temperature, suggesting a more pronounced change in rotation angles of ultrathin SIO across the STO phase transition. The peak observed at 300 K at $L = 1.5$ corresponds to the STO substrate and is indicative of tetragonal distortions in STO above the transition point.

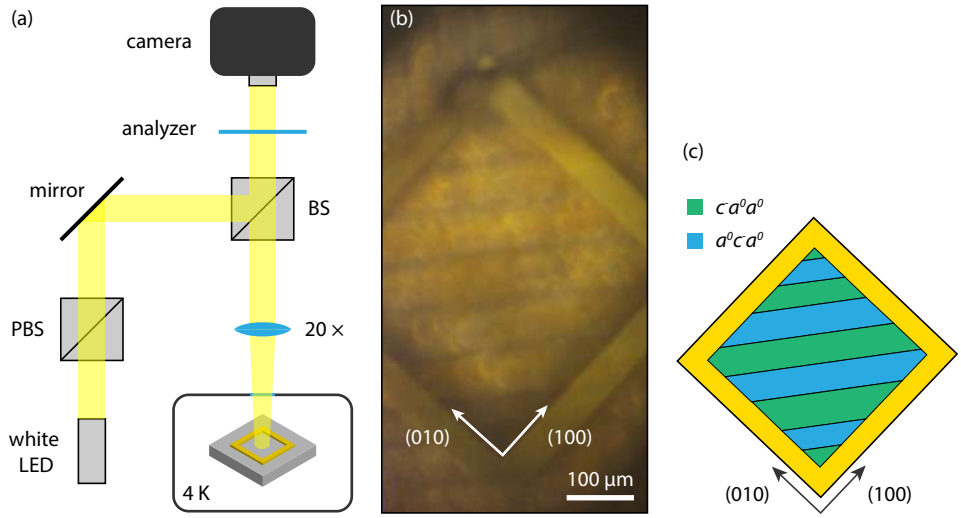

Figure 3.10: (a) Schematic illustration of the polarized light microscopy setup, (b) image recorded with crossed polarizers, showing STO tetragonal domains and (c) illustration of (b) showcasing the different domains joined by twin boundaries.

3.5.5. IMAGING TETRAGONAL DOMAINS IN STO

Below 105 K the structure of STO is split into three types of tetragonal domains, each corresponding to a rotation and elongation of the unit cell along one of three equivalent directions. We demonstrated that to minimize the lattice mismatch, $c^-a^0a^0$ and $a^0c^-a^0$ domains in the STO substrate are coupled to $a^-a^+c^-$ and $a^+a^-c^-$ domains in the overlying SIO film, respectively. Since tetragonal domains in STO are birefringent [134], this provides an opportunity to optically study the multi-domain state. Here we use polarized-light microscopy to visualize the domain structure of a STO substrate (see Fig. 3.10a). The light from an LED source was collimated, polarized with a Glan-Taylor prism and focused on the sample surface by an optical objective. The light reflected from the sample was collected by the same objective and directed to the sensor area of a digital camera. The polarization contrast was acquired by placing a second polarizer (analyzer) in the optical path of the reflected beam such that the mutual polarizations of the two polarizers were nearly orthogonal (cross-Nikol configuration). To maximize the signal, the measurements were done at the lowest accessible stable temperature of 4 K. As discussed in ref. [104], $a^0c^-a^0$ and $c^-a^0a^0$ domains in STO are joined by twin boundaries oriented at approximately 45° with respect to the (100) or (010) lattice axis. In the vicinity of the domain boundary, the STO unit cells are distorted, resulting in a locally modified birefringence. Accordingly, in the cross-Nikol configuration, the tetragonal domains appear bright and the boundaries between them appear dark. In Fig. 3.10b, we show a microscopy image of the polarization contrast obtained in the cross-Nikol configuration. To facilitate comparison with the devices discussed in section 3.2, a Cr/Au open square geometry of inner width 375 µm is patterned on top. Nine different domains are discernible within the square area. Fig. 3.10c shows a trace of the domains. Note that

this experiment only identifies the domain boundaries and not the domains themselves. The illustration in (c) represents therefore only one of two possible configurations. The relatively large size of the domains with respect to the device dimensions leads to an increased probability of encountering an unequal distribution of domain areas. In this particular example, we find a distribution of four versus five with the majority domain type having of about 4% larger surface area within the square. As the probing area of a van der Pauw device is smaller than the full square area, the imbalance probed in a transport experiment is statistically likely to be larger.

3.5.6. DFT COMPUTATIONAL METHODOLOGY

DFT calculations were carried out within the generalized gradient approximation (GGA), by using the plane-wave VASP package and the PBEsol for the exchange-correlation functional with spin-orbit coupling [135, 136]. Computations were performed for a supercell with 4 formula units of STO and 4 formula units of SIO, with the in-phase axis parallel to the growth axis, as well as a supercell with 8 formula units of STO and 8 formula units of SIO with the in-phase axis perpendicular to the growth axis. A $8 \times 8 \times 2$ and $6 \times 6 \times 2$ k-point Monkhorst-Pack grid was used for all calculations on the supercells of 40 and 80 atoms, respectively. The structural relaxation was performed separately for each volume. Hubbard U effects between Ir sites were included within the GGA + U [137], with a value $J_{\mathrm{H}} = 0.15U$ for the Hund's coupling. Experimentally observed insulating behaviour is reproduced by introducing G-type antiferromagnetic order with $U = 1.47\,\mathrm{eV}$. This value is close to the previously reported value for antiferromagnetic SIO [108].

4

THE ANOMALOUS HALL EFFECT IN ULTRATHIN SRO

"I thought one should have the attitude of: 'What do you care what other people think!'."

– Richard Feynman

Three-dimensional strontium ruthenate $SrRuO_3$ is an itinerant ferromagnet that features Weyl points acting as sources of an emergent magnetic field. Integrating $SrRuO_3$ in oxide heterostructures is potentially a novel route to engineer emergent electrodynamics, but its electronic band topology in the two-dimensional limit remains unknown. In this chapter, we show that ultrathin $SrRuO_3$ exhibits topologically non-trivial bands at the Fermi energy. Their band anti-crossings show an enhanced Berry curvature and act as competing sources of emergent magnetic fields. We control their balance by designing heterostructures with symmetric ($SrTiO_3$/$SrRuO_3$/$SrTiO_3$ and $SrIrO_3$/$SrRuO_3$/$SrIrO_3$) and asymmetric interfaces ($SrTiO_3$/$SrRuO_3$/$SrIrO_3$). Symmetric structures exhibit an interface-tunable single-channel anomalous Hall effect, while ultrathin $SrRuO_3$ embedded in asymmetric structures shows hump-like features consistent with multiple anomalous Hall contributions. We further demonstrate that this effect can be mimicked by designing ultrathin $SrRuO_3$ bilayers separated by an insulating $SrTiO_3$ spacer, forming an all-oxide extraordinary Hall balance device.

Parts of this chapter have been published by D.J. Groenendijk*, C. Autieri*, T.C. van Thiel*, W. Brzezicki* et al. in *Phys. Rev. Res.* **2(2)**, 023404 (2020) and by T.C. van Thiel*, D.J. Groenendijk* and A.D. Caviglia in *J. Phys. Mater.* **3(2)**, 025005 (2020).

Theoretical results were obtained by C. Autieri, W. Brzezicki, P. Barone, A. Filippetti, S. Picozzi and M. Cuoco. STEM characterization was performed by N. Gauquelin, D. Jannis, K.W.H. van den Bos, S. van Aert and J. Verbeeck. Magneto-optical characterization was performed by J.R. Hortensius and D. Afanasiev. SQUID measurements were performed in collaboration with M. Gibert.

THE Berry phase refers to the phase acquired by a quantum state when it adiabatically traverses a closed path in parameter space [76]. In crystals, this mechanism applies to the electron wavefunction in the space spanned by the Bloch momentum coordinates. Analogous to the phase acquired by moving charges in a magnetic field, the Berry phase mechanism causes electrons in an electric field $\mathscr{E}$ to acquire an anomalous component to their group velocity

$$\boldsymbol{v}(\boldsymbol{k}) = \frac{1}{\hbar}\frac{\partial \boldsymbol{E}(\boldsymbol{k})}{\partial \boldsymbol{k}} - \frac{e}{\hbar}\mathscr{E} \times \boldsymbol{b}(\boldsymbol{k}), \tag{4.1}$$

where $E(\boldsymbol{k})$ is the dispersion relation and $\boldsymbol{b}(\boldsymbol{k})$ is the momentum-space Berry curvature. The latter term describes the non-trivial geometry of the band structure and acts as an effective magnetic flux, which generally underlies topological transport phenomena such as the quantum, spin and anomalous Hall effect (AHE) [72, 76, 138–140]. The anomalous velocity is transverse to the electric field and gives rise to a Hall voltage, with a sign and magnitude that depend sensitively on the band structure topology. In systems with ferromagnetic order and an appreciable spin–orbit coupling, the Berry curvature is strongly enhanced near avoided band crossings, which act as a source or sink of the emergent magnetic field [141]. A prototypical system is the transition-metal oxide $SrRuO_3$ (SRO), a $4d$ itinerant ferromagnet [68]. Its anomalous Hall conductivity in the bulk depends sensitively on the magnetization and on the position of the Fermi energy with respect to the Weyl points in the three-dimensional electronic structure [65, 72, 142, 143]. Extrinsic (scattering) mechanisms are known to contribute to the AHE in SRO [75, 144, 145]. However, when the Weyl points are in close proximity to the Fermi energy the intrinsic Berry curvature mechanism becomes dominant [143], particularly at temperatures far below the Curie point [72, 75].

The Berry curvature is particularly sensitive to electronic reconstructions. Accordingly, integrating ultrathin SRO within heterostructures is a promising route to engineer topological transport phenomena. A suitable material for this purpose is $SrIrO_3$ (SIO), a $5d$ paramagnetic semimetal with strong atomic spin-orbit coupling(~ 0.4 eV) [45, 46, 108, 109, 146] and excellent structural compatibility with SRO. Recently, the behavior and control of the AHE in SRO ultrathin films and heterostructures have been at the center of intense research [147–155], fueled by the observation of hump-like features in the transverse resistivity [37]. Such features are generally considered to be a manifestation of the topological Hall effect (THE). In this scenario, topologically non-trivial spin textures give rise to Berry curvature sources in real-space [156–158]. Embedding SRO in $SrTiO_3$ (STO) and SIO heterostructures (SIO/SRO/STO) sets a favorable environment for non-collinear spin-textures (e.g., skyrmions) because of the strong spin-orbit coupling present in SIO and the breaking of inversion symmetry across the interface [37, 147]. Moreover, hump-like features in the Hall response have also been observed in SRO thin films interfaced with STO and vacuum [41, 151, 159, 160], pointing to an important role played by asymmetric boundary conditions and momentum-space sources of Berry curvature.

In this chapter, we describe a theoretical analysis of the low-energy electronic structure and band topology of SRO in the two-dimensional limit. The analysis reveals a set of topologically non-trivial bands at the Fermi energy, associated with sources of Berry

curvature, bringing about competing contributions to the anomalous Hall response. We subsequently use these insights to investigate theoretically and experimentally the AHE in ultrathin SRO films with (a)symmetric boundary conditions. Asymmetric heterostructures show hump-like features in the vicinity of the magnetization reversal, which we show are well described by a phenomenological two-channel model. We subsequently demonstrate that this effect is mimicked by ultrathin SRO bilayers separated by an insulating STO spacer, where the two SRO layers have slightly different thicknesses.

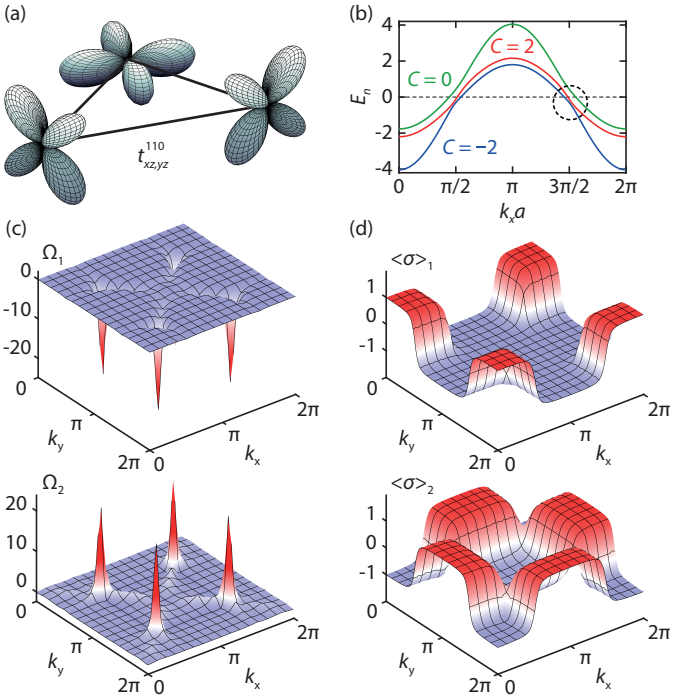

Figure 4.1: Topological bands in ultrathin SRO. (a) Next-nearest-neighbor interorbital hopping. (b) Dispersion of Ru t_{2g} bands along $k_x = k_y$ for a representative value of the magnetization. (c) Berry curvature associated with topologically non-trivial Ru t_{2g} bands close to the Fermi level with Chern numbers $C = \pm 2$. (d) Spin polarizations $\langle\sigma_z\rangle_n$ for the corresponding bands.

4.1. TOPOLOGICAL BANDS

We first discuss the topological properties of monolayer SRO, starting from the Ru-based t_{2g} electronic structure. In section 4.6.1, we show that different contributions to the Hamiltonian— the spin-orbit coupling, nearest neighbour and next-nearest neighbour hopping in the (xy)-plane—all preserve the product of the spin state and orbital parity, referred to as the spin-orbital parity. It then follows that any matrix elements in a tight-binding Hamiltonian that couple spin-orbital states with different parities are zero, analogous to a selection rule. In other words, one can group states with positive and negative spin-orbital parity such that the 6×6 Hamiltonian becomes block diagonal, with

each block spanning a 3×3 submatrix. The positive parity submatrix is spanned by the states $|-1\downarrow\rangle$, $|+1\downarrow\rangle$ and $|0\uparrow\rangle$. Similarly, the negative submatrix is spanned by the states $|-1\uparrow\rangle$, $|+1\uparrow\rangle$ and $|0\downarrow\rangle$. There are a number of remarks to be made about the parity conservation. First, it permits to investigate the band structure of monolayer SRO separately for each parity sector [161]. Second, it is valid in the presence of a spin splitting (due to e.g., an external magnetic field or intrinsic magnetization), but only for (effective) fields oriented along the quantization (z) axis. Third, in the absence of such a spin splitting, the two sectors are degenerate. Introducing an external magnetic field or magnetization therefore has the effect of lifting the degeneracy of the parity sectors i.e., shifting the constituent bands in energy. Density-functional theory (DFT) derived tight-binding calculations for the monolayer reveal that in the presence of spin-orbit coupling, the next-nearest neighbour inter-orbital hopping (see Fig. 4.1a) mixes bands with a d_{xz} and d_{yz} character, producing two topologically non-trivial bands carrying a Chern number $C = \pm 2$, accompanied by a single, trivial band with $C = 0$, (see Fig. 4.1b). The ensuing Berry curvature of the topological bands is shown in Fig. 4.1c, which exhibits sharp peaks located at the avoided band crossings. Since the lowest energy bands in Fig. 4.1b are non-trivial, the Berry curvature contribution of each band cannot vanish and is robust to changes in the Fermi level or, in general, of the corresponding electron occupation[1]. Their splitting and relative occupation leads to a dominance of one of the contributions, including sign changes, when considering the averaged Berry curvature. The spin-orbit coupling causes the bands with opposite Berry curvature and $d_{xz/yz}$ orbital character to have a distinct momentum dependence of the spin polarization $\langle\sigma_z\rangle$, with an opposite sign developing nearby the points of maximal Berry curvature accumulation, as shown in Fig. 4.1d. This illustrates the connection between the Berry curvature spikes and a swift change in the spin-orbital state, which has recently been experimentally verified through synchrotron CD-ARPES[2] measurements [162].

We note that the opposite parity sectors produces bands with precisely opposite Chern numbers, meaning that in the absence of a net magnetization, the electronic structure becomes trivial. The magnetization is therefore an important parameter governing the overall magnitude and sign of the Berry curvature and therefore the anomalous Hall effect.

4.2. INTERFACE RECONSTRUCTIONS

We first investigate SRO films with symmetric boundary conditions. We consider heterostructures composed of STO/SIO(2)/SRO(4)/SIO(2)/STO(10) and STO/SRO(4)/STO(10), where the number in brackets denotes the number of unit cells. Strikingly, we find that the sign of the AHE is opposite for SIO/SRO/SIO (Fig. 4.2a) and STO/SRO/STO (Fig. 4.2b) heterostructures. This immediately shows that symmetry breaking in ultrathin SRO directly controls the magnitude and sign of the Berry curvature. The magnitude of the AHE (R_{yx}^{AH}) as a function of temperature is shown in Fig. 4.2c. While R_{yx}^{AH} of the STO/SRO/STO is predominantly negative, R_{yx}^{AH} for SIO/SRO/SIO remains positive in the entire temperature range, confirming the expectation that the occupation of the topologically active

[1] This concept is further explored in Chapter 5.
[2] circular dichroism angle-resolved photoemission spectroscopy

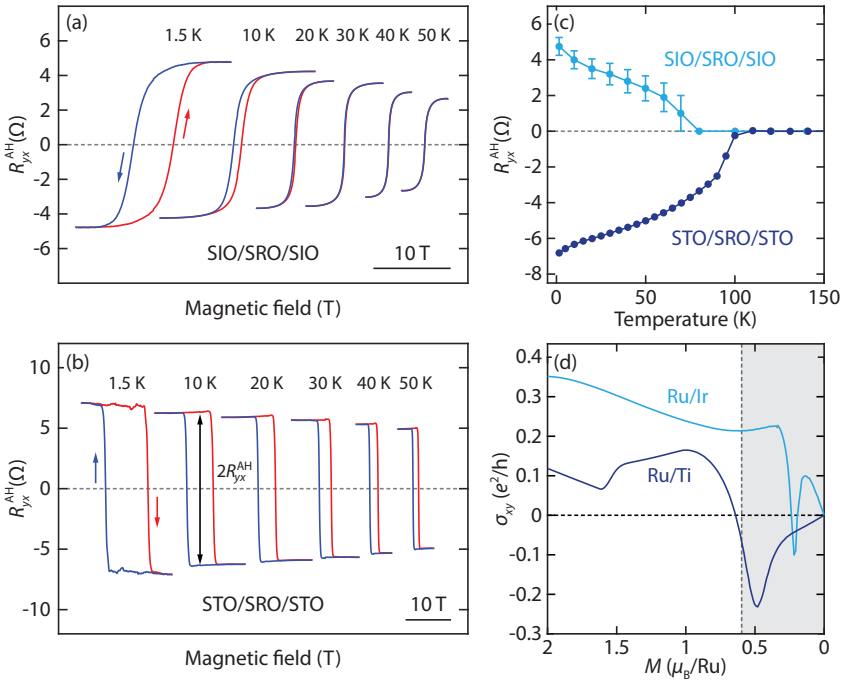

Figure 4.2: AHE in SRO/STO and SRO/SIO. (a-b) Hall resistance of symmetric (a) SIO/SRO/SIO and (b) STO/SRO/STO heterostructures as function of temperature. The curves are offset horizontally and the classical (linear) Hall effect has been subtracted. (c) Evolution of the experimentally measured AHE amplitude (R_{yx}^{AH}) in temperature. (d) Evolution of the calculated intrinsic contribution to σ_{xy} for Ru/Ti and Ru/Ir bilayers as a function of the average Ru magnetization. The dashed black line indicates the approximate saturation magnetization value of the STO/SRO/STO heterostructure, as estimated from SQUID measurements.

Ru t_{2g} bands depends sensitively on the electronic and magnetic reconstruction at the interface. This behaviour can be qualitatively captured by modelling Ru/Ti and Ru/Ir bilayers i.e., systems with a single SRO unit cell coupled to a single STO or SIO unit cell[3]. As shown in Fig. 4.2d, for a small/intermediate amplitude of the Ru magnetization, the AH conductivity of the Ru/Ti bilayer is negative, while for the Ru/Ir bilayer it is positive. In the former, only the Ru $d_{xz,yz}$ bands contribute since STO is electronically inert, while for the latter, the intrinsic competition of the topological Ru bands is modified through the hybridization of the Ir/Ru $d_{xz,yz}$ orbitals, and possibly through interface-driven spin canting. Indeed, the qualitative shapes of the hysteresis loops shown in Fig. 4.2a are consistent with a stronger in-plane component to the magnetic anisotropy as compared to Fig. 4.2b.

We also note that the rather large coercive fields observed are likely caused by, or in large part contributed to, the presence of defects acting as pinning sites [163, 164]. Thicker films were found to have smaller coercive fields, suggesting (i) that interface disorder is a contributing factor and (ii) that surface anisotropy is prominent. The latter typically

[3]The out-of-plane next-nearest neighbour hopping is neglected, conserving the spin-orbital parity.

leads to a perpendicular magnetic anisotropy for thin films, with an effective anisotropy constant [165]

$$K_{\text{eff}} = K_v + \frac{2K_s}{d}, \tag{4.2}$$

where d is the film thickness and subscripts (v, s) denote volume and surface contributions, respectively. In the ultrathin limit, the surface contribution is expected to dominate.

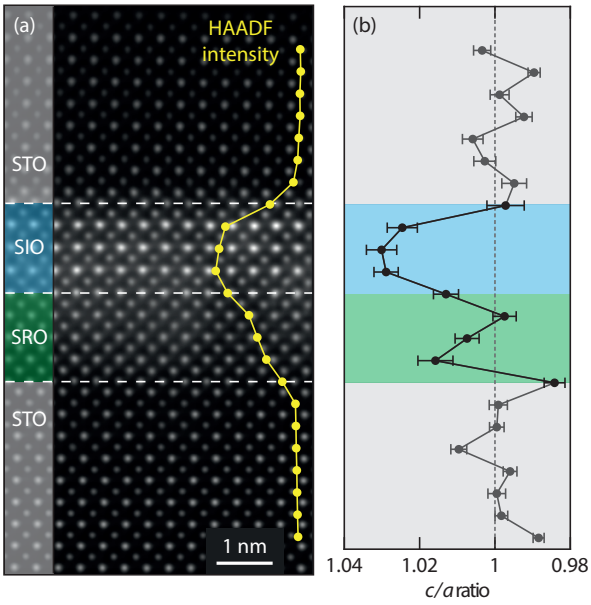

Figure 4.3: HAADF-STEM. (a) HAADF-STEM measurement of a STO/SRO/SIO heterostructure. (b) Mean c/a ratio of the perovskite unit cell across the heterostructure.

To study the effect of asymmetric boundary conditions, we now investigate the tricolor STO/SRO/SIO system. Given the different trends observed in the symmetric systems, we expect competition in the total R_{yx}^{AH} in this case. The atomic arrangement at the interfaces is investigated by high-angle annular dark-field scanning transmission electron microscopy (HAADF-STEM) and is displayed in Fig. 4.3a (see also section 4.6.4). Compositional analysis by electron energy loss spectroscopy (EELS) shows that the Ti/Ru and Ti/Ir interfaces are atomically sharp, while at the Ru/Ir interface, a slightly larger degree of intermixing is observed. After quantifying the atomic column positions in the HAADF-STEM image, a detailed analysis of the atomic positions shows that octahedral tilts are suppressed and both the SRO and SIO tend towards a tetragonal rather than an orthorhombic symmetry. In addition, we find that the c/a ratio (tetragonality) of the unit cell varies across the SRO and SIO layers (Fig. 4.3b). Since the magnetic anisotropy of SRO is known to be sensitive to strain and tetragonality [166–168], this potentially af-

fects the easy axis direction of the different SRO layers and hence the local magnetization of the Ru atoms.

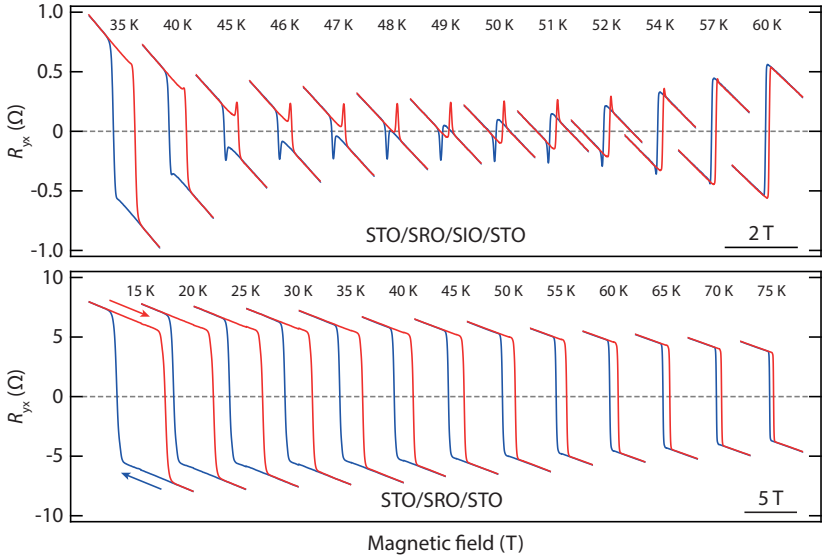

Figure 4.4: AHE in asymmetric heterostructures. Measured Hall resistance of (top) an asymmetric STO/SRO/SIO heterostructure and (bottom) a symmetric STO/SRO/STO heterostructure as function of temperature. The curves are offset horizontally.

The measured AHE of the asymmetric STO/SRO/SIO is shown in the top panel of Fig. 4.4. With increasing temperature, the AHE changes sign at the reversal temperature $T_R = 48$ K and peaks appear to be superimposed on the Hall effect, slightly above or below the coercive field (B_c). This is in stark contrast with the AHE of the STO/SRO/STO heterostructure (bottom panel), where the magnitude (R_{yx}^{AH}) decreases with increasing temperature. The peaks seemingly superimposed on the Hall effect are present between 35 and 58 K and reach their maximum amplitude at T_R, i.e., when R_{yx}^{AH} appears to be zero. This strongly suggests that their occurrence can be intrinsically linked to the sign reversal of the AHE. In the following section, we will explore this concept further.

4.3. THE TWO-CHANNEL MODEL

Having assessed the sign tunability of the AHE in symmetric STO/SRO/STO and SIO/SRO/SIO heterostructures, we next consider the anomalies of the Hall resistivity in asymmetric STO/SRO/SIO. One would expect that the resulting AHE in the asymmetric heterostructures can be considered as a superposition of AH channels with opposite signs and suitable weights [169–171]. Indeed, the data is well described by two such contributions, each having a slightly different coercive field (see Fig. 4.5a). When a current is applied in the plane of the heterostructure and an out-of-plane magnetic field is varied in the range $[0, B, -B, 0]$, the total AHE is given by the sum of the AHE of the two contributions. Depending on their relative magnitudes, three different behaviors

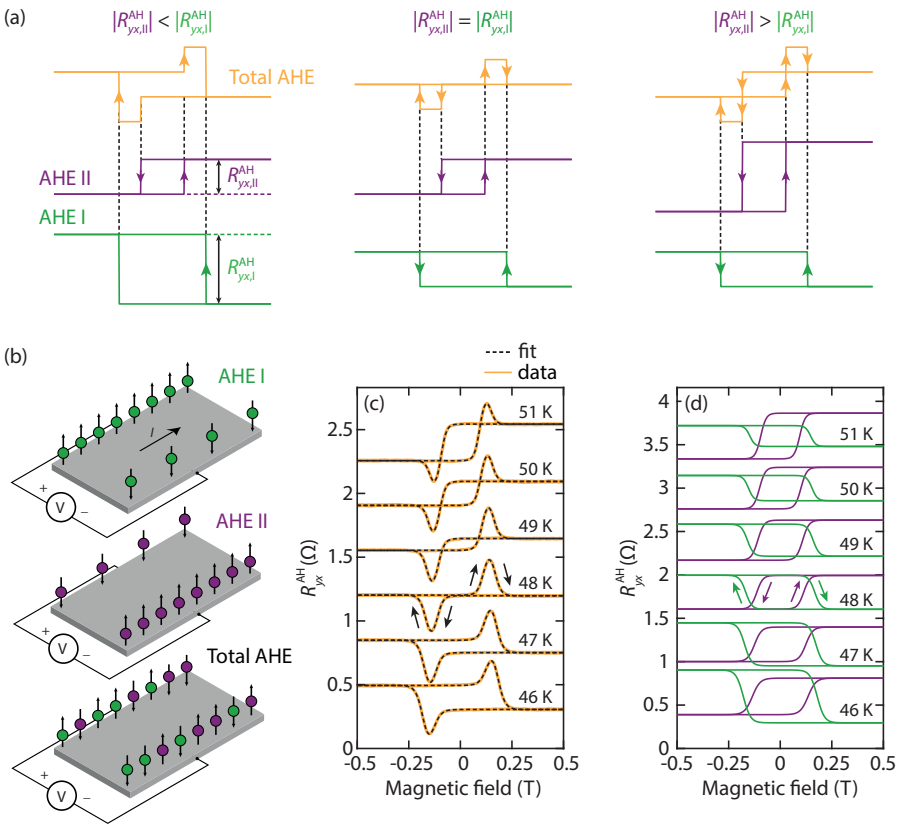

Figure 4.5: Two-channel AHE model. (a) Addition of two AHE contributions with opposite signs of R^{AH}_{yx} and different coercive fields. (b) Illustration showing the opposite spin accumulation of the two individual contributions. (c) Measured total AHE curves with the ordinary Hall component subtracted. The black dashed lines represent a fit to two individual loops. (d) The two anomalous Hall components that add up to the total R_{AH} curves in (c).

can be discerned for $B_{c,II} < B_{c,I}$. For opposite signs of the anomalous amplitude, majority spin is accumulated on opposite terminals, resulting in opposite Hall voltages (see Fig. 4.5b). When the anomalous amplitudes are equal in magnitude, the total AHE reduces to zero. In Fig. 4.5c, the ordinary Hall component has been subtracted and the remaining anomalous Hall component (R_{AH}) is presented. As the temperature is increased from 46 K towards 51 K, the behavior of the total AHE evolves from the leftmost scenario in Fig. 4.5a to the rightmost scenario, with the middle scenario emerging at $T_R = 48$ K. In section 4.6.2, we show that in the small Hall angle limit ($R_{yx} \ll R_{xx}$), the summation of two Hall channels R^{i}_{yx} and R^{ii}_{yx} is given by

$$R^{tot}_{yx} \simeq \left(\frac{R^{tot}_{xx}}{R^{i}_{xx}}\right)^2 R^{i}_{yx} + \left(\frac{R^{tot}_{xx}}{R^{ii}_{xx}}\right)^2 R^{ii}_{yx} \tag{4.3}$$

i.e., the two Hall resistances are scaled by the fraction of the total current they carry. Since in ultrathin SRO films the longitudinal resistance is about three orders of magnitude larger than the Hall resistance, this expression is valid and the total Hall resistance can indeed be investigated as a linear sum of two individual channels, as depicted in Fig. 4.5a. Combining equation (4.3) with the empirical relation [65] $R_{yx}^{\mathrm{AH}} = R_s M_z$, we introduce the following phenomenological model

$$\begin{aligned} R_{yx}^{\mathrm{AH,tot}} &= R_s^i M_z^i + R_s^{ii} M_z^{ii} \\ &= R_s^i \tanh\left[\omega^i\left(B - B_c^i\right)\right] + R_s^{ii} \tanh\left[\omega^{ii}\left(B - B_c^{ii}\right)\right], \end{aligned} \tag{4.4}$$

where R_s is the anomalous Hall coefficient, M_z the out-of-plane component of the magnetization, B_c the coercive field and ω a parameter describing the slope at $B = B_c$. The hyperbolic tangent is a sigmoid function that simulates the switching of the magnetization at the coercive field. For simplicity, we have assumed the current fractions to be approximately equal and absorb the scaling factor into R_s. An excellent agreement is obtained between this model (dashed black lines in Fig. 4.5c) and the data, enabling us to extract the individual AH components as a function of temperature (Fig. 4.5d). The corresponding R_{yx}^{AH} values are shown in Fig. 4.6a; both components show a smooth evolution in temperature, with one disappearing above 58 K (green) and the other below 35 K (purple). At 48 K the two components are equal, leading to the fully compensated case. The dashed lines illustrate a possible dependence of $R_{yx}^{\mathrm{AH}}(T)$ at higher and lower temperatures, which suggests that R_{yx}^{AH} and B_c of the two contributions follow a qualitatively similar temperature dependence, shifted by 23 K. This implies that, for $T < 35$ K and $T > 58$ K, R_{yx}^{AH} of the two contributions are of the same sign or one of the contributions is below the detection limit of our experiment, rendering the total AHE indistinguishable from that of a single spin-polarized channel.

There are various observations to be made concerning the relationship between the two opposite sign AH channels and the role of inhomogeneities in the magnetization. First, we point out that the magnetic anisotropy is affected by asymmetric boundary conditions. Fig. 4.6b compares the in- and out-of-plane magnetization for a STO/SRO/STO and STO/SRO/SIO heterostructure[4]. We observe that at SRO/SIO interfaces, the out-of-plane component of the magnetization is reduced and an in-plane component emerges. Considering the tetragonality profile discussed in Fig. 4.3a, a non-uniform magnetization along the growth axis may be expected. Second, we note that an in-plane distribution of coercive fields is also likely to play a role. Possibly, the combination of compressive and tensile strain exerted by the STO and SIO layers, respectively, promotes the formation of spatial domains with varying unit cell dimensions, which could result into magnetic domains with different switching fields and AHE amplitudes. The agreement of the data with the two-channel model then suggests a bimodal distribution of switching fields, which manifests most prominently in the vicinity of a sign change of the AHE.

[4] The largely out-of-plane component of the magnetization suggests that the magneto-crystalline and/or surface anisotropy dominate over the shape anisotropy, which tends to favour an in-plane orientation of the magnetization for thin films. However, this may not be the case in devices with different shapes or in the presence of magnetic domains.

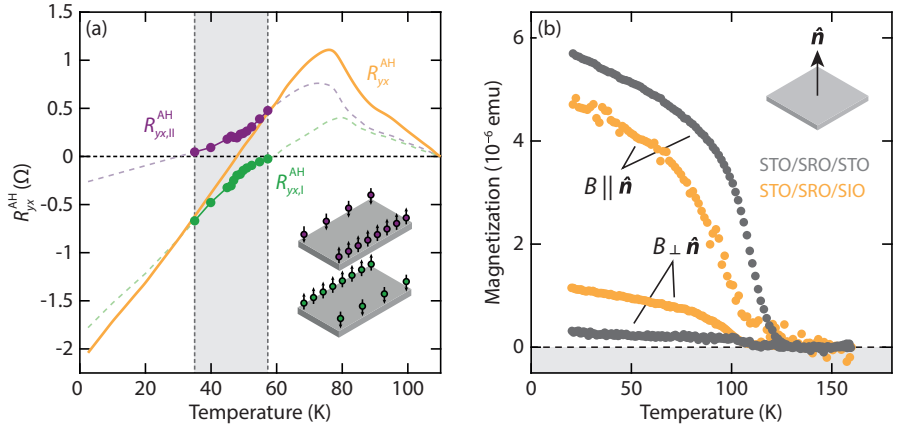

Figure 4.6: Temperature dependence of the double AHE. (a) Total R_{yx}^{AH} and the extracted R_{yx}^{AH} from the two anomalous Hall components as a function of temperature. The dashed lines illustrate a possible temperature dependence of R_{yx}^{AH}. (b) In- and out-of-plane magnetization for a (green) STO/SRO/STO and (purple) STO/SRO/SIO heterostructure, measured by SQUID.

For the employed phenomenological model, the choice of two AH loops with slightly different coercive fields is fully compatible with the field and temperature dependence of the AHE and of the magnetization, as extracted from measurements of the magneto-optical Faraday effect (Fig. 4.7a). In particular, comparing the hysteresis loops for the double or single AH model (Figs. 4.7b-d), we find that it is virtually impossible to discern the presence of two components with different switching fields from magnetization measurements, even when the two magnetizations have the same magnitude. This also supports the notion that it may be impossible to distinguish two AHE contributions when they are of the same sign. The two-channel AH model should also be of relevance to other systems displaying the topological Hall effect, provided that a sign inversion is enabled by a temperature-dependent Hall response. It has recently also been proposed in the context of magnetically doped topological insulators [172].

4.4. EXTRAORDINARY HALL BALANCE

To further exemplify the two-channel model, we synthesize a heterostructure consisting of two layers of ultrathin SRO, separated by an insulating STO spacer. We tailor the SRO layer thicknesses such that they exhibit different magnetic properties, while retaining similar resistance values. For this purpose, we chose the SRO layer thicknesses to be 4 u.c. and 5 u.c. for the bottom and top layers respectively, with a 4 u.c. STO spacer in between. A heterostructure consisting of distinct ferromagnetic layers is known as an extraordinary Hall balance (EHB), which acts as a memory device with four states [170]. The longitudinal resistance is shown as a function of temperature in Fig. 4.8a. The derivative $(\mathrm{d}R/\mathrm{d}T)$ is shown in the inset, where a sharp peak is observed at approximately 130 K. While a slight difference has been reported in the $\mathrm{d}R/\mathrm{d}T$ behaviour between bulk crystals and thin films [173–175], in both cases the peak is suggested to be caused by a logarithmic divergence of the specific heat due to short-range spin fluctuations across

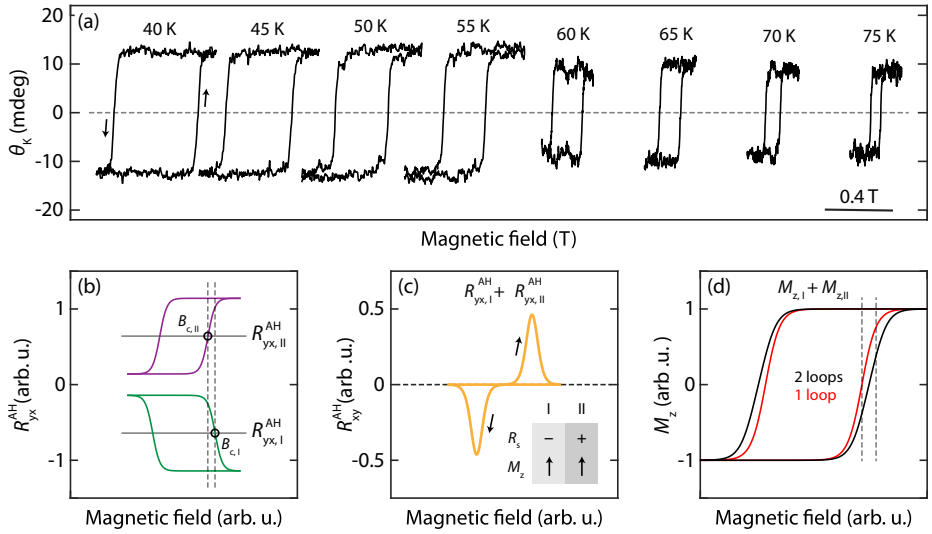

Figure 4.7: Superposition of AH and magnetization loops. (a) Measured Faraday rotation angle as a function of the applied field for various temperatures ranging from 40 K to 75 K. The curves are offset horizontally for visual clarity. (b) Simulation of two separate (opposite) AH components as a function of the applied field and (c) the resulting total R_{yx}^{AH} for the case of two different coercive fields (indicated by the open circles). (d) Simulated magnetization profile as a function of the applied field, comparing a single loop with a double loop scenario. The two magnetization loops are extracted from the curves in (b) and are equal in magnitude.

the magnetic phase transition [68, 176, 177]. As such, the peak at 130 K in the $\mathrm{d}R/\mathrm{d}T$ identifies the Curie temperature of one of the SRO layers. Careful inspection reveals a shoulder at ~ 115 K, identifying the magnetic phase transition of the second SRO layer. Considering that the T_{C} in SRO depends sensitively on the layer thickness in the vicinity of the thickness-driven metal–insulator transition [178, 179], we attribute the high and low T_{C} to the 5 u.c. and 4 u.c. layers, respectively. This confirms a different temperature evolution of the magnetizations of the two layers, resulting in two distinct spin-polarized conduction channels. In Fig. 4.8b, we show the magnetic field dependence of the Hall effect at 10 K. The data shows that two magnetic transitions take place at different B_c. We clearly recognize that the magnetization of one channel switches abruptly, while the other channel switches more gradually and at a slightly larger coercive field. We attribute the channel that switches abruptly to the bottom SRO layer, as it is likely more ordered due to the growth on the atomically flat surface of the STO substrate. This is consistent with the abrupt switching typically observed for a single SRO layer. We expect the second SRO layer to be more disordered as it is grown on top of the SRO/STO stack, which has accumulated some surface roughness. The concomitant variations in surface topography could give rise to additional pinning sites and magnetic domains with switching fields having a broader distribution than those of the bottom layer, resulting in a shallower slope at B_c.

The temperature dependence of the AHE is shown in Fig. 4.8c and is measured in a four-point Van der Pauw configuration. By cooling under application of + and −50 mT

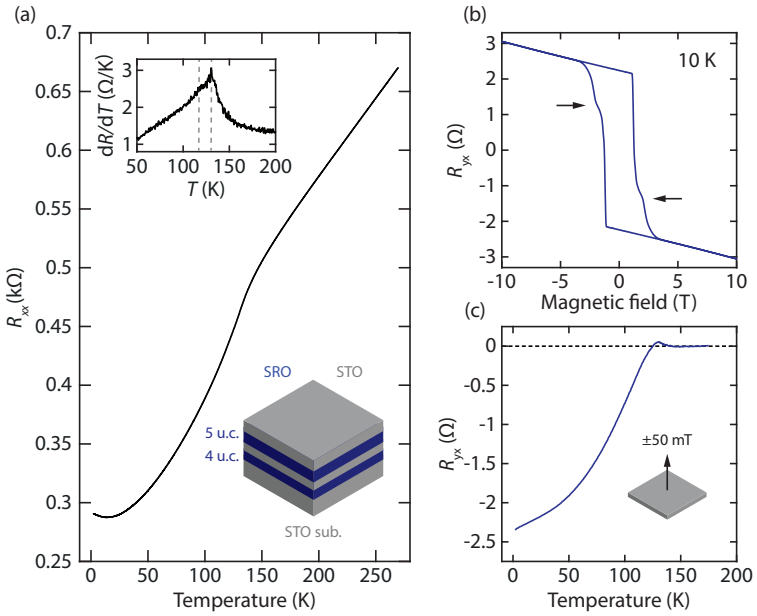

Figure 4.8: SRO bilayers (a) Longitudinal resistance (R) versus temperature (T). The inset shows the derivative ($\mathrm{d}R/\mathrm{d}T$), with the gray dashed lines denoting the Curie temperatures of the two layers. (b) Transverse resistance as a function of magnetic field at $T = 10\,\mathrm{K}$. The arrows indicate the coercive field of the 5 u.c. layer. (c) Anomalous Hall effect as a function of temperature.

magnetic fields, saturation of the magnetization is ensured. Subsequent subtraction of the two curves and dividing by 2 removes the voltage offset originating from misalignment of the contacts and gives the total Hall resistance. This can be expressed as the sum of an anomalous and ordinary Hall component $R_{yx} = R_{yx}^{\mathrm{AH}} + R_{yx}^{\mathrm{ord}}$. Due to the high carrier density of SRO ($\sim 10^{22}\mathrm{cm}^{-3}$), the ordinary Hall component for a 50 mT field is in the order of tens of mΩ and therefore much smaller than the anomalous component, which is in the order of several Ω. We can therefore neglect R_{yx}^{ord} such that $R_{yx} \simeq R_{yx}^{\mathrm{AH}}$. At $\sim 120\,\mathrm{K}$, we observe a sign change, which is characteristic of the intrinsic topological contribution to the AHE [180]. Above this temperature, the positive contribution dominates up until the Curie temperature, where the magnetization vanishes.

For an EHB device, it is required that the two layers have different coercive fields. While this property has been established in Fig. 4.8b, there are no field values at 10 K where the magnetic state is perfectly stable i.e., plateaus where $\mathrm{d}R_{yx}/\mathrm{d}B \simeq 0$. We therefore proceed to study temperature dependent magnetic field sweeps to identify a regime where multiple magnetic states can be stabilized. A particularly interesting region is in the vicinity of the sign change observed in Fig. 4.8c. Considering the different temperature evolutions of the two channels, it is likely that in this range, one channel exhibits a positive AHE while the other remains negative. Accordingly, we can expect a variety of different magnetic and electronic configurations. In Fig. 4.9a, we show magnetic field sweeps in the temperature range $90\,\mathrm{K} < T < 130\,\mathrm{K}$. Fig. 4.9b gives an enlarged view of sweeps

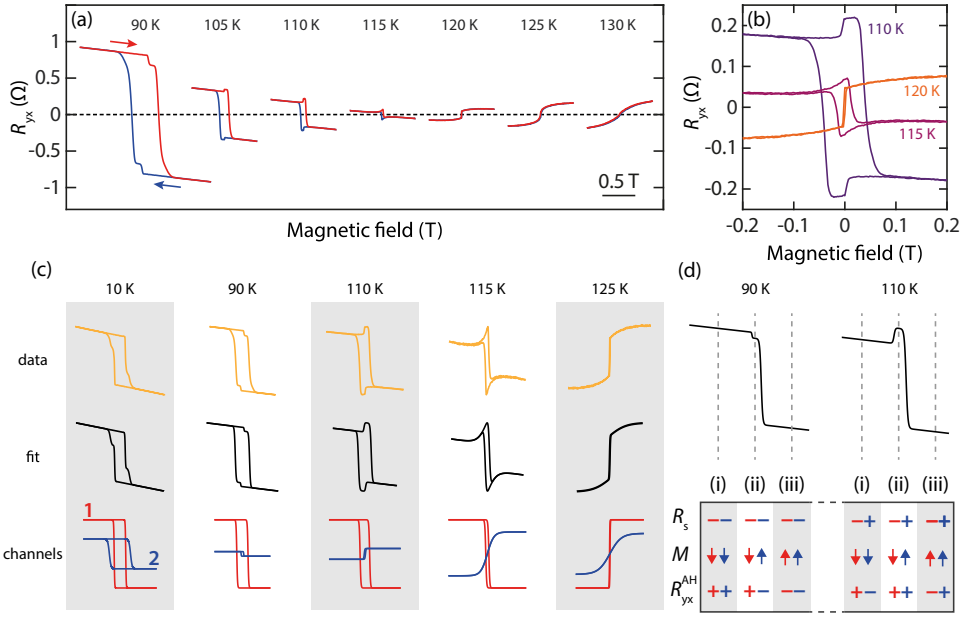

Figure 4.9: Temperature evolution. (a) AHE sweeps for various temperatures. The curves are offset horizontally for visual clarity. (b) Enlarged view of sweeps in the vicinity of the sign reversal temperature. (c) Disentanglement of the AHE data into two individual channels, labelled '1' (red) and '2' (blue). (d) The configurations of the anomalous coefficient R_s, magnetization M and anomalous amplitude R_{yx}^{AH} at 90 K and 110 K for the two channels along three points of the sweep. Arithmetic operators '+' and '-' denote the sign and the arrows denote the magnetization orientation.

recorded at 110 K, 115 K and 120 K. In agreement with Fig. 4.8c, we find that with increasing temperature, the overall sign of the AHE changes from negative to positive between 115 K and 120 K. In addition, we find that for several temperatures — particularly for 90 K and 110 K — three plateaus are present with a stable magnetic state. Remarkably, for 90 K, the first plateau has a higher R_{yx} value than the second plateau, whereas the situation is inverted at 110 K. To gain more insight in the behaviour of the two channels, it is necessary to separate the signal into its two individual components. Fitting equation (4.4) to the experimental data permits to simulate the AHE of the two individual channels, the results of which are shown in Fig. 4.9c. The top row shows the measured R_{yx}, while the middle and bottom rows show simulated AH curves. The blue and red curves (bottom row) are the individual AH channels used for the simulation. The ordinary Hall component is subtracted with a linear fit at high field. Note that both the width (B_c) and the height (R_{xy}^{AH}) of the hysteresis loops in this figure are rescaled for visual clarity. The simulated curves provide an excellent description of the experimentally observed behaviour. Both AH components show a sign change, as well as a decrease of B_c with increasing temperature, consistent with the behaviour of single SRO layers. Channel 1 (red) changes sign at ~ 100 K and channel 2 (blue) at ~ 120 K. Additionally, the coercive fields of the two channels are well separated, which is essential for an EHB device. In Fig. 4.9d, we illustrate the EHB functionality of the heterostructure for 90 K and 110 K,

where stable plateaus are observed. The three different magnetic states of the forward sweeps $B < B_{c,2} < B_{c,1}$, $B_{c,2} < B < B_{c,1}$ and $B_{c,2} < B_{c,1} < B$ are labelled (i), (ii) and (iii), respectively. The table summarizes the signs of the anomalous coefficients (R_s), the orientation of the magnetization (M) and the resulting AHE amplitude (R_{xy}^{AH}) for channels 1 and 2 (red and blue). The key difference between the two temperatures is the sign of channel 2, which is negative at 90 K, but positive at 110 K. This causes the different behaviour in state (ii) for the two temperatures, resulting in a step down of R_{xy}^{AH} at 90 K, but a step up at 110 K.

4.5. CONCLUSIONS

Finally, we discuss the two-channel scenario in the context of recent studies performed on SRO thin films and heterostructures, where similar anomalous Hall characteristics were observed and attributed to the skyrmion-driven topological Hall effect [37, 147, 181]. Within this picture, the topological Hall effect would be enhanced in the case of SIO/SRO/SIO due to Dzyaloshinskii-Moriya interaction at both interfaces (contrary to our observation). However, our data cannot exclude contributions from real-space Berry curvature effects due to non-collinear spin textures forming in a specific range of temperature and magnetic fields. Our analysis suggests robust topological effects due to the Berry curvature in reciprocal space and that this scenario explains the superposition of AH components in asymmetric structures. We remark that, due to the strong connection between the magnetization and AHE, there would likely be an interplay between non-collinear magnetism and the momentum-space Berry curvature. Hence, SRO-based heterostructures represent a unique platform to exploit and investigate the interplay of Berry curvature effects in both real and momentum space. The evolution of 3D Weyl points to pairs of topological bands in the 2D limit is a phenomenon that is not limited to ruthenates, but extends to magnetic t_{2g} systems in general. The same holds for the sensitivity of the total Berry curvature to interface effects and thus we expect that similar phenomenology would arise in other heterostructures based on ferromagnetic t_{2g} systems.

4.6. SUPPLEMENTARY INFORMATION

4.6.1. CONSERVATION OF SPIN-ORBITAL PARITY

A mirror image operation with respect to the (x, y) plane is given by a parity operation $(x, y, z) \rightarrow (-x, -y, -z)$ followed by a π rotation around the z-axis $(-x, -y, -z) \rightarrow (x, y, -z)$. Angular momentum is invariant under parity, thus only the rotation operation needs to be considered. In the basis spanned by the d-orbital cubic harmonics $|xy\rangle$, $|yz\rangle$ and $|zx\rangle$, the mirror operation is given by

$$\hat{Q}_z^l = \begin{pmatrix} 1 & 0 & 0 \\ 0 & -1 & 0 \\ 0 & 0 & -1 \end{pmatrix}. \tag{4.5}$$

The orbital angular momentum operators in this basis are expressed as

$$\hat{L}_x = \hbar \begin{pmatrix} 0 & 0 & i \\ 0 & 0 & 0 \\ -i & 0 & 0 \end{pmatrix}, \quad \hat{L}_y = \hbar \begin{pmatrix} 0 & -i & 0 \\ i & 0 & 0 \\ 0 & 0 & 0 \end{pmatrix} \quad \text{and} \quad \hat{L}_z = \hbar \begin{pmatrix} 0 & 0 & 0 \\ 0 & 0 & -i \\ 0 & i & 0 \end{pmatrix} \tag{4.6}$$

and the squared operators are given by

$$\hat{L}_x^2 = \hbar^2 \begin{pmatrix} 1 & 0 & 0 \\ 0 & 0 & 0 \\ 0 & 0 & 1 \end{pmatrix}, \quad \hat{L}_y^2 = \hbar^2 \begin{pmatrix} 1 & 0 & 0 \\ 0 & 1 & 0 \\ 0 & 0 & 0 \end{pmatrix} \quad \text{and} \quad \hat{L}_z^2 = \hbar^2 \begin{pmatrix} 0 & 0 & 0 \\ 0 & 1 & 0 \\ 0 & 0 & 1 \end{pmatrix}, \tag{4.7}$$

from which we find the relation $\hat{Q}_z^l = I - 2\hat{l}_z^2$ with $\hat{l}_z = \hat{L}_z/\hbar$. The spin state is invariant under parity, but transforms under a π rotation around the z-axis as $i\hat{\sigma}_z$, such that $\hat{Q}_z^s = i\hat{\sigma}_z$ with $\hat{\sigma}_z$ the Pauli spin matrix for the z-component. This motivates to define the spin-orbital parity operator

$$\hat{P} = \hat{\sigma}_z \otimes \left(I - 2\hat{l}_z^2\right), \tag{4.8}$$

with I the identity matrix. The full mirror symmetry operation is given by $\hat{Q}_z = \hat{M} \otimes \hat{Q}_z^s \otimes \hat{Q}_z^l = -i\hat{M} \otimes \hat{P}$, where $\hat{M}$ mirrors the positions of the lattice sites n along z[5]. In other words, the spin-orbital parity can be interpreted as the spin-orbital part of a mirror symmetry operation with respect to the (x, y) plane. For spin-orbitals in the spherical harmonic basis, the spin-orbital parity can be expressed as $2m_s(-1)^{m_l}$, with m_s and m_l the spin and magnetic quantum numbers, respectively. The $|xy\rangle$ orbital, being a linear combination of $m_l = \pm 2$ states, has even orbital parity. Similarly, the $|yz\rangle$ and $|zx\rangle$ orbitals are linear combinations of the $m_l = \pm 1$ states and therefore have odd orbital parity.

We first determine how the spin-orbit coupling behaves under parity. In terms of the spin ($\hat{S}_\pm = \hat{S}_x \pm i\hat{S}_y$) and orbital ladder operators ($\hat{L}_\pm = \hat{L}_x \pm i\hat{L}_y$), the spin-orbit coupling is expressed as

$$\begin{aligned} \hat{L} \cdot \hat{S} &= \hat{L}_x \hat{S}_x + \hat{L}_y \hat{S}_y + \hat{L}_z \hat{S}_z \\ &= \frac{1}{2}\left(\hat{L}_+ \hat{S}_- + \hat{L}_- \hat{S}_+\right) + \hat{L}_z \hat{S}_z, \end{aligned} \tag{4.9}$$

which commutes with $\hat{P}$ and therefore preserves the spin-orbital parity. Another way to see this is from the opposite signs of the spin and orbital ladder operators, which simultaneously flip the spin and orbital parity such that the spin-orbital parity is conserved, despite them not being conserved separately.

Next, we consider the nearest and next-nearest neighbour hopping. The Slater-Koster interatomic matrix elements are shown in Table 4.1. To find the nearest neighbour hopping term along e.g., the x-axis in a cubic lattice, we set $l = 1$ and $(m, n) = 0$. We first consider the direct (d–d) hopping between the nearest neighbours in a cubic geometry[6], for which we find

[5] This is an $n \times n$ matrix where n is equal to the number of layers.

[6] The direct hopping is small compared to oxygen-mediated hopping, but is included for the sake of completeness.

$$\hat{H}_{dd}^{100} = \begin{pmatrix} V_{dd\pi} & 0 & 0 \\ 0 & V_{dd\delta} & 0 \\ 0 & 0 & V_{dd\pi} \end{pmatrix}, \quad \hat{H}_{dd}^{010} = \begin{pmatrix} V_{dd\pi} & 0 & 0 \\ 0 & V_{dd\pi} & 0 \\ 0 & 0 & V_{dd\delta} \end{pmatrix}$$

$$\text{and} \quad \hat{H}_{dd}^{001} = \begin{pmatrix} V_{dd\delta} & 0 & 0 \\ 0 & V_{dd\pi} & 0 \\ 0 & 0 & V_{dd\pi} \end{pmatrix}. \tag{4.10}$$

Note that all matrices are diagonal, indicating that nearest neighbour hopping is only allowed between the same orbitals. In addition, the spin state is unaffected, meaning that both the spin and orbital parities are conserved. We further remark that the $V_{dd\delta}$ term is generally small and can be neglected [183]. Setting it to zero yields

$$\hat{H}_{dd}^{100} \simeq V_{dd\pi} \begin{pmatrix} 1 & 0 & 0 \\ 0 & 0 & 0 \\ 0 & 0 & 1 \end{pmatrix} = \frac{V_{dd\pi}}{\hbar^2} \hat{L}_x^2$$

and similarly

$$\hat{H}_{dd}^{010} \simeq \frac{V_{dd\pi}}{\hbar^2} \hat{L}_y^2, \quad \hat{H}_{dd}^{001} \simeq \frac{V_{dd\pi}}{\hbar^2} \hat{L}_z^2. \tag{4.11}$$

Table 4.1: Slater-Koster interatomic matrix elements [182]. Variables l, m, n denote the direction cosines and $V_{dd\sigma}$, $V_{dd\pi}$, $V_{dd\delta}$ the two-center integrals of two atomic sites of choice for σ, π and δ hybridizations of the $p-$ and d-orbitals.

element	expression
$t_{x,xy}$	$\sqrt{3}l^2 m V_{pd\sigma} + m(1-2l^2)V_{pd\pi}$
$t_{x,yz}$	$\sqrt{3}lmn V_{pd\sigma} - 2lmn V_{pd\pi}$
$t_{x,zx}$	$\sqrt{3}l^2 n V_{pd\sigma} + n(1-2l^2)V_{pd\pi}$
$t_{y,xy}$	$\sqrt{3}lm^2 V_{pd\sigma} + l(1-2m^2)V_{pd\pi}$
$t_{y,yz}$	$\sqrt{3}m^2 n V_{pd\sigma} + n(1-2m^2)V_{pd\pi}$
$t_{y,zx}$	$\sqrt{3}lmn V_{pd\sigma} - 2lmn V_{pd\pi}$
$t_{z,xy}$	$\sqrt{3}lmn V_{pd\sigma} - 2lmn V_{pd\pi}$
$t_{z,yz}$	$\sqrt{3}mn^2 V_{pd\sigma} + m(1-2n^2)V_{pd\pi}$
$t_{z,zx}$	$\sqrt{3}ln^2 V_{pd\sigma} + l(1-2n^2)V_{pd\pi}$
$t_{xy,xy}$	$3l^2m^2 V_{dd\sigma} + (l^2+m^2-4l^2m^2)V_{dd\pi} + (n^2+l^2m^2)V_{dd\delta}$
$t_{yz,yz}$	$3m^2n^2 V_{dd\sigma} + (m^2+n^2-4m^2n^2)V_{dd\pi} + (l^2+m^2n^2)V_{dd\delta}$
$t_{zx,zx}$	$3l^2n^2 V_{dd\sigma} + (l^2+n^2-4l^2n^2)V_{dd\pi} + (m^2+l^2n^2)V_{dd\delta}$
$t_{xy,yz}$	$3lm^2n V_{dd\sigma} + ln(1-4m^2)V_{dd\pi} + ln(m^2-1)V_{dd\delta}$
$t_{xy,zx}$	$3l^2mn V_{dd\sigma} + mn(1-4l^2)V_{dd\pi} + mn(l^2-1)V_{dd\delta}$
$t_{yz,zx}$	$3lmn^2 V_{dd\sigma} + lm(1-4n^2)V_{dd\pi} + lm(n^2-1)V_{dd\delta}$

For the hopping via the p-orbitals of the oxygen ligands, we consider an effective hopping term [184, 185]

$$t_{ij}^{\text{eff}} = \frac{1}{\Delta}\sum_k t_{ik}^{dp} \cdot t_{kj}^{pd}, \tag{4.12}$$

where $k = (x, y, z)$, $(i, j) = (xy, yz, zx)$ and Δ is the charge transfer energy between the metal ion and oxygen ligand. For $l = 1$ and $m, n = 0$, the only nonzero terms are $t_{y,xy}$ $(= -t_{xy,y})$ and $t_{z,zx}$ $(= -t_{zx,z})$. The Hamiltonian is then given by

$$\hat{H}_{dpd}^{100} = -\frac{V_{pd\pi}^2}{\Delta}\begin{pmatrix}1 & 0 & 0\\ 0 & 0 & 0\\ 0 & 0 & 1\end{pmatrix} = -\frac{V_{pd\pi}^2}{\hbar^2\Delta}\hat{L}_x^2. \tag{4.13}$$

Similarly, we find for the other nearest neighbours

$$\hat{H}_{dpd}^{010} = -\frac{V_{pd\pi}^2}{\hbar^2\Delta}\hat{L}_y^2 \quad \text{and} \quad \hat{H}_{dpd}^{001} = -\frac{V_{pd\pi}^2}{\hbar^2\Delta}\hat{L}_z^2. \tag{4.14}$$

The combined Hamiltonians are then given by

$$\begin{aligned}
\hat{H}^{100} &\simeq \frac{1}{\hbar^2}\left(V_{dd\pi} - \frac{V_{pd\pi}^2}{\Delta}\right)\hat{L}_x^2\\
\hat{H}^{010} &\simeq \frac{1}{\hbar^2}\left(V_{dd\pi} - \frac{V_{pd\pi}^2}{\Delta}\right)\hat{L}_y^2\\
\hat{H}^{001} &\simeq \frac{1}{\hbar^2}\left(V_{dd\pi} - \frac{V_{pd\pi}^2}{\Delta}\right)\hat{L}_z^2,
\end{aligned} \tag{4.15}$$

which shows that the nearest-neighbour hopping along lattice axis a is directly proportional to the corresponding component of the squared orbital angular momentum operator $\hat{L}_a$. Since the matrices are diagonal, the spin-orbital parity is conserved. For the next-nearest neighbour terms, we only need to consider the direct d–d hopping. Neglecting $V_{dd\delta}$, we find these terms to be

$$\begin{aligned}
\hat{H}^{110} &= \begin{pmatrix}3V_{dd\sigma} - 2V_{dd\pi} & 0 & 0\\ 0 & V_{dd\pi} & V_{dd\pi}\\ 0 & V_{dd\pi} & V_{dd\pi}\end{pmatrix},\\
\hat{H}^{101} &= \begin{pmatrix}V_{dd\pi} & V_{dd\pi} & 0\\ V_{dd\pi} & V_{dd\pi} & 0\\ 0 & 0 & 3V_{dd\sigma} - 2V_{dd\pi}\end{pmatrix},\\
\hat{H}^{011} &= \begin{pmatrix}V_{dd\pi} & 0 & V_{dd\pi}\\ 0 & 3V_{dd\sigma} - 2V_{dd\pi} & 0\\ V_{dd\pi} & 0 & V_{dd\pi}\end{pmatrix}.
\end{aligned} \tag{4.16}$$

Separating the Hamiltonian into diagonal $\hat{H}_d$ and off-diagonal parts $\hat{H}_{od}$, we find for the latter

$$\hat{H}_{od}^{110} = V_{dd\pi}\begin{pmatrix}0&0&0\\0&0&1\\0&1&0\end{pmatrix},$$
$$\hat{H}_{od}^{101} = V_{dd\pi}\begin{pmatrix}0&1&0\\1&0&0\\0&0&0\end{pmatrix},$$
$$\hat{H}_{od}^{011} = V_{dd\pi}\begin{pmatrix}0&0&1\\0&0&0\\1&0&0\end{pmatrix}. \tag{4.17}$$

Now we note that

$$\{\hat{L}_x, \hat{L}_y\} = \hat{L}_x\hat{L}_y + \hat{L}_y\hat{L}_x = -\hbar^2\begin{pmatrix}0&0&0\\0&0&1\\0&1&0\end{pmatrix}$$

and similarly

$$\{\hat{L}_y, \hat{L}_z\} = -\hbar^2\begin{pmatrix}0&0&1\\0&0&0\\1&0&0\end{pmatrix}, \quad \{\hat{L}_z, \hat{L}_x\} = -\hbar^2\begin{pmatrix}0&1&0\\1&0&0\\0&0&0\end{pmatrix}. \tag{4.18}$$

Comparing equations (4.18) and (4.17), we find

$$\hat{H}_{od}^{110} = -\frac{V_{dd\pi}}{\hbar^2}\{\hat{L}_x, \hat{L}_y\}, \quad \hat{H}_{od}^{101} = -\frac{V_{dd\pi}}{\hbar^2}\{\hat{L}_z, \hat{L}_x\}$$
$$\text{and} \quad \hat{H}_{od}^{011} = -\frac{V_{dd\pi}}{\hbar^2}\{\hat{L}_y, \hat{L}_z\}, \tag{4.19}$$

which shows that the inter-orbital hopping between next-nearest neighbours in the (a,b) plane is proportional to the anti-commutator between the corresponding orbital angular momentum operators as $\{\hat{L}_a, \hat{L}_b\}$. To examine how these terms affect the orbital parity, we express $\hat{L}_x$ and $\hat{L}_y$ in terms of the ladder operators, which gives

$$\{\hat{L}_x, \hat{L}_y\} = \frac{1}{2i}(\hat{L}_+^2 - \hat{L}_-^2). \tag{4.20}$$

Operating on a state with magnetic quantum number m_l, we can see that the result is always a superposition of only states with $m_l \pm 2$ (or zero). Since the orbital parity is given by $(-1)^{m_l}$, we see that it is conserved for inter-orbital hopping in the (xy)-plane. For the other hopping terms, we find

$$\{\hat{L}_y, \hat{L}_z\} = \frac{1}{2i}\left(\hat{L}_+\hat{L}_z + \hat{L}_z\hat{L}_+ - \hat{L}_-\hat{L}_z - \hat{L}_z\hat{L}_-\right)$$
$$\{\hat{L}_z, \hat{L}_x\} = \frac{1}{2}\left(\hat{L}_z\hat{L}_+ + \hat{L}_+\hat{L}_z + \hat{L}_z\hat{L}_- + \hat{L}_-\hat{L}_z\right), \tag{4.21}$$

which produces a superposition of states with $m_l \pm 1$ and therefore does not conserve the orbital parity. Finally, we note that an external magnetic field or intrinsic magnetization along the z-axis produces only terms proportional to $\hat{L}_z$ and $\hat{S}_z$ and therefore also preserves the spin-orbital parity[7].

We conclude that the spin-orbit coupling, nearest neighbour, next-nearest neighbour hopping in the (x, y) plane and external fields or magnetization along the z-axis all conserve the spin-orbital parity. Then the Hamiltonian becomes block diagonal with the 3×3 positive (negative) parity submatrix spanned by the t_{2g} ($L_{\text{eff}} = 1$) states $|-1\downarrow\rangle$ ($|-1\uparrow\rangle$), $|+1\downarrow\rangle$ ($|+1\uparrow\rangle$) and $|0\uparrow\rangle$ ($|0\downarrow\rangle$), with $|0\rangle \sim |xy\rangle$ and $|\pm 1\rangle \sim \frac{1}{\sqrt{2}}\left(|zx\rangle \pm i\,|yz\rangle\right)$ [186].

4.6.2. SUMMING TRANSVERSE VOLTAGES

Two transverse resistances can in general not be added linearly. It is valid however, to linearly add two transverse conductances as

$$\sigma_{xy}^{\text{tot}} = \sigma_{xy}^{i} + \sigma_{xy}^{ii}, \tag{4.22}$$

with i and ii denoting two individual contributions to the Hall conductivity. To express the conductance in terms of resistance, one has to invert the conductance matrix $\mathscr{S}$ given by

$$\mathscr{S} = \begin{pmatrix} \sigma_{xx} & \sigma_{xy} \\ -\sigma_{xy} & \sigma_{xx} \end{pmatrix}, \tag{4.23}$$

where we have assumed isotropic conductance ($\sigma_{xx} = \sigma_{yy}$) and implemented $\sigma_{yx} = -\sigma_{xy}$ i.e., the Onsager-Casimir relation [187]. Inverting this matrix gives

$$\mathscr{R} = \mathscr{S}^{-1} = \begin{pmatrix} \sigma_{xx} & \sigma_{xy} \\ -\sigma_{xy} & \sigma_{xx} \end{pmatrix}^{-1} = \frac{1}{\sigma_{xx}^2 + \sigma_{xy}^2}\begin{pmatrix} \sigma_{xx} & -\sigma_{xy} \\ \sigma_{xy} & \sigma_{xx} \end{pmatrix} = \begin{pmatrix} R_{xx} & R_{xy} \\ R_{yx} & R_{xx} \end{pmatrix}, \tag{4.24}$$

such that

$$R_{xx} = \frac{\sigma_{xx}}{\sigma_{xx}^2 + \sigma_{xy}^2} \quad \text{and} \quad R_{yx} = \frac{\sigma_{xy}}{\sigma_{xx}^2 + \sigma_{xy}^2}. \tag{4.25}$$

In the small Hall angle limit ($R_{yx} \ll R_{xx}$ or equivalently $\sigma_{xy} \ll \sigma_{xx}$), we have $\sigma_{xx}^2 + \sigma_{xy}^2 \approx \sigma_{xx}^2$ and the above expressions simplify to

$$R_{xx} = \frac{1}{\sigma_{xx}} \quad \text{and} \quad R_{yx} = \frac{\sigma_{xy}}{\sigma_{xx}^2} = R_{xx}^2\sigma_{xy}, \tag{4.26}$$

such that $\sigma_{xy} = R_{yx}/R_{xx}^2$. Then equation (4.22) becomes

[7] This is not the case for fields along the x or y axes.

$$\sigma_{xy}^{\text{tot}} = \frac{R_{yx}^{i}}{\left(R_{xx}^{i}\right)^2} + \frac{R_{yx}^{ii}}{\left(R_{xx}^{ii}\right)^2}. \tag{4.27}$$

The total longitudinal resistance of the two parallel channels is given by

$$R_{xx}^{\text{tot}} = \frac{R_{xx}^{i} R_{xx}^{ii}}{R_{xx}^{i} + R_{xx}^{ii}}. \tag{4.28}$$

Implementing $\sigma_{xy}^{\text{tot}} = R_{yx}^{\text{tot}} / \left(R_{xx}^{\text{tot}}\right)^2$ finally gives

$$R_{yx}^{\text{tot}} = \left(\frac{R_{xx}^{ii}}{R_{xx}^{i} + R_{xx}^{ii}}\right)^2 R_{yx}^{i} + \left(\frac{R_{xx}^{i}}{R_{xx}^{i} + R_{xx}^{ii}}\right)^2 R_{yx}^{ii} \tag{4.29}$$

$$= \left(\frac{R_{xx}^{\text{tot}}}{R_{xx}^{i}}\right)^2 R_{yx}^{i} + \left(\frac{R_{xx}^{\text{tot}}}{R_{xx}^{ii}}\right)^2 R_{yx}^{ii}, \tag{4.30}$$

which shows that the total transverse resistance is the sum of the individual contributions, weighted by the fraction of the total current they carry.

4.6.3. DFT COMPUTATIONAL METHODOLOGY

DFT calculations were performed using the VASP package [188] based on the plane wave basis set and projector augmented wave method, with an energy cut-off of 500 eV [135]. In the treatment of the exchange-correlation, the LSDA (local spin density approximation) with the Perdew-Zunger parametrization of the Ceperly-Alder data was employed for the exchange-correlation functional [189, 190]. The STO/SRO/SIO heterostructure was constructed using a lateral supercell of $\sqrt{2}a \times \sqrt{2}a$. The in-plane lattice parameter was fixed to the STO substrate, while for the out-of-plane lattice parameters the experimental values of the single unit cell of SRO and SIO were used. The hopping parameters were estimated from the electronic structure of the non-magnetic SRO/SIO and SRO/STO interfaces without Coulomb repulsion. After obtaining the Bloch wave functions from DFT, the maximally localized Wannier functions [191, 192] were constructed using the WANNIER90 code [193]. Starting from an initial projection of atomic d-basis functions belonging to the t_{2g} manifold and centered on metal sites, the t_{2g}-like Wannier functions were obtained. To extract the hopping parameters from the electronic bands at low energies, the Slater-Koster interpolation, as implemented in WANNIER90, was used. This approach is applied to determine the real-space Hamiltonian matrix elements in the t_{2g}-like Wannier function basis for the SRO/SIO and SRO/STO interfaces. Atomic relaxation was performed for all the considered systems. The internal degrees of freedom were optimized by minimizing the total energy to be less than 10^{-5} eV and the remaining forces to be less than 10 meV Å^{-1}. A $6 \times 6 \times 1$ k-point grid centered in Γ was used for the calculation of the heterostructure. Hubbard U effects on the Ru and Ir sites were included within the LSDA+U approach, using the rotational invariant scheme [137].

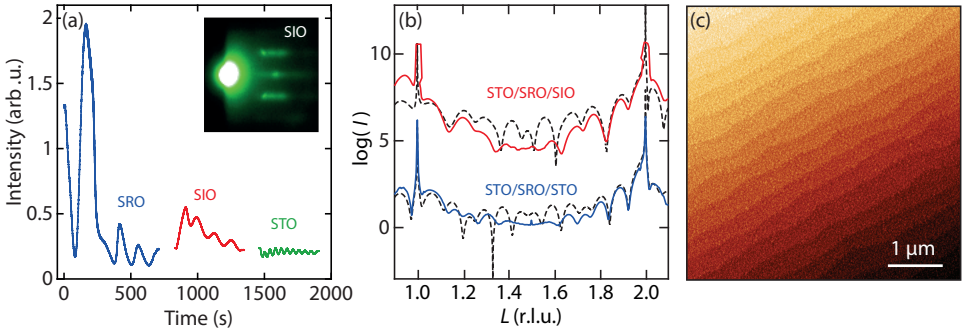

Figure 4.10: Surface and X-ray characterization. (a) RHEED intensity oscillations during the growth of SRO, SIO, and STO, with the inset showing the diffraction pattern after the SIO growth. (b) Synchrotron X-ray diffraction measurements of STO/SRO/STO and STO/SRO/SIO heterostructures. The black dashed lines are simulations of the diffracted intensity. (c) AFM topographic image of the surface of a STO/SRO/SIO/STO heterostructure, displaying a step-and-terrace morphology.

4

4.6.4. STRUCTURAL, TRANSPORT AND MAGNETIC CHARACTERIZATION

Fig. 4.10a shows the RHEED intensity during the growth of a SRO(4)/SIO(4)/STO(10) heterostructure on a TiO_2-terminated STO(001) substrate. The clear intensity oscillations indicate that all three layers grow in a layer-by-layer fashion. The anomalous initial oscillation during the SRO growth can be attributed to a change in surface termination from TiO_2 to SrO [88]. The number of unit cells quantified by X-ray diffraction and STEM was generally found to be one less compared to estimations based on first-order spot RHEED oscillations. Likely, the desorption of RuO_2 during the growth of the first unit cell leads to a strongly intermixed first layer with a small Ru content, which is difficult to detect by other structural characterization techniques [194]. Therefore, we adopt the convention of discarding the first oscillation in determining the number of unit cells grown, as estimated from RHEED oscillations. Fig. 4.10b and Fig. 4.10c show synchrotron X-ray diffraction measurements of a SRO(4)/SIO(2)/STO(10) heterostructure and an AFM topographic map of a SRO(4)/SIO(4)/STO(10) heterostructure, respectively. The clear Laue oscillations, as well as the step-and-terrace morphology are indicative of long-range crystal coherence and flat surfaces. The atomic structures were further investigated using high-angle annular dark-field scanning transmission electron microscopy (HAADF-STEM), in combination with electron energy loss spectroscopy (EELS) at the Ti-$L_{2,3}$, Ru-$M_{4,5}$, Sr-$L_{2,3}$ and Ir-$M_{4,5}$ edges. A dark-field measurement and EELS compositional map are shown in Fig. 4.11. The EELS compositional map is obtained from the normalized integrated intensities of the aforementioned edges. The color code in the color composite (middle panel) is Sr (red), Ti (yellow), Ir (blue) and Ru (green). A profile of the normalized integrated intensities along the growth direction is shown in the rightmost panel. Since the A-site Sr-ion is shared throughout the heterostructure, the interfaces are formed at the B-sites. Hence, the Sr intensity profile is omitted. The Ti/Ru and Ti/Ir interfaces are found to display intermixing within only a single layer, whereas at the Ru/Ir interface, the intermixing extends into the subsequent RuO_2 layer, corresponding to an Ir content of approximately $20 \pm 10\%$.

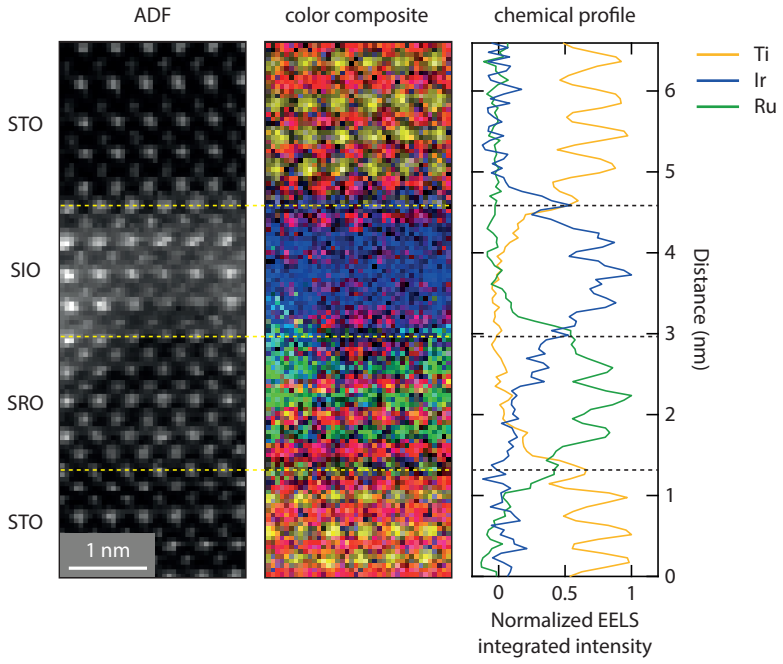

Figure 4.11: Compositional analysis. From left to right: ADF atomic Z-contrast image for a SRO/SIO heterostructure with simultaneously acquired EELS maps of the Ti-$L_{2,3}$, Ru-$M_{4,5}$, Sr-$L_{2,3}$ and Ir-$M_{4,5}$ edges. All atomic maps are overlapped to form a color composite (middle panel) with Sr (red), Ti (yellow), Ir (blue) and Ru (green). The right panel shows the normalized intensity profile of the B-sites.

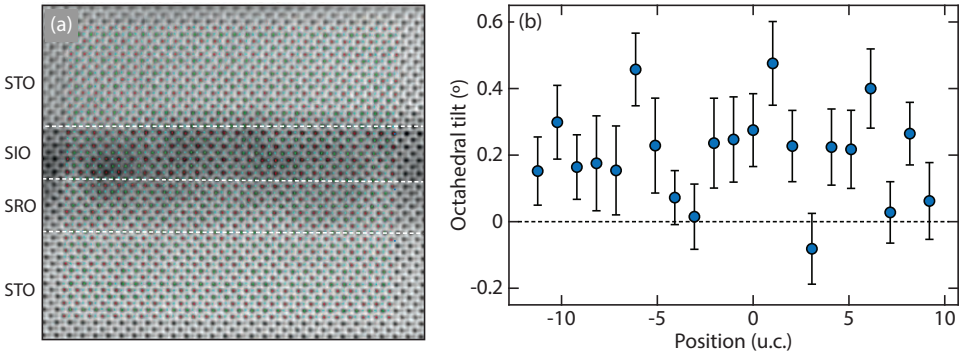

Figure 4.12: Octahedral tilts. (a) ABF image of the STO/SRO/SIO heterostructure. (b) Octahedral tilt angles determined from the oxygen positions.

In- and out-of-plane lattice parameters of the STO/SRO/SIO heterostructure were determined by extracting the atomic positions from the HAADF-STEM image (Fig. 4.3).

StatSTEM was used to model the image as a superposition of Gaussian peaks using statistical parameter estimation theory [195], which takes into account the overlap of neighbouring intensities. The tetragonality was then determined by dividing the out-of-plane (c) over the in-plane (a) lattice parameter of each unit cell. These measurements are averaged row-by-row and the corresponding statistical errors are determined. An annular bright-field (ABF) image of the heterostructure is shown in Fig. 4.12a, which permits visualization of the oxygen sites. Analysis of the oxygen positions shows that the octahedral tilts across the heterostructure are close to zero, indicating that the films are in a nearly tetragonal state (see Fig. 4.12b).

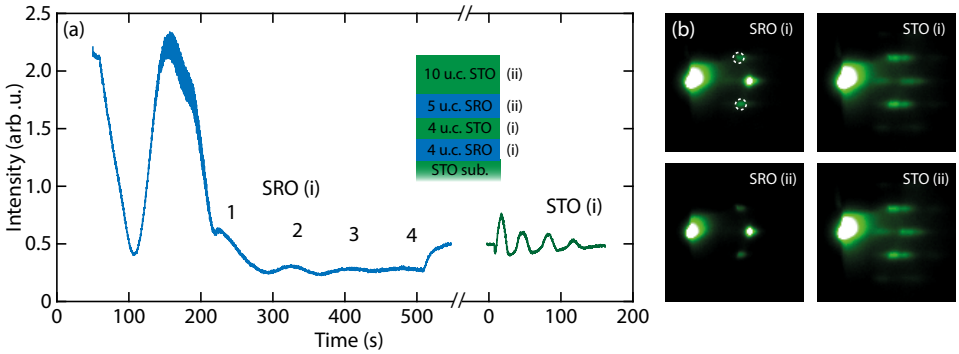

Figure 4.13: Synthesis of ultrathin SRO bilayers. (a) RHEED intensity of the first-order diffraction spot during PLD growth of the first SRO and STO layers. The inset shows an illustration of the grown heterostructure on the STO substrate, which consists of 4 u.c. SRO, 4 u.c. STO, 5 u.c. SRO and a 10 u.c. STO capping layer. (b) Post-growth RHEED patterns after each layer.

In Fig. 4.13a, we show the RHEED intensity of the EHB bilayer sample during the growth of the bottom SRO layer. As discussed prior, the initial oscillation is associated with a termination conversion from RuO_2 to SrO [88, 194], which results in an enhancement of the surface diffusion of the ablated species. Discarding the initial oscillation, we stop the deposition at the fourth intensity maximum, after which a strong intensity recovery is observed, indicative of a high mobility of the atomic species at the surface. We subsequently grow the 4 u.c. STO spacer, followed by the 5 u.c. SRO layer and finally a 10 u.c. STO capping layer that provides a symmetric boundary condition to the heterostructure, as well as protection from ambient conditions. The RHEED patterns after completion of each layer are shown in Fig. 4.13b. The well-defined spots of the SRO surfaces indicate that they are atomically smooth, whereas the slightly streaked spots of the STO surfaces are indicative of a shorter crystal coherence length compared to the SRO surfaces.

Fig. 4.14a shows the sheet resistance versus temperature curves of SRO(4)/STO(10) and SRO(4)/SIO(2)/STO(10) heterostructures. We find that the introduction of 2 u.c. of SIO reduces the sheet resistance, confirming that the SIO layers participate in transport and therefore mix with SRO states at the Fermi level. Interestingly, we find also a slight reduction of the T_C, identified from the abrupt slope change. This may be related to the interfacial coupling between Ru and Ir (e.g., charge transfer [196]) or to the intermixing observed in the top layers. Regardless, this observation indicates that interface effects have

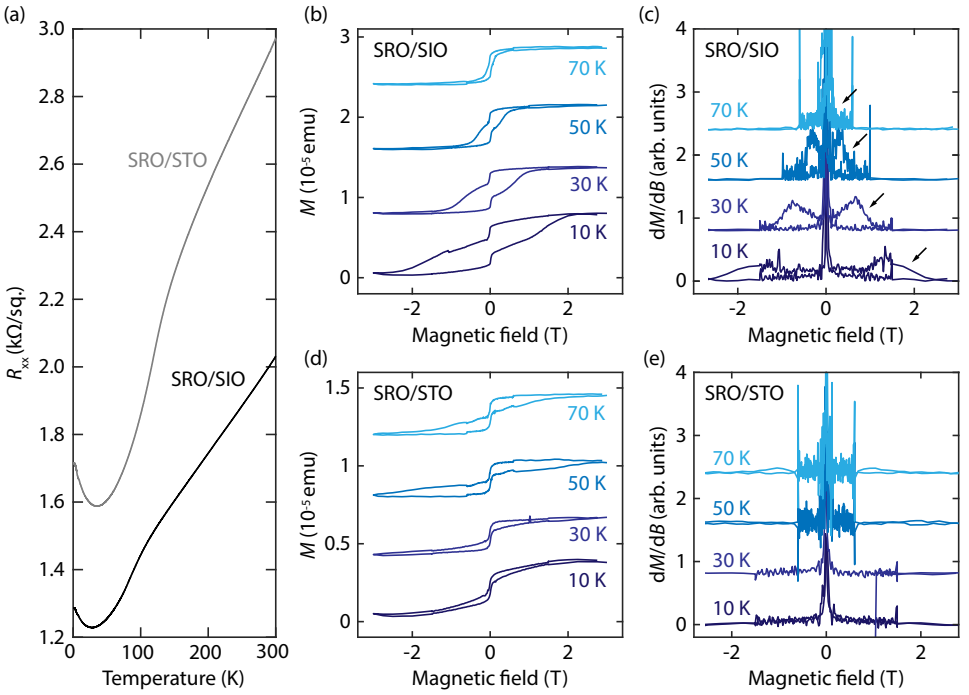

Figure 4.14: Longitudinal resistance and in-plane SQUID magnetometry. (a) Resistance as a function of temperature for SRO(4)/STO(10) and SRO(4)/SIO(2)/STO(10) heterostructures. (b) Magnetization of the SRO/SIO heterostructure as a function of in-plane magnetic field and (c) the corresponding derivative. The arrows indicate the coercive field. Panels (d) and (e) show the magnetization and corresponding derivative, respectively, for the SRO/STO heterostructure.

an impact on the magnetic properties of SRO. Figs. 4.14b-e show in-plane SQUID magnetometry as a function of field and the corresponding derivatives of SRO(4)/SIO(2) and SRO(4)/STO(10) heterostructures. The derivatives exhibit peaks at the magnetization reversal i.e., the coercive fields. For the SRO/SIO heterostructure, we observe peaks in the derivative, confirming the presence of an in-plane component of the magnetization. The additional step in the $M(B)$ and corresponding peaks in the $\mathrm{d}M/\mathrm{d}B$ data at approximately zero field may be attributed to magnetic contributions of the STO substrate [197]. For the STO/SRO/STO sample, we do not observe clear signatures of in-plane magnetic switching, likely due to a much smaller in-plane component of the magnetization compared to SRO/SIO. This points to a perpendicular orientation of the magnetic easy-axis with respect to the film plane for the SRO/STO samples, while the SRO/SIO samples are slightly more canted.

Further magnetic characterization of the heterostructures was performed using the magneto-optical Faraday effect, which is proportional to the out-of-plane component of the sample magnetization M_z via $\theta_F = V M_z t$, where t is the sample thickness and V the Verdet constant. Representative samples were grown on double-side polished STO substrates to allow for transmission measurements. The rotation of the polarization plane

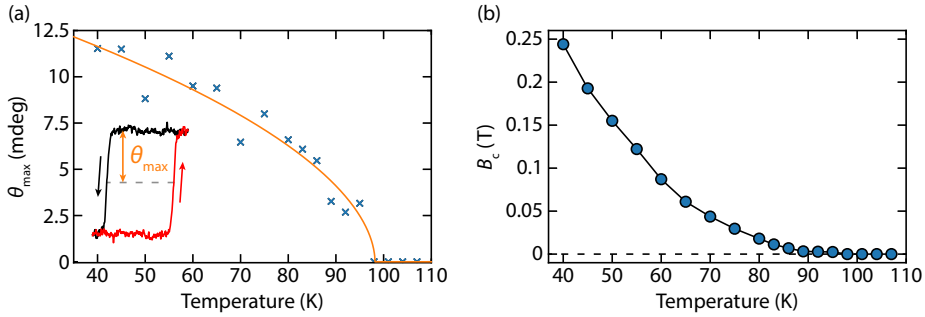

Figure 4.15: Magneto-optical Faraday effect. (a) Temperature dependence of the height of the magneto-optical hysteresis loop (θ_{max}). The solid line shows a Landau fit. (b) Coercive field B_c as a function of temperature.

of linearly polarized laser light ($\lambda = 633$ nm, $h\nu = 2.0$ eV), was measured at normal incidence as a function of applied (out-of-plane) magnetic field and temperature. The changes in the polarization of the transmitted light were measured using a Wollaston prism, which splits the beam into two perpendicularly polarized components. The difference in intensity of the two beam components resulting from the magneto-optical Faraday effect is proportional to the polarization rotation (θ_{F}) and was measured with a pair of balanced photodiodes. The small thicknesses of the samples and the transmission geometry of the experiment ensure that the entire SRO film is probed homogeneously. Fig. 4.15a shows the height of the hysteresis loop (θ_{max}) as function of temperature. Fitting the data with a power law of the form $\theta_{\mathrm{max}} = A(T_{\mathrm{C}} - T)^{\alpha}$ yields a Curie temperature of 98 K and a critical exponent α of 0.53, in excellent agreement with a second-order phase transition, expected for an itinerant ferromagnet. This indicates that, in the considered range, the Verdet constant is at most only weakly dependent on temperature, in contrast to the strong temperature dependence of $R_{\mathrm{xy}}^{\mathrm{AH}}$, which changes sign and varies significantly in magnitude. The Curie temperature agrees well with the value determined from magnetotransport measurements. As discussed in section 4.3, while two separate anomalous Hall components could be clearly identified between 35 K and 58 K due to their opposite signs, two magnetization components with different coercive fields cannot be identified in the magneto-optical response. A single coercive field value is extracted and shown as a function of temperature in Fig. 4.15b.

5

CHARGE AND TOPOLOGICAL RECONSTRUCTIONS AT THE LAO/SRO INTERFACE

"Further, science is a collaborative effort."

– John Bardeen

In oxide heterostructures, different materials are integrated into a single artificial crystal, resulting in a breaking of inversion-symmetry across the heterointerfaces. A notable example are polar interfaces, where valence discontinuities lead to otherwise inaccessible charge and spin states. This approach paved the way to the discovery of numerous unconventional properties absent in the bulk constituents. However, control of the geometric structure of the electronic wavefunctions in correlated oxides remains an open challenge. In this chapter, we create heterostructures consisting of ultrathin $SrRuO_3$, an itinerant ferromagnet hosting momentum-space sources of Berry curvature, and $LaAlO_3$, a wide-bandgap insulator. Transmission electron microscopy reveals a $LaO/RuO_2/SrO$ interface configuration, leading to excess charge being pinned near the $LaAlO_3/SrRuO_3$ interface. We demonstrate through magneto-optical characterization, theoretical calculations and transport measurements that the real-space charge reconstruction modifies the momentum-space Berry curvature in $SrRuO_3$, driving a reorganization of the topological charges in the band structure.

Parts of this chapter have been published in *Phys. Rev. Lett.* **127 (12)**, 12720-2 (2021) by T.C. van Thiel, W. Brzezicki, C. Autieri, J.R. Hortensius, D. Afanasiev, N. Gauquelin, D. Jaen, N. Janssen, D.J. Groenendijk, J. Fatermans, S. van Aert, J. Verbeeck, M. Cuoco and A.D. Caviglia.

STEM characterization was performed by N. Gauquelin, D. Jaen, J. Fatermans, S. van Aert and J. Verbeeck. Magneto-optical characterization was performed by J.R Hortensius and D. Afanasiev. Theoretical results were obtained by W. Brzezicki, C. Autieri and M. Cuoco.

IN recent years, an increasing amount of attention has been focused on topological phases in condensed matter [198]. Symmetry is a decisive element, as it can either be essential or detrimental for topological order [199, 200]. An iconic example is the quantum Hall effect, where the breaking of time-reversal symmetry is associated with a nonzero Chern number [201]. A second example is the Weyl semimetal, which breaks either time-reversal symmetry, inversion symmetry or both [202]. Transitions between different topological phases may be achieved through e.g., external electric or magnetic fields [203–205], a change in chemical composition [206–209], or application of pressure [210–212]. While typically associated with an energy gap, such transitions are not limited to insulators and semimetals. They may also occur in strongly metallic systems [213], which are usually characterized by a high density of interacting electrons [214]. A candidate material is the itinerant ferromagnet $SrRuO_3$ (SRO) [65], which over the past years has been the subject of intense research [37, 41, 147, 155, 160, 215–219]. However, manipulating the topological properties of SRO-based heterostructures remains an experimental open challenge. Unlike insulators and semimetals, the high carrier density renders electrostatic gating, although possible [147, 218, 220, 221], an inefficient method for manipulating the position of the Fermi level with respect to the momentum-space sources of Berry curvature. This calls for a different approach where the focus lies not on tuning the position of the Fermi level, but rather on changing the topological charges within the Brillouin zone i.e., inducing a topological transition. In this respect, oxide heterostructures provide an ideal platform due to the strong breaking of inversion-symmetry across the interfaces, especially between materials with different charge states [8, 42, 222, 223].

In this chapter, we demonstrate control of the momentum-space topological properties of ultrathin SRO, by creating a charge-frustrated interface. We synthesize RuO_2-terminated SRO ultrathin films interfaced with the wide-bandgap insulator $LaAlO_3$ (LAO). The charge frustration at the polar interface leads to charge doping of SRO well beyond the capabilities of a conventional electrostatic gate, therefore forming a pronounced profile of excess charge along the growth axis. We then demonstrate that in the ultrathin limit, this charge reconstruction modifies the momentum-space Berry curvature and leads to a reversal of its sign for all temperatures below the magnetic transition, thereby controlling a topological transition in momentum-space.

5.1. INTERFACE CHARGE-FRUSTRATION.

In Fig. 5.1, we present scanning transmission electron microscopy (STEM) data of a non-polar STO/SRO/STO and polar STO/SRO/LAO heterostructure. Due to both STO and SRO having the same Sr A-site cation, the interface between these two ABO_3 perovskites consists of BO_2 layers (B = Ti, Ru) separated by a shared SrO plane. Consequently, both STO and SRO preserve the B^{4+} valence state and the planar charges are zero on both sides of the interface. In contrast, we find that SRO and LAO are not separated by SrO, but by a shared LaO plane, indicating that the SRO film is RuO_2-terminated. This is a surprising observation since, due to the highly volatile nature of Ru_xO_y species, the SrO-termination has been argued to be more stable in oxidizing conditions [68, 88]. Recently, water-leaching has been demonstrated as a viable method for the synthesis of RuO_2-

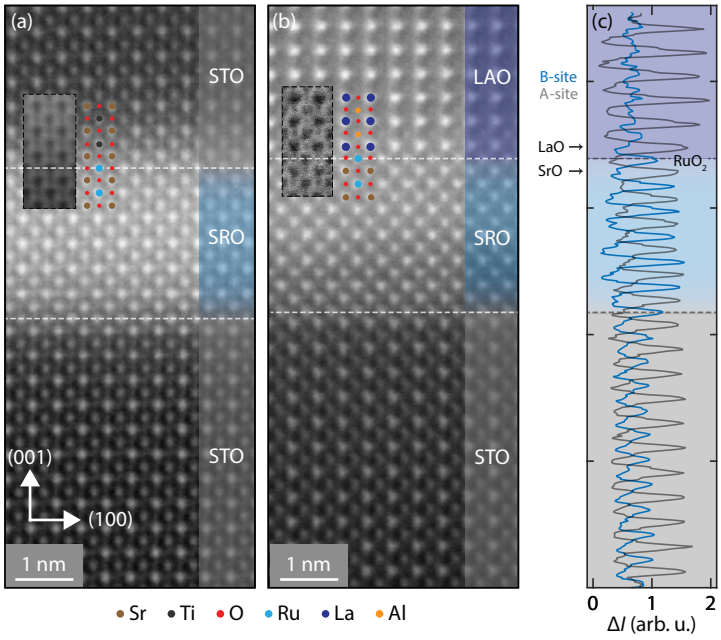

Figure 5.1: Atomic characterization. High-angle annular dark-field images of (a) STO/SRO/STO and (b) STO/SRO/LAO heterostructures with the insets showing bright-field images of the interface regions. (c) Intensity profile along the growth-axis for the atomic A (gray) and B-sites (blue) of (b).

terminated SRO films [224]. However, the SRO surface has been reported to decompose upon heating after exposure to ambient conditions, complicating the synthesis of SRO-based heterostructures with ex-situ chemical treatments [225]. From this perspective, the in-situ stabilization observed here poses a substantial advantage over ex-situ approaches and is a promising mechanism that invites further exploration. Irrespective of its origin, the observed $LaO/RuO_2/SrO$ interface has important consequences for the Ru charge state. On the SRO side Sr^{2+} requires Ru^{4+} for charge neutrality, while on the LAO side La^{3+} requires Ru^{3+}, therefore rendering the interface effectively equivalent to the hybrid compound $Sr_{0.5}La_{0.5}RuO_3$. In a fully ionic picture, charge neutrality is then accomplished by a $Ru^{3.5+}$ charge state i.e., a $-0.5e$ excess charge at the interfacial layer (see Fig. 5.2a). In conjunction with the charge doping, the polarity in the LAO layers creates an attractive electric potential drawing charges towards the interface. Due to the abundance of free carriers in $SrRuO_3$ ($n_e \sim 10^{22}\text{cm}^{-3}$), the corresponding electric field is screened over a length r, which can be estimated by the average distance between free carriers [226]. For our films, this estimate yields $r \sim (n_e)^{-\frac{1}{3}} = 5\text{Å}$ or 1-2 crystal unit cells. Fig. 5.2b shows the out-of-plane unit cell deformation along the growth axis. We find that for both heterostructures, the SRO film, as well as the STO and LAO overlayers, are coherently matched to the in-plane unit cell parameter of the substrate. The mismatch between the unit cell sizes is accommodated through a c-axis elongation in SRO and contraction in LAO, indicating that the lattice structure is governed by the substrate

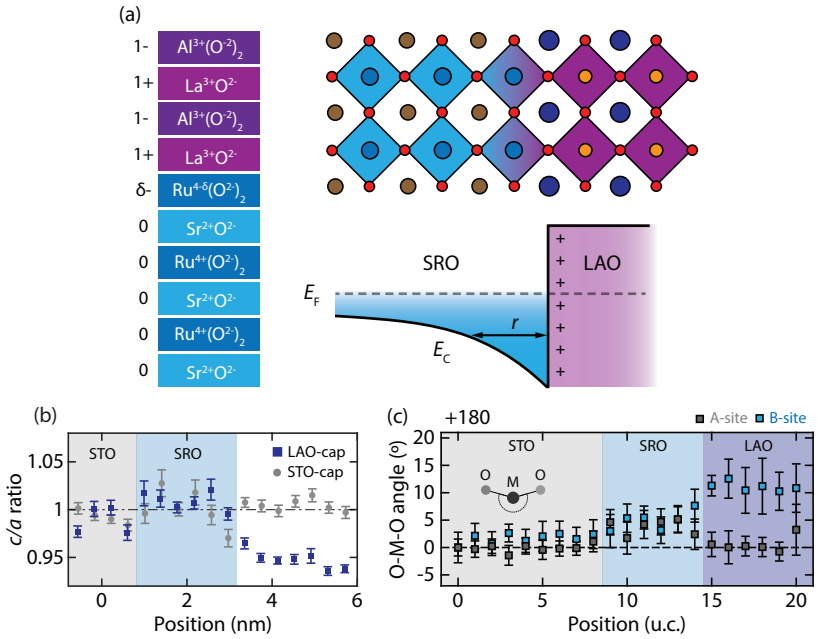

Figure 5.2: Charge and structural profile. (a) Illustration of the charge frustration and the resulting profile of the chemical potential E_C close to the Fermi energy E_F at the LaO/RuO_2 interface. (b) The c/a ratio along the growth axis. (c) O-M-O bond angles for the A and B-sites of the STO/SRO/LAO heterostructure, defined with respect to the STO substrate.

and not by the capping layer. This is further substantiated by a strong suppression of the octahedral tilts, yielding a tetragonal lattice symmetry (see section 5.6.1). The absence of antiferrodistortive tilts indicates that the polar field in LAO must be compensated in another manner. In the well-known LAO/STO system, this is accomplished by a polar mode in the LAO layer, where the O-Al-O bonds buckle in response to the internal electric field [227, 228], a distortion which propagates into the top few unit cells of the STO substrate. Here, we observe a similar phenomenology i.e., a polar mode in the LAO layer that propagates into the top unit cell of the SRO layer (Fig. 5.2c).

5.2. MAGNETIC RECONSTRUCTION

We next investigate a second consequence anticipated for the excess charge accumulation i.e., a change in the spin state of the Ru ions. In contrast to some of its magnetic $3d$ counterparts, the crystal-field splitting in SRO (~ 3 eV) is larger than both the Hund's interaction (~ 0.3 eV) and the Coulomb repulsion (~ 2 eV), owing to the spatially larger $4d$ orbitals [229–231]. As a result, the four d electrons in SRO reside in the t_{2g} orbitals, producing a ($4d^4$) $S = 1$ spin state. Any additional charge transferred from the LAO layer also occupies the t_{2g} manifold, reducing the average spin state to $3/4 < S_{avg} < 1$ due to the spin flip. Such a reduction of the spin moment directly manifests in the value of the saturation magnetization M_s and the Curie temperature T_C, which both scale with

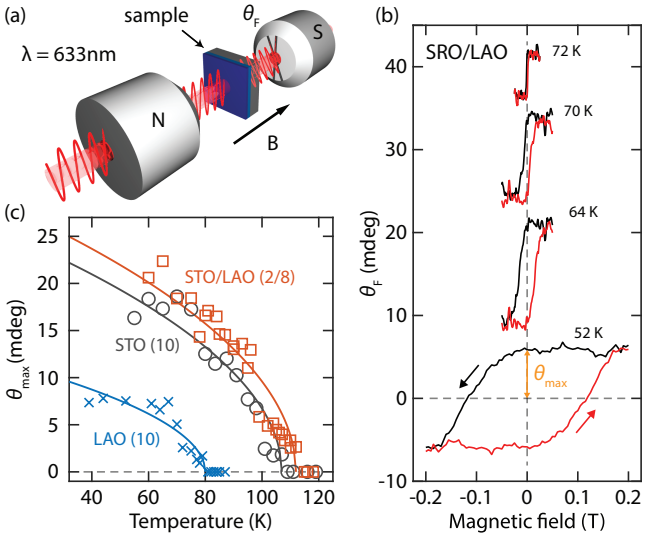

Figure 5.3: Magneto-optical Faraday effect. (a) Illustration of the experimental geometry for probing the magneto-optical Faraday rotation. (b) Faraday rotation as a function of applied magnetic field for a SRO(5)/LAO(10) heterostructure for various temperatures. (c) The amplitude of the hysteresis loop θ_{max} as a function of applied field for SRO(5)/STO(10) (gray), SRO(5)/STO(2)/LAO(8) (orange) and SRO(5)/LAO(10) (blue) heterostructures. The solid lines represent Landau fits.

$S(S+1)$. In magnetic systems, both T_C and M_s can thus serve as indicators of a charge reconstruction and are expected to be lowered when electronic charge is transferred to SRO. Indeed, La^{3+} doping has been demonstrated to efficiently suppress ferromagnetism in $La_xSr_{1-x}RuO_3$ compounds, which was attributed to the low-spin Ru^{3+} oxidation state [232–234]. We therefore proceed to investigate the spontaneous magnetization as a function of temperature, by means of the magneto-optical Faraday effect (Figs. 5.3a-b), which is directly proportional to the out-of-plane component of the magnetization M_z. In Fig. 5.3c, we show the Faraday rotation θ_F as a function of temperature for SRO films with various capping layers. To compare the different M_s and T_C, we fit the data to $\theta = \theta_{T=0}|T - T_C|^{0.5}$, treating θ as the magnetization M. According to expectation, we find a clear suppression of both T_C and θ_F for the SRO(5)/LAO(10) sample, as compared to SRO(5)/STO(10). To verify that this is an interface-driven effect, we also investigated SRO(5)/STO(2)/LAO(8), which is structurally similar to SRO(5)/LAO(10), but has two layers of STO that shield SRO from the valence discontinuity. As expected, both M_s and T_C are significantly larger compared to the LAO-capped sample and nearly identical to the STO-capped sample, further supporting that the charge and magnetic reconstruction are driven by the charge frustration at the LaO/RuO_2 interface.

5.3. CHARGE-DRIVEN SYMMETRY BREAKING

We now turn to the question of how the interface-driven charge and magnetic reconstruction affects the momentum-space Berry curvature and the anomalous Hall effect

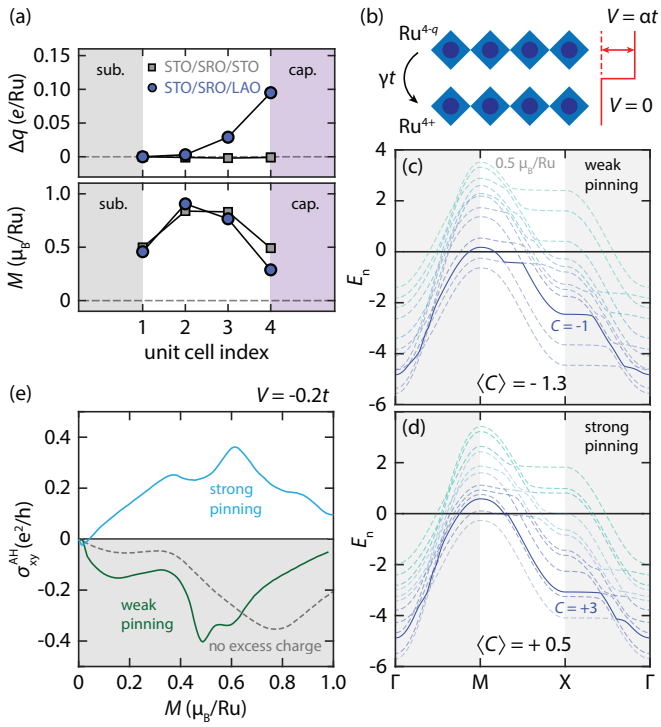

Figure 5.4: Excess charge profile and topological reconstruction. (a) Layer-resolved charge and magnetization profile for STO/SRO(4)/STO (gray) and STO/SRO/LAO (blue) calculated by DFT. (b) Effective tight-binding model of two coupled SRO monolayers, with excess charge $q = -0.5e$ in the top layer, as well as an on-site electrostatic potential V and interlayer coupling γt. (c-d) Dispersion relations of the 12 Ru t_{2g} bands at $M = 0.5\,\mu_B$/Ru for the effective model with (c) a weak pinning ($\gamma = 1$) and (d) a strong pinning ($\gamma = 0.5$) scenario, including an orbital Rashba SOC $\lambda_R = 0.04t$ correction and an on-site potential $V = -0.2t$ in the top layer.(e) Calculated anomalous Hall conductivity σ^{AH}_{xy}, in which the grey dashed line represents the reference case with two Ru^{4+} layers ($q = 0$) and the coloured solid lines represent the scenarios with excess charge $q = -0.5$e with either weak (green) or strong pinning (blue).

(AHE). Aside from the altered magnetization, the charge frustration introduces two elements; (i) a shift in the chemical potential due to the charge doping and (ii) breaking of inversion-symmetry due to the electric field along the growth axis. To determine their impact, we first address the question of how far the field penetrates into the SRO film. The top panel in Fig. 5.4a shows the DFT-calculated charge profile across the SRO layers, using the Ru site closest to the STO substrate as a baseline value. As expected, charge doping is absent for the STO-capped heterostructure, yielding a symmetric charge profile. For the LAO-capped sample however, we find, in accordance with the previous estimate for the screening length r, a doping of approximately $-0.1e$ and $-0.04e$ for the two unit cells closest to the SRO/LAO interface, leading to a strongly asymmetric charge profile. Note that the charges do not add up to -0.5e due to the covalent bonding between ions considered in DFT i.e., a considerable portion of the additional charge resides in the interstitial space and oxygen ligands. The impact on the magnetization is immediately

clear from the bottom panel of Fig. 5.4a, which, in agreement with the magneto-optical characterization, shows that the two unit cells near the interface have a lower magnetization compared to the STO/SRO/STO reference case, which has also been proposed by a recent theoretical study [235]. These results provide a clear picture; the SRO film experiences an electronic and magnetic reconstruction that persists 2 u.c. from the interface and causes a strong inversion-symmetry breaking.

To determine the effect of the reconstruction on the momentum-space Berry curvature, we introduce an effective tight-binding model of a SRO bilayer with interlayer coupling γt, where t is the nearest-neighbour hopping energy (see Fig. 5.4b)[1]. The charge-frustration and symmetry breaking is simulated by including an additional charge $-0.5e$ in the top layer, an attractive electrostatic potential $V = -0.2t$ and a small orbital Rashba correction $\lambda_R = 0.04t$ (see section 5.6.4). The parameter γ represents the tendency of the excess charge being pinned to the top layer i.e., the screening length r defined in Fig. 5.2a. From a band structure perspective, this translates to a steeper bending of the chemical potential E_C near the interface. We consider two scenarios; weak and strong charge pinning, or high and low γ, respectively. Figs. 5.4c-d show the dispersion relations of the twelve Ru t_{2g} bands for the two scenarios, at a representative value of the magnetization. The kinks that can be observed at the band anticrossings represent momentum-space (anti-)vortices of the Berry connection, acting as either positive or negative charges of Berry curvature. We highlight one band as an example, whose Chern number transitions from $C = -1$ to $C = +3$ between the weak and strong pinning scenarios. In the dispersion, this manifests as a change in the position and character of the band (anti-)crossings. Overall, we find a substantial evolution of the topological charges between the two scenarios.

One can approximate the total Berry curvature by the averaged Chern number $\langle C \rangle$, which is calculated by summing the Chern numbers of the individual bands, weighted by their occupation. We find a transition of $\langle C \rangle = -1.3$ to $\langle C \rangle = +0.5$, between the weak and strong pinning scenarios, respectively. Concurrently, the filling factors between the two scenarios remain virtually unchanged. In fact, it can be shown that for any linearly decreasing profile of the filling factors with energy, the sign of the total Berry curvature is purely determined by the sum of the Chern numbers associated with the indirect gaps of the twelve t_{2g} bands (see section 5.6.5). This indicates that the sign change is driven by a topological transition in momentum-space and is not simply due to a change in band occupation. To further demonstrate the robustness of this result, we directly calculate the anomalous Hall conductivity for a wide range of values for the magnetization (Fig. 5.4e). In agreement with the topological charge reconstruction, we find a transition from a fully negative to a fully positive AHE for nearly all magnetization values. These results identify the charge pinning, and the resulting inversion-symmetry breaking, as the dominant effect in altering the topological charges and reconstructing the Berry curvature.

[1] The next-nearest-neighbour hopping energy was set to $0.16t$

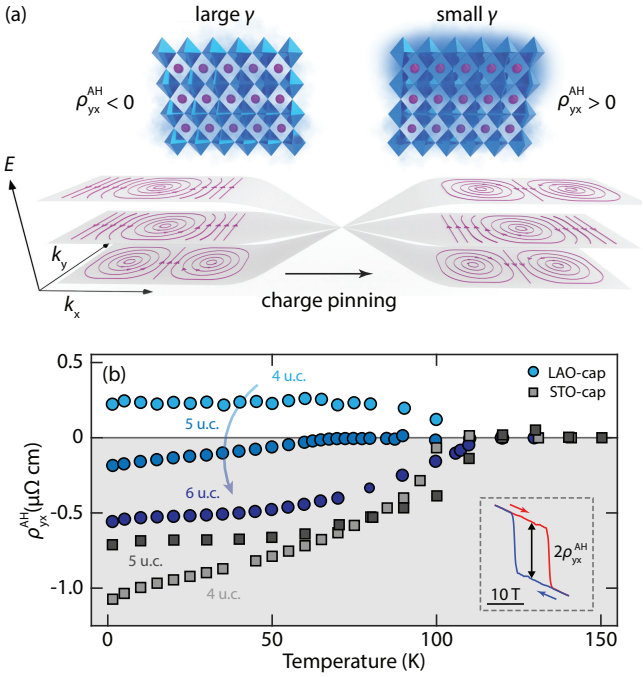

Figure 5.5: Anomalous Hall effect. (a) Illustration representing the evolution of the momentum-space topological charges. Upon increasing the charge pinning, the system moves through a Weyl point in the synthetic space spanned by k_x, k_y and the charge pinning parameter γ. (b) Measured anomalous Hall resistivity ρ_{yx}^{AH} for SRO films of varying thickness capped by both STO and LAO as a function of temperature. The inset in (b) shows an example of the magnetic-field dependence of the AHE, from which the amplitude ρ_{yx}^{AH} is extracted.

5.4. MOMENTUM-SPACE TOPOLOGICAL RECONSTRUCTION

To illustrate the topological reconstruction, we consider a three-dimensional parameter space, spanned by the Bloch momentum coordinates k_x and k_y and the charge pinning parameter γ as the third dimension. The reconstruction can then be understood as the system moving through a Weyl point, where the bands experience a closing and reopening of an energy gap upon increasing the charge pinning parameter γ. The evolution changes both the number and sign of the topological charges in the two-dimensional Brillouin zone. We have visualized this concept in Fig. 5.5a, where the sources of Berry curvature are represented by chiral vortex-like objects of the Berry connection, which change both in winding direction and in number across the transition. In a transport experiment, this translates to an inversion of the sign of the emergent field and consequently the AHE. Fig. 5.5b shows the AHE amplitude as a function of temperature for films of various thicknesses m capped by STO and LAO. For the thinnest films ($m = 4$), we find a positive AHE for the LAO-capped sample for all temperatures below the T_{C}. In contrast, it is negative for the 4 u.c. STO-capped sample. These two heterostructures represent the left and right scenarios in Fig. 5.5a and the sign inversion of the AHE

can be understood as the system experiencing a magnetic and topological reconstruction, driven by the onset of charge pinning at the polar interface. As the thickness is increased for the LAO-capped samples, we find a transition to a more negative behaviour of the AHE in temperature, which can be understood as the contribution of the charge-reconstructed layers becoming increasingly diluted as the total film thickness increases, effectively diminishing the impact of the interface on the anomalous Hall response. Accordingly, one expects both heterostructures to converge to the same state as the number of layers is increased. Indeed, for increasing layer thickness, both heterostructures tend towards the same behavior of the AHE.

5.5. CONCLUSIONS

While electric field penetration in bulk metals can be safely ignored, its importance in the ultrathin limit cannot be neglected. The key element is the extremely short penetration depth of the electrostatic potential in metals, which can cause a strong inversion-symmetry breaking in the near-interface region. The resulting electronic and magnetic reconstructions can have a decisive effect on the momentum-space topological properties of correlated systems, including, but not limited to $SrRuO_3$. The charge frustration arising from the interface with $LaAlO_3$ provides a unique opportunity for studying the effect of symmetry breaking on its momentum-space topology. Due to the insulating nature of $LaAlO_3$, there is neither mixing of states at the Fermi energy nor interface-driven spin canting, as has been reported in e.g., the $SrRuO_3$/$SrIrO_3$ interface, which has been the topic of multiple studies in recent years [37, 147, 181, 217, 236]. In this sense, the system considered here offers a more direct approach towards controlling the momentum-space topology in ultrathin $SrRuO_3$ and potentially other correlated metals. Our results are also of relevance to the scenario of uncapped $SrRuO_3$ films, as exposed surfaces with dangling bonds can manifest as an electrostatic boundary condition, albeit complicated by the unavoidable interaction with adsorbed ambient chemical species.

In summary, we have demonstrated how a valence charge discontinuity induces both a magnetic and topological reconstruction in ultrathin films of the itinerant ferromagnet $SrRuO_3$. We identify the pinning of the excess charge donated by the polar $LaAlO_3$ overlayer and the resulting inversion-symmetry breaking to be the dominant effect in altering the magnetization and momentum-space Berry curvature, leading to a full inversion of the sign of the emergent magnetic field. These results demonstrate how engineering charge discontinuities can be utilized to control the topological properties in oxide heterostructures and establish the potential of interface design towards the manipulation of the geometric structure of wavefunctions in correlated matter.

5.6. SUPPLEMENTARY INFORMATION

5.6.1. STRUCTURAL CHARACTERIZATION

All samples were grown on (001) TiO_2-terminated $SrTiO_3$ (STO) substrates by pulsed-laser deposition (PLD), using a 248 nm KrF excimer laser at a 1 Hz repetition rate. The laser fluences were 1.2 Jcm^{-2} for SRO and 1.0 Jcm^{-2} for the LAO and STO capping layers. STO substrates were mechanically clamped onto a heater stage, which was heated by an infrared diode laser. SRO layers were deposited at ~ 600 °C in an oxygen partial pres-

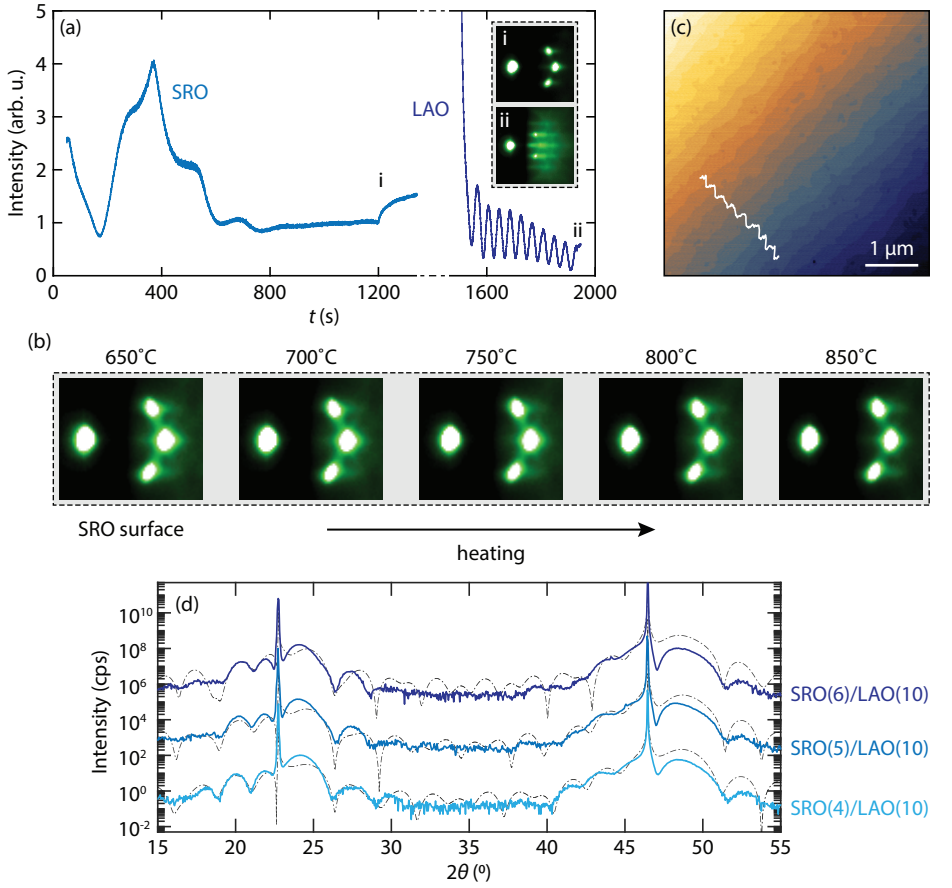

Figure 5.6: Growth and surface characterization. (a) Intensity of the first-order RHEED spot during the growth of a SRO/LAO heterostructure. The inset shows the RHEED pattern after the growth of (i) the SRO and (ii) the LAO layers. (b) RHEED pattern of the SRO surface during the heating prior to the deposition of LAO and (c) an AFM topographic image of the LAO surface. The inset shows the height profile. (e) X-ray diffraction θ-2θ scans, with the solid lines representing the data and the black dashed line simulations. The curves are shifted vertically for visual clarity.

sure of 0.1 mbar. The growth was monitored with in-situ RHEED, recording the first-order diffraction spot (see Fig. 5.6a). The first oscillation corresponds to a change in surface termination of the substrate from TiO_2 to SrO [88]. Subsequent oscillations represent depositions of full unit cells (consisting of RuO_2 and SrO planes). Starting from a SrO layer, this nominally leads to a SrO-terminated film. The deposition is stopped at an intensity maximum, after which an intensity recovery is observed, indicative of a high surface mobility of atomic species in the top layer. The final RHEED pattern of the SRO surface is shown in the inset and exhibits intense spots, implying an atomically smooth surface. Next, the oxygen partial pressure is reduced to 6×10^{-5} mbar and the sample is further heated to an estimated ~ 800 °C at a rate of 10 °C/min. To verify that

the SRO surface does not degrade, the RHEED patterns were monitored during heating (see Fig. 5.6b). Evidently, the surface quality is maintained up to high temperatures (> 850 °C). To refill oxygen vacancies that may have formed during the growth, all samples are post-annealed in 300 mbar O_2 for 1h and subsequently cooled to room temperature at 20 °C/min in the same pressure. An AFM topographic image of the LAO surface is shown in Fig. 5.6c, which shows the heterostructure adopts the step-and-terrace morphology of the substrate. Fig. 5.6d shows θ-2θ X-ray diffraction measurements (solid lines), as well as simulations (dashed lines) [237]. The simulations were obtained with the designated number of SRO unit cells with $c = 3.98$ Å (compressive strain) and 10 u.c. LAO with $c = 3.72$ Å (tensile strain) for the LAO capping layer.

The SrO/AlO_2 interface configuration would form the hybrid compound $La_{1-x}Sr_xAlO_3$ which, due to the available charge states of Sr (2+), La (3+) and Al (3+), has a net charge (for $x \neq 0$) and would therefore require off-stoichiometry to achieve charge neutrality, therefore a LaO/RuO_2 interface may be more likely. Lastly, it is worth noting that since the average kinetic energy of ablated La in the previously discussed growth conditions is in the order of several tens of eV (for Al, it is several times less). Under these conditions, adatoms have sufficient energy to disassociate SrO bonds (~ 5 eV [238]), which constitute the surface of the SRO layer prior to LAO growth [83, 88]. For higher oxygen pressures ($p \sim 10^{-1}$ mbar), this is no longer the case. The stopping power of adatoms is ~ 100 eV/nm [239], which suggests that at energies in the order of tens of eV, cation implantation is unlikely, but intermixing will still occur over a length scale of ~1 u.c., in agreement with the STEM data shown in Fig. 5.1. To further exclude kinetic damage to the SRO film during capping layer growth as a contributing factor, we grew the 5 u.c. SRO film with a 10 u.c. STO capping layer in the same conditions as the LAO layer, which results in Sr cations arriving at the substrate with a similar energy as La [83, 85]. The STO-capped sample was found to have a $T_C \approx 140$ K i.e., significantly higher than its LAO-capped counter part ($T_C \approx 110$ K), in agreement with a recent report [163]. This suggests that in case Ru-deficiency is induced by kinetic plume damage, it does not significantly impact the critical temperature. Indeed, it was recently shown that the T_C of MBE-grown films with thickness < 5 nm (~ 12 u.c.) is unaffected by Ru-deficiency as high as 30% [164]. Rather, interfacial disorder was concluded to dominate decay of the itinerant ferromagnetic properties for ultrathin films. This interpretation also agrees with our observations of the SRO/SIO interface discussed in Chapter 4.

In Figs. 5.7a-b, we show the ABF images of the STO/SRO/LAO and STO/SRO/STO heterostructures. The STO-capped sample was grown in 0.1 mbar O_2 at $T = 600$ °C. In agreement with the HAADF images, the adjacent positions of La ($Z = 57$) and Ru ($Z = 44$) atoms across the SRO/LAO interface are indicative of a LaO/RuO_2 configuration. The insets illustrate the fitted positions for the oxygen atoms, as well as the A- and B-site cations, which are used to determine the profile of the O−M−O bond angle (M = A, B) along the growth axis. In contrast to the LAO-capped heterostructure, for the STO-capped heterostructure we observe buckling of both the O−A−O and O−B−O bonds that becomes more pronounced towards the sample surface. We also find somewhat larger buckling angles in the SRO film, which may be due to the larger angles observed in the

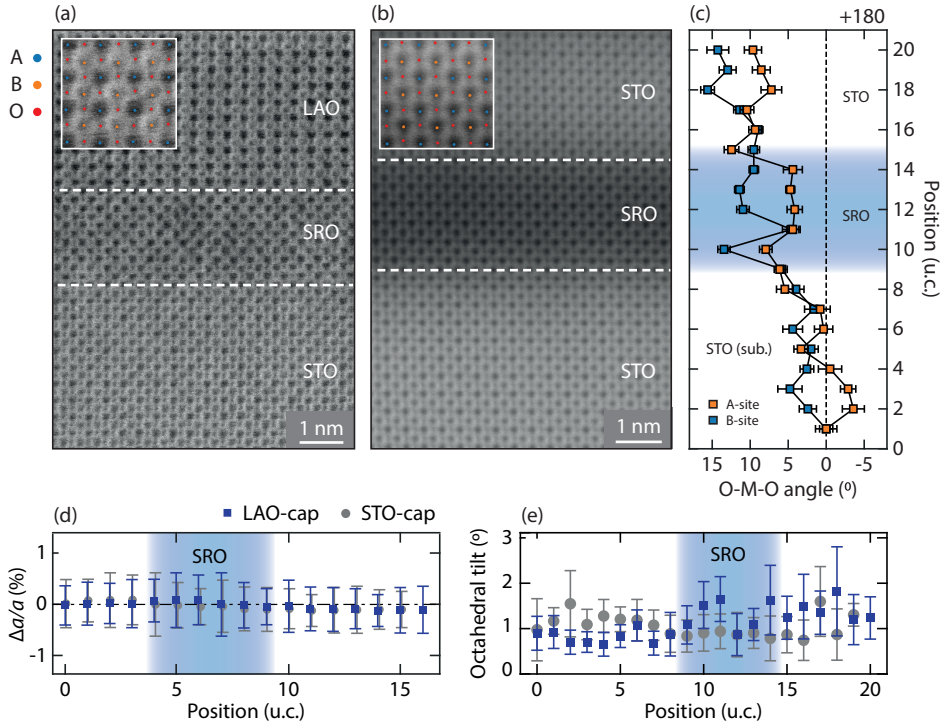

Figure 5.7: STEM characterization. Annular bright-field images of the (a) STO/SRO/LAO and (b) STO/SRO/STO heterostructures. The insets illustrate the fitted atomic positions for the (red) oxygen anion, as well as the (orange) A- and (blue) B-site cations. (c) Bond angle profile for the STO/SRO/STO heterostructure. Panels (d) and (e) show the in-plane unit cell deformation and octahedral tilts along the growth axis for STO- and LAO-capped SRO films, respectively.

STO capping layer. This in turn may be attributed to off-stoichiometry promoting polar nano regions [240]. Figs. 5.7d-e show the in-plane unit cell deformation and octahedral tilts along the growth axis for the two heterostructures. In agreement with the X-ray characterization shown in Fig. 5.6d, we find that the lattice parameters of the SRO film and the LAO- and STO-capping layers are coherently matched to the STO substrate ($a = 3.905$ Å). The unit cell size mismatch is then accommodated through compressive and tensile strain in the SRO and LAO layers, respectively. We also find a strong suppression of the octahedral tilts for both samples.

5.6.2. MAGNETIC AND TRANSPORT CHARACTERIZATION

The magneto-optical characterization was performed in the same manner as discussed in section 4.6.4 (see also Fig. 5.8a). The Faraday rotation of three heterostructures with different capping layers (see Fig. 5.8b) is shown in Figs. 5.8c-e. The height of the hysteresis loop (indicated by the orange arrow) is directly proportional to the out-of-plane component of the sample magnetization M_z. As discussed in the main text, we find a suppression of the Faraday rotation for the LAO(10) capping layer compared to the

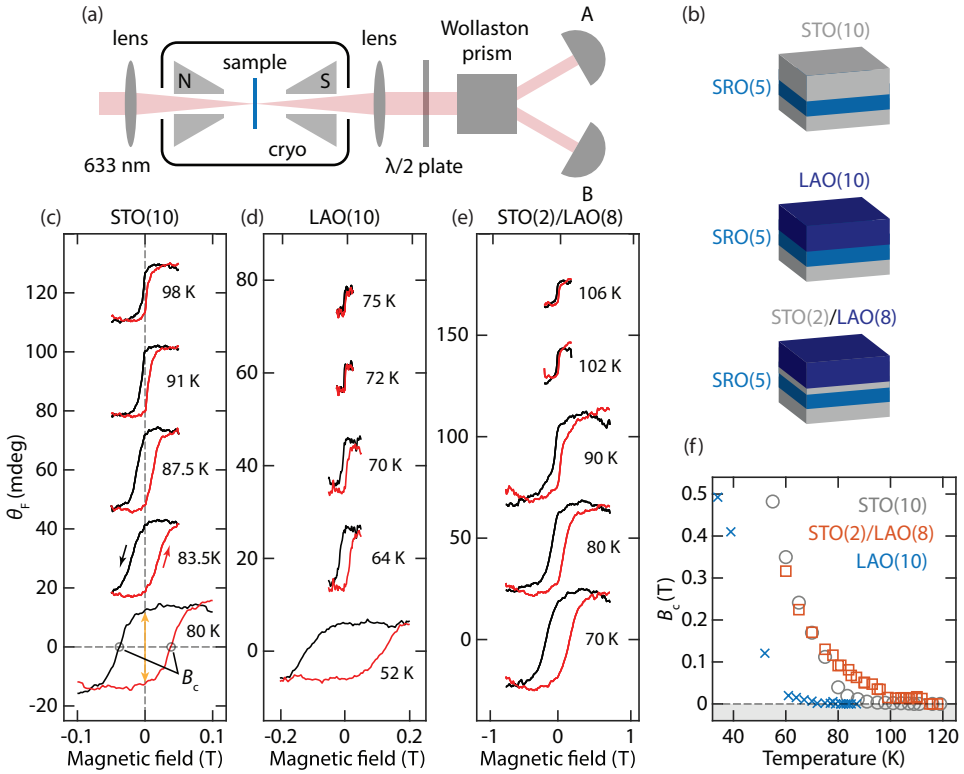

Figure 5.8: Magneto-optical characterization. Illustrations of (a) the experimental setup for probing the magneto-optical Faraday effect (WP: Wollaston prism) and (b) the three different samples measured. (c-e) Faraday rotation θ_F as a function of magnetic field for the heterostructures indicated in (b). The curves are shifted vertically for visual clarity. (f) Coercive field B_c as a function of temperature.

STO(2)/LAO(10) and STO(10) capping layers, which we attribute to an altered valence and spin state of Ru at the RuO_2/LaO interface. We also find a suppression of the coercive field (Fig. 5.8f), indicating a weakened magnetic state.

In Fig. 5.9, we show the magnetic-field-dependent Hall effect. Note the opposite orientation of the loops between the SRO(4)/LAO(10) and SRO(4)/STO(10) samples (Figs. 5.9a-b), an indicator of an opposite sign of the momentum-space Berry curvature between the two scenarios. As discussed in Chapter 4, the peaks seemingly superposed on the hysteresis loop for the LAO-capped sample have over the past years been a source of debate, with them either being attributed to real-space magnetic skyrmions (see e.g., refs. [37, 147]), or to a spatially inhomogeneous profile of the magnetization (e.g., refs. [160, 217]). They only occur in the vicinity of the coercive field (i.e., during the magnetization reversal) and do not affect the anomalous amplitude in the fully magnetized state. While interesting in their own right, the peaks are not relevant to the discussion on the momentum-space sources of Berry curvature considered here. We also note that they are

absent in STO-capped samples and vanish in the LAO-capped samples as the SRO layer thickness is increased (see Fig. 5.9c). The large values for the coercive field observed in all samples may be attributed to Ru-deficiency, which causes a pinning of magnetic domain walls during the switching of the magnetization [163, 164].

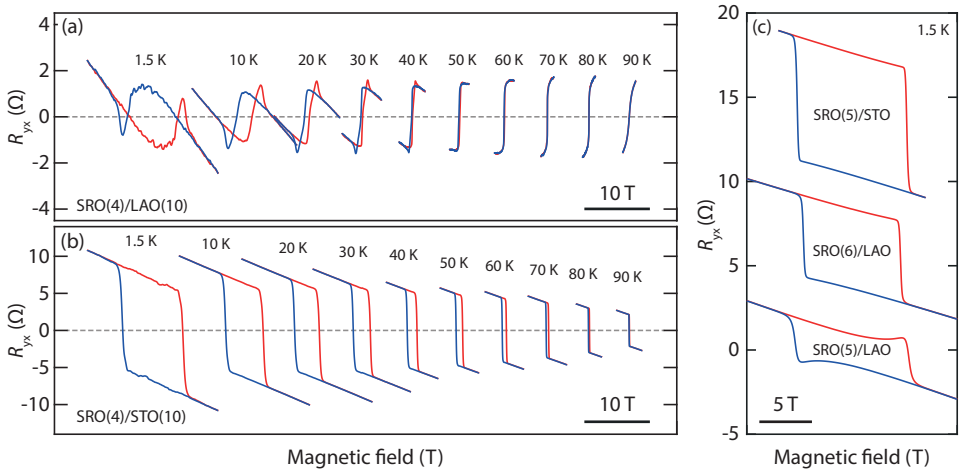

Figure 5.9: Hall effect. Transverse resistance as a function of magnetic field and for various temperatures for (a) a SRO(4)/LAO(10) and (b) a SRO(4)/STO(10) heterostructure. (c) Comparison of the magnetic-field dependent Hall effect at 1.5 K for SRO(5)/LAO, SRO(6)/LAO(10) and SRO(5)/STO(10).

In Fig. 5.10a, we show the sheet resistance as a function of temperature for various STO- and LAO-capped SRO ultrathin films. According to expectation, we observe a lowering of the sheet resistance with an increasing number of SRO layers. For the thinnest films, slight upturns at low temperature can be observed, indicative of disorder-induced carrier localization, resulting from the close proximity to the thickness-driven metal-insulator transition [179]. The slightly increased resistivity of the LAO-capped samples with respect to the STO-capped samples may be attributed to a more resistive interface resulting from La-doping, which creates a nearly filled hole-like t_{2g} band with a lower conductivity [232, 233, 241]. Another explanation may be enhanced scattering due to La intermixing, which has also been reported in La-doped Sr_2RuO_4 [242]. Additionally, polar interfaces are susceptible to defects (e.g., oxygen vacancies) [10, 196], which may contribute to a more resistive interfacial layer.

As discussed in Chapter 4, at the Curie temperature T_C, $R(T)$ exhibits an inflection point, caused by short-range spin fluctuations across the magnetic phase transition [176]. The inflection point corresponds to a peak in the dR/dT, the center of which is used to identify T_C, which is shown in the inset as a function of the SRO layer thickness m. We find (1) a suppressed Curie temperature in LAO-capped samples and (2) a requirement of 2 additional unit cells in LAO-capped samples to recover the T_C of the STO-capped samples. To verify that the growth conditions do not significantly affect the SRO properties, we grew the STO capping layer for the SRO(5)/STO(10) sample in the same conditions as the LAO capping layers. The T_C was found to be ~ 140 K, in agreement with a recent

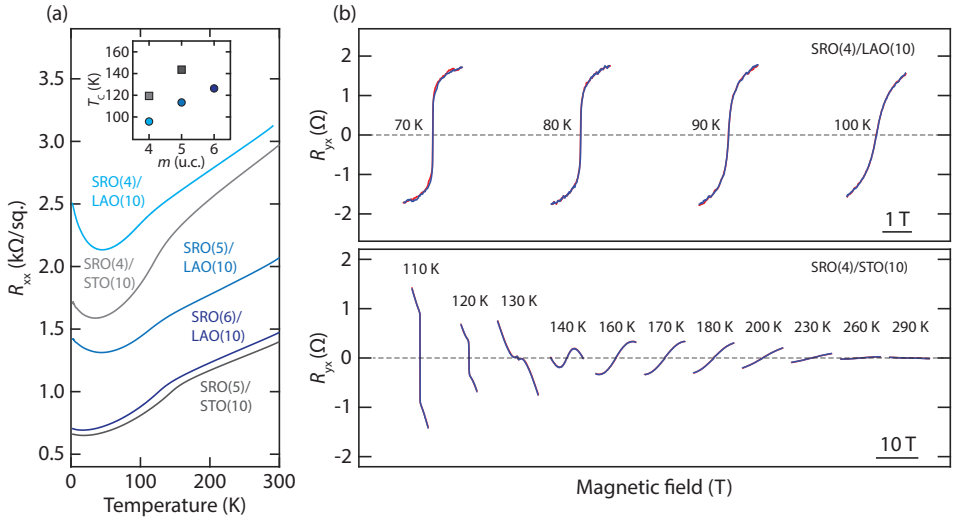

Figure 5.10: Ferromagnetic transition. (a) Sheet resistance as a function of temperature for various heterostructures, with the inset showing T_C extracted from the peak in the $\mathrm{d}R/\mathrm{d}T$. (b) Hall effect in the vicinity of T_C for (top) the SRO(4)/LAO(10) and (bottom) the SRO(4)/STO(10) sample.

report [163]. This indicates that neither low pressure annealing nor the growth kinetics under these conditions have a significant impact on the critical temperature of the ferromagnetic state.

Fig. 5.10b shows the Hall effect in the vicinity of the Curie point for the SRO(4)/LAO(10) and SRO(4)/STO(10) samples. We consider a state ferromagnetic if a finite remanence is present. For both heterostructures we find that as the temperature is increased towards T_C the hysteresis tends to zero, but a small remanence remains observable as a vertical 'jump' at low field. When T_C is exceeded, the system enters a phase characterized by fluctuating residual moments [70, 243, 244], which are readily aligned by an external magnetic field. In the Hall effect, this manifests as the presence of an appreciable slope at zero magnetic field, yet the absence of a remanence. For the LAO-capped sample, we observe a deviation from a perfect vertical slope in the vicinity of 90 K. For the STO-capped samples the same phenomenology is observed, but shifted up in temperature by 20-30 K. These observations are in agreement with the R-T curves shown in Fig. 5.10a, as well as the magneto-optical characterization (Fig. 5.8).

5.6.3. DFT COMPUTATIONAL METHODOLOGY

Spin-polarized first-principles density-functional theory calculations were performed within the Local Spin Density Approximation (LSDA), by using the plane wave VASP DFT package [188, 245] and the Perdew-Zunger parametrization [189] of the Ceperley-Alder data for the exchange-correlation functional [190]. The interaction between the core and the valence electrons was treated with the projector augmented wave (PAW) method [246] and a cutoff of 500 eV was used for the plane wave basis. For Brillouin

zone integrations, a $12 \times 12 \times 1$ k-point grid was used for the geometric relaxation and a $24 \times 24 \times 1$ k-point grid for the determination of the density of states (DOS), electron charge and magnetization profiles. The atomic charge was calculated by integrating a sphere of 1.402 Å radius around the Ru sites. The internal degrees of freedom are optimized by minimizing the total energy to be less than 3×10^{-5} eV and the Hellmann-Feynman forces to be less than 20 meV/Å. The Coulomb interaction U at the Ru and Ti sites was included in the LSDA+U approach using the rotationally invariant scheme proposed by Liechtenstein [137]. $U = 4$ eV was used for the Ti $3d$ states, whereas $U = 0.20$ eV and $J_H = 0.15U$ are considered for the Ru $4d$ states. The hopping parameters were determined as described in section 4.6.3.

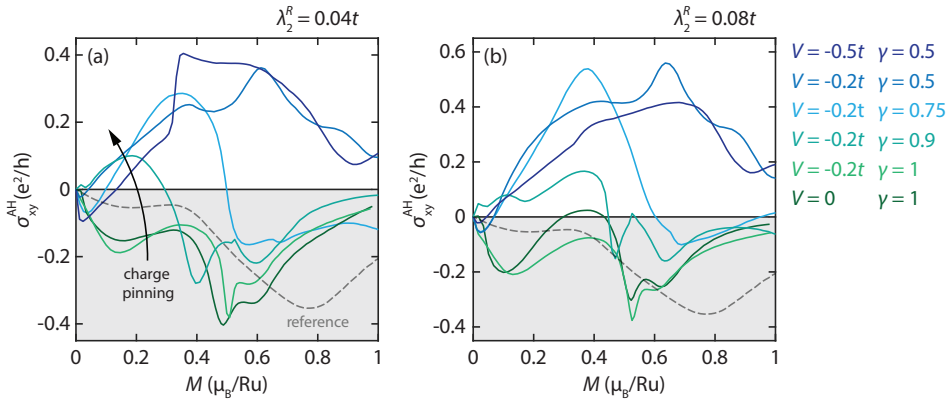

Figure 5.11: Anomalous Hall conductance. Calculated anomalous Hall conductance $\sigma_{xy}^{\mathrm{AH}}$ for the bilayer model with various on-site potentials V and interlayer hopping parameters γt as a function of magnetization. The orbital Rashba corrections are (a) $\lambda_2^R = 0.04t$ and (b) $\lambda_2^R = 0.08t$. The gray dashed lines represent the reference curves with no additional charge.

5.6.4. SYMMETRY BREAKING IN THE BILAYER MODEL

In Fig. 5.11, the anomalous Hall conductance curves discussed in section 5.3 are shown for additional values for the on-site potentials V and interlayer coupling γ, as well as two different values for the orbital Rashba correction in the top layer λ_2^R. As discussed previously, these parameters represent the degree of charge pinning to the top layer and therefore the inversion symmetry breaking along the z-axis. From the curves, it becomes apparent that γ is the most influential parameter, followed by λ_2^R and the on-site potential V. To elucidate the influence of γ, the role of the interlayer coupling in the total anomalous Hall conductance $\sigma_{xy}^{\mathrm{AH}}$ must be assessed. The bilayer model system has contributions coming from the individual layers σ_1, σ_2 and a term σ_{12} that represents the interference between the two layers, the latter of which is directly affected by the interlayer coupling γt. The layer decomposition of the bilayer anomalous Hall conductance is shown in Fig. 5.12. The contributions of the individual layers for the charge-symmetric reference case are shown in Fig. 5.12a and a charge-asymmetric case is shown in Fig. 5.12b. It is clear there is a pronounced role of the term σ_{12} in determining $\sigma_{\mathrm{tot}}^{\mathrm{AH}}$. If σ_{12} is neglected, the computed anomalous Hall conductance is found to be widely off, il-

lustrating that the interlayer coupling is a crucial parameter. The pronounced influence of the charge pinning can therefore be attributed to its role in altering the interference between the layer-resolved anomalous Hall 'channels'.

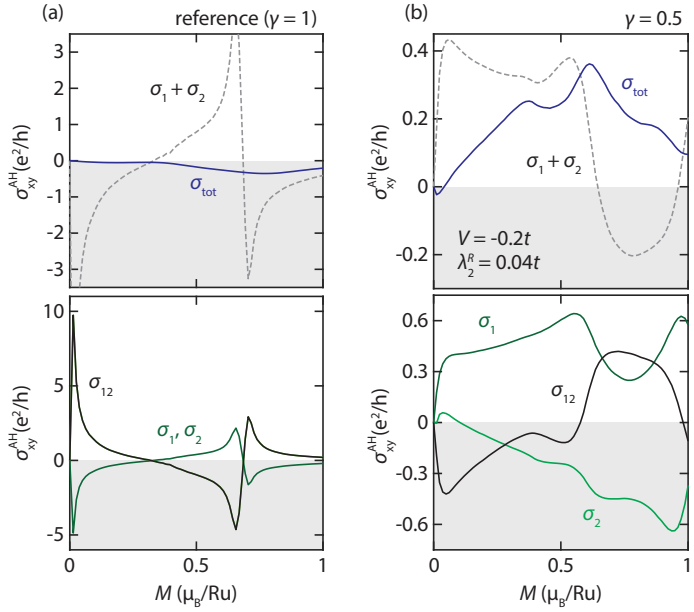

Figure 5.12: Layer decomposition of the anomalous Hall conductance. Calculated anomalous Hall conductance $\sigma_{xy}^{\mathrm{AH}}$ as a function of magnetization for (a) the charge-symmetric reference case and (b) a charge-asymmetric case with $\gamma = 0.5$, $V = -0.2t$ and $\lambda_2^R = 0.04t$. The bottom panels show the layer-resolved contributions σ_1 and σ_2, as well as the interference term σ_{12}. The top panels show the direct sum of σ_1 and σ_2 and the total anomalous Hall conductance σ_{tot}.

To illustrate the role of the orbital Rashba effect, we consider a simple symmetry breaking potential along the z-axis $\mathcal{V} = -e\mathscr{E}_0 z$, where e is the elementary charge and $\mathscr{E}_0$ the corresponding electric field strength. Because $\mathcal{V}$ is odd under a mirror reflection with respect to the (x, y) plane, it inverts the orbital parity. In a first-order approximation, the symmetry $\mathcal{V}$ acts only once; either in the direct d–d hopping or in one of the two metal-oxygen hopping terms, described in equation (4.12) in section 4.6.1. In the latter, the potential hybridizes d- and p-orbitals with opposite parities. The second step comes from the unperturbed nearest neighbour hopping terms, described in Table 4.1, which couples orbitals with the same parity. Along the x- and y-directions, this leads to the following possibilities, respectively

$$\begin{array}{ccccc} |xy\rangle & \rightarrow & |z\rangle & \rightarrow & |zx\rangle \\ |yz\rangle & \rightarrow & |y\rangle & \rightarrow & |xy\rangle \\ |zx\rangle & \rightarrow & |z\rangle & \rightarrow & |xy\rangle \end{array} \quad \text{and} \quad \begin{array}{ccccc} |xy\rangle & \rightarrow & |z\rangle & \rightarrow & |yz\rangle \\ |yz\rangle & \rightarrow & |x\rangle & \rightarrow & |xy\rangle. \\ |zx\rangle & \rightarrow & |x\rangle & \rightarrow & |xy\rangle \end{array}$$

Only the terms that behave like axial vectors will contribute to the Rashba effect i.e., terms that rotate by π radians in the (x, y) plane upon the mirror reflection $z \rightarrow -z$. The

other terms preserve (x, y) inversion symmetry and will be proportional to $\cos(k_x a)$ and $\cos(k_y a)$. Discarding the inversion symmetric terms and incorporating the Bloch phase factors along the appropriate hopping directions, one finds the Rashba terms to be

$$\hat{H}' = 2i\lambda_R \begin{pmatrix} 0 & \sin(k_x a) & \sin(k_y a) \\ -\sin(k_x a) & 0 & 0 \\ -\sin(k_y a) & 0 & 0 \end{pmatrix}, \tag{5.1}$$

with λ_R the coupling constant given by $\left(\gamma t_{pd}\mathscr{E}_0 + n t_{pd}^2\right)/\Delta_{pd}$, where $\gamma\mathscr{E}_0$ is the induced interorbital hopping amplitude from the electric field, t_{pd} the metal-oxygen hopping amplitude, Δ_{pd} the charge transfer energy and $n t_{pd}^2$ a correction resulting from the buckling of the metal-oxygen-metal bonds i.e., the polar mode along the field direction [185]. Equation (5.1) in terms of the orbital angular momentum operators reads

$$\hat{H}' = \frac{2\lambda_R}{\hbar}\left[\sin(k_y a)\hat{L}_x - \sin(k_x a)\hat{L}_y\right]. \tag{5.2}$$

The spin dependence arises when the orbital Rashba effect is combined with the atomic spin-orbit coupling. For a hopping process along the x-direction, for example, $\hat{H}'$ couples the spin-orbital state $|xy,\sigma\rangle$ to $|yz,\sigma\rangle$, which in turn couples to $|xy,\sigma'\rangle$ via the $\lambda_{so}\hat{L}_y\hat{S}_y$ term of the atomic spin-orbit coupling (and vice versa). The energy denominator in this perturbation process is the splitting Δ_z between the $|xy\rangle$ and $|yz\rangle, |xz\rangle$ orbitals, induced by the potential $\mathscr{V}$ along z. One then finds the following energy corrections

$$\begin{aligned} E'_{xy} &= \frac{2\lambda_R\lambda_{so}}{\Delta_z}\left[\sin(k_y a)\hat{\sigma}_x - \sin(k_x a)\hat{\sigma}_y\right] \\ E'_{yz} &= \frac{2\lambda_R\lambda_{so}}{\Delta_z}\sin(k_x a)\hat{\sigma}_y \\ E'_{zx} &= \frac{2\lambda_R\lambda_{so}}{-\Delta_z}\sin(k_y a)\hat{\sigma}_x, \end{aligned} \tag{5.3}$$

where λ_{so} is the atomic spin-orbit coupling constant and $\hat{\sigma}$ are the Pauli spin matrices. From equations (5.2) and (5.3), it becomes apparent that the role of the Rashba effect is to induce (spin-dependent) nearest neighbour interorbital hopping, which can induce additional (time-reversal invariant) sources that can contribute to higher order moments of the Berry curvature. From Fig. 5.11 however, it becomes apparent that these sources produce only subtle differences to the net integrated Berry curvature.

5.6.5. CHERN NUMBERS

In Fig. 5.13, we show the twelve t_{2g} bands and their Chern numbers for the weak and strong pinning scenarios discussed in section 5.3. We proceed by demonstrating (i) that for a band occupation that decreases linearly with energy, an approximate expression for the anomalous Hall conductivity can be obtained in terms of the band-resolved Chern numbers and (ii) that the sign of the anomalous Hall effect is then purely determined by

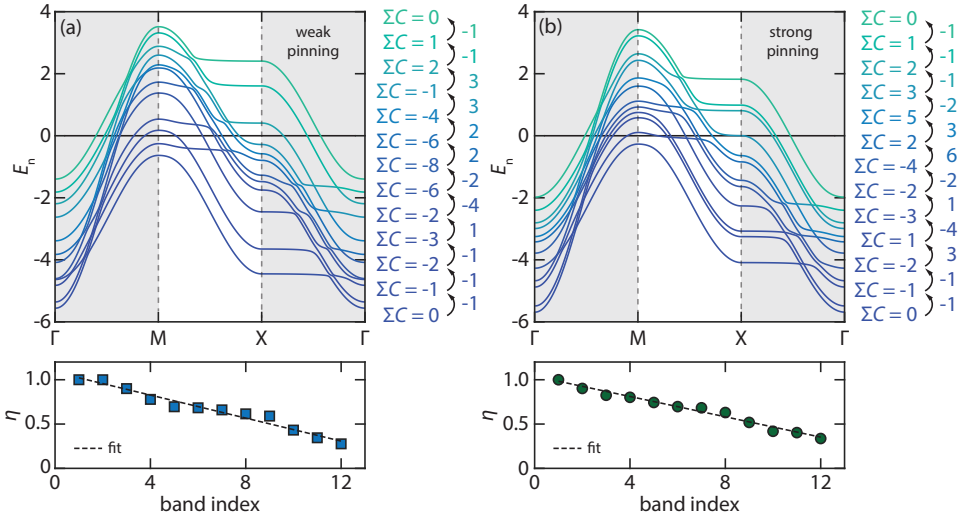

Figure 5.13: Band-resolved Chern numbers. Electronic (top) bands and (bottom) filling factors η derived from the bilayer tight-binding model for (a) the weak and (b) the strong pinning scenario for a magnetization value $0.5\,\mu_B$/Ru. The Chern numbers associated with the indirect gaps between bands n and $n+1$ are indicated to the right as ΣC. The differences between subsequent ΣC correspond to the Chern numbers of the invididual bands.

the sum of the Chern numbers associated with the indirect band gaps. The anomalous Hall conductivity $\sigma_{xy}^{\mathrm{AH}}$ depends on the momentum-space Berry curvature Ω_k^n as

$$\sigma_{xy}^{\mathrm{AH}} = \frac{e^2}{h} \sum_{n=1}^{N} \int_{\mathrm{BZ}} f(\epsilon_{\mathbf{k}}^n) \Omega_{\mathbf{k}}^n \, \mathrm{d}^2\mathbf{k}, \tag{5.4}$$

where N is the total number of bands (twelve in this case) and $f(\epsilon_{\mathbf{k}}^n)$ is the Fermi-Dirac function of band n at energy $E(\mathbf{k})$. The Chern number for band n is given by

$$C_n = \frac{1}{2\pi} \int \Omega_{\mathbf{k}}^n \, \mathrm{d}^2\mathbf{k}. \tag{5.5}$$

Now we make a rough approximation, replacing the Berry curvature by its momentum-space averaged value $\Omega_{\mathbf{k}}^n \approx \bar{\Omega}_n$. Implementation in (5.5) yields

$$\begin{aligned} C_n &= \frac{1}{2\pi} \bar{\Omega}_n \int_{\mathrm{BZ}} \mathrm{d}^2\mathbf{k} \\ &= 2\pi \bar{\Omega}_n, \end{aligned} \tag{5.6}$$

such that

$$\Omega_{\mathbf{k}}^n \approx \frac{1}{2\pi} C_n. \tag{5.7}$$

Then (5.4) can be approximated as

$$\sigma_{xy}^{\mathrm{AH}} \approx \frac{e^2}{h}\frac{1}{2\pi}\sum_{n=1}^{N} C_n\left(\int_{\mathrm{BZ}} f(\epsilon_{\mathbf{k}}^{n})\,\mathrm{d}^2\mathbf{k}\right), \tag{5.8}$$

where the final term in brackets is the filling factor η_n of band n, simplifying (5.8) to

$$\sigma_{xy}^{\mathrm{AH}} \approx \frac{e^2}{h}\frac{1}{2\pi}\sum_{n=1}^{N} \eta_n C_n. \tag{5.9}$$

While the filling factors have to be explicitly computed, it is anticipated that if the bands are ordered in such a way that $n = 1$ is the lowest in energy, $n = 2$ is the second lowest, etc., then the filling factor η_n decreases with n. The simplest form would be to assume a linear relation $\eta_n \approx \alpha - \beta n$ with α and β real positive coefficients with the constraints $\alpha \geq \beta N$ and $\alpha - \beta \leq 1$ to ensure $0 \leq \eta_n \leq 1$. From the filling factors shown in Fig. 5.13, we find that the linear approximation works reasonably well. Now (5.9) becomes

5

$$\begin{aligned}\sigma_{xy}^{\mathrm{AH}} &\approx \frac{e^2}{h}\frac{1}{2\pi}\sum_{n=1}^{N}(\alpha-\beta n)C_n.\\ &= \frac{e^2}{h}\frac{1}{2\pi}\left(\alpha\sum_{n=1}^{N} C_n - \beta\sum_{n=1}^{N} nC_n\right).\end{aligned} \tag{5.10}$$

First we note that the direct sum of all Chern numbers is zero, causing the first term in brackets to vanish. The second term can be deconstructed as

$$\begin{aligned}\sum_{n=1}^{N} nC_n = C_1 + 2C_2 + 3C_3 + 4C_4 + \ldots + (N-1)C_{N-1} + NC_N\\ = C_1 + C_2 + C_3 + C_4 + \ldots + C_{N-1} + C_N\\ + C_2 + C_3 + C_4 + \ldots + C_{N-1} + C_N\\ + C_3 + C_4 + \ldots + C_{N-1} + C_N\\ + C_4 + \ldots + C_{N-1} + C_N\\ \vdots\\ + \ldots + C_{N-1} + C_N\\ + C_{N-1} + C_N\\ + C_N,\end{aligned} \tag{5.11}$$

which using $\sum_{n=1}^{N} C_n = 0$ can be written as

$$
\begin{aligned}
\sum_{n=1}^{N} nC_n = 0 \\
&-(C_1) \\
&-(C_1+C_2) \\
&-(C_1+C_2+C_3) \\
&-(C_1+C_2+C_3+C_4) \\
&\qquad\vdots \\
&-(C_1+C_2+C_3+C_4+\ldots+C_{N-1}) \\
&-(C_1+C_2+C_3+C_4+\ldots+C_{N-1}+C_N) \\
&= -\sum_{n=1}^{N} \mathscr{C}_n,
\end{aligned}
\tag{5.12}
$$

with $\mathscr{C}_n = \sum_{m=1}^{n} C_m$ the sum of the Chern numbers up to band n, or alternatively, the Chern number associated with the indirect gap between bands n and $n+1$ (indicated by ΣC in Fig. 5.13). Implementing this in (5.10), we obtain

$$
\sigma_{xy}^{\mathrm{AH}} \approx \frac{e^2}{h}\frac{\beta}{2\pi}\sum_{n=1}^{N}\mathscr{C}_n. \tag{5.13}
$$

Thus, the anomalous Hall conductivity can be approximated by the sum of all Chern numbers associated with the indirect gaps. Note that since $\beta > 0$, the sign of $\sigma_{xy}^{\mathrm{AH}}$ is solely determined by $\sum_{n=1}^{N}\mathscr{C}_n$ and is robust to changes in filling factors produced by e.g., a shift in the Fermi energy.

6

QUANTUM TRANSPORT IN (111) SRO/STO HETEROSTRUCTURES

"Every sentence I utter must be understood not as an affirmation, but as a question."

– Niels Bohr

Heteroepitaxy is a powerful tool that can be used to exercise control over both the crystal symmetry and dimensionality of a condensed matter system. Projected onto the (111) crystal plane, cubic perovskites exhibit a two-dimensional hexagonal lattice symmetry, with distortions to the unit cell leading to the breaking of mirror line symmetries in the plane. In conjunction with time-reversal symmetry breaking, this sets the stage for the manifestation of both zero and higher order moments of the Berry curvature. Ferromagnetic $SrRuO_3$ grown along the (111) crystal orientation is therefore an ideal system to study the interplay between spatial and time-reversal symmetry breaking, as well as their impact on the emergent field in momentum-space. In this chapter, we synthesize $SrRuO_3$ thin films on $SrTiO_3$ (111) substrates and determine their structural and electronic properties as a function of thickness, by means of transmission electron microscopy, X-ray diffraction and high-field transport measurements. Our structural analysis is consistent with a $Pbnm$-type octahedral tilt pattern, with the in-phase rotation axis oriented along the (001) crystal direction. In transport, all films exhibit hole-like characteristics, with thicker films showing evidence of a high-mobility band, as well as an unsaturating linear positive magnetoresistance, which we attribute to guiding center motion in strong magnetic fields. These results set apart (111) thin films from their (001) counterparts and highlight the potential of heteroepitaxy and crystal symmetry as a method for engineering novel electronic properties in perovskites.

Parts of this chapter are in preparation for submission by T.C. van Thiel, P. Eck, U. Filippozzi, N. Gauquelin, D. Jaen, D. Pizzirani, C. Müller, E. Lesne, J. Verbeeck, S. Wiedmann, C. Ortix, G. Sangiovanni, M. Cuoco and A.D. Caviglia.

STEM analysis was performed by N. Gauquelin, D. Jaen and J. Verbeeck. High-field measurements were performed in collaboration with D. Pizzirani, C. Müller and S. Wiedmann.

RECENTLY, crystal symmetry and heteroepitaxial strain have emerged as key factors in realizing novel material properties. Examples include, but are not limited to, superconductivity in (110) oriented RuO_2 films [18, 19], multi-condensate superconductivity in (110) oriented $LaAlO_3/SrTiO_3$ [247] and two-dimensional gate-tunable superconductivity at (110) and (111) $KTaO_3$ surfaces [248–250]. Of particular interest are (111) oriented perovskite ultrathin films which, in the case of a cubic or rhombohedral lattice, exhibit a buckled honeycomb lattice structure, with a threefold in-plane rotational symmetry [251, 252]. If the unit cell symmetry is lowered, due to e.g., a symmetry mismatch across the substrate/film interface, substrate-induced strain or simply due to the bulk compound having a priori lower symmetry, a breaking of mirror lines in the plane can easily manifest, which is in contrast to more commonly studied (001) oriented crystal thin films. In combination with inversion symmetry breaking at interfaces, this permits nonlinear responses to applied electric fields [253–255], with efficient photon detection and rectifying schemes as a possible application [256]. In this context, the itinerant ferromagnetic perovskite $SrRuO_3$ (SRO) is of particular interest. In the three-dimensional bulk limit, time-reversal symmetry breaking enables the presence of Weyl points acting as sources and sinks of an emergent field [65, 219]. In (111) oriented films, the $Pbnm$ orthorhombic symmetry breaks the $\mathcal{M}_{1\bar{1}0}$ and $\mathcal{M}_{11\bar{2}}$ mirror lines in the plane of the film, which towards the two-dimensional limit can be expected to have a progressively more prominent impact on the electronic structure. In addition, the three-dimensional strain imposed by the substrate is expected to lower the octahedral symmetry of the crystal field to trigonal, leading to a splitting of the t_{2g} orbitals into a a_{1g} singlet and e_g^π doublet [186]. Accordingly, (111) oriented SRO thin films and heterostructures are of fundamental interest to study the combination of symmetry-breaking, dimensionality and topology.

In this chapter, we determine the thickness-dependent properties of (111) oriented SRO thin films grown on $SrTiO_3$ (STO), by means of transmission electron microscopy, X-ray diffraction and (high-field) transport measurements. Our structural analysis is consistent with a $Pbnm$-type $a^-b^-c^+$ octahedral rotation pattern, with the in-phase rotation axis oriented along the (001) crystal direction. In addition, thicker films are found to exhibit larger rotations compared to thinner films. We propose that the triaxial compressive strain exerted by the substrate is accommodated through the formation of Ruddlesden-Popper defects, as opposed to monoclinic distortions to the unit cell. In transport, we find evidence of a dimensional crossover below ~ 5 nm film thickness. Unlike in (001) oriented films, Hall effect measurements indicate, with decreasing film thickness, a progressively more prominent hole-like band. High-field measurements on thicker films suggest the presence of semiclassical contributions to the magnetotransport in the form of guiding-center motion magnetoresistance, made possible by the combination of sufficiently high magnetic fields and mobility. These results unequivocally separate (111) oriented films from their (001) oriented counterparts in terms of both lattice and electronic structure.

6.1. ATOMIC STRUCTURE

The cubic perovskite lattice structure and (two-dimensional) first Brillouin zone projected onto the (111) crystal face are shown in Fig. 6.1a. In this basis, there are three in-

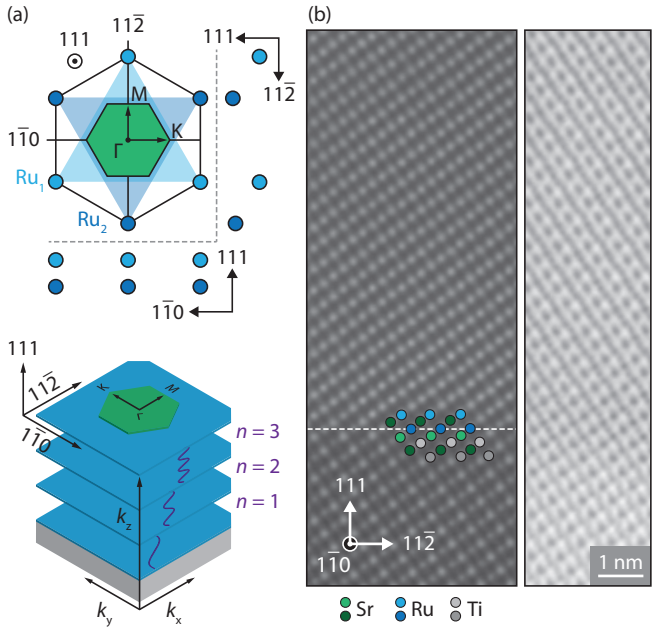

Figure 6.1: Buckled honeycomb lattice. Illustration of (a, top) the cubic perovskite unit cell projected onto the (111) orientation in both real and reciprocal space and (bottom) illustration of replica bands for multiple layers. The symbols Γ, *M* and *K* denote the high-symmetry points of the two-dimensional hexagonal unit cell. (b, left) HAADF-STEM and (right) ABF image of a (21 nm) SRO (111) thin film on STO.

6

equivalent Ru sites; one in the center and the other two spanning two triangles mirrored in the $1\bar{1}0$ axis, which have different vertical positions. The Sr site is situated in the center of the unit cell at a height between the two triangles, which yields a buckled honeycomb lattice structure in the ultrathin limit capturing one molecular formula unit of SRO. Experimentally, we view the lattice structure in two planes, namely the plane spanned by the (111, $11\bar{2}$), as well as the (111, $1\bar{1}0$) vectors. Henceforth, we shall refer to the former and latter as the α- and β-plane, respectively. Starting from a three-dimensional (bulk-like) structure, one can imagine thinning down the crystal along the (111) direction towards the two-dimensional limit. For progressively thinner crystal slabs, one expects to reach a quasi-2D regime, where a discrete set of k_z values is allowed in the form of replica bands (see Fig. 6.1a). Fig. 6.1b shows HAADF-STEM and ABF images of the α-plane of a ~ 21 nm film, with the overlay illustrating the lattice configuration at the interface between the STO substrate and the SRO film.

To study the strain state of the films, we perform X-ray characterization. Fig. 6.2a shows a Bragg diffraction scan around the (111) peak of a 94 u.c. film, with a simulated c-axis lattice parameter of 2.28 Å [237]. This corresponds to 94 repetitions of the bilayer unit cell, which are coherently strained (~ 1% compressive strain) to the $1\bar{1}0$ lattice axis of the substrate, as evident from the reciprocal space map shown in Fig. 6.2b. The thickness was also confirmed by X-ray reflectometry, shown in the left inset of Fig. 6.2a. The right inset shows the rocking curves of the substrate as well as the SRO film around the (111)

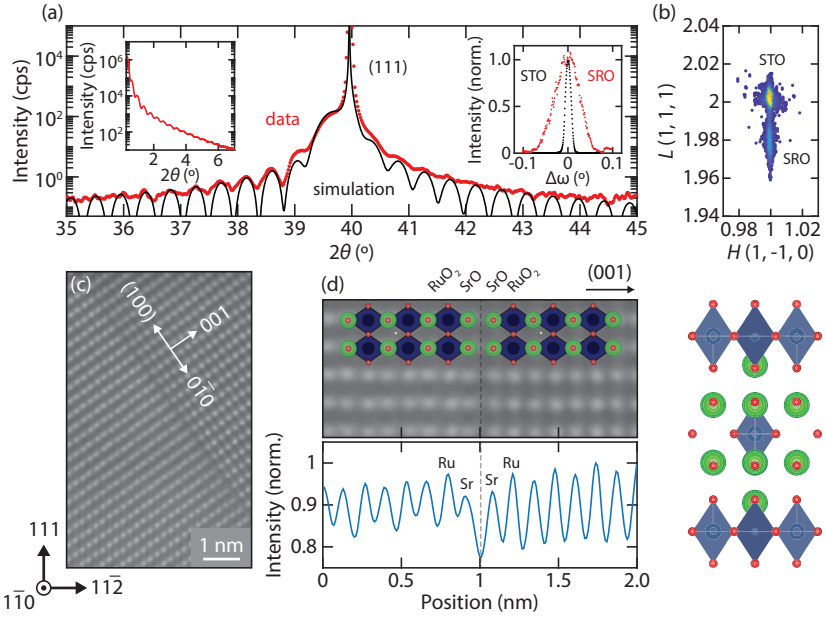

Figure 6.2: Ruddlesden-Popper defect. (a) Bragg X-ray diffraction on a 21 nm film, with the insets showing (left) X-ray reflectometry and (right) the rocking curve around the (111) peak. (b) Reciprocal space map around the 312 peak of the STO substrate. (c) HAADF-STEM image showing a RP-defect oriented at an angle with respect to the growth direction. (d, top) Enlarged view of the area around the defect and (bottom) intensity as a function of position. The illustration to the right depicts the unit cell of Sr_2RuO_4, which exhibits double SrO planes.

peak, the latter of which has a FWHM of ~ 0.06°. The rocking curve indicates stronger mosaicity of the film with respect to the substrate, with a slight hint of an additional peak, possibly pointing to crystal twinning. Fig. 6.2c shows a possible type of defect that may contribute to this observation, namely a double SrO plane along the (001) crystal orientation (see also section 6.6.2). In Fig. 6.2d, we show a rotated enlarged view of the defected area, with an overlay of the crystal structure. This so-called Ruddlesden-Popper (RP) defect corresponds to a single unit cell of Sr_2RuO_4 i.e., a missing RuO_2 plane along the (001) direction. Since the missing RuO_2 plane is not parallel to the growth direction, we speculate that a line defect must have formed in a particular layer that has propagated along the appropriate lattice direction as subsequent layers were deposited. In Sr_2RuO_4, adjacent SrO layers are believed to be more weakly bonded compared to adjacent RuO_2 and SrO layers, resulting in a natural cleavage plane [257, 258]. Previously, significant monoclinic shearing has been reported in $PbTiO_3$ films grown on (111) STO, resulting from the three-dimensional character of the strain imposed by the substrate [259]. Such shear strain might also be expected in our films, which could potentially lead to flexoelectricity and result in a so-called polar metal [260]. However, we do not find clear evidence of such shear strain (see section 6.6.2). We propose that the observed RP defects contribute to the accommodation of shear strain imposed by the substrate, thereby diminishing monoclinic distortions to the unit cell.

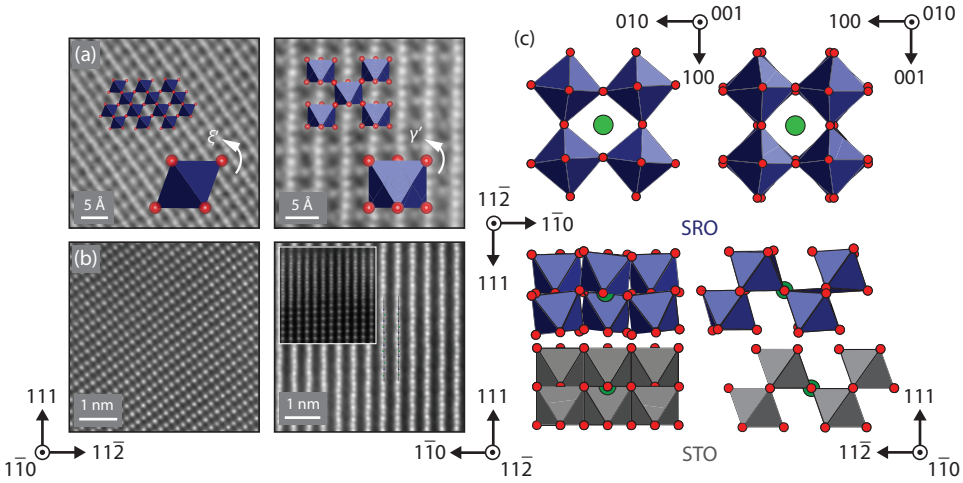

Figure 6.3: Rotation angles. (a) Inverted contrast ABF images of the 21 nm sample with (left) the $1\bar{1}0$ and (right) the $11\bar{2}$ lattice vector oriented into the page. The insets illustrate the rotation angles ξ' and γ' as viewed in the rotated basis. (b) Dark-field images of the same film, with the inset showing a dark-field image of a 2 nm (11 u.c.) sample. (c, top) Determined rotation angles in the pseudocubic basis and (bottom) the lattice structure near the interface in the rotated basis. The visualized rotation angles are to scale.

As illustrated in Fig. 6.3a, bright-field imaging of the α and β planes gives access to the oxygen positions and therefore the octahedral rotation angles ξ' and γ' about the $1\bar{1}0$ and $11\bar{2}$ axes, respectively. These angles are a convolution of rotations in the pseudocubic basis and must be disentangled to identify the octahedral rotation pattern in Glazer notation. However, in an alternating tilt pattern, the phase information about the rotation angle is scrambled and there are a number of possible configurations that correspond to a given set of extracted angles ξ' and γ'. A second piece of information that is therefore required, is the plane in which the cation displacements occur. In $Pbnm$ orthorhombic perovskites, to which bulk SRO belongs, A-site cation displacements occur in the plane perpendicular to the axis of the in-phase rotation [57]. While other lattice symmetries (e.g., monoclinic) resulting from expitaxial constraints are possible, we assume in the following that the structure is $Pbnm$ orthorhombic with minimal monoclinic distortions, the latter being accommodated by RP defects. The dark field images presented in Fig. 6.3b show that displacements are visible in the β plane and (virtually) absent in the α plane, which indicates that the in-phase axis lies in the latter. Furthermore, it is restricted to one of the three pseudocubic lattice axes; (100), (010) or (001). It is easily verified that only the latter lies in the α plane and can therefore be identified as the axis along which the in-phase rotation occurs[1]. From the STEM characterization, we find $\xi' \approx 3°$ and $\gamma' \approx 4°$, respectively. Using the approach outlined in section 6.6.1, we find a number of possible rotation angles that can correspond to this observation, namely either $(6°, 6°, 0°)$ or $(3°, 3°, 5°)$. In the $Pbnm$ structure, the out-of-phase rotations are equal

[1] In the case where the in-phase axis lies along the (100) or (010) direction, displacements of approximately equal magnitude are expected to be visible in both planes.

in magnitude, whereas the in-phase rotations differ [120]. Accordingly, the only two possible sets of $(a^- b^- c^+)$ rotation patterns are $(-6°, -6°, 0°)$ or $(-3°, -3°, 5°)$. Since the former should not produce any displacements due to the absence of in-phase rotation, we propose the latter as the rotational pattern of the films. We note that this implies that the in-phase rotation axis has a strong component along the $11\bar{2}$ axis, but no component along the $1\bar{1}0$ axis. For the 2 nm film, the angles ξ' and γ', as well as the cation displacements in the α plane (see the inset in Fig. 6.3b) are close to zero, indicating that in the ultrathin limit, the SRO films tend towards an unrotated structure[2]. The structural pattern of the thick film is visualized in Fig. 6.3c in the pseudocubic basis (top) and in the rotated basis (bottom).

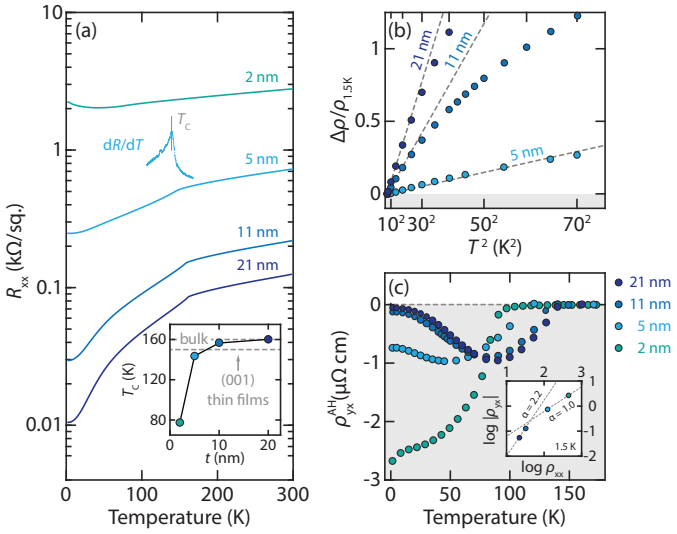

Figure 6.4: Longitudinal resistance and anomalous Hall amplitude. (a) Sheet resistance as a function of temperature for SRO (111) films of thicknesses t in the range 2 nm to 21 nm. The inset shows the Curie temperature T_C as a function of t, with the dashed lines indicating T_C for SRO (001) thin films and single-crystals from literature. (b) Relative resistance change as a function of the temperature squared. The dashed lines represent low temperature quadratic fits. (c) Anomalous Hall amplitude ρ_{yx}^{AH} as a function of temperature. The inset shows the relation between ρ_{yx}^{AH} and ρ_{xx} at 1.5 K, displayed on a logarithmic scale.

6.2. DIMENSIONAL CROSSOVER

Having determined the structural properties of the films, we proceed to investigate their electronic properties by means of transport measurements. Fig. 6.4a shows the resistance versus temperature characteristics of four SRO (111) films with thicknesses in the range 2 nm to 21 nm. With increasing thickness, we find progressively lower resistance, with the residual resistivity ratio (RRR) $\rho_{293K}/\rho_{1.5K}$ increasing from ~ 1.2 to ~ 12. These values are higher than typically reported for PLD-grown (001) and (111) oriented films [261,

[2] Possibly, rhombohedral distortions manifest near the interface due to the different unit cell volumes between SRO and STO.

262], but lower than recently reported values for machine-learning assisted MBE growth of (001) oriented SRO [263]. The upturn at low temperature observed for the 2 nm film has previously been linked to Efros-Shklovskii type variable-range hopping [262], which is associated with a Coulomb gap. This is in contrast to (001) ultrathin films, where the resistivity upturn has been attributed to Mott-type variable range hopping due to disorder [264]. As illustrated for the 5 nm sample, the Curie temperature T_C is extracted from the peak in the dR/dT. The extracted T_C are shown in the inset as a function of thickness. We find that both the 11 nm and 21 nm film exceed the T_C that is reported for SRO films grown on STO (001) of ~ 150 K, even those with much larger RRR values than reported here [65, 219, 263]. The 21 nm film is found to reach the bulk single-crystal T_C of ~ 160 K [68]. Recent works have reported an enhancement of $T_C \approx 168$ K for SRO thin films grown on tensile (110) $DyScO_3$ (DSO) substrates [265, 266], the origin of which is yet to be elucidated. The presence of a high-spin state in SRO (111) has been suggested [267, 268], however this interpretation was questioned by subsequent XMCD measurements [269].

In Fig. 6.4b, we show the relative change in resistivity as a function of T^2 for the 5 nm, 11 nm and 21 nm films. For the latter two we observe, similar to previous reports in (001) films [219, 265], a quadratic dependence of the resistivity with temperature for $T < 25$ K i.e., a Fermi liquid behavior. The 5 nm film also shows a good agreement with T^2 behaviour. However, we attribute this to the presence of a small upturn, seeing as the resistance saturates at slightly higher temperature compared to the two thickest films. This means that the quadratic behavior cannot be ascribed to Fermi liquid behavior, but is rather due to disorder. These observations are consistent with an increasing (effective) electron-electron repulsion strength, driving the system towards a correlated insulating state in the two-dimensional limit. Recently, confinement effects in (001) oriented films have been shown to experience orbital-selective confinement effects i.e., a primary involvement of the $d_{yz,zx}$ orbitals [162, 270]. In the monolayer limit, a non-magnetic incoherent d_{xy} band with a soft gap was observed [162]. For (111) oriented films, the d_{xy}, d_{yz} and d_{zx} orbitals are projected isometrically onto the film plane. Therefore, confinement of the crystal affects all orbitals nominally equally, which implies that it acts fundamentally differently for (111) oriented films.

Fig. 6.4c shows the anomalous Hall resistivity ρ_{yx}^{AH} as a function of temperature for the four films. We find that the AHE is always negative, with a progressively smaller low-temperature amplitude for increasing thickness. For the two thickest films, the curves are similar to reports of single crystals [65]. The curves nearly overlap, suggesting that their electronic structures are similar and that the anomalous Hall resistance R_{yx}^{AH} scales linearly with the thickness. In contrast, the two thinnest films show a different behaviour, with the anomalous Hall resistance no longer scaling linearly with the film thickness, suggestive of a thickness dependence of the electronic structure. This motivates to separate the four films into a 3D (bulk-like) and a quasi-2D regime, with the 2 nm and 5 nm films belonging to the latter and the 11 nm and 21 nm belonging to the former. The inset shows $|\rho_{yx}|$ at 1.5 K as a function of ρ_{xx} on a logarithmic scale. The dependence of the AHE on the longitudinal resistance can be modelled as

$$\rho_{yx}^{\mathrm{AH}} = a\rho_{xx} + b\rho_{xx}^{2}, \tag{6.1}$$

with the linear term representing the skew scattering contribution and the quadratic term representing both the side-jump and intrinsic mechanism [72]. Conventionally, one is then to assume the relation $\rho_{yx}^{\mathrm{AH}} \propto \rho_{xx}^{\alpha}$ and to fit the exponent. On a logarithmic scale, such a relation is linear with a slope α. However, we find a nonlinear behaviour, complicating such an analysis. Counterintuitively, for the 3D bulk-like films we find $\alpha = 2.2$, whereas for the quasi-2D films α is found to be 1.0. If skew scattering were to play a role, one would expect it to be more dominant for the thicker films, which have much lower residual resistivity.

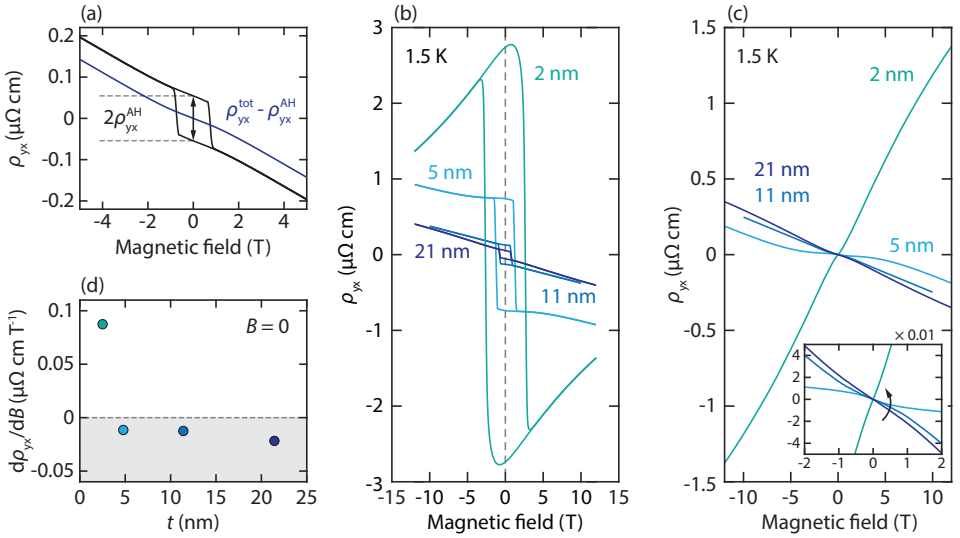

Figure 6.5: nonlinear classical Hall effect. (a) Total Hall effect of the 21 nm film at 1.5 K ρ_{yx}^{tot} and ρ_{yx} with the anomalous component ρ_{yx}^{AH} subtracted. (b) Total and (c) classical Hall effect at 1.5 K for the four different film thicknesses, with the inset in (c) showing an enlarged view of the low-field region. (d) Zero-field slope as a function of film thickness.

6.3. MULTI-BAND TRANSPORT

We proceed to study the electronic properties of the films via the Hall effect. Fig. 6.5a shows the Hall resistivity at 1.5 K for the 21 nm film. The anomalous component is immediately apparent from the sharp hysteresis loop. By considering the branches of the hysteresis loop where no magnetic switching occurs i.e., when the field is aligned with the magnetization, the anomalous component can be subtracted and the classical Hall component distilled from ρ_{yx}. We find that the classical Hall effect is nonlinear, in contrast to (001) oriented films, where typically a linear behaviour is observed for ultrathin films. Fig. 6.5b and 6.5c show the low-temperature total Hall effect and classical Hall effect for the four different thicknesses, respectively. The nonlinearity is found to become

more prominent as the film thickness is reduced. For the 2 nm film, the Hall effect is found to be fully positive up to the measurement limit, although a decrease in slope towards 12 T is observed. Considering the negative slopes of the other films at large fields, it is likely that an electron-like behaviour would be recovered for $B \gg 12$ T. Fig. 6.5c illustrates a transition of the low-field slope from negative to positive below 5 nm. To interpret this observation, we consider the two-band model for the ordinary Hall effect in the low-field limit [271]

$$\lim_{B\to 0} \frac{\mathrm{d}\rho_{yx}}{\mathrm{d}B} = \frac{1}{e} \frac{\pm n_I \mu_I^2 \pm n_{II} \mu_{II}^2}{\left(n_I \mu_I + n_{II} \mu_{II}\right)^2}, \tag{6.2}$$

where the subscripts I, II denote the respective channels, e is the elementary charge, n the carrier density and μ the mobility. The denominator is the square of the total conductivity of the two channels and the signs in the nominator depend on the carrier type of the individual channels, with a positive (negative) sign indicating hole-like (electron-like) carriers. From equation (6.2) it is clear that, to produce a positive low-field slope, one or both terms in the nominator is necessarily hole-like. The slope in the high-field limit is given by

$$\lim_{B\to \infty} \frac{\mathrm{d}\rho_{yx}}{\mathrm{d}B} = \frac{1}{e(\pm n_I \pm n_{II})}. \tag{6.3}$$

Considering the electron-like behaviour for the thicker films and the change in slope towards 12 T for the 2 nm film, one of the channels is likely to be electron-like ($n_I = -n_e$, $\mu_I = \mu_e$), implying that the second channel must be hole-like ($n_{II} = n_h$, $\mu_{II} = \mu_h$) and that $n_h \mu_h^2 > n_e \mu_e^2$. The electron-like behaviour at high fields means that $n_e > n_h$. Accordingly, the most likely scenario is that of a lower density higher mobility hole-like band and a higher density lower mobility electron-like band. This scenario also accounts for the shallower low-field slope of the thicker films[3]. Interestingly, with the exception of the 2 nm film, all samples show virtually identical low-field slopes. These observations are suggestive of a (quasi-)2D hole-like band, with possible replica bands crossing the Fermi energy as the film thickness is increased. In the 3D bulk-like regime, replica bands transition into a continuous spectrum for k_z. Their energy separation directly depends on the confinement i.e., the film thickness. In a simple particle-in-the-box picture, one finds that the number of replica bands intersecting the Fermi energy is of the order t/a, with t the film thickness and a the in-plane lattice constant (see section 6.6.3), which gives ~ 3 bands for the 2 nm film and ~ 8 bands for the 5 nm film.

For the two thickest films, we expect that k_z can be safely approximated as a continuous variable. Fig. 6.6a shows a two-band fit for the 21 nm film. We find a good agreement in the low-field region, whereas a slight deviation from linearity is observed towards 12 T. This suggests that caution should be taken from fitted parameters, particularly since without proper constraints, the problem is degenerate i.e., many choices of parameters can fit the same curve. Indeed, following the fitting procedure described in section 6.6.5,

[3] We note that the negative slope in thicker films means that $n_e \mu_e^2 > n_h \mu_h^2$.

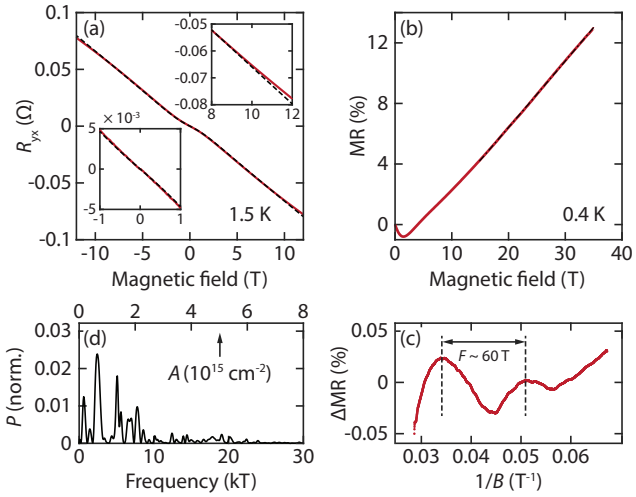

Figure 6.6: Shubnikov-de-Haas spectroscopy. (a) Hall resistance R_{yx} as a function of magnetic field at 0.4 K for the 21 nm film, with the insets showing enlarged views of the (top) high-field and (bottom) low-field regions. The dashed lines represent a two-band fit. (b) Longitudinal magnetoresistance with the current oriented along the $(11\bar{2})$ lattice axis and the magnetic field oriented out-of-plane. The dashed line represents a second-order polynomial fit. (c) Magnetoresistance as a function of the inverse magnetic field with the second-order polynomial background subtracted. Gaussian smoothening has been applied to filter out faster frequencies. (d) Shubnikov-de-Haas spectrum as a function of frequency. The top axis indicates the corresponding Fermi surface area.

the fit would point to a hole density of ~ 10^9 cm^{-2} with a mobility of ~ 4000 cm^2(Vs)$^{-1}$. For such low densities, the average spacing between quasiparticles is several thousand times larger than the Bohr radius and carriers are expected to condense into a Wigner crystal with effectively zero mobility [190, 272]. Accordingly these numbers can be considered unphysical and information about the band parameters must be gathered with other techniques. For this purpose, we perform low-temperature (~ 0.4 K) high-field magnetotransport measurements. Fig. 6.6b shows the longitudinal magnetoresistance measured up to 35 T. The unsaturating linear behavior will be the subject of the next section, while here we focus on the Shubnikov-de-Haas effect. Fig. 6.6c shows the MR as a function of inverse field, after subtracting a second-order polynomial background and subsequently filtering out fast oscillations. We find a sinusoidal behavior with a frequency of ~ 60 T, corresponding to a Fermi surface area of $A \approx 3 \times 10^{12}$ cm^{-2}. For such quantum oscillations to manifest, one must have $\mu B_s > 1$ [273], which provides a lower bound estimate for the mobility $\mu > 1/B_s \approx 600$ cm^2(Vs)$^{-1}$. As we show in section 6.6.5, this number agrees well with the mobility estimated from the two-band model, provided one incorporates the density obtained from the SdH spectroscopy. However, from Fig. 6.6d, we find that the Fermi surface exhibits many more than just two contributions and more refined electronic structure calculations will be required to fully elucidate the transport properties. Nevertheless, as we shall discuss in the next section, the behavior of the magnetoresistance for the two thickest films might be explained semiclassically.

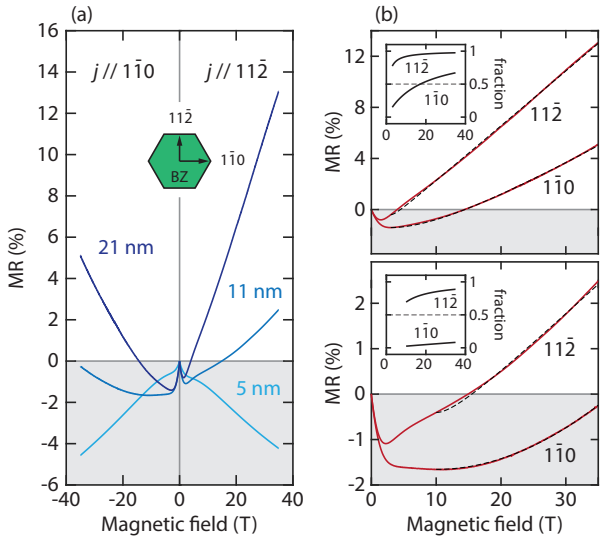

Figure 6.7: High-field transport. (a) Longitudinal magnetoresistance as a function of out-of-plane magnetic field with the current oriented along the (left) $1\bar{1}0$ and (right) $11\bar{2}$ directions at 0.4 K. (b) Parallel resistor model fits to the data of (a) for the (top) 21 nm and (bottom) 11 nm films. The solid and dashed lines represent the data and fits, respectively. The insets show the resulting current fractions of the linear term as a function of magnetic field.

6.4. GUIDING CENTER MOTION MAGNETORESISTANCE

Fig. 6.7a shows the magnetoresistance (MR) measured along the $1\bar{1}0$ and $11\bar{2}$ lattice axes as a function of out-of-plane magnetic field. With increasing thickness we find for both current directions a transition from a negative to a positive magnetoresistance, similar to prior reports on (001) films [219, 263]. A negative magnetoresistance is a common observation in ferromagnets and is conventionally ascribed to either a suppression of spin-dependent scattering events with increasing field [274–276] or more recently to Berry curvature-dependent collision events [277]. An unsaturating positive linear magnetoresistance on the other hand, can have multiple origins, of which two are potentially relevant for the system under study[4]; (i) the quantum magnetoresistance, which has a linear B dependence [278] and (ii) guiding center motion magnetoresistance (GCM MR), which has linear and quadratic contributions, depending on whether for the involved carriers $k_z < k_z^*$ (linear) or $k_z > k_z^*$ (quadratic), with k_z^* determined by the disorder potential landscape of the system [279]. We simulate this by a simple model consisting of two parallel resistors $R_1 = \alpha B$ and $R_2 = \beta B^2$ (see section 6.6.4). The fits for the 21 nm and 11 nm films are shown in the top and bottom panels of Fig. 6.7b, respectively, with the insets showing the extracted current fraction for the linear channel. This mechanism is valid if carriers have a finite k_z and for $B > B_t = m^* v_F/(e\xi)$, with ξ the disorder correlation length. For bulk SRO, we have $m^* \approx 5m_0$ and $v_F \sim 10^5$ m/s [179, 280, 281]. We approximate ξ as the averaged distance between defects, which gives ξ on the order of a

[4]The classical magnetoresistance can also be relevant, but leads only to either a quadratic or saturated MR.

few nm, for c_i anywhere between 10^{-1} and 10^{-3}. Then $B_t \sim 500\,\mathrm{T}$, indicating that guiding center motion is irrelevant for the main Fermi surface. However for the low-density band (estimating $m^* \sim m_0$), we find $B_t \sim 10\,\mathrm{T}$, in good agreement with the experimental data. For the thinner films, we expect that the combination of a quenched k_z and more disorder near the interfaces renders the fields required to observe the GCM MR too large. Its magnitude can be can be estimated as [279]

$$\mathrm{MR} = \frac{\rho_{xx}(B) - \rho_{xx}(0)}{\rho_{xx}(0)} \approx \mu B \mathscr{G}, \tag{6.4}$$

with μ the mobility, B the magnetic field and $\mathscr{G}$ given by

$$\mathscr{G} = \tan\theta_H / \left(1 + \tan^2\theta_H\right), \tag{6.5}$$

with θ_H the Hall angle ρ_{yx}/ρ_{xx}. From Fig. 6.5c, we estimate for the 21 nm film through extrapolation $\rho_{xy}(35T) \approx 1.2\,\mu\Omega\mathrm{cm}$, which for $\rho_{xx} \approx 25\,\mu\Omega\mathrm{cm}$ gives $\tan\theta_H \approx \mathscr{G} \approx 0.05$. With the estimated mobility $\mu \approx 600\,\mathrm{cm}^2/\mathrm{Vs}$, equation (6.4) returns MR(35 T) ≈ 10%, in good agreement with Fig. 6.7. While these estimates are rough, they suggest that the experimentally observed data has the correct order of magnitude for GCM MR to be present. Note that, since magnetoresistance effects in SRO are otherwise small, even a moderate GCM MR may be observable.

Finally, we note that mechanism (i) might also be relevant, which can occur when a small pocket in an otherwise large Fermi surface occupies the lowest Landau level [278]. In a Drude picture, the necessary conditions [282] can be formulated as $ne\rho/B \ll c_i \ll 1$. For $B \sim 10\,\mathrm{T}$, $\rho = 10\,\Omega/\mathrm{sq.}$ and $c_i \sim 10^{-2}$, this condition is satisfied for $n \ll 10^{13}\,\mathrm{cm}^{-2}$, in line with the condition for the linear MR due to GCM[5].

6.5. CONCLUSIONS

In summary, we have shown that SRO thin films grown on STO (111) substrates are coherently and compressively strained with the in-phase octahedral rotation axis along the (001) pseudocubic lattice axis. Transport measurements suggest that the electronic structure exhibits a dimensional crossover below ∼ 5 nm, which occurs simultaneously with a reduction of the Curie temperature. Films of all thicknesses in the range 2 nm to 21 nm exhibit a nonlinear classical Hall effect, with the most prominent nonlinear behaviour observed in the thinnest films. While the two-band Hall effect model was found to fall short in describing the complex Fermi surface, high-field Shubnikov-de-Haas measurements on the thickest film identified a low-density pocket with mobility $\sim 600\,\mathrm{cm}^2(\mathrm{Vs})^{-1}$. We attribute the concurrently observed linear unsaturating positive MR to guiding-center motion magnetoresistance, arising from the combination of sufficiently high fields and mobility. We expect that electronic structure calculations will elucidate the dimensional crossover and potentially to reveal the band responsible for the high-mobility transport observed.

[5] For a three dimensional band, the estimate yields $n \ll 10^{18}\,\mathrm{cm}^{-3}$

6.6. SUPPLEMENTARY INFORMATION

6.6.1. CHANGE OF BASIS FOR ROTATION ANGLES

We let

$$\hat{z}' = \frac{1}{\sqrt{3}}\begin{pmatrix}1\\1\\1\end{pmatrix}, \quad \hat{y}' = \frac{1}{\sqrt{6}}\begin{pmatrix}1\\1\\-2\end{pmatrix} \quad \text{and} \quad \hat{x}' = \frac{1}{\sqrt{2}}\begin{pmatrix}1\\-1\\0\end{pmatrix} \tag{6.6}$$

denote the basis vectors in the rotated coordinate system. The vectors $(\hat{x}', \hat{y}', \hat{z}')$ map to $(\hat{x}, \hat{y}, \hat{z})$ via subsequent $\xi = \arccos(1/\sqrt{3})$ and $\phi = \pi/4$ rotations about the x- and z-axes, respectively, denoted by $\hat{R} = \hat{R}_z^{\phi}\hat{R}_x^{\xi}$. In matrix form, this is expressed as

$$\hat{R} = \begin{pmatrix}\cos\phi & \cos\xi\sin\phi & \sin\phi\sin\xi\\ -\sin\phi & \cos\phi\cos\xi & \cos\phi\sin\xi\\ 0 & -\sin\xi & \cos\xi\end{pmatrix}. \tag{6.7}$$

We consider a vector $\mathbf{r}'$ with $|\mathbf{r}'| = 1$ and of which the rotations about the x'-and y' axes ξ' and γ', respectively, are known. We choose vectors parallel to the z' axis to have $\gamma' = 0$ and $\xi' = 0$, respectively and define anticlockwise rotations to be positive. Then we have the following set of equations;

$$\tan\phi' = -\cot\gamma'\tan\xi', \tag{6.8a}$$

$$\tan\theta' = \frac{\cos\gamma'}{|\cos\gamma'|}\sqrt{\tan^2\gamma' + \tan^2\xi'}, \tag{6.8b}$$

where θ' and ϕ' are the polar and azimuthal angles, respectively, in spherical coordinates. This convention requires $\gamma' \neq 0$ and $\xi' \neq \pi/2$. The vector $\mathbf{r}'$ can now be expressed as

$$\mathbf{r}' = \begin{pmatrix}\cos\phi'\sin\theta'\\ \sin\phi'\sin\theta'\\ \cos\theta'\end{pmatrix} \tag{6.9}$$

and $\mathbf{r} = (r_x, r_y, r_z)$ can be computed via $\mathbf{r} = \hat{R}\mathbf{r}'$. Its rotation angles in the reference basis (x, y, z) are finally given by

$$\xi = \arctan\left(\frac{r_y}{r_z}\right) \tag{6.10a}$$

$$\gamma = \arctan\left(\frac{r_x}{r_z}\right) \tag{6.10b}$$

$$\phi = \arctan\left(\frac{r_y}{r_x}\right). \tag{6.10c}$$

The resulting angles are shown in Fig. 6.8.

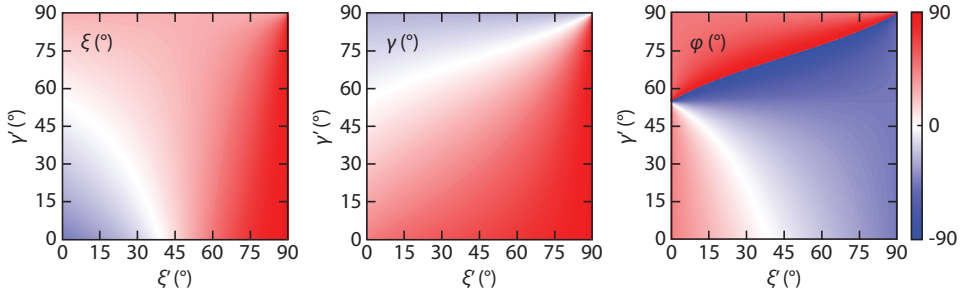

Figure 6.8: Rotation angles. Rotation angles in the pseudocubic basis about the x and y axes ξ, γ and ϕ, respectively, as a function of rotation angles in the rotated basis ξ' and γ'.

6.6.2. SHEAR STRAIN

Fig. 6.9a shows a dark field image of a 11 nm film exhibiting a Ruddlesden-Popper defect. In the vicinity of the defect, we find that the atomic positions are aberrated, arising from atomic dislocations. $PbTiO_3$ (PTO) films grown on STO (111) substrates have previously been demonstrated to exhibit significant monoclinic shearing, resulting from the three-dimensional character of the strain exerted by the substrate [259]. From Figs. 6.9b-c, it is clear that no evidence of shearing is observed in our films. This is further substantiated in Fig. 6.9d, which shows that the angle ξ between adjacent cation sites is constant throughout the film. While STEM analysis is not sensitive enough to fully rule out monoclinic distortions to the unit cell, we can conclude that they are significantly smaller compared to what is reported in ref. [259] and likely subtle at best. The symmetry discrepancy between PTO and SRO grown on STO (111) may be attributed to the closer lattice matching between SRO and STO, as compared to PTO and STO, as well as the previously discussed defects contributing to strain accommodation. Accordingly, we propose that the SRO films retain a $Pbnm$ octahedral rotation pattern, with ultrathin films tending towards an unrotated structure.

6.6.3. HOLE IN A BOX

A two-dimensional (hole-like) quasiparticle subject to confinement can be described by

$$E_n(k) = -\epsilon_n(t) - \frac{\hbar^2 k^2}{2m}, \tag{6.11}$$

where $\epsilon_n(t)$ is the energy at the top of each replica band that depends on the confinement width t, m is the effective mass and n the band index. If we assume the lowest band ($n = 0$) to be occupied with a fraction η and set $\epsilon_0 = 0$, we have $k_F = \eta\pi/a$, and $E_F = \eta^2\pi^2\hbar^2/2ma^2$. The number of states per area for a spin-degenerate two-dimensional system is $N(k) \approx k^2/2\pi$, implementation of which gives

$$N_n = \frac{\pi\eta^2}{2a^2} - \frac{m}{\pi\hbar^2}\epsilon_n(t), \tag{6.12}$$

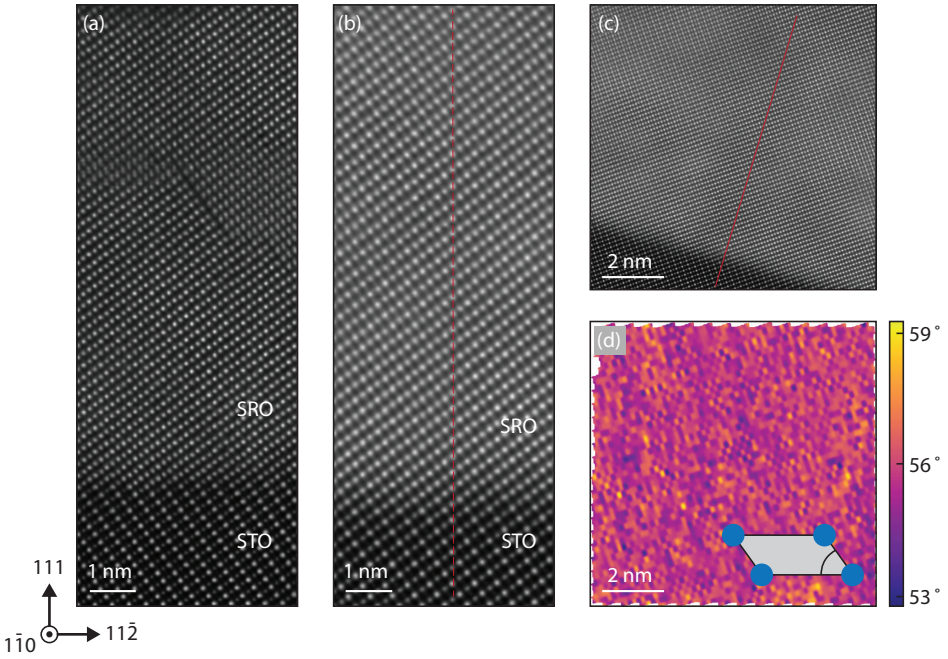

Figure 6.9: Absence of monoclinic shearing. HAADF-STEM images of (a) a 11 nm film and (b-c) a 21 nm film. The red lines illustrate the alignment of atomic columns along the (111) crystallographic orientation. (d) Spatial profile of the angle ξ between adjacent cation sites, extracted from the image in (c).

with N_n the number of states per area at the Fermi energy for each band n. For the particle-in-a-box scenario, we have

$$\epsilon_n = \frac{n^2\pi^2\hbar^2}{2mt^2}, \tag{6.13}$$

such that

$$N_n = \frac{\pi}{2}\left(\frac{\eta^2}{a^2} - \frac{n^2}{t^2}\right). \tag{6.14}$$

To determine the number of bands intersecting the Fermi energy, we look for the highest n that satisfies $N_n \neq 0$, which gives $n \approx 1 + \eta t/a$. The in-plane lattice parameter of SRO (111) thin films is ~ 0.6 nm. For a half filled lowest band $\eta \sim 0.5$ and a confinement width of ~ 2 nm, this simple model predicts 2-3 bands to intersect the Fermi energy, with higher order replica bands having a progressively smaller carrier density.

6.6.4. PARALLEL RESISTOR MODEL

We consider a simple circuit with a field-independent resistor R_0 in series with two parallel field-dependent resistors $R_1 = \alpha\tilde{B}$ and $R_2 = \beta\tilde{B}^2$, with $\tilde{B} = B - B_t$ and B_t a threshold

field beyond which the linear and quadratic contributions dominate the field-dependence of the resistivity. Then the magnetoresistance is given by R_{12}/R_0, with

$$R_{12} = \frac{R_1 R_2}{R_1 + R_2} = \frac{\alpha\beta\tilde{B}^2}{\alpha + \beta\tilde{B}}. \tag{6.15}$$

The relative current fractions passing through the two resistors R_1 and R_2 are given by

$$\eta_1 = \frac{\beta\tilde{B}}{\alpha + \beta\tilde{B}} \tag{6.16a}$$

$$\eta_2 = \frac{\alpha}{\alpha + \beta\tilde{B}}, \tag{6.16b}$$

such that $\eta_1 + \eta_2 = 1$. Fitting the magnetoresistance data to (6.15) then permits quantification of the current fractions (for $B > B_t$). According to expectation, the quadratic term dominates for low fields whereas the linear term dominates for high fields. The field where the current fractions are equal is $B_t + \alpha/\beta$.

6.6.5. ESTIMATING THE MOBILITY

For an electron- and a hole-like band, the two-band model for the Hall effect is given by

$$R_{yx} = \frac{-n_e\mu_e^2 + n_h\mu_h^2 + n\left(\mu_e\mu_h B\right)^2}{\left(n_e\mu_e + n_h\mu_h\right)^2 + \left(n\mu_e\mu_h B\right)^2}\frac{B}{e} \tag{6.17}$$

with n_e, n_h, the electron and hole sheet carrier densities, $n = n_h - n_e$ the total sheet carrier density and μ_e, μ_h the electron and hole mobilities. In the high-field limit, this reduces to

$$\lim_{B\to\infty} R_{yx} = \frac{B}{ne} = hB, \tag{6.18}$$

with h the high-field slope given by $h = 1/ne$. In the low-field limit, we obtain

$$\lim_{B\to 0} R_{yx} = \frac{-n_e\mu_e^2 + n_h\mu_h^2}{\left(n_e\mu_e + n_h\mu_h\right)^2}\frac{B}{e} \tag{6.19}$$

$$= lB. \tag{6.20}$$

Defining $\sigma_0 = e\left(n_e\mu_e + n_h\mu_h\right)$ and $\theta = \left(\mu_e\mu_h/\sigma_0\right)^2$, we can rewrite (6.17) as

$$R_{yx} = \frac{l + \frac{\theta}{h}B^2}{1 + \frac{\theta}{h^2}B^2}B. \tag{6.21}$$

We further approximate $n_e \gg n_h$ and $n_e\mu_e \gg n_h\mu_h$, such that we can write

$$l \approx \frac{1}{e}\frac{-n_e\mu_e^2 + n_h\mu_h^2}{n_e^2\mu_e^2} \tag{6.22}$$

$$\approx h\left(1 - \frac{n_h}{n_e}\frac{\mu_h^2}{\mu_e^2}\right) \tag{6.23}$$

and

$$\mu_h \approx \mu_e\sqrt{\frac{n_e}{n_h}\left(1 - \frac{l}{h}\right)}, \tag{6.24}$$

which boils down to $n_h\mu_h^2 \sim n_e\mu_e^2$ i.e., if two bands are observable in the classical Hall effect, the product of their densities and squared mobilities is of the same order. From the fit shown for the 21 nm film in Fig. 6.6a, we obtain $l/h = 0.643$ and $n_e \approx -1/(eh) = 9.3\times10^{16}\,\mathrm{cm}^{-2}$. From the low-temperature sheet resistance (Fig. 6.4a), we estimate $\mu_e \approx 1/(n_e e R_0) = 6\,\mathrm{cm}^2(\mathrm{Vs})^{-1}$ and from Fig. 6.6c we find $n_h \approx 3\times10^{12}\,\mathrm{cm}^{-2}$. Implementing these numbers in equation (6.24) gives $\mu_h \approx 620\,\mathrm{cm}^2(\mathrm{Vs})^{-1}$. To observe quantum oscillations, one requires [273] $\omega_c\tau = \mu B > 1$. For the extracted μ_h, we find $B > 16\,\mathrm{T}$, in good agreement with the oscillation observed in Fig. 6.6c. However, the θ extracted from the fit in Fig. 6.6 predicts a lower sheet density $n_h \sim 10^9\,\mathrm{cm}^{-2}$ and a higher mobility $\sim 4000\,\mathrm{cm}^2(\mathrm{Vs})^{-1}$. As discussed in section 6.3, such a low density is expected to result in a localization of carriers through condensation into a Wigner crystal (with effectively zero mobility). We suggest these numbers to be an artefact resulting from the inability of the two-band model to accurately describe the complex Fermi surface.

6.6.6. TEMPERATURE-DEPENDENT MAGNETOTRANSPORT

The temperature dependence of the magnetoresistance and classical Hall effect are shown in Fig. 6.10. The MR only shows a positive behavior at the lowest temperature (1.5 K) and transitions to negative for $T > 10\,\mathrm{K}$. This can be understood as the thermal energy exceeding the cyclotron resonance energy i.e., $k_B T > \hbar\omega$ and a reduction of the mobility below the threshold value. As a result, the criteria for observing the guiding center motion magnetoresistance are no longer fulfilled. In the Hall effect, we find that the low-field slope becomes progressively more strongly positive with increasing temperature. This may be explained by the hole-like band increasing its carrier density through thermal occupation and/or the magnetization shifting bands and increasing its Fermi surface.

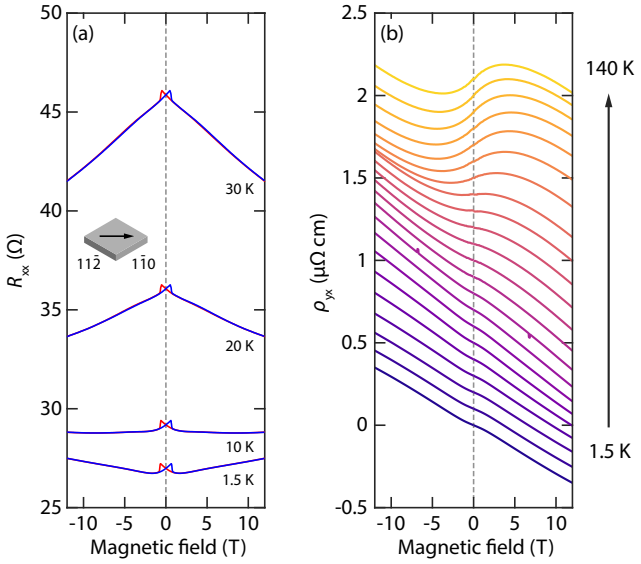

Figure 6.10: Temperature dependence. (a) Longitudinal resistance R_{xx} and (b) classical Hall effect R_{yx} of the 21 nm sample as a function of magnetic field for various temperatures ranging from 1.5 K to 140 K, measured along the diagonal of the sample plane ($10\bar{1}$ axis).

7

Conclusions and perspectives

“One never notices what has been done; one can only see what remains to be done."

– Marie Curie

This chapter concludes the findings of this thesis and provides a brief outlook for promising future directions to explore.

HETEROSTRUCTURES of transition-metal oxides have been and continue to be an exciting platform for realizing novel physical phenomena. Arguably, this field started with the discovery of a high-mobility electron gas at the LAO/STO interface [7], which could be considered one of the canonical examples of emergent phenomena in the field of complex oxides. Since then, interface engineering has become an indispensable member of the 'complex oxide toolbox'. Throughout this thesis, we have utilized this toolbox to try and uncover how interfaces affect structural, electronic and magnetic properties in terms of crystal symmetry, charge states and topologically protected quantities.

In Chapter 3, we demonstrated that the cubic-tetragonal transition of $SrTiO_3$ couples to the orthorhombic domains of spin-orbit semimetal $SrIrO_3$. In the vicinity of the $SrIrO_3$ metal-to-insulator transition, the crystal anisotropy was found to produce anisotropic transport properties. This, in turn, was found to cause an anomaly in the temperature dependence of the resistivity, which we attributed to a reorientation of the current paths resulting from the adaptation of orthorhombic domains in the film to the tetragonal domains in the substrate. Since the $Pbnm$ structure is common among perovskite oxides, we expect that such a coupling of domains is not limited to the iridates, but can manifest in a wide variety of orthorhombic oxides, such as nickelates, manganites, ruthenates and ferrites. This provides numerous potential opportunities to manipulate electronic and magnetic properties through interaction with a tetragonal substrate.

In Chapter 4, we analyzed the electronic structure of the itinerant ferromagnet $SrRuO_3$ in the ultrathin limit, revealing a set of topological bands as the source of the anomalous Hall effect. We subsequently showed that in symmetrically sandwiched heterostructures, the sign of the anomalous Hall effect can be controlled by interfacing $SrRuO_3$ with $SrIrO_3$ and $SrTiO_3$. In asymmetric heterostructures, the magnetic field dependence of the AHE was found to be well described by a phenomenological two-channel model and could be mimicked by ultrathin $SrRuO_3$ bilayers, separated by a $SrTiO_3$ spacer. Then, in Chapter 5, we created a polar discontinuity in $LaAlO_3/SrRuO_3$ heterostructures, inducing a magnetic and electronic reconstruction, as well as a breaking of inversion symmetry along the growth direction. We subsequently showed that this reconstruction leads to a reorganization of the two-dimensional topological charges in the Brillouin zone and concurrently a reversal of the sign of the momentum-space Berry curvature. These results have helped to understand the topological and global magnetic properties of ultrathin $SrRuO_3$, but there is still much to uncover about the microscopic features of the magnetic state. To this end, spatially-resolved measurements of the magnetization, such as magnetic force microscopy, scanning SQUID microscopy or diamond nitrogen-vacancy center magnetometry are invaluable.

In Chapter 6, we investigated the role of crystal symmetry on the properties of $SrRuO_3$, by studying the thickness-dependent properties of (111) oriented $SrRuO_3$ thin films. Structural analysis revealed more prominent octahedral rotations for thicker films as compared to thinner films, with the in-phase rotation axis along the (001) pseudocubic crystal orientation. We also found that, in contrast to (001) oriented films, the ordinary Hall effect is nonlinear and indicates the presence of a hole-like band. High-field

magnetotransport measurements showed evidence of highly mobile carriers and a linear unsaturating positive magnetoresistance, which we attributed to guiding center motion. To fully elucidate the origin of the observed transport features and shed light on which symmetries, or the lack thereof, are responsible for the multi-band transport, electronic structure calculations will be required.

In the final few paragraphs, we will discuss a number of ongoing and future research directions, which we expect will further improve our grasp of the interplay between symmetry breaking, topology and correlation effects in oxide heterostructures.

7.1. CORRELATED MAGNETISM AND CURRENT FLOW IN SRO

Transport characterization of large devices is a widely used and efficient method to determine material properties at the macroscopic scale. However, its strength is simultaneously its weakness; microscopic features tend to go unnoticed due to spatial averaging over large areas. Therefore, spatially resolved techniques are essential to obtain a more complete picture of the features of complex condensed matter systems. An example of such a technique is scanning SQUID microscopy, which utilizes a superconducting ring with two Josephson junctions to sense extremely subtle magnetic fields [125]. Such fields may originate either from current flow [103, 283], or from the magnetization of magnetically ordered materials [284, 285].

Fig. 7.1 shows scanning SQUID images of an ultrathin SRO film, with both STO and LAO capping layers. Spatial information of the magnetization reversal is obtained by first traversing the hysteresis loop at a temperature just below the Curie temperature T_C and subsequently fixing the magnetic field while cooling to base temperature. Finally, the external field is removed and the magnetic flux emanating from the sample is recorded in a scanning fashion. During the magnetization reversal, the SRO thin film is found to form large stripe domains, sized up to hundreds of µm (see Fig. 7.1a). In contrast, zero-field cooling leads to a random domain pattern. In thick SRO films, stripe domains were reported to be spaced several hundreds of nm [286], which falls below the spatial resolution of the scanning SQUID technique ($\sim 1\,\mu$m) and are therefore distinct from the stripes observed here. We also find that the current flow is modulated over the magnetic domains, which points to a magnetization-dependent resistivity or possibly to a role of the domain walls [287]. A similar phenomenology is observed in the LAO-capped sample (see Fig. 7.1b), even though the magnetic domains during the reversal are found to be less ordered. An comparable magnetization reversal pattern has been observed in SRO/SIO heterostructures [37].

Whether the shape of the domains is related to the shape of the device (mm sized Hall bars in this case) or whether they couple to STO structural domains, as illustrated for SIO in Chapter 3, will require further investigation. We anticipate that spatial imaging of the magnetization reversal dynamics in ultrathin SRO will be essential to fully elucidate the intriguing magnetic properties of ultrathin SRO-based heterostructures.

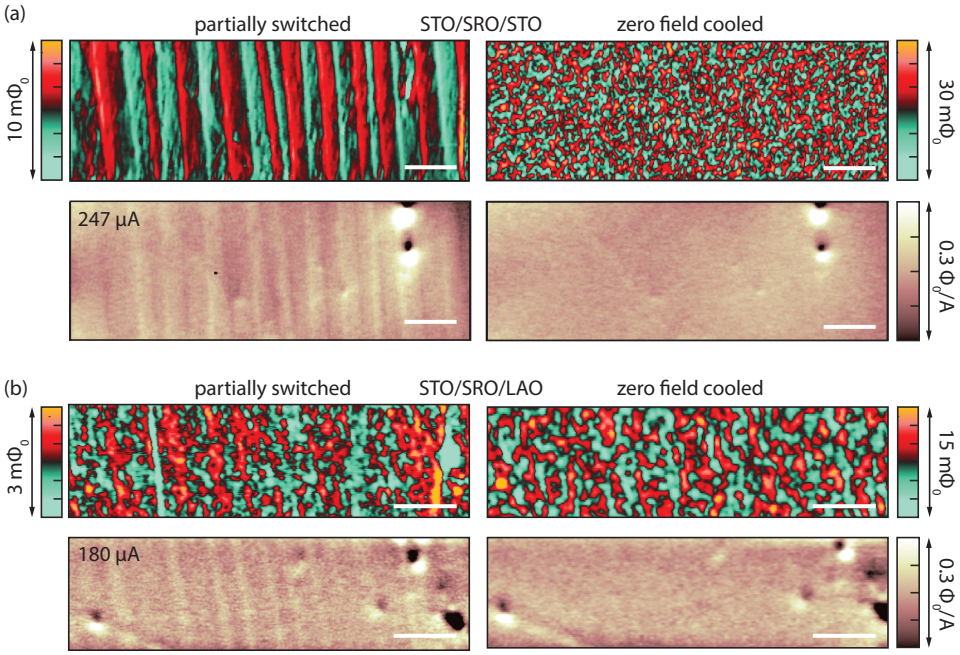

Figure 7.1: Magnetic domains in ultrathin SRO. (a, top) Spatially-resolved magnetic flux and (bottom) current flow of a 4 u.c. SRO sample with a 10 u.c. STO capping, imaged by scanning SQUID. The left and right panels compare a partially switched and zero field cooled magnetization. (b) The same measurements as in (a), but for a 4 u.c. SRO sample with a 10 u.c. LAO capping. The scale bars denote 20μm. Scanning SQUID measurements were performed by A. Sirohi, S. Weitz Sobelman and B. Kalisky.

7

7.2. POLAR IRIDATE HETEROSTRUCTURES

In Chapter 5, we considered the effects of a polar discontinuity on the magnetic and topological properties of ultrathin SRO. Due to the structural similarity between SRO and SIO, one would expect similar electronic reconstructions to manifest when SIO is interfaced with LAO. Whereas the perovskite $LaRuO_3$ can and has been synthesized [232], synthesis of $LaIrO_3$ has thus far been elusive. In case of a simple rigid Fermi level shift, full substitution of Sr^{2+} by La^{3+} should result in a band insulator, with the gap determined by the crystal field splitting, similar to $LaRhO_3$ [288, 289]. On the other hand, dilute La^{3+} doping of the layered perovskites Sr_2RuO_4 and Sr_2IrO_4 has been investigated theoretically and experimentally. Efforts to induce charge doping in Sr_2IrO_4 have been motivated by theoretical predictions of unconventional superconductivity [290, 291], of which hints were observed by scanning tunneling microscopy [292]. Importantly, electron doping has been reported to induce conductive behaviour in otherwise insulating Sr_2IrO_4 [293–295]. In contrast, La-doping in Sr_2RuO_4 has been shown to produce a rigid Fermi level shift and a suppression of superconductivity [242, 296]. Needless to say, altering charge states in oxides is a potent method for manipulating electronic properties in oxides and its extension to spin-orbit semimetal $SrIrO_3$ is an interesting avenue to consider.

To test the impact of a possible polar discontinuity on spin-orbit semimetal SIO, we synthesized SIO ultrathin films with 10 u.c. LAO and STO capping layers. The SIO films were grown at $T = 600\,°C$ in $p_{O_2} = 0.1\,mbar$, with a laser fluence $F = 1\,J/cm^2$. The LAO and STO capping layers were both grown at the same temperature in an oxygen pressure $p_{O_2} = 6 \times 10^{-5}\,mbar$.

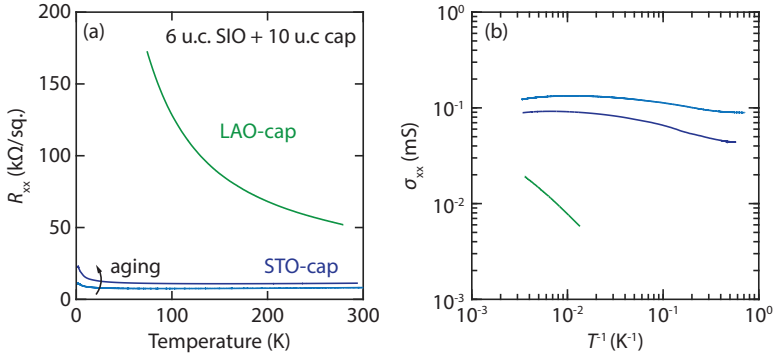

Figure 7.2: LAO/SIO and STO/SIO heterostructures. (a) Sheet resistance as a function of temperature for STO- and LAO-capped (10 u.c.) SIO thin films (6 u.c.) grown in identical conditions. (b) Sheet conductance as a function of inverse temperature on a logarithmic scale. The two curves for the STO-capped sample were measured 5 months apart. Sample growth and measurements were performed in collaboration with U. Filippozzi.

In Fig. 7.2, we show the sheet resistance and conductance of the two films. The STO-capped sample is found to be semimetallic, whereas the LAO-capped sample is insulating. In spite of the protective layer, we find evidence of aging effects, with the sheet resistance increasing slightly over a period of several months. The discrepancy in electronic properties are immediately evident. Since the carrier density of SIO is approximately two orders of magnitudes smaller than SRO [51], one would expect a more pronounced impact from possible polar fields on the transport properties. Electron doping via electrostatic gating and oxygen vacancy generation has previously been shown to increase resistivity which, in conjunction with thermoelectric measurements, pointed towards hole-dominated transport [51]. Further taking into account that La doping promotes a fully filled $J_{\text{eff}} = 1/2$ band, the observed insulating behaviour is not entirely unexpected. It is not directly evident what behavior may be anticipated in case of more dilute doping. In the case of a rigid Fermi level shift, the electronic structure considered in Chapter 3 would predict a depopulation of the hole-like pockets in favour of more electron-like transport. However, such a simple picture does not take into account any modifications to the band structure that may arise from the increased electron density (e.g., enhanced Coulomb repulsion) or inversion (mirror) symmetry breaking, which has been proposed to realise either a topological or band insulating state [61]. Further, SIO is known to be chemically active [297, 298], susceptible to disorder [62] and as discussed in Chapter 3, sensitive to structural distortions. Therefore, careful study of the electronic, structural and magnetic features of these heterostructures will be required to disentangle contributions arising from chemical activity, charge doping and structural distortions.

7.3. BERRY CURVATURE IN TIME-REVERSAL INVARIANT OXIDES

A large portion of this thesis has focused on the perovskite $SrRuO_3$, which due to its itinerant ferromagnetic ground state exhibits broken time-reversal invariance. As discussed in section 1.4, this permits a nonzero net Berry curvature when integrating over all occupied states in the Brillouin zone, with the anomalous Hall effect as a consequence. The anomalous Hall effect is therefore a manifestation of a net 'Berry charge' in momentum space, which can loosely be referred to as a first-order moment. However, higher order moments of the Berry curvature may be present, even if time-reversal invariance is preserved. The second-order moment is the Berry curvature dipole (BCD), which in two dimensions is given by [255]

$$D_j = \int_k f_0\left(\nabla_j \Omega_z\right), \tag{7.1}$$

with ∇_j denoting partial differentiation with respect to the (momentum-space) coordinate j and f_0 the Fermi-Dirac distribution. The dipole has a net zero Berry charge and arises from Berry curvature hotspots with opposite signs at different locations in the Brillouin zone. Importantly, in contrast to the anomalous Hall effect, the response to current is nonlinear and leads to additional contributions in transport i.e., higher harmonic generation and rectification which, aside from fundamental interest, have direct applications in photon detection [256]. In the presence of magnetic fields, BCDs produce the so-called quantum nonlinear Hall effect [299].BCDs have been recently reported in Weyl semimetal WTe_2 [253, 254, 300], but have so far remained elusive in oxides.

A necessary ingredient for BCDs to emerge in two-dimensional electronic structures is the presence of precisely one mirror symmetry line of the crystal. Such a situation can be realized at the LAO/STO (111) interface which, alike its (001) counterpart, hosts a superconducting two-dimensional electron system [301]. A sketch of the Fermi surface is shown in Fig. 7.3a; the trigonal crystal field splitting produces two sets of bands at different energies [302, 303]. In combination with the Rashba spin-orbit coupling resulting from the inversion symmetry breaking, this leads to a trigonal warping effect, which produces a spin texture characterized by meron and anti-meron wedges with out-of-plane components (see Figs. 7.3a-b). The system has a threefold rotational symmetry, which leads to the presence of three dipole moments that precisely cancel one another. For a single dipole to manifest, the symmetry of either the spin texture, or the crystal itself must be reduced [255]. The former may be accomplished by applying an in-plane magnetic field, whereas the latter may be realized by electric fields in the low-temperature quantum paraelectric phase of STO [304]. We therefore propose that the LAO/STO (111) system in the presence of magnetic or electric fields is a strong candidate to host a BCD and the concomitant quantum nonlinear Hall effect.

A new system that has recently emerged is the KTO (111) surface, which upon doping by e.g., a-EuO or a-LAO overlayers (see Fig. 7.3c) hosts a two-dimensional superconducting state with a critical temperature of ~ 2 K [248]. Being a $5d$ element, Ta exhibits a large atomic spin-orbit coupling. In combination with the symmetry-breaking occurring near

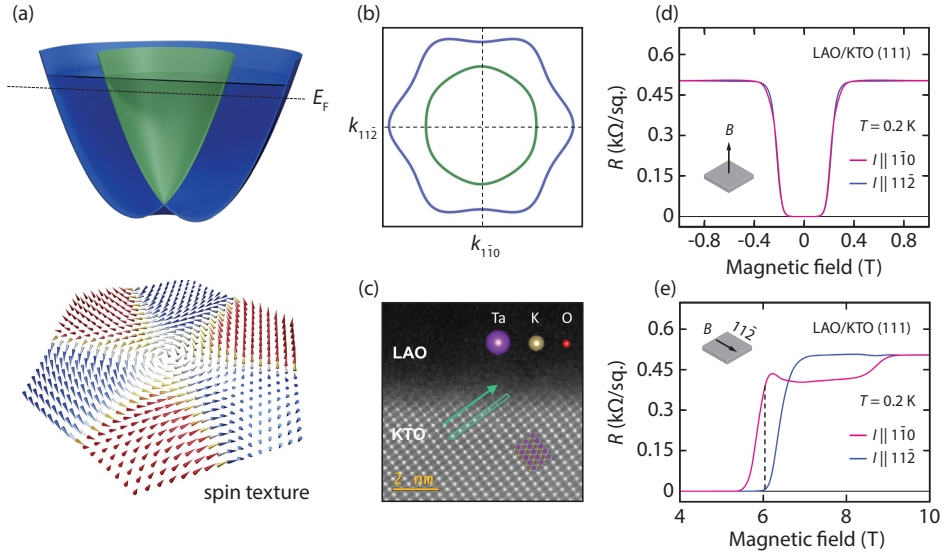

Figure 7.3: Berry curvature dipoles. (a) Visualization of the two-dimensional electronic band structure of trigonal LAO/STO (111). (b) Fermi surface of the trigonally warped electronic structure. (c) HAADF-STEM image of a (111) a-LAO/KTO heterostructure. Sheet resistance of LAO/KTO (111) as a function of (d) out-of-plane and (e) in-plane magnetic field. Panels (a-b) produced by R. Battilomo and C. Ortix. Panels (c-e) adapted from ref. [248].

surfaces and interfaces, this is expected to produce prominent Rashba spin-orbit effects. Interestingly, the superconducting state has been reported to exhibit a strong in-plane anisotropy (see Figs. 7.3d-e) due to nematic order and broken rotational symmetry [248]. These properties render the KTO (111) system a unique platform to study the interplay between superconductivity, spin-orbit coupling and momentum-space Berry curvature.

REFERENCES

[1] K. Song, S. Ryu, H. Lee, T. R. Paudel, et al. *Direct imaging of the electron liquid at oxide interfaces.* Nature Nanotechnology **13,** 198–203 (2018).

[2] W. Shockley, M. Sparks, and G. K. Teal. *p-n Junction Transistors.* Physical Review **83,** 151 (1951).

[3] H. Kroemer. *Theory of a wide-gap emitter for transistors.* Proceedings of the IRE **45,** 1535–1537 (1957).

[4] R. Anderson. *Germanium-gallium arsenide heterojunctions [letter to the editor].* IBM Journal of Research and Development **4,** 283–287 (1960).

[5] H. Kroemer. *Nobel Lecture: Quasielectric fields and band offsets: teaching electrons new tricks.* Reviews of Modern Physics **73,** 783 (2001).

[6] L. Esaki and R. Tsu. *Superlattice and negative differential conductivity in semiconductors.* IBM Journal of Research and Development **14,** 61–65 (1970).

[7] A. Ohtomo and H. Hwang. *A high-mobility electron gas at the $LaAlO_3$/$SrTiO_3$ heterointerface.* Nature **427,** 423–426 (2004).

[8] N. Reyren, S. Thiel, A. Caviglia, L. F. Kourkoutis, et al. *Superconducting interfaces between insulating oxides.* Science **317,** 1196–1199 (2007).

[9] A. Caviglia, S. Gariglio, N. Reyren, D. Jaccard, et al. *Electric field control of the $LaAlO_3$/$SrTiO_3$ interface ground state.* Nature **456,** 624–627 (2008).

[10] N. Nakagawa, H. Y. Hwang, and D. A. Muller. *Why some interfaces cannot be sharp.* Nature Materials **5,** 204–209 (2006).

[11] C. S. Koonce, M. L. Cohen, J. F. Schooley, W. R. Hosler, and E. R. Pfeiffer. *Superconducting Transition Temperatures of Semiconducting $SrTiO_3$.* Physical Review **163,** 380–390 (2 1967).

[12] A. Manchon, H. C. Koo, J. Nitta, S. Frolov, and R. Duine. *New perspectives for Rashba spin–orbit coupling.* Nature Materials **14,** 871–882 (2015).

[13] E. Lesne, Y. Fu, S. Oyarzun, J. Rojas-Sánchez, et al. *Highly efficient and tunable spin-to-charge conversion through Rashba coupling at oxide interfaces.* Nature Materials **15,** 1261–1266 (2016).

[14] P. Noël, F. Trier, L. M. V. Arche, J. Bréhin, et al. *Non-volatile electric control of spin–charge conversion in a $SrTiO_3$ Rashba system.* Nature **580,** 483–486 (2020).

[15] A. Barthelemy, N. Bergeal, M. Bibes, A. Caviglia, et al. *Quasi-two-dimensional electron gas at the oxide interfaces for topological quantum physics.* Europhysics Letters **133,** 17001 (2021).

[16] J. Nichols, X. Gao, S. Lee, T. Meyer, et al. *Emerging magnetism and anomalous Hall effect in iridate-manganite heterostructures.* Nature Communications **7** (2016).

[17] K. Ahadi, L. Galletti, Y. Li, S. Salmani-Rezaie, W. Wu, and S. Stemmer. *Enhancing superconductivity in $SrTiO_3$ films with strain.* Science Advances **5,** eaaw0120 (2019).

[18] M. Uchida, T. Nomoto, M. Musashi, R. Arita, and M. Kawasaki. *Superconductivity in Uniquely Strained RuO_2 Films*. Physical Review Letters **125,** 147001 (2020).

[19] J. P. Ruf, H. Paik, N. J. Schreiber, H. P. Nair, et al. *Strain-stabilized superconductivity*. Nature Communications **12,** 1–8 (2021).

[20] P.-H. Xiang, N. Zhong, C.-G. Duan, X. Tang, et al. *Strain controlled metal-insulator transition in epitaxial $NdNiO_3$ thin films*. Journal of Applied Physics **114,** 243713 (2013).

[21] S. Catalano, M. Gibert, V. Bisogni, O. Peil, et al. *Electronic transitions in strained $SmNiO_3$ thin films*. APL Materials **2,** 116110 (2014).

[22] Z. Liao, N. Gauquelin, R. J. Green, K. Müller-Caspary, et al. *Metal–insulator-transition engineering by modulation tilt-control in perovskite nickelates for room temperature optical switching*. Proceedings of the National Academy of Sciences **115,** 9515–9520 (2018).

[23] Y. Segal, K. Garrity, C. Vaz, J. Hoffman, F. Walker, S. Ismail-Beigi, and C. Ahn. *Dynamic evanescent phonon coupling across the $La_{1-x}Sr_xMnO_3/SrTiO_3$ interface*. Physical Review Letters **107,** 105501 (2011).

[24] A. D. Caviglia, R. Scherwitzl, P. Popovich, W. Hu, et al. *Ultrafast strain engineering in complex oxide heterostructures*. Physical Review Letters **108,** 136801 (2012).

[25] M. N. Baibich, J. M. Broto, A. Fert, F. N. Van Dau, et al. *Giant magnetoresistance of (001) Fe/(001) Cr magnetic superlattices*. Physical Review Letters **61,** 2472 (1988).

[26] G. Binasch, P. Grünberg, F. Saurenbach, and W. Zinn. *Enhanced magnetoresistance in layered magnetic structures with antiferromagnetic interlayer exchange*. Physical Review B **39,** 4828 (1989).

[27] K. Takahashi, M. Kawasaki, and Y. Tokura. *Interface ferromagnetism in oxide superlattices of $CaMnO_3/CaRuO_3$*. Applied Physics Letters **79,** 1324–1326 (2001).

[28] A. Bhattacharya, S. May, S. Te Velthuis, M. Warusawithana, et al. *Metal-insulator transition and its relation to magnetic structure in $(LaMnO_3)_{2n}/(SrMnO_3)_n$ superlattices*. Physical Review Letters **100,** 257203 (2008).

[29] S. Okamoto, J. Nichols, C. Sohn, S. Y. Kim, T. W. Noh, and H. N. Lee. *Charge transfer in iridate-manganite superlattices*. Nano Letters **17,** 2126–2130 (2017).

[30] Z. Liao, M. Huijben, Z. Zhong, N. Gauquelin, et al. *Controlled lateral anisotropy in correlated manganite heterostructures by interface-engineered oxygen octahedral coupling*. Nature Materials **15,** 425–431 (2016).

[31] D. Kan, R. Aso, R. Sato, M. Haruta, H. Kurata, and Y. Shimakawa. *Tuning magnetic anisotropy by interfacially engineering the oxygen coordination environment in a transition metal oxide*. Nature Materials **15,** 432–437 (2016).

[32] M. Gibert, P. Zubko, R. Scherwitzl, J. Íñiguez, and J.-M. Triscone. *Exchange bias in $LaNiO_3$–$LaMnO_3$ superlattices*. Nature Materials **11,** 195–198 (2012).

[33] M. Bowen, M. Bibes, A. Barthélémy, J.-P. Contour, A. Anane, Y. Lemaıtre, and A. Fert. *Nearly total spin polarization in $La_{2/3}Sr_{1/3}MnO_3$ from tunneling experiments*. Applied Physics Letters **82,** 233–235 (2003).

[34] A. Haghiri-Gosnet, T. Arnal, R. Soulimane, M. Koubaa, and J. Renard. *Spintronics: perspectives for the half-metallic oxides*. Physica Status Solidi (A) **201,** 1392–1397 (2004).

[35] A. Fert, V. Cros, and J. Sampaio. *Skyrmions on the track*. Nature Nanotechnology **8,** 152–156 (2013).

[36] X. Yu, Y. Onose, N. Kanazawa, J. H. Park, et al. *Real-space observation of a two-dimensional skyrmion crystal.* Nature **465,** 901–904 (2010).

[37] J. Matsuno, N. Ogawa, K. Yasuda, F. Kagawa, et al. *Interface-driven topological Hall effect in $SrRuO_3$-$SrIrO_3$ bilayer.* Science Advances **2,** e1600304 (2016).

[38] N. Nagaosa and Y. Tokura. *Topological properties and dynamics of magnetic skyrmions.* Nature Nanotechnology **8,** 899–911 (2013).

[39] T. Moriya. *Anisotropic superexchange interaction and weak ferromagnetism.* Physical Review **120,** 91 (1960).

[40] P. M. Levy and A. Fert. *Anisotropy induced by nonmagnetic impurities in CuMn spin-glass alloys.* Physical Review B **23,** 4667 (1981).

[41] L. Wang, Q. Feng, Y. Kim, R. Kim, et al. *Ferroelectrically tunable magnetic skyrmions in ultrathin oxide heterostructures.* Nature Materials **17,** 1087–1094 (2018).

[42] E. Skoropata, J. Nichols, J. M. Ok, R. V. Chopdekar, et al. *Interfacial tuning of chiral magnetic interactions for large topological Hall effects in $LaMnO_3$/$SrIrO_3$ heterostructures.* Science Advances **6,** eaaz3902 (2020).

[43] S. Heinze, K. Von Bergmann, M. Menzel, J. Brede, et al. *Spontaneous atomic-scale magnetic skyrmion lattice in two dimensions.* Nature Physics **7,** 713–718 (2011).

[44] G. Jackeli and G. Khaliullin. *Mott insulators in the strong spin-orbit coupling limit: from Heisenberg to a quantum compass and Kitaev models.* Physical Review Letters **102,** 017205 (2009).

[45] S. Moon, H. Jin, K. W. Kim, W. Choi, et al. *Dimensionality-Controlled Insulator-Metal Transition and Correlated Metallic State in 5d Transition Metal Oxides $Sr_{n+1}Ir_nO_{3n+1}$ (n = 1, 2, and ∞).* Physical Review Letters **101,** 226402 (2008).

[46] Y. Nie, P. King, C. Kim, M. Uchida, et al. *Interplay of Spin-Orbit Interactions, Dimensionality, and Octahedral Rotations in Semimetallic $SrIrO_3$.* Physical Review Letters **114,** 016401 (2015).

[47] G. L. Stamokostas and G. A. Fiete. *Mixing of t_{2g} - e_g orbitals in $4d$ and $5d$ transition metal oxides.* Physical Review B **97,** 085150 (2018).

[48] H. Gretarsson, J. Clancy, X. Liu, J. Hill, et al. *Crystal-field splitting and correlation effect on the electronic structure of A_2IrO_3.* Physical Review Letters **110,** 076402 (2013).

[49] B. Kim, H. Jin, S. Moon, J.-Y. Kim, et al. *Novel $J_{eff} = 1/2$ Mott state induced by relativistic spin-orbit coupling in Sr_2IrO_4.* Physical Review Letters **101,** 076402 (2008).

[50] Y. Ding, L. Yang, C.-C. Chen, H.-S. Kim, et al. *Pressure-induced confined metal from the mott insulator $Sr_3Ir_2O_7$.* Physical Review Letters **116,** 216402 (2016).

[51] N. Manca, D. Groenendijk, I. Pallecchi, C. Autieri, et al. *Balanced electron-hole transport in spin-orbit semimetal $SrIrO_3$ heterostructures.* Physical Review B **97,** 081105 (2018).

[52] A. S. Patri, K. Hwang, H.-W. Lee, and Y. B. Kim. *Theory of large intrinsic spin Hall effect in iridate semimetals.* Scientific Reports **8,** 1–10 (2018).

[53] L. Liu, Q. Qin, W. Lin, C. Li, et al. *Current-induced magnetization switching in all-oxide heterostructures.* Nature Nanotechnology **14,** 939–944 (2019).

[54] T. Takayama, A. Yaresko, and H. Takagi. *Monoclinic $SrIrO_3$—a Dirac semimetal produced by non-symmorphic symmetry and spin–orbit coupling.* Journal of Physics: Condensed Matter **31,** 074001 (2018).

[55] L. Zhang, B. Pang, Y. Chen, and Y. Chen. *Review of spin–orbit coupled semimetal $SrIrO_3$ in thin film form.* Critical Reviews in Solid State and Materials Sciences **43,** 367–391 (2018).

[56] J. Zhao, L. Yang, Y. Yu, F. Li, et al. *High-pressure synthesis of orthorhombic $SrIrO_3$ perovskite and its positive magnetoresistance.* Journal of Applied Physics **103,** 103706 (2008).

[57] M. Brahlek, A. Choquette, C. Smith, R. Engel-Herbert, and S. May. *Structural refinement of Pbnm-type perovskite films from analysis of half-order diffraction peaks.* Journal of Applied Physics **121,** 045303 (2017).

[58] A. Glazer. *Simple ways of determining perovskite structures.* Acta Crystallographica Section A: Crystal Physics, Diffraction, Theoretical and General Crystallography **31,** 756–762 (1975).

[59] Y. Chen, H.-S. Kim, and H.-Y. Kee. *Topological crystalline semimetals in nonsymmorphic lattices.* Physical Review B **93,** 155140 (2016).

[60] J. Liu, D. Kriegner, L. Horak, D. Puggioni, et al. *Strain-induced nonsymmorphic symmetry breaking and removal of Dirac semimetallic nodal line in an orthoperovskite iridate.* Physical Review B **93,** 085118 (2016).

[61] J.-M. Carter, V. V. Shankar, M. A. Zeb, and H.-Y. Kee. *Semimetal and topological insulator in perovskite iridates.* Physical Review B **85,** 115105 (2012).

[62] A. Biswas, K.-S. Kim, and Y. H. Jeong. *Metal insulator transitions in perovskite $SrIrO_3$ thin films.* Journal of Applied Physics **116,** 213704 (2014).

[63] S.-Y. Yang, H. Yang, E. Derunova, S. S. Parkin, B. Yan, and M. N. Ali. *Symmetry demanded topological nodal-line materials.* Advances in Physics: X **3,** 1414631 (2018).

[64] J. M. Rondinelli, N. M. Caffrey, S. Sanvito, and N. A. Spaldin. *Electronic properties of bulk and thin film $SrRuO_3$: search for the metal-insulator transition.* Physical Review B **78,** 155107 (2008).

[65] Z. Fang, N. Nagaosa, K. S. Takahashi, A. Asamitsu, et al. *The anomalous Hall effect and magnetic monopoles in momentum space.* Science **302,** 92–95 (2003).

[66] D. Kan, M. Anada, Y. Wakabayashi, H. Tajiri, and Y. Shimakawa. *Oxygen octahedral distortions in compressively strained $SrRuO_3$ epitaxial thin films.* Journal of Applied Physics **123,** 235303 (2018).

[67] W. Lu, P. Yang, W. D. Song, G. M. Chow, and J. S. Chen. *Control of oxygen octahedral rotations and physical properties in $SrRuO_3$ films.* Physical Review B **88,** 214115 (2013).

[68] G. Koster, L. Klein, W. Siemons, G. Rijnders, et al. *Structure, physical properties, and applications of $SrRuO_3$ thin films.* Reviews of Modern Physics **84,** 253 (2012).

[69] H. Yang, C. Fan, Z. Liu, Q. Yao, et al. *Comparative angle-resolved photoemission spectroscopy study of $CaRuO_3$ and $SrRuO_3$ thin films: pronounced spectral weight transfer and possible precursor of lower Hubbard band.* Physical Review B **94,** 115151 (2016).

[70] M. Kim and B. Min. *Nature of itinerant ferromagnetism of $SrRuO_3$: A DFT+ DMFT study.* Physical Review B **91,** 205116 (2015).

[71] D. J. Singh. *Electronic and magnetic properties of the 4d itinerant ferromagnet $SrRuO_3$.* Journal of Applied Physics **79,** 4818–4820 (1996).

[72] N. Nagaosa, J. Sinova, S. Onoda, A. MacDonald, and N. Ong. *Anomalous Hall Effect.* Reviews of Modern Physics **82,** 1539 (2010).

[73] J. Smit. *The spontaneous Hall effect in ferromagnetics II.* Physica **24,** 39–51 (1958).

[74] L. Berger. *Side-jump mechanism for the Hall effect of ferromagnets.* Physical Review B **2,** 4559 (1970).

[75] Y. Kats, I. Genish, L. Klein, J. W. Reiner, and M. Beasley. *Testing the Berry phase model for extraordinary Hall effect in $SrRuO_3$.* Physical Review B **70,** 180407 (2004).

[76] M. V. Berry. *Quantal phase factors accompanying adiabatic changes.* Proceedings of the Royal Society of London. A. Mathematical and Physical Sciences **392,** 45–57 (1984).

[77] F. Haldane. *Berry curvature on the Fermi surface: Anomalous Hall effect as a topological Fermi-liquid property.* Physical Review Letters **93,** 206602 (2004).

[78] H. M. Smith and A. Turner. *Vacuum deposited thin films using a ruby laser.* Applied Optics **4,** 147–148 (1965).

[79] D. Dijkkamp, T. Venkatesan, X. Wu, S. Shaheen, et al. *Preparation of Y-Ba-Cu oxide superconductor thin films using pulsed laser evaporation from high T_c bulk material.* Applied Physics Letters **51,** 619–621 (1987).

[80] D. H. Lowndes, D. Geohegan, A. Puretzky, D. Norton, and C. Rouleau. *Synthesis of novel thin-film materials by pulsed laser deposition.* Science **273,** 898–903 (1996).

[81] M. Kawasaki, K. Takahashi, T. Maeda, R. Tsuchiya, et al. *Atomic control of the $SrTiO_3$ crystal surface.* Science **266,** 1540–1542 (1994).

[82] T. Nishimura, A. Ikeda, H. Namba, T. Morishita, and Y. Kido. *Structure change of TiO_2-terminated $SrTiO_3$ (001) surfaces by annealing in O_2 atmosphere and ultrahigh vacuum.* Surface science **421,** 273–278 (1999).

[83] C. Aruta, S. Amoruso, R. Bruzzese, X. Wang, D. Maccariello, F. Miletto Granozio, and U. Scotti di Uccio. *Pulsed laser deposition of $SrTiO_3$/$LaGaO_3$ and $SrTiO_3$/$LaAlO_3$: Plasma plume effects.* Applied Physics Letters **97,** 252105 (2010).

[84] C. Aruta, S. Amoruso, G. Ausanio, R. Bruzzese, et al. *Critical influence of target-to-substrate distance on conductive properties of $LaGaO_3$/$SrTiO_3$ interfaces deposited at 0.1 mbar oxygen pressure.* Applied Physics Letters **101,** 031602 (2012).

[85] H. N. Lee, S. S. A. Seo, W. S. Choi, and C. M. Rouleau. *Growth control of oxygen stoichiometry in homoepitaxial $SrTiO_3$ films by pulsed laser epitaxy in high vacuum.* Scientific Reports **6,** 1–7 (2016).

[86] S. Ino. *Some new techniques in reflection high energy electron diffraction (RHEED) application to surface structure studies.* Japanese Journal of Applied Physics **16,** 891 (1977).

[87] S. Hasegawa. *Reflection high-energy electron diffraction.* Characterization of Materials **97,** 1925–1938 (2012).

[88] G. Rijnders, D. H. Blank, J. Choi, and C.-B. Eom. *Enhanced surface diffusion through termination conversion during epitaxial $SrRuO_3$ growth.* Applied Physics Letters **84,** 505–507 (2004).

[89] D. Groenendijk, N. Manca, G. Mattoni, L. Kootstra, et al. *Epitaxial growth and thermodynamic stability of $SrIrO_3$/$SrTiO_3$ heterostructures.* Applied Physics Letters **109,** 041906 (2016).

[90] J. R. Hook and H. E. Hall. *Solid State Physics.* Manchester Physics Series (1991).

[91] H. Qiu, M. Yang, Y. Dong, H. Xu, et al. *The tetragonal-like to rutile structural phase transition in epitaxial VO_2/TiO_2 (001) thick films.* New Journal of Physics **17,** 113016 (2015).

[92] S. May, J.-W. Kim, J. Rondinelli, E. Karapetrova, N. Spaldin, A. Bhattacharya, and P. Ryan. *Quantifying octahedral rotations in strained perovskite oxide films.* Physical Review B **82,** 014110 (2010).

[93] J. Fowlie, C. Lichtensteiger, M. Gibert, H. Meley, P. Willmott, and J.-M. Triscone. *Thickness-dependent perovskite octahedral distortions at heterointerfaces.* Nano letters **19,** 4188–4194 (2019).

[94] *QTRay-ivvi-p.* `http://qtwork.tudelft.nl/~schouten/ivvi/index-ivvi.htm`. Accessed: 6-11-2022.

[95] J. M. Rondinelli, S. J. May, and J. W. Freeland. *Control of octahedral connectivity in perovskite oxide heterostructures: An emerging route to multifunctional materials discovery.* MRS Bulletin **37,** 261–270 (2012).

[96] D. Kan, R. Aso, H. Kurata, and Y. Shimakawa. *Research Update: Interface-engineered oxygen octahedral tilts in perovskite oxide heterostructures.* APL Materials **3,** 062302 (2015).

[97] Z. Liao, R. J. Green, N. Gauquelin, S. Macke, et al. *Long-Range Domain structure and symmetry engineering by interfacial oxygen octahedral coupling at heterostructure interface.* Advanced Functional Materials **26,** 6627–6634 (2016).

[98] A. J. Grutter, A. Vailionis, J. A. Borchers, B. J. Kirby, et al. *Interfacial symmetry control of emergent ferromagnetism at the nanoscale.* Nano Letters **16,** 5647–5651 (2016).

[99] H. Guo, Z. Wang, S. Dong, S. Ghosh, et al. *Interface-induced multiferroism by design in complex oxide superlattices.* Proceedings of the National Academy of Sciences, 201706814 (2017).

[100] A. Paul, C. Reitinger, C. Autieri, B. Sanyal, et al. *Exotic exchange bias at epitaxial ferroelectric-ferromagnetic interfaces.* Applied Physics Letters **105,** 022409 (2014).

[101] Y.-M. Kim, A. Kumar, A. Hatt, A. N. Morozovska, et al. *Interplay of octahedral tilts and polar order in $BiFeO_3$ films.* Advanced Materials **25,** 2497–2504 (2013).

[102] J. Seidel, L. W. Martin, Q. He, Q. Zhan, et al. *Conduction at domain walls in oxide multiferroics.* Nature Materials **8,** 229 (2009).

[103] B. Kalisky, E. M. Spanton, H. Noad, J. R. Kirtley, et al. *Locally enhanced conductivity due to the tetragonal domain structure in $LaAlO_3$/$SrTiO_3$ heterointerfaces.* Nature Materials **12,** 1091–1095 (2013).

[104] M. Honig, J. A. Sulpizio, J. Drori, A. Joshua, E. Zeldov, and S. Ilani. *Local electrostatic imaging of striped domain order in $LaAlO_3$/$SrTiO_3$.* Nature Materials **12,** 1112 (2013).

[105] J.-Y. Chauleau, T. Chirac, S. Fusil, V. Garcia, et al. *Electric and antiferromagnetic chiral textures at multiferroic domain walls.* Nature Materials, 1–5 (2019).

[106] J. Seidel. *Nanoelectronics based on topological structures.* Nature Materials **18,** 188 (2019).

[107] F. W. Lytle. *X-Ray diffractometry of low-temperature phase transformations in strontium titanate.* Journal of Applied Physics **35,** 2212–2215 (1964).

[108] D. Groenendijk, C. Autieri, J. Girovsky, M. Martinez-Velarte, et al. *Spin-orbit semimetal $SrIrO_3$ in the two-dimensional limit.* Physical Review Letters **119,** 256403 (2017).

[109] P. Schütz, D. Di Sante, L. Dudy, J. Gabel, et al. *Dimensionality-Driven Metal-Insulator Transition in Spin-Orbit-Coupled $SrIrO_3$.* Physical Review Letters **119,** 256404 (2017).

[110] Y. Chen, Y.-M. Lu, and H.-Y. Kee. *Topological crystalline metal in orthorhombic perovskite iridates.* Nature Communications **6,** 6593 (2015).

[111] H.-S. Kim, Y. Chen, and H.-Y. Kee. *Surface states of perovskite iridates $AIrO_3$: signatures of a topological crystalline metal with nontrivial Z_2 index.* Physical Review B **91,** 235103 (2015).

[112] J. Fujioka, R. Yamada, M. Kawamura, S. Sakai, et al. *Strong-correlation induced high-mobility electrons in Dirac semimetal of perovskite oxide.* Nature Communications **10,** 362 (2019).

[113] R. Yamada, J. Fujioka, M. Kawamura, S. Sakai, et al. *Large Variation of Dirac Semimetal State in Perovskite $CaIrO_3$ with Pressure-Tuning of Electron Correlation.* Physical Review Letters **123,** 216601 (2019).

[114] K. Momma and F. Izumi. *VESTA 3 for three-dimensional visualization of crystal, volumetric and morphology data.* Journal of Applied Crystallography **44,** 1272–1276 (2011).

[115] C. H. Kronbo, M. B. Nielsen, S. M. Kevy, P. Parisiades, and M. Bremholm. *High pressure structure studies of 6H-$SrIrO_3$ and the octahedral tilting in 3C-$SrIrO_3$ towards A post-perovskite.* Journal of Solid State Chemistry **238,** 74–82 (2016).

[116] U. Bianchi, W. Kleemann, and J. Bednorz. *Raman scattering of ferroelectric $Sr_{1-x}Ca_xTiO_3$, x=0.007.* Journal of Physics: Condensed Matter **6,** 1229 (1994).

[117] M. Guzhva, P. Markovin, and W. Kleemann. *Spontaneous photorefractive effect in $Sr_{1-x}Ca_xTiO_3$ (x=0.014).* Physics of the Solid State **39,** 625–627 (1997).

[118] C. Menoret, J. Kiat, B. Dkhil, M. Dunlop, H. Dammak, and O. Hernandez. *Structural evolution and polar order in $Sr_{1-x}Ba_xTiO_3$.* Physical Review B **65,** 224104 (2002).

[119] R. A. Evarestov, E. Blokhin, D. Gryaznov, E. A. Kotomin, and J. Maier. *Phonon calculations in cubic and tetragonal phases of $SrTiO_3$: A comparative LCAO and plane-wave study.* Physical Review B **83,** 134108 (2011).

[120] A. K. Choquette, C. Smith, R. Sichel-Tissot, E. Moon, et al. *Octahedral rotation patterns in strained $EuFeO_3$ and other Pbnm perovskite films: Implications for hybrid improper ferroelectricity.* Physical Review B **94,** 024105 (2016).

[121] L. Horák, D. Kriegner, J. Liu, C. Frontera, X. Marti, and V. Hol. *Structure of epitaxial $SrIrO_3$ perovskite studied by interference between X-ray waves diffracted by the substrate and the thin film.* Journal of Applied Crystallography **50** (2017).

[122] J.-S. Zhou and J. B. Goodenough. *Intrinsic structural distortion in orthorhombic perovskite oxides.* Physical Review B **77,** 132104 (2008).

[123] J. H. Gruenewald, J. Nichols, J. Terzic, G. Cao, J. W. Brill, and S. S. A. Seo. *Compressive strain-induced metal–insulator transition in orthorhombic $SrIrO_3$ thin films.* Journal of Materials Research **29,** 2491–2496 (2014).

[124] Y. Frenkel, N. Haham, Y. Shperber, C. Bell, et al. *Anisotropic Transport at the $LaAlO_3$/$SrTiO_3$ Interface Explained by Microscopic Imaging of Channel-Flow over $SrTiO_3$ Domains.* ACS Applied Materials & Interfaces **8,** 12514–12519 (2016).

[125] E. Persky and B. Kalisky. *Scanning SQUID view of oxide interfaces.* Advanced Materials **30,** 1706653 (2018).

[126] W. Guo, D. Ji, Z. Gu, J. Zhou, Y. Nie, and X. Pan. *Engineering of octahedral rotations and electronic structure in ultrathin $SrIrO_3$ films.* Physical Review B **101,** 085101 (2020).

[127] Y. Liu, L. Yang, and J. Li. *Strain-engineered orthorhombic-rhombohedral phase boundary in epitaxial bismuth ferrite films.* Journal of Applied Physics **113,** 183524 (2013).

[128] S. Bhattacharjee, E. Bousquet, and P. Ghosez. *Engineering multiferroism in $CaMnO_3$.* Physical Review Letters **102,** 117602 (2009).

[129] E. Bousquet and A. Cano. *Non-collinear magnetism in multiferroic perovskites.* Journal of Physics: Condensed Matter **28,** 123001 (2016).

[130] M. Gibert, M. Viret, A. Torres-Pardo, C. Piamonteze, et al. *Interfacial control of magnetic properties at $LaMnO_3$/$LaNiO_3$ interfaces.* Nano Letters **15,** 7355–7361 (2015).

[131] D. Li, K. Lee, B. Y. Wang, M. Osada, et al. *Superconductivity in an infinite-layer nickelate.* Nature **572,** 624–627 (2019).

[132] D. Osterman, K. Mohanty, and J. Axe. *Observation of the antiferroelectric order parameter in surface layers of $SrTiO_3$.* Journal of Physics C: Solid State Physics **21,** 2635 (1988).

[133] S. Doi and I. Takahashi. *Critical behaviour of the $SrTiO_3$ (001) surface at the structural phase transition.* Philosophical Magazine A **80,** 1889–1899 (2000).

[134] M. Geday and A. Glazer. *Birefringence of $SrTiO_3$ at the ferroelastic phase transition.* Journal of Physics: Condensed Matter **16,** 3303 (2004).

[135] G. Kresse and D. Joubert. *From ultrasoft pseudopotentials to the projector augmented-wave method.* Physical Review B **59,** 1758 (1999).

[136] J. Perdew, A. Ruzsinszky, G. I. Csonka, O. A. Vydrov, et al. *Restoring the density-gradient expansion for exchange in solids and surfaces.* Physical Review Letters **100,** 136406 (2008).

[137] A. Liechtenstein, V. Anisimov, and J. Zaanen. *Density-functional theory and strong interactions: Orbital ordering in Mott-Hubbard insulators.* Physical Review B **52,** R5467 (1995).

[138] K. Von Klitzing. *The quantized Hall effect.* Reviews of Modern Physics **58,** 519 (1986).

[139] T. Jungwirth, J. Wunderlich, and K. Olejník. *Spin Hall effect devices.* Nature Materials **11,** 382–390 (2012).

[140] R. Karplus and J. Luttinger. *Hall effect in ferromagnetics.* Physical Review **95,** 1154 (1954).

[141] S. Itoh, Y. Endoh, T. Yokoo, S. Ibuka, et al. *Weyl fermions and spin dynamics of metallic ferromagnet $SrRuO_3$.* Nature Communications **7,** 11788 (2016).

[142] N. Sinitsyn, Q. Niu, J. Sinova, and K. Nomura. *Disorder effects in the anomalous Hall effect induced by Berry curvature.* Physical Review B **72,** 045346 (2005).

[143] S. Onoda, N. Sugimoto, and N. Nagaosa. *Intrinsic versus extrinsic anomalous Hall effect in ferromagnets.* Physical Review Letters **97,** 126602 (2006).

[144] M.-H. Kim, G. Acbas, M.-H. Yang, M. Eginligil, et al. *Infrared anomalous Hall effect in $SrRuO_3$: Exploring evidence for crossover to intrinsic behavior.* Physical Review B **81,** 235218 (2010).

[145] N. Haham, Y. Shperber, M. Schultz, N. Naftalis, E. Shimshoni, J. W. Reiner, and L. Klein. *Scaling of the anomalous Hall effect in $SrRuO_3$.* Physical Review B **84,** 174439 (2011).

[146] T. C. van Thiel, J. Fowlie, C. Autieri, N. Manca, et al. *Coupling lattice instabilities across the interface in ultrathin oxide heterostructures.* ACS Materials Letters **2,** 389–394 (4 2020).

[147] Y. Ohuchi, J. Matsuno, N. Ogawa, Y. Kozuka, M. Uchida, Y. Tokura, and M. Kawasaki. *Electric-field control of anomalous and topological Hall effects in oxide bilayer thin films.* Nature Communications **9,** 1–7 (2018).

[148] L. Wysocki, J. Schöpf, M. Ziese, L. Yang, et al. *Electronic Inhomogeneity Influence on the Anomalous Hall Resistivity Loops of $SrRuO_3$ Epitaxially Interfaced with 5d Perovskites.* ACS Omega **5,** 5824–5833 (2020).

[149] Y. Gu, C. Song, Q. Zhang, F. Li, et al. *Interfacial Control of Ferromagnetism in Ultrathin $SrRuO_3$ Films Sandwiched between Ferroelectric $BaTiO_3$ Layers.* ACS Applied Materials & Interfaces **12,** 6707–6715 (2020).

[150] D. Kan, T. Moriyama, and Y. Shimakawa. *Field-sweep-rate and time dependence of transverse resistivity anomalies in ultrathin $SrRuO_3$ films.* Physical Review B **101,** 014448 (2020).

[151] P.-C. Wu, H. Song, Y. Yuan, B. Feng, et al. *Thickness dependence of transport behaviors in $SrRuO_3$/$SrTiO_3$ superlattices.* Physical Review Materials **4,** 014401 (2020).

[152] B. Sohn, B. Kim, J. W. Choi, S. H. Chang, J. H. Han, and C. Kim. *Hump-like structure in Hall signal from ultra-thin $SrRuO_3$ films without inhomogeneous anomalous Hall effect.* Current Applied Physics **20,** 186–190 (2020).

[153] Z. Ren, F. Shao, P. Liu, M. Wang, et al. *Nonvolatile Ferroelectric Field Control of the Anomalous Hall Effect in $BiFeO_3$/$SrRuO_3$ Bilayer.* Physical Review Applied **13,** 024044 (2020).

[154] M. Ziese, L. Jin, and I. Lindfors-Vrejoiu. *Unconventional anomalous Hall effect driven by oxygen-octahedra-tailoring of the $SrRuO_3$ structure.* Journal of Physics: Materials **2,** 034008 (2019).

[155] Z. Li, S. Shen, Z. Tian, K. Hwangbo, et al. *Reversible manipulation of the magnetic state in $SrRuO_3$ through electric-field controlled proton evolution.* Nature Communications **11,** 1–9 (2020).

[156] S. Nakatsuji, N. Kiyohara, and T. Higo. *Large anomalous Hall effect in a non-collinear antiferromagnet at room temperature.* Nature **527,** 212 (2015).

[157] A. K. Nayak, J. E. Fischer, Y. Sun, B. Yan, et al. *Large anomalous Hall effect driven by a nonvanishing Berry curvature in the noncolinear antiferromagnet Mn_3Ge.* Sci. Adv. **2,** e101870 (2016).

[158] P. K. Rout, P. V. Madduri, S. K. Manna, and A. K. Nayak. *Large anomalous Hall effect driven by a nonvanishing Berry curvature in the noncolinear antiferromagnet Mn_3Ge.* Physical Review B **99,** 094430 (2019).

[159] B. Sohn, B. Kim, S. Y. Park, H. Y. Choi, et al. *Emergence of robust 2D skyrmions in $SrRuO_3$ ultrathin film without the capping layer.* arXiv:1810.01615 (2018).

[160] D. Kan, T. Moriyama, K. Kobayashi, and Y. Shimakawa. *Alternative to the topological interpretation of the transverse resistivity anomalies in $SrRuO_3$.* Physical Review B **98,** 180408(R) (2018).

[161] R. Barnett, G. R. Boyd, and V. Galitski. *SU(3) spin-orbit coupling in systems of ultracold atoms.* Physical Review Letters **109,** 235308 (2012).

[162] B. Sohn, J. R. Kim, C. H. Kim, S. Lee, et al. *Observation of metallic electronic structure in a single-atomic-layer oxide.* Nature Communications **12,** 1–8 (2021).

[163] E. K. Ko, J. Mun, H. G. Lee, J. Kim, et al. *Oxygen Vacancy Engineering for Highly Tunable Ferromagnetic Properties: A Case of $SrRuO_3$ Ultrathin Film with a $SrTiO_3$ Capping Layer.* Advanced Functional Materials **30,** 2001486 (2020).

[164] Y. K. Wakabayashi, S. Kaneta-Takada, Y. Krockenberger, K. Takiguchi, et al. *Structural and transport properties of highly Ru-deficient $SrRu_{0.7}O_3$ thin films prepared by molecular beam epitaxy: Comparison with stoichiometric $SrRuO_3$.* AIP Advances **11,** 035226 (2021).

[165] P. Gruszecki, C. Banerjee, M. Mruczkiewicz, O. Hellwig, A. Barman, and M. Krawczyk. *The influence of the internal domain wall structure on spin wave band structure in periodic magnetic stripe domain patterns.* Solid State Physics **70,** 79–132 (2019).

[166] Q. Gan, R. Rao, C. Eom, J. Garrett, and M. Lee. *Direct measurement of strain effects on magnetic and electrical properties of epitaxial $SrRuO_3$ thin films.* Applied Physics Letters **72,** 978–980 (1998).

[167] C. Jung, H. Yamada, M. Kawasaki, and Y. Tokura. *Magnetic anisotropy control of $SrRuO_3$ films by tunable epitaxial strain.* Applied Physics Letters **84,** 2590–2592 (2004).

[168] D. Kan, R. Aso, H. Kurata, and Y. Shimakawa. *Epitaxial strain effect in tetragonal $SrRuO_3$ thin films.* Journal of Applied Physics **113,** 173912 (2013).

[169] T. Kobayashi, H. Tsuji, S. Tsunashima, and S. Uchiyama. *Magnetization process of exchange-coupled ferrimagnetic double-layered films.* Japanese Journal of Applied Physics **20,** 2089 (1981).

[170] S. Zhang, Y. Liu, L. Collins-McIntyre, T. Hesjedal, J. Zhang, S. Wang, and G. Yu. *Extraordinary Hall balance.* Scientific Reports **3,** 2087 (2013).

[171] S. Zhang and T. Hesjedal. *The magneto-Hall difference and the planar extraordinary Hall balance.* AIP Advances **6,** 045019 (2016).

[172] K. M. Fijalkowski, M. Hartl, M. Winnerlein, P. Mandal, et al. *Coexistence of surface and bulk ferromagnetism mimics skyrmion Hall effect in a topological insulator.* Physical Review X **10,** 011012 (2020).

[173] L. Klein, J. Dodge, C. Ahn, G. Snyder, T. Geballe, M. Beasley, and A. Kapitulnik. *Anomalous spin scattering effects in the badly metallic itinerant ferromagnet $SrRuO_3$.* Physical ReviewLetters **77,** 2774 (1996).

[174] R. Roussev and A. Millis. *Resistive Anomalies at Ferromagnetic Transitions Revisited: The case of $SrRuO_3$.* Physical Review Letters **84,** 2279 (2000).

[175] L. Klein, J. Dodge, T. Geballe, M. Beasley, and A. Kapitulnik. *Klein et al. Reply.* Physical Review Letters **84,** 2280 (2000).

[176] M. E. Fisher and J. Langer. *Resistive anomalies at magnetic critical points.* Physical Review Letters **20,** 665 (1968).

[177] S. Alexander, J. Helman, and I. Balberg. *Critical behavior of the electrical resistivity in magnetic systems.* Physical Review B **13,** 304 (1976).

[178] J. Xia, W. Siemons, G. Koster, M. Beasley, and A. Kapitulnik. *Critical thickness for itinerant ferromagnetism in ultrathin films of $SrRuO_3$.* Physical Review B **79,** 140407 (2009).

[179] Y. J. Chang, C. H. Kim, S.-H. Phark, Y. Kim, J. Yu, and T. Noh. *Fundamental thickness limit of itinerant ferromagnetic $SrRuO_3$ thin films.* Physical Review Letters **103,** 057201 (2009).

[180] C. Fang, L. Lu, J. Liu, and L. Fu. *Topological semimetals with helicoid surface states.* Nature Physics (2016).

[181] B. Pang, L. Zhang, Y. Chen, J. Zhou, S. Yao, S. Zhang, and Y. Chen. *Spin-glass-like behavior and topological Hall effect in $SrRuO_3$/$SrIrO_3$ superlattices for oxide spintronics applications.* ACS Applied Materials & Interfaces (2017).

[182] J. C. Slater and G. F. Koster. *Simplified LCAO method for the periodic potential problem.* Physical Review **94,** 1498 (1954).

[183] W. A. Harrison. *Electronic structure and the properties of solids: the physics of the chemical bond.* Chap. 20 (Courier Corporation, 2012).

[184] J. Malrieu, P. Durand, and J. Daudey. *Intermediate Hamiltonians as a new class of effective Hamiltonians.* Journal of Physics A: Mathematical and General **18,** 809 (1985).

[185] G. Khalsa, B. Lee, and A. H. MacDonald. *Theory of t_{2g} electron-gas Rashba interactions.* Physical Review B **88,** 041302 (2013).

[186] D. Khomskii. *Transition Metal Compounds* (Cambridge University Press, 2014).

[187] H. Casimir. *On Onsager's principle of microscopic reversibility.* Reviews of Modern Physics **17,** 343 (1945).

[188] G. Kresse and J. Furthmüller. *Efficiency of ab-initio total energy calculations for metals and semiconductors using a plane-wave basis set.* Computational Materials Science **6,** 15–50 (1996).

[189] J. P. Perdew and A. Zunger. *Self-interaction correction to density-functional approximations for many-electron systems.* Physical Review B **23,** 5048 (1981).

[190] D. M. Ceperley and B. J. Alder. *Ground state of the electron gas by a stochastic method.* Physical Review Letters **45,** 566 (1980).

[191] N. Marzari and D. Vanderbilt. *Maximally localized generalized Wannier functions for composite energy bands.* Physical Review B **56,** 12847 (1997).

[192] I. Souza, N. Marzari, and D. Vanderbilt. *Maximally localized Wannier functions for entangled energy bands.* Physical Review B **65,** 035109 (2001).

[193] A. A. Mostofi, J. R. Yates, Y.-S. Lee, I. Souza, D. Vanderbilt, and N. Marzari. *wannier90: A tool for obtaining maximally-localised Wannier functions.* Computer physics communications **178,** 685–699 (2008).

[194] J. Choi, C.-B. Eom, G. Rijnders, H. Rogalla, and D. H. Blank. *Growth mode transition from layer by layer to step flow during the growth of heteroepitaxial $SrRuO_3$ on (001) $SrTiO_3$.* Applied Physics Letters **79,** 1447–1449 (2001).

[195] A. De Backer, K. Van den Bos, W. Van den Broek, J. Sijbers, and S. Van Aert. *StatSTEM: an efficient approach for accurate and precise model-based quantification of atomic resolution electron microscopy images.* Ultramicroscopy **171,** 104–116 (2016).

[196] Z. Zhong and P. Hansmann. *Band alignment and charge transfer in complex oxide interfaces.* Physical Review X **7,** 011023 (2017).

[197] J. Coey, M. Venkatesan, and P. Stamenov. *Surface magnetism of strontium titanate.* Journal of Physics: Condensed Matter **28,** 485001 (2016).

[198] J. Wang and S.-C. Zhang. *Topological states of condensed matter.* Nature Materials **16,** 1062–1067 (2017).

[199] M. Z. Hasan and C. L. Kane. *Colloquium: topological insulators.* Reviews of Modern Physics **82,** 3045 (2010).

[200] X.-G. Wen. *Colloquium: Zoo of quantum-topological phases of matter.* Reviews of Modern Physics **89,** 041004 (2017).

[201] F. D. M. Haldane. *Model for a quantum Hall effect without Landau levels: Condensed-matter realization of the "parity anomaly".* Physical Review Letters **61,** 2015 (1988).

[202] A. Zyuzin, S. Wu, and A. Burkov. *Weyl semimetal with broken time reversal and inversion symmetries.* Physical Review B **85,** 165110 (2012).

[203] T. Zhang, J. Ha, N. Levy, Y. Kuk, and J. Stroscio. *Electric-field tuning of the surface band structure of topological insulator Sb_2Te_3 thin films.* Physical Review Letters **111,** 056803 (2013).

[204] C.-Z. Chang, J. Zhang, X. Feng, J. Shen, et al. *Experimental observation of the quantum anomalous Hall effect in a magnetic topological insulator*. Science **340,** 167–170 (2013).

[205] X. Qian, J. Liu, L. Fu, and J. Li. *Quantum spin Hall effect in two-dimensional transition metal dichalcogenides*. Science **346,** 1344–1347 (2014).

[206] B. A. Bernevig and S.-C. Zhang. *Quantum spin Hall effect*. Physical Review Letters **96,** 106802 (2006).

[207] M. König, S. Wiedmann, C. Brüne, A. Roth, et al. *Quantum spin Hall insulator state in HgTe quantum wells*. Science **318,** 766–770 (2007).

[208] D. Hsieh, D. Qian, L. Wray, Y. Xia, Y. S. Hor, R. J. Cava, and M. Z. Hasan. *A topological Dirac insulator in a quantum spin Hall phase*. Nature **452,** 970–974 (2008).

[209] P. Dziawa, B. Kowalski, K. Dybko, R. Buczko, et al. *Topological crystalline insulator states in $Pb_{1-x}SnSe$*. Nature Materials **11,** 1023–1027 (2012).

[210] X. Xi, C. Ma, Z. Liu, Z. Chen, et al. *Signatures of a pressure-induced topological quantum phase transition in BiTeI*. Physical Review Letters **111,** 155701 (2013).

[211] T. Liang, S. Kushwaha, J. Kim, Q. Gibson, et al. *A pressure-induced topological phase with large Berry curvature in $Pb_{1-x}Sn_xTe$*. Science Advances **3,** e1602510 (2017).

[212] T. Ideue, M. Hirayama, H. Taiko, T. Takahashi, et al. *Pressure-induced topological phase transition in noncentrosymmetric elemental tellurium*. Proceedings of the National Academy of Sciences **116,** 25530–25534 (2019).

[213] X. Ying and A. Kamenev. *Topological transitions in metals*. Physical Review B **99,** 245411 (2019).

[214] D. Pesin and L. Balents. *Mott physics and band topology in materials with strong spin–orbit interaction*. Nature Physics **6,** 376 (2010).

[215] T. van Thiel, D. Groenendijk, and A. Caviglia. *Extraordinary Hall balance in ultrathin Sr-RuO_3 bilayers*. Journal of Physics: Materials **3,** 025005 (2020).

[216] L. Wang, Q. Feng, H. G. Lee, E. K. Ko, Q. Lu, and T. W. Noh. *Controllable Thickness Inhomogeneity and Berry Curvature Engineering of Anomalous Hall Effect in $SrRuO_3$ Ultrathin Films*. Nano Letters **20,** 2468–2477 (2020).

[217] D. J. Groenendijk, C. Autieri, T. C. van Thiel, W. Brzezicki, et al. *Berry phase engineering at oxide interfaces*. Physical Review Research **2,** 023404 (2020).

[218] D. Kan, K. Kobayashi, and Y. Shimakawa. *Electric field induced modulation of transverse resistivity anomalies in ultrathin $SrRuO_3$ epitaxial films*. Physical Review B **101,** 144405 (2020).

[219] K. Takiguchi, Y. K. Wakabayashi, H. Irie, Y. Krockenberger, et al. *Quantum transport evidence of Weyl fermions in an epitaxial ferromagnetic oxide*. Nature Communications **11,** 1–12 (2020).

[220] S. Shimizu, K. S. Takahashi, M. Kubota, M. Kawasaki, Y. Tokura, and Y. Iwasa. *Gate tuning of anomalous Hall effect in ferromagnetic metal $SrRuO_3$*. Applied Physics Letters **105,** 163509 (2014).

[221] H. Mizuno, K. T. Yamada, D. Kan, T. Moriyama, Y. Shimakawa, and T. Ono. *Electric-field-induced modulation of the anomalous Hall effect in a heterostructured itinerant ferromagnet $SrRuO_3$*. Physical Review B **96,** 214422 (2017).

[222] A. Tsukazaki, A. Ohtomo, T. Kita, Y. Ohno, H. Ohno, and M. Kawasaki. *Quantum Hall effect in polar oxide heterostructures*. Science **315,** 1388–1391 (2007).

[223] H. Y. Hwang, Y. Iwasa, M. Kawasaki, B. Keimer, N. Nagaosa, and Y. Tokura. *Emergent phenomena at oxide interfaces.* Nature Materials **11,** 103–113 (2012).

[224] H. G. Lee, L. Wang, L. Si, X. He, et al. *Atomic-Scale Metal–Insulator Transition in $SrRuO_3$ Ultrathin Films Triggered by Surface Termination Conversion.* Advanced Materials **32,** 1905815 (2020).

[225] J. Shin, S. Kalinin, H. Lee, H. Christen, R. Moore, E. Plummer, and A. Baddorf. *Surface stability of epitaxial $SrRuO_3$ films.* Surface science **581,** 118–132 (2005).

[226] J. C. Slater. *A simplification of the Hartree-Fock method.* Physical Review **81,** 385 (1951).

[227] M. Huijben, A. Brinkman, G. Koster, G. Rijnders, H. Hilgenkamp, and D. H. Blank. *Structure–property relation of $SrTiO_3$/$LaAlO_3$ interfaces.* Advanced Materials **21,** 1665–1677 (2009).

[228] J. Gazquez, M. Stengel, R. Mishra, M. Scigaj, et al. *Competition between polar and nonpolar lattice distortions in oxide quantum wells: new critical thickness at polar interfaces.* Physical Review Letters **119,** 106102 (2017).

[229] J. Lee, Y. Lee, T. Noh, K. Char, et al. *Optical investigation of the electronic structures of $Y_2Ru_2O_7$, $CaRuO_3$, $SrRuO_3$, and $Bi_2Ru_2O_7$.* Physical Review B **64,** 245107 (2001).

[230] M. Laad and E. Müller-Hartmann. *Origin of the Non-Fermi Liquid Behavior of $SrRuO_3$.* Physical Review Letters **87,** 246402 (2001).

[231] H. T. Dang, J. Mravlje, A. Georges, and A. J. Millis. *Electronic correlations, magnetism, and Hund's rule coupling in the ruthenium perovskites $SrRuO_3$ and $CaRuO_3$.* Physical Review B **91,** 195149 (2015).

[232] R. Bouchard and J. Weiher. *$La_xSr_{1-x}RuO_3$: a new perovskite series.* Journal of Solid State Chemistry **4,** 80–86 (1972).

[233] J. B. Goodenough. *Coexistence of localized and itinerant d electrons.* Materials Research Bulletin **6,** 967–976 (1971).

[234] A. Sinclair, J. A. Rodgers, C. V. Topping, M. Mıšek, et al. *Synthesis and properties of lanthanide ruthenium (III) oxide perovskites.* Angewandte Chemie International Edition **53,** 8343–8347 (2014).

[235] R. Karthikeyan and M. K. Niranjan. *Interface Local Magnetic Moment and Its Near Periodic Modulation in Oxide $SrRuO_3$|$LaAlO_3$ Heterojunctions: An Ab Initio Investigation.* IEEE Transactions on Magnetics **54,** 1–7 (2018).

[236] Z. Zeng, J. Feng, X. Zheng, C. Wang, et al. *Emergent ferromagnetism with tunable perpendicular magnetic anisotropy in short-periodic $SrIrO_3$/$SrRuO_3$ superlattices.* Applied Physics Letters **116,** 142401 (2020).

[237] C. Lichtensteiger. *InteractiveXRDFit: a new tool to simulate and fit X-ray diffractograms of oxide thin films and heterostructures.* Journal of Applied Crystallography **51,** 1745 (2018).

[238] D. R. Lide. *CRC Handbook of Chemistry and Physics* (CRC press, 2004).

[239] A. Anders. *Atomic scale heating in cathodic arc plasma deposition.* Applied Physics Letters **80,** 1100–1102 (2002).

[240] H. Jang, A. Kumar, S. Denev, M. D. Biegalski, et al. *Ferroelectricity in strain-free $SrTiO_3$ thin films.* Physical Review Letters **104,** 197601 (2010).

[241] N. K. Labhsetwar, A. Watanabe, and T. Mitsuhashi. *New improved syntheses of $LaRuO_3$ perovskites and their applications in environmental catalysis.* Applied Catalysis B: Environmental **40,** 21–30 (2003).

[242] N. Kikugawa, A. Mackenzie, C. Bergemann, R. Borzi, S. Grigera, and Y. Maeno. *Rigid-band shift of the Fermi level in the strongly correlated metal: $Sr_{2-y}La_yRuO_4$.* Physical Review B **70,** 060508 (2004).

[243] J. Cho, Q. Jia, X. Wu, S. Foltyn, and M. Maley. *Magnetotransport properties of $SrRuO_3$ epitaxial thin films on (100) $LaAlO_3$: Presence of localized magnetic moments.* Physical Review B **54,** 37 (1996).

[244] D. Kim, B. Zink, F. Hellman, S. McCall, G. Cao, and J. Crow. *Mean-field behavior with Gaussian fluctuations at the ferromagnetic phase transition of $SrRuO_3$.* Physical Review B **67,** 100406 (2003).

[245] G. Kresse and J. Furthmüller. *Efficient iterative schemes for ab initio total-energy calculations using a plane-wave basis set.* Physical Review B **54,** 11169 (1996).

[246] P. E. Blöchl, O. Jepsen, and O. K. Andersen. *Improved tetrahedron method for Brillouin-zone integrations.* Physical Review B **49,** 16223 (1994).

[247] G. Singh, A. Jouan, G. Herranz, M. Scigaj, et al. *Gap suppression at a Lifshitz transition in a multi-condensate superconductor.* Nature Materials **18,** 948–954 (2019).

[248] C. Liu, X. Yan, D. Jin, Y. Ma, et al. *Two-dimensional superconductivity and anisotropic transport at $KTaO_3$ (111) interfaces.* Science **371,** 716–721 (2021).

[249] Z. Chen, Z. Liu, Y. Sun, X. Chen, et al. *Two-Dimensional Superconductivity at the $LaAlO_3/KTaO_3$ (110) Heterointerface.* Physical Review Letters **126,** 026802 (2021).

[250] Z. Chen, Y. Liu, H. Zhang, Z. Liu, et al. *Electric field control of superconductivity at the $LaAlO_3/KTaO_3$ (111) interface.* Science **372,** 721–724 (2021).

[251] J. Chakhalian, A. Millis, and J. Rondinelli. *Whither the oxide interface.* Nature Materials **11,** 92–94 (2012).

[252] S. Okamoto. *Doped mott insulators in (111) bilayers of perovskite transition-metal oxides with a strong spin-orbit coupling.* Physical Review Letters **110,** 066403 (2013).

[253] S.-Y. Xu, Q. Ma, H. Shen, V. Fatemi, et al. *Electrically switchable Berry curvature dipole in the monolayer topological insulator WTe_2.* Nature Physics **14,** 900–906 (2018).

[254] Q. Ma, S.-Y. Xu, H. Shen, D. MacNeill, et al. *Observation of the nonlinear Hall effect under time-reversal-symmetric conditions.* Nature **565,** 337–342 (2019).

[255] C. Ortix. *Nonlinear Hall effect with time-reversal symmetry: Theory and material realizations.* arXiv preprint arXiv:2104.06690 (2021).

[256] H. Isobe, S.-Y. Xu, and L. Fu. *High-frequency rectification via chiral Bloch electrons.* Science Advances **6,** eaay2497 (2020).

[257] H. Kambara, Y. Niimi, K. Takizawa, H. Yaguchi, Y. Maeno, and H. Fukuyama. *Scanning Tunneling Microscopy and Spectroscopy of Sr_2RuO_4.* in *AIP Conference Proceedings* **850** (2006), 539–540.

[258] Y. Pennec, N. Ingle, I. Elfimov, E. Varene, Y. Maeno, A. Damascelli, and J. Barth. *Cleaving-temperature dependence of layered-oxide surfaces.* Physical Review Letters **101,** 216103 (2008).

[259] Y. Tang, Y. Zhu, X. Ma, Z. Hong, et al. *A coherently strained monoclinic [111] $PbTiO_3$ film exhibiting zero poisson's ratio state.* Advanced Functional Materials **29,** 1901687 (2019).

[260] A. Zabalo and M. Stengel. *Switching a polar metal via strain gradients.* Physical Review Letters **126,** 127601 (2021).

[261] W. Siemons, G. Koster, A. Vailionis, H. Yamamoto, D. H. Blank, and M. R. Beasley. *Dependence of the electronic structure of $SrRuO_3$ and its degree of correlation on cation off-stoichiometry.* Physical Review B **76,** 075126 (2007).

[262] A. Rastogi, M. Brahlek, J. M. Ok, Z. Liao, C. Sohn, S. Feldman, and H. N. Lee. *Metal-insulator transition in (111) $SrRuO_3$ ultrathin films.* APL Materials **7,** 091106 (2019).

[263] S. Kaneta-Takada, Y. K. Wakabayashi, Y. Krockenberger, S. Ohya, M. Tanaka, Y. Taniyasu, and H. Yamamoto. *Thickness-dependent quantum transport of Weyl fermions in ultra-high-quality $SrRuO_3$ films.* Applied Physics Letters **118,** 092408 (2021).

[264] X. Shen, X. Qiu, D. Su, S. Zhou, A. Li, and D. Wu. *Thickness-dependent metal-insulator transition in epitaxial $SrRuO_3$ ultrathin films.* Journal of Applied Physics **117,** 015307 (2015).

[265] Y. Wang, G. Bossé, H. Nair, N. Schreiber, et al. *Subterahertz Momentum Drag and Violation of Matthiessen's Rule in an Ultraclean Ferromagnetic $SrRuO_3$ Metallic Thin Film.* Physical Review Letters **125,** 217401 (2020).

[266] Y. K. Wakabayashi, S. Kaneta-Takada, Y. Krockenberger, Y. Taniyasu, and H. Yamamoto. *Wide-range epitaxial strain control of electrical and magnetic properties in high-quality $SrRuO_3$ films.* ACS Applied Electronic Materials (2021).

[267] A. Grutter, F. Wong, E. Arenholz, M. Liberati, A. Vailionis, and Y. Suzuki. *Enhanced magnetism in epitaxial $SrRuO_3$ thin films.* Applied Physics Letters **96,** 082509 (2010).

[268] A. Grutter, F. Wong, E. Arenholz, A. Vailionis, and Y. Suzuki. *Evidence of high-spin Ru and universal magnetic anisotropy in $SrRuO_3$ thin films.* Physical Review B **85,** 134429 (2012).

[269] S. Agrestini, Z. Hu, C.-Y. Kuo, M. Haverkort, et al. *Electronic and spin states of $SrRuO_3$ thin films: An X-ray magnetic circular dichroism study.* Physical Review B **91,** 075127 (2015).

[270] S. Kang, Y. Tseng, B. H. Kim, S. Yun, et al. *Orbital-selective confinement effect of Ru 4d orbitals in $SrRuO_3$ ultrathin film.* Physical Review B **99,** 045113 (2019).

[271] G. Mattoni. *Metal–Insulator Transitions in Heterostructures of Quantum Materials.* PhD thesis (Delft University of Technology, 2017).

[272] B. Tanatar and D. M. Ceperley. *Ground state of the two-dimensional electron gas.* Physical Review B **39,** 5005 (1989).

[273] A. Caviglia, S. Gariglio, C. Cancellieri, B. Sacépé, et al. *Two-dimensional quantum oscillations of the conductance at $LaAlO_3$/$SrTiO_3$ interfaces.* Physical Review Letters **105,** 236802 (2010).

[274] H. Yamada and S. Takada. *Negative magnetoresistance of ferromagnetic metals due to spin fluctuations.* Progress of Theoretical Physics **48,** 1828–1848 (1972).

[275] K. Ueda. *Effect of magnetic field on spin fluctuations in weakly ferromagnetic metals.* Solid State Communications **19,** 965–968 (1976).

[276] M. Kataoka. *Resistivity and magnetoresistance of ferromagnetic metals with localized spins.* Physical Review B **63,** 134435 (2001).

[277] C. Xiao, H. Chen, Y. Gao, D. Xiao, A. H. MacDonald, and Q. Niu. *Linear magnetoresistance induced by intra-scattering semiclassics of Bloch electrons.* Physical Review B **101,** 201410 (2020).

[278] A. Abrikosov. *Quantum linear magnetoresistance.* EPL (Europhysics Letters) **49,** 789 (2000).

[279] J. C. Song, G. Refael, and P. A. Lee. *Linear magnetoresistance in metals: Guiding center diffusion in a smooth random potential.* Physical Review B **92,** 180204 (2015).

[280] J. Okamoto, T. Mizokawa, A. Fujimori, I. Hase, et al. *Correlation effects in the electronic structure of $SrRuO_3$.* Physical Review B **60,** 2281 (1999).

[281] C. Alexander, S. McCall, P. Schlottmann, J. Crow, and G. Cao. *Angle-resolved de Haas–van Alphen study of $SrRuO_3$.* Physical Review B **72,** 024415 (2005).

[282] A. Abrikosov. *Quantum linear magnetoresistance; solution of an old mystery.* Journal of Physics A: Mathematical and General **36,** 9119 (2003).

[283] E. Persky, N. Vardi, A. M. R. Monteiro, T. C. van Thiel, et al. *Non-universal current flow near the metal-insulator transition in an oxide interface.* Nature Communications **12,** 1–7 (2021).

[284] J. R. Kirtley and J. P. Wikswo Jr. *Scanning SQUID microscopy.* Annual Review of Materials Science **29,** 117–148 (1999).

[285] P. Reith, X. Renshaw Wang, and H. Hilgenkamp. *Analysing magnetism using scanning SQUID microscopy.* Review of Scientific Instruments **88,** 123706 (2017).

[286] A. Marshall, L. Klein, J. Dodge, C. Ahn, et al. *Lorentz transmission electron microscope study of ferromagnetic domain walls in $SrRuO_3$: statics, dynamics, and crystal structure correlation.* Journal of Applied Physics **85,** 4131–4140 (1999).

[287] L. Klein, Y. Kats, A. Marshall, J. Reiner, T. Geballe, M. Beasley, and A. Kapitulnik. *Domain wall resistivity in $SrRuO_3$.* Physical Review Letters **84,** 6090 (2000).

[288] P. T. Barton, R. Seshadri, and M. J. Rosseinsky. *Electrical and magnetic properties of the complete solid solution series between $SrRuO_3$ and $LaRhO_3$: Filling t_{2g} versus tilting.* Physical Review B **83,** 064417 (2011).

[289] J. Jiang, A. T. Lee, S. Lee, C. Lau, et al. *Electronic properties of epitaxial $La_{1-x}Sr_xRhO_3$ thin films.* Physical Review B **103,** 195153 (2021).

[290] F. Wang and T. Senthil. *Twisted Hubbard model for Sr_2IrO_4: magnetism and possible high temperature superconductivity.* Physical Review Letters **106,** 136402 (2011).

[291] H. Watanabe, T. Shirakawa, and S. Yunoki. *Monte Carlo study of an unconventional superconducting phase in iridium oxide $J_{eff} = 1/2$ Mott insulators induced by carrier doping.* Physical Review Letters **110,** 027002 (2013).

[292] Y. Yan, M. Ren, H. Xu, B. Xie, et al. *Electron-doped Sr_2IrO_4: An analogue of hole-doped cuprate superconductors demonstrated by scanning tunneling microscopy.* Physical Review X **5,** 041018 (2015).

[293] Y. Klein and I. Terasaki. *Insight on the electronic state of Sr_2IrO_4 revealed by cationic substitutions.* Journal of Physics: Condensed Matter **20,** 295201 (2008).

[294] M. Ge, T. Qi, O. Korneta, D. De Long, P. Schlottmann, W. Crummett, and G. Cao. *Lattice-driven magnetoresistivity and metal-insulator transition in single-layered iridates.* Physical Review B **84,** 100402 (2011).

[295] T. Qi, O. Korneta, S. Chikara, M. Ge, et al. *Electron doped $Sr_2IrO_{4-\delta}$ ($0 \le \delta \le 0.04$): Evolution of a disordered $J_{eff} = 1/2$ Mott insulator into an exotic metallic state.* Journal of Applied Physics **109,** 07D906 (2011).

[296] K. Shen, N. Kikugawa, C. Bergemann, L. Balicas, et al. *Evolution of the Fermi surface and quasiparticle renormalization through a van Hove singularity in $Sr_{2-y}La_yRuO_4$.* Physical Review Letters **99,** 187001 (2007).

[297] L. C. Seitz, C. F. Dickens, K. Nishio, Y. Hikita, et al. *A highly active and stable $IrO_x/SrIrO_3$ catalyst for the oxygen evolution reaction.* Science **353,** 1011–1014 (2016).

[298] G. Wan, J. W. Freeland, J. Kloppenburg, G. Petretto, et al. *Amorphization mechanism of $SrIrO_3$ electrocatalyst: How oxygen redox initiates ionic diffusion and structural reorganization*. Science Advances **7,** eabc7323 (2021).

[299] I. Sodemann and L. Fu. *Quantum nonlinear Hall effect induced by Berry curvature dipole in time-reversal invariant materials*. Physical Review Letters **115,** 216806 (2015).

[300] K. Kang, T. Li, E. Sohn, J. Shan, and K. F. Mak. *Nonlinear anomalous Hall effect in few-layer WTe_2*. Nature Materials **18,** 324–328 (2019).

[301] A. Monteiro, D. Groenendijk, I. Groen, J. de Bruijckere, R. Gaudenzi, H. Van Der Zant, and A. Caviglia. *Two-dimensional superconductivity at the (111) $LaAlO_3$/$SrTiO_3$ interface*. Physical Review B **96,** 020504 (2017).

[302] A. Monteiro, M. Vivek, D. Groenendijk, P. Bruneel, et al. *Band inversion driven by electronic correlations at the (111) $LaAlO_3$/$SrTiO_3$ interface*. Physical Review B **99,** 201102 (2019).

[303] U. Khanna, P. K. Rout, M. Mograbi, G. Tuvia, et al. *Symmetry and correlation effects on band structure explain the anomalous transport properties of (111) $LaAlO_3$/$SrTiO_3$*. Physical Review Letters **123,** 036805 (2019).

[304] X. Li, T. Qiu, J. Zhang, E. Baldini, J. Lu, A. M. Rappe, and K. A. Nelson. *Terahertz field–induced ferroelectricity in quantum paraelectric $SrTiO_3$*. Science **364,** 1079–1082 (2019).

CURRICULUM VITÆ

Thierry Christiaan VAN THIEL

04/01/1994 Born in Hoogeveen, Netherlands.

EDUCATION

2005 – 2011 VWO Gymnasium
Johan de Witt Gymnasium
Dordrecht, Netherlands

2011 – 2015 BSc in Applied Physics
Delft University of Technology
Delft, Netherlands

2015 – 2017 MSc in Applied Physics
Delft University of Technology
Delft, Netherlands
Thesis: *Magnetotransport in $SrRuO_3$/$SrIrO_3$ heterostructures*
Supervisor: Dr. A.D. Caviglia

2017 Research Internship, TNO
Topic: Fast optical coherence tomography
Supervisor: L. Cheng

2017 – 2021 PhD in Applied Physics
Delft University of Technology
Delft, Netherlands

Thesis: *Coupling lattice, charge and topological reconstructions at oxide interfaces*
Promotors: Dr. A.D. Caviglia
Dr. A.R. Akhmerov

List of Publications

11. E. Lesne, Y.G. Sağlam, R. Battilomo, **T.C. van Thiel**, U. Filippozzi, M. Cuoco, G.A. Steele, C. Ortix and A.D. Caviglia. *Designing Berry curvature dipoles and the quantum nonlinear Hall effect at oxide interfaces.* In preparation.

10. M. Lee, J.R. Renshof, K.J. van Zeggeren, M.J.A. Houmes, E. Lesne, M. Šiškins, **T.C. van Thiel**, M.R. van Blankenstein, A.D. Caviglia, H.S.J. van der Zant and P.G. Steeneken. *Nanomechanics of ferroelectric switching in suspended van der Waals-complex oxide heterostructures.* In preparation.

9. M. Lee*, **T.C. van Thiel***, S. Mañas-Valero, Y.M. Blanter, T.M. Klapwijk, E. Coronado, P.G. Steeneken, A.D. Caviglia and H.S.J. van der Zant. *Single-crystal van der Waals superconductor microbridge and gate independence.* In preparation.

8. V. Shalabaeva, **T.C. van Thiel**, M. Lee, R. Hogenbirk, P.G. Steeneken and A.D. Caviglia. *Interface engineering of single crystal WO_3/$SrTiO_3$ heterostructures for ultra-sensitive hydrogen sensing in air.* In preparation.

7. M. Lee, M. Robin, R. Guis, U. Filippozzi, D.H. Shin, **T.C. van Thiel**, S. Paardekoper, J.R. Renshof, H.S.J. van der Zant, A.D. Caviglia, G.J. Verbiest, and P.G. Steeneken. *Self-sealing complex oxide resonators.* arXiv:2109.03978. Under review.

6. **T.C. van Thiel**, W. Brzezicki, C. Autieri, J.R. Hortensius, D. Afanasiev, N. Gauquelin, D. Jannis, N. Janssen, D.J. Groenendijk, J. Fatermans, S. van Aert, J. Verbeeck, M. Cuoco and A.D. Caviglia. *Coupling charge and topological reconstructions at polar oxide interfaces.* Physical Review Letters, **127(12)**, 12720-2 (2021).

5. E. Persky, N. Vardi, A.M.R.V.L. Monteiro, **T.C. van Thiel**, H. Yoon, Y. Xie, B. Fauqué, A.D. Caviglia, H.Y. Hwang, K. Behnia, J. Ruhman and B. Kalisky. *Non-universal current flow near the metal-insulator transition in an oxide interface.* Nature Communications, **12(1)**, 1-7 (2021).

4. D.J. Groenendijk*, C. Autieri*, **T.C. van Thiel***, W. Brzezicki*, J.R. Hortensius, D. Afanasiev, N. Gauquelin, P. Barone, K. H. W. van den Bos, S. van Aert, J. Verbeeck, A. Filippetti, S. Picozzi, M. Cuoco, and A. D. Caviglia. *Berry phase engineering at oxide interfaces.* Physical Review Research, **2(2)**, 023404 (2020).

3. M. Matthiesen, D. Afanasiev, J.R. Hortensius, **T.C. van Thiel**, R. Medapalli, E.E. Fullerton and A.D. Caviglia. *Temperature dependent inverse spin Hall effect in Co/Pt spintronic emitters.* Applied Physics Letters, **116(21)**, 212405 (2020).

2. **T.C. van Thiel**, J. Fowlie, C. Autieri, N. Manca, M. Šiškins, D. Afanasiev, S. Gariglio and A.D. Caviglia. *Coupling lattice instabilities across the interface in ultrathin oxide heterostructures.* ACS Materials Letters, **2(4)**, 389-394 (2020).

1. **T. C. van Thiel***, D.J. Groenendijk* and A.D. Caviglia. *Extraordinary Hall balance in ultrathin $SrRuO_3$ bilayers.* Journal of Physics: Materials, **3(2)**, 025005 (2020).

*equal contribution

ACKNOWLEDGEMENTS

I have wandered around TU Delft for over 10 years and have over time come to view it as a second home. The Oxford learner's dictionary defines the word *home* as *the house or flat that you live in, especially with your family*. The word family here is particularly important, since it is the amazing people I have had the opportunity to meet that made TU Delft and in particular the QN department feel like home to me. The following is by no means exhaustive, but a concise summary of all those that have made my time here memorable.

I will start with my promotors **Andrea** and **Anton**, whose mentoring and supervision have been instrumental. **Andrea**, we met during the MSc course on advanced solid-state physics that you taught together with **Yaroslav**. From the first minute, your enthusiasm for condensed matter physics was infectious. Together with **Bas**, **Jorrit** and later **Andrew**, I was drawn to your group to pursue a MSc project, during which I had a fantastic time. I was very happy when you offered me a PhD position and I gladly accepted. While the scientific part may not have been the smoothest of roads, with at times tough reviewers and stubborn equipment to deal with, I would certainly do it again given the choice. Your supervision style left room for me to explore a wide variety of projects, which were not always successful, nor were they directly related to the project I was hired for. For this, I am very grateful. When it came to discussing scientific projects, you were always enthusiastic and managed to motivate with your positive attitude, even if things did not look promising. We had many long conversations over the phone, which usually started out scientific but often transitioned into a more personal chat, something I always found very pleasant. Thank you for everything. I wish you all the best with your new position in Geneva. Delft will surely miss you!

Anton, even though your supervisory role was mostly formal, you were always very welcoming and your door was always open for questions and discussion. I still chuckle when I think about that time at a dinner I managed to impress you with my Dutch skills while ordering a drink. I guess those 25 years of practice paid off. I wish you the best with your quest for Open Science, a movement that will undoubtedly be a change for the better in the scientific community.

I owe a significant debt of gratitude to those who agreed to go through this thesis in detail and examine it, the committee members. **Yaroslav**, I have been a student of yours twice over, first during my time in the BSc programme where you taught modern physics and then later in the advanced solid-state physics course as part of the MSc programme. I always thoroughly enjoyed your teaching and am very happy that I eventually got to work with you as a teaching assistant, which was both an educational and fun experience. Thank you for the nice chats during spontaneous coffee breaks, I will miss them.

Mario, I view you as my adopted supervisor. Whenever I was confused about a theoretical concept, you were always immediately available to help. I cherish our long online meetings where we passionately discussed about physics and sporadically about other topics, often relating to Italian culture. Your contributions to this thesis have been invaluable and I am deeply grateful I had the opportunity to work with you.

Beena, when **Mafalda** finished her PhD, she told me her collaboration with you was the best one she ever had. Now at the end of my own stint, I can only say that I fully agree. Time and time again, I have been amazed by the beautiful data you and your group have measured on the samples we sent you. I thoroughly enjoyed the many stimulating discussions about the underlying physics, as well as the friendly chats we had. I am looking forward to see what exciting discoveries will come from your lab in the future!

Sonia, you are probably the most cheerful P.I. in the department. Seeing your interaction with your group members, as well as other department members is uplifting. Aside from leading an expanding group, you managed to find the time to develop the social core of the department together with **Sonakshi**, **Victoria**, **Gary** and **Lizzy**, which in my view is essential for a pleasant working environment. It's a shame we did not get to collaborate more scientifically, but your efforts for the department have still made an important contribution to my time here.

Thom Palstra, we only interacted briefly, yet your extensive knowledge of condensed matter physics became immediately apparent. I am excited to have someone of your calibre in my committee. Thank you for the improvement suggestions on my thesis, they have been very helpful!

Peter, ever since our group started to develop freestanding oxides, a synergy with your group emerged. While my involvement with the freestanding oxide projects was minor, we still got to collaborate in other fun projects that were spearheaded by one of your rebellious students, co-supervised by **Herre**. Even though those projects often strayed from the main objectives of your research, you indulged us in our scientific mischief. Thank you!

The purpose of a PhD programme is often phrased as the candidate developing into an independent scientist. Starting out, I found this term confusing, wondering whether it meant that all scientific results must be obtained independently. As time went on, I came to realise that this was not the right approach and that teamwork and collaboration are vital. Indeed, many people have made important contributions to the results presented in this thesis, both scientific or otherwise. **Carmine**, **Wojtek**, together with **Mario** you were the theory dream team. Thank you for putting up with all my emails about theoretical concepts and derivations I had trouble wrapping my head around. You have made invaluable contributions to this thesis and I am extremely grateful we got to work together on so many interesting projects. **Nicolas**, **Daen**, in spite of your busy schedules, you always managed to find the time to slip in our samples and produce gorgeous images and crucial structural data. Thank you for all your efforts. **Jennifer**, **Stefano**, thanks for all your help on the iridate project, your expertise on half-order peaks was crucial. The measurement campaign we had at the synchrotron at Diamond was great fun! **Eylon**, **Sepir**, **Anshu**, as mentioned before, our collaboration with you has been phenomenal. The data you acquired with **Beena** is impressive, both in terms of the content and the amount. I look forward to when we finally get to present it in its full

glory to the outside world! **Philipp**, **Giorgio**, **Carmine** (the other Carmine), thank you for the collaboration and all the nice meetings, including the one where we were stranded in Denver. I learned a lot from interacting with you and I am certain that all our efforts over the past years will soon pay off! **Steffen**, **Davide**, **Claudius**, thank you for all the help during the measurement campaign at the HFML. I apologize for the clumsy, albeit spectacular, chair incident.

Support comes in many forms, sometimes scientific, other times technical or logistical. Both are vital towards the successful completion of a PhD. **Tino**, thanks for the chats during breaks and for the trips to Enschede and Leiden to drop off whatever piece of equipment was broken at the time. I imagine I gave you a bit of a scare with the RHEED incident (and myself as well), but thankfully it all turned out to not be as bad as it may have initially seemed. **Tom**, a mechanical wizard and above all kind person, thanks for always immediately helping us with any technical aspect we were clueless about. It was truly a pleasure to work with you! The same goes for **Ronald**, whose machining skills have evolved into legend. **Marijke**, **Heleen**, **Maria**, **Erika**, **Lizzy**, **Etty**, thank you for always swiftly helping us to take care of the logistics of sample shipping, figuring out Alusta, reminding us to fill in our hours so we get paid and of course for organizing all the fun QN activities! A big thanks as well to all the unsung heroes that work in the cleanroom, including but not limited to **Marc**, **Mark**, **Arnold**, **Marco**, **Eugène**, **Ewan**, **Charles**, **Anja**, **Hozanna**, **Pauline**, **Bas** and **Lodi**. I owe a debt of gratitude to DEMO and all those involved with engineering such fantastic equipment for sensitive electrical measurements and of course for their always useful advice!

Up next are the quantum founders, the ones who witnessed the birth of the lab and made it into what it is today. **Emre**, we did not get to interact much, but the laptop I inherited from you is still going strong. Best of luck with the injectable electronics! **Giordano**, aside from an impressive scientific output, you created an extremely user-friendly measurement setup, which has been instrumental for many projects. I am sad that eventually Python 2 had to be retired, but the next edition of the code is heavily inspired by your work. I wish you all the best in Japan and wherever your aspirations bring you next! **Mafalda**, when I started, you and **Dirk** showed me the ropes and were always there with good advice. Even when you were close to finishing your PhD, you took the time to teach me about that pesky dilution refrigerator. It took two years, but we ultimately managed to get it working properly again (knock on wood). A.T. Kearney has gained a valuable employee, while science has lost out. **Dirk**, my guide ever since I joined as a MSc student. Starting out, you provided me with projects, taught me the skills needed to grow films, fabricate devices and perform transport measurements. We thought our work on Berry phase engineering would take the community by storm. Sadly, it didn't turn out to be so easy. While it may not have gone the way we hoped, I think we still managed to shake things up in the community, with our message now getting the attention I think it deserves. Thank you for all your help! **Nicola**, thanks for the fun measurement campaign in Didcot and for the great conference in Genova! I hope you are getting more sleep now.

Taking over from the quantum founders was the next (and last) generation of the Delft lab. **Dima**, apart from being a terrific scientist, you are a fantastic colleague and above all a great friend. I am glad I met someone who is as enthusiastic about horror movies (or even more so). Thank you for all the fun conferences we attended together, the climbing

sessions, trips to Fontainebleau and of course the very very lengthy phone conversations about random topics. You managed to get that coveted tenure track position in Nijmegen and well-deservedly so. I am extremely happy for you and I am certain that you will be very successful. All the best to you and **Albina**, be sure to stay in touch!

Jorrit, partner in crime together with **Dima**, pumping *alles wat los en vast zit*[1]. Your discipline and work ethic is legendary and has rewarded you with many impressive scientific results. Thank you for all the spontaneous conversations during breaks and of course for all the fun conferences! I normally do not often catch colds, but the ones I did catch always seemed to occur right before pretty much all conferences we attended together. I hope you can forgive me for repeatedly infecting you with my germs (although **Iacopo** is probably also partly to blame). It was all purely coincidental, I think. **Yildiz**, you were tasked with an incredibly challenging project. Still, you managed to keep pushing and keep in good spirits. I wish you the best of luck finalizing the PhD and with your new position at ASML.

Edouard, you are a true academic, always eager to engage in long discussions about physics (and other equally important aspects of life). Thanks for being a fellow devil's advocate during lab meetings, a role that I personally feel is essential for a proper academic discussion. You were always happy to spend time helping those who needed it, a quality that is too often undervalued. Thanks for all the stimulating discussions over the course of many after-work beers, dinners and barbecues. All the best to you and **Franzi** in Dresden!

Mattias, one of the brightest people I have met, with a tireless can-do attitude. When a crystal shatters, it is not broken, but has multiplied into many functional samples. I hope you will not give up on the moka moka† experiment, although incorporating a blast shelter or at least some safety goggles for the next run is probably a good idea. **Patrick**, you are working on an incredibly challenging project with many hurdles to overcome. The group moving to Geneva also does not make things any easier. Nevertheless, I have great respect for all the hard work you are putting in and I am positive that it will ultimately pay off! **Victoria**, I will miss the passionate discussions about Russian and Italian culture, particularly relating to how they sometimes clash with the Dutch one. It was very nice to have you as a colleague and I hope you will be very happy at the start-up in Rotterdam.

Ulderico, also known as *Rik Philips* or *Rik Filipizza*, an exceedingly bright student with a passion for physics and kind personality to match. The equipment moving to Geneva adds extra difficulty, but if there is someone who can make it work, it is you. I really enjoyed working together with you this past year and regret it has to end, particularly the clowning around in the lab after 4pm (or sometimes earlier). Aside from physics, you are a man of multiple talents, including but not limited to coffee brewing, fine craftsmanship, cooking and meat grilling. We made sure you got some practice in the latter after the Euro 2021. Thank you and **Federica** both for all the lovely after-work drinks and dinners, I hope the future will bring many more of them!

Martin, perhaps not *de jure*, but a *de facto* member of the lab and the keeper of the stamping wisdom in the department. Our collaboration and friendship has been one of the highlights of my PhD and I will fondly look back on it. Even though many of the

[1] everything loose and fast

'Friday afternoon' projects we tried were unsuccessful, it did not make them any less fun! Thanks for the always enjoyable spontaneous (procrastination) coffee breaks, for introducing me to KFC and for the lovely pastries produced with **Sara**. Good luck in Munich and be sure to stay in touch!

Lastly, the students I had the privilege of working with during their graduation projects and who had large contributions in making my time in Delft memorable. **Niels**, you were incredibly hard working and very thorough. In spite of personal issues troubling you towards the end, you managed to produce a beautiful thesis. I am happy I had the chance of working with you and getting to know you! **Hélène**, your perseverance is unparalleled. Even with a broken arm, you still insisted on continuing experimental work. While the project did not yield the experimental results we were hoping for, the theoretical modelling you did was very impressive. Good luck with your PhD in the group of **Anton**, I am sure it will be a successful one! **Ludwig**, your enthusiasm is astonishing, both for physics (and in particular LAO/STO), as well as for surfing, baking and climbing. You went through a daunting amount of literature, learned how to operate a tricky old dilution refrigerator and truly made the project your own. On top of that, you have an exceptionally warm and welcoming personality. Together with **Ulderico**, **Martin** and **Edouard**, we made an impressive team in the lab, our experimental prowess eclipsed only by our poor taste in jokes (admittedly mostly my fault, apologies). Thank you for all the relaxing coffee breaks together with **Isacco**, the climbing sessions, dinners and fun at the beach. Hopefully flunky ball will at some point become an Olympic event.

The QN department is and has been home to many more amazing people, whom words alone fail to describe or acknowledge. **Holger**, a true physicist, always willing to engage in discussions and brainstorms with newbie PhD students, even if it does not directly relate to your own work. Thank you for the weekly drinks, dinners and football matches we watched together with, among others, **Nikos**, **Iacopo**, **Joeri**, **Pascal**, **Marc** and **Edouard**. **Makars**, thanks for the collaboration on the iridates and for the summer evening drinks on the roof, it was a pleasure! Rest assured, the secret passage shall remain secret! **Nikos**, together with **Martin** one of the best examples of the PhD student delocalization phenomenon. Thanks for working together on the *Frosti*! **João**, good luck at ING, I hope your physics background is serving you well! **Dejan**, sorry for my part in the *Belastingdienst* prank! **Ranko**, it was always a nice to talk to you! I hope you are no longer hiding your mastery of the Dutch language now. **Davide**, thanks for the climbing sessions and for introducing me to *Secret Hitler*, probably one of my all time favorite games! **Lorenzo**, I had great fun T-A-ing (if that is a word) advanced solid-state physics together! **Iacopo**, expert on (in no particular order) Italian and Greek cuisine, fine wines, spin waves, sailing, NV centers, skiing, karaoke and convincing people to come for a drink at TeePee. When the department was ruled by Italians in the MED days, tradition was to rebaptize Dutch members with an Italian name. It only seems fair to return the favour. *Jakob Bartels*, thanks for the many dinners and gin-tonics at GRK&ZO and of course the legendary APS trip, together with **Jorrit** and **Adrian**! **Brecht**, you are as resilient as you are friendly. Your hard work developing those wretched tips is finally paying dividends and it is more than deserved. Thanks for always being such a pleasant person to talk to. I wish you good luck with the final stint of the PhD! **Samer**, the extraordinarily happy and above all friendly postdoc. Your enthusiasm for science and drive

for personal development are inspiring and rivalled only by your tremendous appetite. All the best to you and **Fran**! **Michael**, it's always fun to talk to you. Thanks for always sharing your dessert with the dinner table! **Joris**, thanks for a memorable winterschool at Courchevel! **Allard**, scanning probe and game show expert, I am looking forward to your next television appearance! **Rasa**, your ever good spirits and kind personality are truly uplifting and a force for good in the department. May it never diminish! Thanks for the always pleasant lunch breaks together with the other members of the Otte gang; **Lukas**, **Letty**, **Alex**, **Evert**, **Rik**, **Hester** and **Sander**. **Adrian**, I enjoyed our frequent philosophical discussions over coffee, often together with **Sarwan**. I hope you realise your goal of becoming a chess master! **Sonakshi**, **Niccolo**, thanks for always lighting up the room! **Luigi**, van der Waals expert, criminal catcher and pun pundit, I would definitely put at least two of those on your CV. **Hristo**, enjoying life to the fullest with always a fun story to tell about your crazy motorcycle road trips. Ride safe and good luck wrapping up the PhD! **Heng**, **Yaojia**, two amazingly friendly and hard working people. I hope you will embrace that European tradition of occasionally taking a long holiday to travel, you will not regret it!

Gary, my mentor, it is always a pleasure to talk to you. Thank you for providing the department with delicious espresso all these years, the fuel that drives progress. If you ever decide to map out that coffee brewing phase space, please share it with me! **Toeno**, thanks for the Colorado mountain trip, a great alternative to a cancelled conference! I wish we had brought a decent pair of shoes though, those 'few' centimeters of snow were surprisingly tough to get through. **Herre**, thanks for always letting me borrow your equipment and for the fun anecdotes. Walking past your lab and seeing a helium balloon the size of an exercise ball never gets old. **Teun**, thank you for the very educational discussions on superconductivity and for holding **Martin** and myself to a high standard. **Maz**, despite you having joined the department only recently, it seems like I have known you for much longer and I am probably not the only one who feels this way. Thanks for immediately embracing the social aspect of working together in a department, QN is lucky to have you!

A special mention goes to a *cluster* of people I hold dear. **Maria**, the stabilizing force and matriarch. On top of your numerous scientific competences, you are an amazing friend with a strong character and an incredibly kind personality. I fondly look back upon the fun activities we did together with **Chunwei**, **Martin**, **Luca** and **Edouard**; the LN_2 ice cream, summer picnics, barbecues and of course the delicious home-cooked dinners. I wish you all the strength in the world. **Sergei**, **Luca** (also known as *Luuk van Oranje*) my office mates, gambling buddies and sparring partners in numerous brainstorms. I will miss our daily chats!

Finally, a big thanks to all those who make/made the QN department what it is; **Kobus**, **Simon**, **Richard**, **Sabina**, **Matvey**, **Behnam**, **Mario**, **Marios**, **Felix**, **Byoung-moo**, **David**, **Kostas**, **Sanchar**, **Thomas**, **Martin**, **Irina**, **Andreas**, **Moritz**, **Jingkun**, **Matthijs**, **Nina**, **Jérémie**, **Miguel**, **Sabrya**, **Maarten**, **Andrea**, **Maurits**, **Dong Hoon**, **Gabriele**, **Pablo**, **Josep**, **Damian**, **Jasper**, **Thomas**, **Jackie** and everyone else!

Zoals eerder genoemd komt steun in meerdere vormen en bovendien vanuit verschillende bronnen. De laatste paragrafen wijd ik toe aan diegenen die mij, zowel expliciet als impliciet, bewust of onbewust, altijd een hart onder de riem wisten te steken tijdens

stressvolle perioden. **Rogier**, **Mariska**, al meer dan 10 jaar lang door dik en dun mijn Delftse lotgenoten, bedankt voor de vele heerlijke zelfgebrouwen biertjes, Mortal Kombat sessies en spelletjesavonden. Veel success met de laatste loodjes! **Ivy**, de tandarts die verdacht veel zoetigheid produceert, bedankt voor alle heerlijke baksels, je enorme gastvrijheid en natuurlijk voor de fantastische vakantie samen met **Chak**. **Chak**, één van de meest energieke maar ook vriendelijke personen die ik ken, met jou is het nooit saai! **Else**, **Rob**, bedankt voor alle uitbundige Sinterklaasspelletjes, hopelijk een blijvende traditie. **Nyrée**, ik zal deze keer sarcasme proberen te vermijden, aangezien dat in het verleden tot de nodige misverstanden heeft geleid. Bedankt voor alle spelletjesavonden, etentjes en nog te organiseren wijnproeverijen met **Maarten**, **Anniek**, **Rianne** en **Ben**. **Wouter**, ik ben blij dat we het contact weer opgepakt hebben, verbazingwekkend hoe de tijd altijd vliegt. **Jermo**, **Marcha**, **Mark**, **Mark**, **Martijn**, **Sam**, op het werk heb ik kennelijk de reputatie dat ik slechte grappen maak. Het is maar goed dat mijn collega's nooit onze *Jackbox* sessies mee hebben gemaakt, dat zou vermoedelijk een traumatische ervaring zijn geweest. Bedankt voor alle klimsessies, motortochtjes, trips naar Fontainebleau en chillavonden!

Mourits, **Christie**, **Jos**, **Roxanna** en de rest van de *Stapeltjes* en *Schijfjes*. Vanaf het begin af aan hebben jullie mij met open armen in de familie verwelkomd en ben ik me er gelijk thuis gaan voelen. Op jullie kan ik altijd rekenen en dat is werkelijk onbetaalbaar. Ik zal er in de toekomst ongetwijfeld nog vaker beroep op gaan doen. Ik ben dankbaar dat ik deel uit mag maken van jullie familie.

Mam, **Pap**, een tijdje leek het erop alsof een loopbaan in de bètawetenschap niets voor mij was en besloot ik bewust een andere kant op te gaan. Mettertijd besefte ik (en misschien jullie ook wel) dat dit een fout was. De rest is geschiedenis. Goede of slechte keuzes, jullie hebben altijd gezorgd voor een fijne thuisomgeving en me altijd op alle mogelijke manieren geholpen. Het is werkelijk van onschatbare waarde geweest. Bedankt voor jullie onvoorwaardelijke liefde en steun! **Pap**, bedankt voor het uitgebreide proeflezen!

Erwin, **Eva**, mijn ooit kleine broertje en zusje, inmiddels volwassen met allerlei diploma's op zak. Het is ontzettend mooi geweest om te zien hoe hard jullie gewerkt hebben de afgelopen jaren, de tegenslagen die jullie hebben overwonnen en de mooie resultaten die jullie behaald hebben. Ik weet zeker dat de toekomst mooie dingen brengen zal. **Eva**, bedankt voor het produceren van alle mooie afbeeldingen en voor het helpen met de omslag! **Ingrid**, bedankt voor alle gezelligheid en voor het spekken van onze (digitale) boekenkast! **Opa**, helaas bent u er niet meer om dit proefschrift mee te maken. Toch ga ik er vanuit dat u er niet minder trots om bent. Rust zacht.

Karlijn, jouw bijdrage aan dit proefschrift is werkelijk niet in woorden uit te drukken. Naast de directe bijdragen als proeflezen en het schetsen van een illustratie voor de omslag, zijn jouw indirecte bijdragen van onschatbare waarde geweest. Jaar in jaar uit was ik laat thuis en vaak met weinig energie over. Ondanks jouw eigen stressvolle baan als arts wist je het toch altijd op te brengen om mij op alle mogelijke manieren te steunen, een teken van jouw grenzeloze zorgzaamheid en geduld. Ik prijs mezelf ontzettend gelukkig dat ik jou in mijn leven heb. Bedankt voor alles. Ik hou van je.

Vlaardingen, 8 Januari 2022

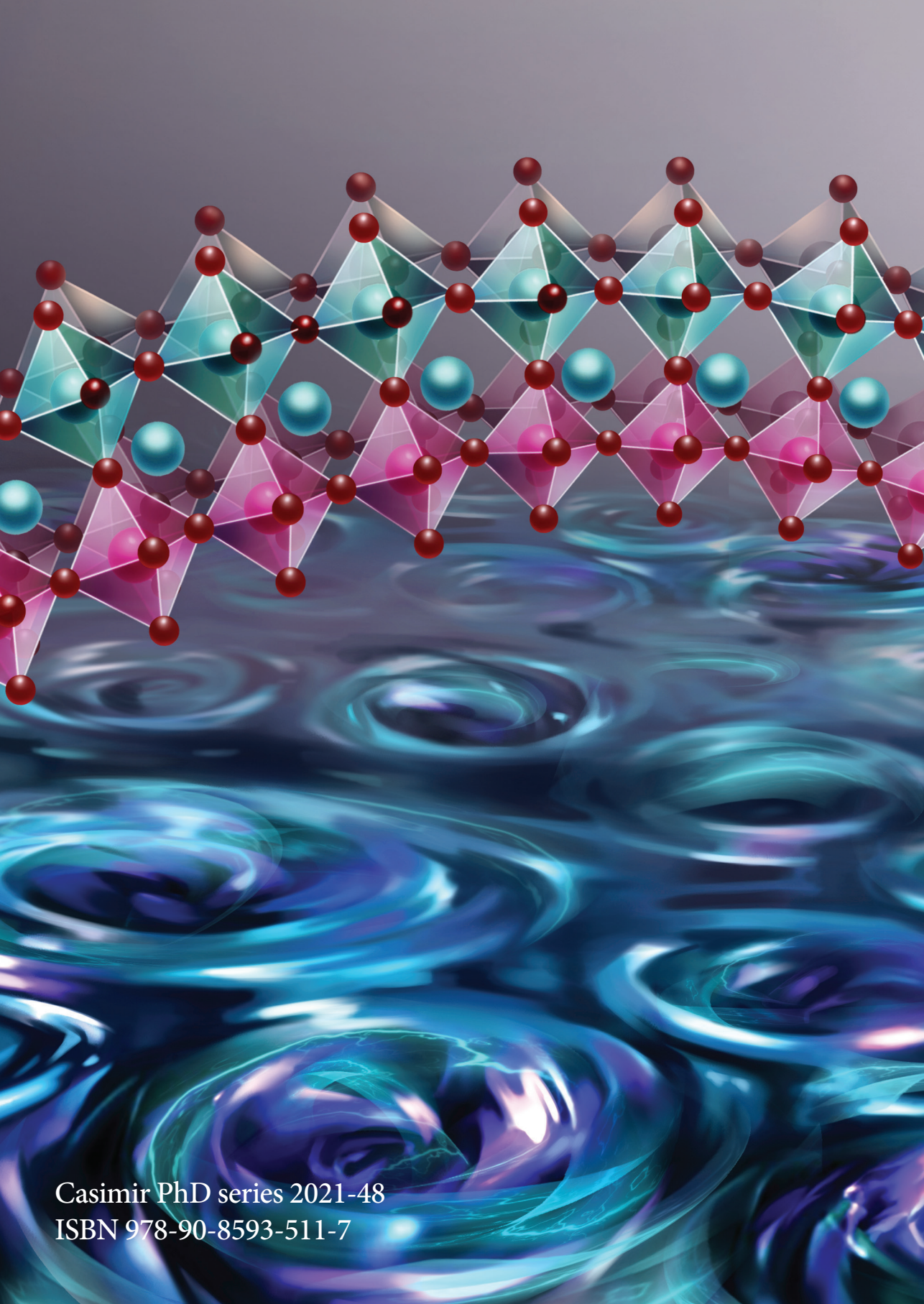

Casimir PhD series 2021-48
ISBN 978-90-8593-511-7